BEILSTEIN JOURNAL OF NANOTECHNOLOGY

Energetic ions and photons for engineering nanomaterials

Edited by Devesh Kumar Avasthi and Venugopal Rao Soma

Imprint

Beilstein Journal of Nanotechnology
www.bjnano.org
ISSN 2190-4286
Email: journals-support@beilstein-institut.de

The *Beilstein Journal of Nanotechnology* is published by the Beilstein-Institut zur Förderung der Chemischen Wissenschaften.

Beilstein-Institut zur Förderung der Chemischen Wissenschaften
Trakehner Straße 7–9
60487 Frankfurt am Main
Germany
www.beilstein-institut.de

BEILSTEIN JOURNAL OF NANOTECHNOLOGY

Effect of wavelength and liquid on formation of Ag, Au, Ag/Au nanoparticles via picosecond laser ablation and SERS-based detection of DMMP

Sree Satya Bharati Moram[1,2], Chandu Byram[1,3] and Venugopal Rao Soma[*1,4]

Full Research Paper

Open Access

Address:
[1]Advanced Centre for Research in High Energy Materials (ACRHEM), DRDO Industry Academia - Centre of Excellence (DIA-COE), University of Hyderabad, Prof. C. R. Rao Road, Hyderabad 500046, Telangana, India, [2]Department of Physics, Indian Institute of Technology Hyderabad, Kandi 502285, Telangana, India, [3]Department of Physics, College of Arts and Sciences, University of Dayton, 300 College Park, Dayton, Ohio 45469, USA and [4]School of Physics, University of Hyderabad, Prof. C. R. Rao Road, Hyderabad 500046, Telangana, India

Email:
Venugopal Rao Soma[*] - soma_venu@uohyd.ac.in

* Corresponding author

Keywords:
dimethyl methyl phosphonate; laser material interaction; metal nanoparticles; picosecond laser ablation; SERS; thiram

Beilstein J. Nanotechnol. **2024,** *15,* 1054–1069.
https://doi.org/10.3762/bjnano.15.86

Received: 15 April 2024
Accepted: 02 August 2024
Published: 19 August 2024

This article is part of the thematic issue "Energetic ions and photons for engineering nanomaterials".

Associate Editor: P. Ayala

Abstract

The present study investigates the effects of input wavelength (1064, 532, and 355 nm) and surrounding liquid environment (distilled water and aqueous NaCl solution) on the picosecond laser ablation on silver (Ag), gold (Au), and Ag/Au alloy targets. The efficacy of the laser ablation technique was meticulously evaluated by analyzing the ablation rates, surface plasmon resonance peak positions, and particle size distributions of the obtained colloids. The nanoparticles (NPs) were characterized using the techniques of UV–visible absorption, transmission electron microscopy, and energy-dispersive X-ray spectroscopy. Furthermore, NPs of various sizes ranging from 6 to 35 nm were loaded onto a filter paper by a simple and effective drop-casting approach to achieve flexible surface-enhanced Raman spectroscopy (SERS) substrates/sensors. These substrates were tested using a simple, portable Raman device to identify various hazardous chemicals (malachite green, methyl salicylate, and thiram). The stability of the substrates was also systematically investigated by determining the decay percentages in the SERS signals over 60 days. The optimized SERS substrate was subsequently employed to detect chemical warfare agent (CWA) simulants such as methyl salicylate (a CWA simulant for sulfur mustard) and dimethyl methyl phosphonate (has some structural similarities to the G-series nerve agents) at different laser excitations (325, 532, and 633 nm). A notably higher SERS efficiency for CWA simulants was observed at a 325 nm Raman excitation. Our findings reveal that a higher ablation yield was observed at IR irradiation than those obtained at the other wavelengths. A size decrease of the NPs was noticed by changing the liquid environment to an electrolyte. These findings have significant implications for developing more efficient and stable SERS substrates for chemical detection applications.

Introduction

Metal nanoparticles (NPs) are versatile materials widely used across various scientific and technological fields due to their distinctive optical, physical, and chemical properties. Over the past few decades, different methods have been developed for NP synthesis, including chemical reduction, electrochemistry, atomic layer deposition, laser ablation synthesis in solution (LASiS), and sputtering [1]. The LASiS technique has been proven to be cost-effective in producing various shapes of NPs with distinct size distributions in a short time (a few minutes). It offers many advantages including high purity, minimal contamination, and precise control over NP size and composition, making it a preferred choice for nanomaterials synthesis [2-5]. The process involves laser plasma interacting with a metal in a liquid; it excites electrons, which then generates atomic vibrations within a few picoseconds, causing rapid heating, melting, and explosive decomposition of the metal surface. This results in an explosive ejection of vapor and liquid from the surface. The metal plume cannot freely expand in water and is slowed down, forming a hot metal layer at the water interface. The hot metal layer heats the water to a supercritical state, mixing metal atoms with water. The expanding metal/water mixture promotes rapid nucleation and growth of small metal NPs and contributes to forming a cavitation bubble. The hot metal layer also breaks into larger droplets due to instabilities, creating NPs of different sizes within a few nanoseconds of laser exposure [6]. The properties of NPs, such as size, shape, crystallinity, productivity, and composition, can be influenced by several experimental parameters during synthesis [4,6-10]. The impact of laser parameters, such as pulse duration, wavelength, repetition rate, and fluence, and of the liquid parameter on NP productivity, shape, and size distribution remains an area of ongoing research [11-15]. Pulsed laser irradiation of liquids (PLIL) can affect the size and shape of NPs. Various approaches are described in the literature, such as (i) laser fragmentation in liquid (LFL), (ii) laser melting in liquid (LML), and (iii) laser defect engineering in liquid (LDL) [16]. In our previous work, we fabricated Ag–Cu alloy NPs using the femtosecond (fs) laser irradiation approach [17]. Similarly, Ag/Au alloy NPs were fabricated by laser ablation of single metal targets in water followed by re-irradiation of mixed colloidal suspensions, as demonstrated by Compagnini et al. [18]. Additionally, Zhang et al. [19] reported the LML approach to synthesize germanium submicron spheres from picosecond (ps) laser irradiation of Ge powders containing nanoscale and microscale particles. Maximova et al. [20] achieved size-controllable Au NPs in stable solutions via femtosecond laser fragmentation, tuning sizes by adjusting fluence. This technique is employed to create various categories of alloy NPs [21]. Alloying by LASiS can mitigate undesired features associated with plasmonic materials, such as high cost, chemical instability, and sustainability issues [22,23]. Menéndez-Manjón et al. [24] reported the synthesis of Ag/Au alloy NPs via picosecond LASiS of solid targets in monomer MMA. Amendola et al. [25] demonstrated the fabrication of magneto-plasmonic alloy NPs, such as Fe–Au, by laser ablating Au/Fe multilayers with varying thicknesses and deposition orders. Jakobi et al. [26] reported the synthesis of Pt–Ir alloy NPs by femtosecond laser ablation of a Pt_9Ir target in acetone and further utilized as PtIr electrodes. In recent years, laser-ablated NPs/NSs have gained prominent interest in many applications, such as photoelectronic devices, biochemical sensors, and surface-enhanced Raman spectroscopy (SERS) substrates, due to their high purity NPs as well as an easy method for altering the structures, NPs/NSs sizes, and morphology by tuning the laser parameters and surrounding media [27-29]. The SERS substrate efficiency mainly depends on the material, size, and shape of the NPs. Recent terrorist activities involving explosives and chemical warfare agents highlight the urgent need for sensitive and selective chemical sensors. These sensors must be using low power and be capable of trace detection. Dimethyl methyl phosphonate (DMMP) is commonly used as a less toxic simulant for sarin, a G-series nerve agent. DMMP can, in general, be used in making chemical weapons. Zheng et al. [30] reviewed various methods for DMMP detection, including mass-sensitive sensors, surface acoustic wave (SAW) sensors, microelectromechanical systems (MEMS), carbon nanotubes, and chemiresistive sensors. SERS-active substrates encounter obstacles in translation toward practical applications, primarily due to the difficulty of sample collection. As a result, there is a persistent need for affordable and accessible fabrication methods which guarantee stability and reproducibility along with accessible sample collection of SERS substrates. There has been significant interest in utilizing flexible materials such as paper, nitrocellulose, polymer film, cotton fabrics, adhesive tape, glass fibers, and biomaterials for constructing flexible SERS substrates, owing to their numerous advantages over traditional options such as glass and silicon [31-39]. Detecting hazardous molecules, such as pesticides, explosives, and chemical threats (nerve agents) using flexible SERS substrates is the central aspect of the sensing field because of its simple sample collection from any rough surface [36,40]. Filter paper (FP) SERS substrates are rigorously investigated for the detection of hazardous dye molecules such as crystal violet (CV) and malachite green (MG) on fish [41], pesticides on vegetables, dals [42], fruit surfaces [43], and explosives on rough surfaces [44,45]. In the last few years, our group has been continuously working on developing a flexible SERS substrate for the detection of various types of hazardous molecules: aggregated Ag and Au NPs on filter paper [46], Au NPs on electrospun polymer nanofibers [33], and alloy Ag/Au NPs on filter paper [44]. However, the size-dependent SERS performance of NPs

over time needed to be investigated, and the optimization of substrates, depending on their stability over time, was aimed to be studied.

This study investigated the impact of 355, 532, and 1064 nm wavelengths on picosecond laser ablation of silver, gold, and silver/gold alloy samples within two distinct liquid media: distilled water (DW) and aqueous NaCl solution. Significant variations in the productivity and size of NPs were observed across different wavelengths and media. Subsequently, a flexible SERS substrate was developed by depositing 18 types of NPs produced onto a filter paper. It was found that substrates containing NPs generated at 1064 nm laser wavelength exhibited prominent performance, characterized by higher yield and larger particle size. Stability tests revealed that NPs in the electrolyte (NaCl) solution displayed a quicker decline in SERS signal than those obtained in DW, despite satisfactory initial signal strengths. However, gold NPs in DW demonstrated optimal long-term stability, maintaining uniform SERS intensities over 60 days. Further, optimized SERS substrates were tested with different Raman excitations to highlight the critical role of molecular resonance absorption. Specifically, an excitation wavelength of 325 nm proved to be the most effective for detecting methyl salicylate and DMMP, underscoring the importance of selecting an appropriate excitation wavelength for enhanced molecular detection.

Experimental

Materials

Dimethyl methyl phosphonate (DMMP, $C_3H_9O_3P$, 98% pure); methyl salicylate (MS, $C_8H_8O_3$, 99% pure), methylene blue (MB, $C_{16}H_{18}ClN_3S$), and thiram ($C_6H_{12}N_2S_4$) were purchased from Sigma-Aldrich. All chemicals were of analytic grade and used for cleaning and diluting the samples. The laser ablation samples were 99% pure and had a thickness of 1 mm.

Synthesis of nanoparticles by laser ablation in liquid

Initially, silver, gold, and silver/gold ($Ag_{50}Au_{50}$) alloy targets (99%) were obtained from a local market and cut into 1 cm × 1 cm pieces. The targets were thoroughly cleaned in an ultrasonic bath using ethanol, acetone, and DW for 10 min. After washing, the targets were fixed at the bottom of the glass beaker filled with 5 mL of DW and aqueous NaCl solution (1 mM). The setup was mounted on the motorized X–Y translation stage (Newport) connected to a motion (ESP-300) controller. The Ag/Au/$Ag_{50}Au_{50}$ targets were ablated using a ps laser (Nd: YAG, EKSPLA PL2351), delivering ≈30 ps pulses at a wavelength of 1064, 532, and 355 nm at a 10 Hz repetition rate. For each wavelength, meticulous alignment of the laser beam was ensured using mirrors explicitly chosen for their optimal performance within the respective wavelength ranges. The laser beam was guided towards the processing region by mirrors and eventually focused on the sample surface by a lens of focal length (*f*) ≈10 cm at normal incidence. Ablation experiments were performed at a pulse energy of 12 mJ with the corresponding laser fluence of ≈30 mJ/cm^2. The moving target was irradiated using a separation of 50 µm between two adjacent lines at a translation speed of 1 mm/s along both directions. The total laser-processing area on the target surface was typically ≈25 mm^2. The ablation experiments lasted for ≈80 min in each case. The ablation process was executed by varying laser wavelengths (355, 532, and 1064 nm) and keeping all the other parameters constant, such as laser pulse energy, repetition rate, quantity of liquid, and focusing conditions. To avoid confusion, the names of the ablated samples and their descriptions are provided in Table 1.

Preparation of filter-paper-based flexible SERS and SERS measurements

Flexible substrates were fabricated using Whatman FP as the base material, which was cut into small squares of 1 cm^2 each. Subsequently, metal and alloy NPs synthesized via laser ablation (encompassing 18 distinct samples) were applied to the FP through a straightforward drop-casting method and then allowed to dry at room temperature. Following this, the analyte of interest was also applied onto the substrate using drop casting. This process took approximately 20 minutes.

Table 1: Summary of the sample descriptions and laser parameters used in this study.

Nanoparticles (NPs)	LaSiS Wavelength					
	355 nm		532 nm		1064 nm	
Solvent	DW	NaCl	DW	NaCl	DW	NaCl
Ag	AgD1	AgN1	AgD2	AgN2	AgD3	AgN3
Au	AuD1	AuN1	AuD2	AuN2	AuD3	AuN3
Ag50Au50	AgAuD1	AgAuN1	AgAuD2	AgAuN2	AgAuD3	AgAuN3

Characterization techniques

The absorption studies were conducted by placing 3 mL of the colloidal solution in a 1 cm quartz cuvette and using a UV–visible absorption spectrometer (PerkinElmer, LAMBDA 750) within the 300–800 nm wavelength range. The distribution of NPs on a FP was analyzed using the INCA software with a field-emission scanning electron microscope (FESEM, Carl Zeiss Ultra 55). Samples were prepared by drop casting 10 µL of NPs onto a FP, followed by sputtering a thin conductive layer of gold onto the FP to facilitate lower magnification imaging due to the nonconductive nature of the FP substrate. FESEM energy-dispersive X-ray spectroscopy (EDX) mapping investigations were conducted on Ag/Au alloy NPs deposited on a Si substrate by drop casting 10 µL to avoid confusion in the data caused by the Au coating. Transmission electron microscopy (TEM) was performed with a JEM-2100F (JEOL, Japan). TEM grids were prepared by drop casting 2 µL of NPs onto the grids. Raman/SERS spectra were collected using a portable Raman spectrometer (B&W Tek) with an excitation wavelength of 785 nm, 10 mW of laser power, 5 s of collection time, and three accumulations. The laser beam spot size on the sample was ≈100 µm. Wavelength-based SERS measurements were performed using a micro-Raman spectrometer (Horiba-Scientific), and 325, 532, and 633 nm laser excitation wavelengths with the same input laser power of ≈1 mW, 5 s of acquisition time, and three accumulations, and these parameters were maintained in all the measurements. For the focusing conditions, a 50× objective was used for the visible wavelengths (532 and 632 nm), while a 40×-NUV objective was employed for the 325 nm wavelength. A baseline correction using the Origin software was applied to all recorded SERS spectra, after which SERS calculations were undertaken.

Results and Discussion

Characterization

Optical absorption studies of as-synthesized nanoparticles

The absorbance measurements were carried out on metallic Ag, Au, and Ag/Au NPs prepared using ps LASiS in both DW and aqueous NaCl solution, covering a wavelength range of 300–800 nm. In Figure 1, the optical absorption spectra of (a) Ag, (b) Au, and (c) Ag/Au NP solutions are presented for both environments obtained at 1064, 532, and 355 nm wavelengths in LASiS. All absorption spectra exhibit a distinct single surface plasmon resonance (SPR) absorption peak, indicating the formation of spherical NPs. The SPR peak of Ag/Au alloy NPs lies between the SPR peak positions of pure Ag and Au NPs. Notably, the plasmon bands of NPs obtained at lower wavelengths (355 and 532 nm) are broadened compared to those of NPs fabricated at higher wavelengths (1064 nm). This broadening could be ascribed to the size/shape of the NPs, their aggregation, and variations in size distribution under different laser wavelengths. The NP productivity in the LASiS approach is mainly influenced by laser wavelength irradiation based on the interaction of the material with the incoming beam, including absorption, reflection, and scattering [47,48]. These interactions significantly vary across the wavelengths from 1064 down to 355 nm, with a unique response of different materials at each wavelength [49]. A key to enhancing the yield is choosing the laser wavelength at which the target material has a high absorption rate. This ensures that a greater energy density is transferred to the target, thereby increasing the volume of material ablated. On the other hand, to minimize energy losses during the process, choosing the surrounding media is also an essential factor, which could prevent the absorption of the aqueous solution at a given laser wavelength. This approach helps to achieve a delicate balance between maximizing the absorption in the target material while minimizing energy loss in the surrounding liquid and NPs, thereby enhancing the overall efficiency and yield of the LASiS process [4,50]. The study reported by Shukri et al. [51] pointed out a size reduction in Au NPs from 19 to 12 nm by decreasing the input laser wavelengths, changing from 1064 to 532 nm in DW. Solati et al. [52] observed a significant increase in the mean size of Ag NPs from 13 to 32 nm while ablating the Ag targets in acetone with laser wavelengths of 532 and 1064 nm. Furthermore, the absorption intensity proportionally increases with the increasing wavelength in both DW and NaCl, demonstrating that the yield of NPs is higher at higher wavelengths. Moreover, the absorption of NPs produced in aqueous NaCl solution was lower than that in DW, indicating a higher NP yield in DW. The observed difference in absorption intensities could be attributed to the influence of NaCl in the NP synthesis process. Salts may affect the kinetics of NP formation, leading to size, shape, and aggregation variations, ultimately impacting their optical properties [53]. Also, from absorbance studies, it is observed that the ablation rate is higher for the Au target than for Ag because of the hardness variation observed in an earlier report by Solati et al. [54]. In another study by Bae et al. [55], the authors demonstrated the Ag NP fabrication by varying the surrounding aqueous NaCl solution concentrations between 0 to 20 mM using a nanosecond laser at an excitation of 355 nm. Their study noticed increased Ag NP absorbance while changing the aqueous NaCl solution concentration from 0 to 5 mM, which decreased further. The SPR peaks were blue shifted for NPs obtained in NaCl compared to those obtained in DW, which could be attributed to an increase in the refractive index of the surrounding medium. The SPR shifts at different wavelengths of LASiS within the same environment suggest the variations of NP particle size or size dispersion. The peak shift is mainly correlated with the size and shape of NPs and their surrounding medium. Naderi-Samani et al. [56] reported the synthesis of Ag

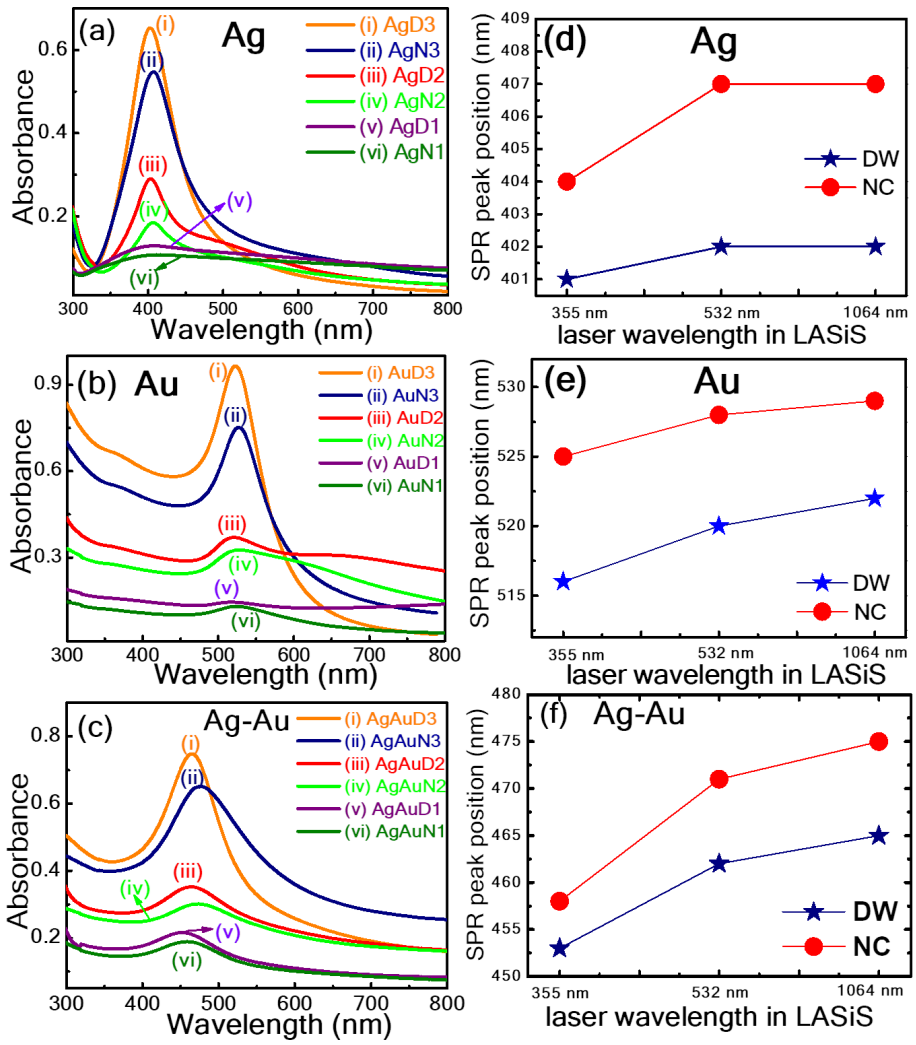

Figure 1: (a)–(c) Absorption spectra of laser-synthesized NPs (a) Ag NPs [AgD1, AgD2, AgD3, AgN1, AgN2, AgN3]; (b) Au NPs [AuD1, AuD2, AuD3, AuN1, AuN2, AuN3]; (c) Ag/Au NPs [AgAuD1, AgAuD2, AgAuD3, AgAuN1, AgAuN2, AgAuN3] obtained at different laser wavelengths (1064, 532, and 355 nm) and different liquids (DW and aqueous NaCl solution). (d–f) The variation of SPR peak position of (d) Ag, (e) Au, and (f) Ag/Au concerning wavelength and surrounding liquid.

NPs by nanosecond laser ablation in different aqueous solutions: water, acetone, cetyltrimethylammonium chloride (CTAC), polyvinylpyrrolidone (PVP), and sodium dodecyl sulfate (SDS). Their outcomes revealed that the productivity of Ag NPs was higher in acetone, followed by CTAC, water, PVP, and SDS. The order of NP formation efficiency was reported to be acetone >CTAC >water >PVP >SDS.

Morphological studies of as-synthesized nanoparticles

Transmission electron microscopy analysis was implemented to study the size and shape of laser-fabricated NPs. Figure 2 shows the TEM images of Ag NPs synthesized in DW at different laser wavelengths: (a) 355, (b) 532, and (c) 1064 nm. It should be noted that the shape of NPs is spherical, and the size distribution of the Ag NPs is strongly dependent on laser wavelength in LASiS. The average size of the NPs was estimated as 12.4 ± 0.3 nm at 355 nm, 23.9 ± 1.0 nm at 532 nm, and 36.3 ± 3.7 nm at 1064 nm, with the size distributions being provided in Supporting Information File 1, Figures S1(a)–(c). It is believed that with increasing wavelength, the NP sizes increase, presumably due to the coexistence of both processes, such as laser ablation and laser fragmentation in liquids at lower wavelengths (i.e., higher energy). The SPR peak is shifted toward a longer wavelength for larger particles, which is evident from the absorption spectra depicted.

Figure 2 depicts the pictures of Ag NPs synthesized using a laser wavelength of (d) 355 nm, (e) 532 nm, and (f) 1064 nm in an aqueous NaCl solution. The average particle size is

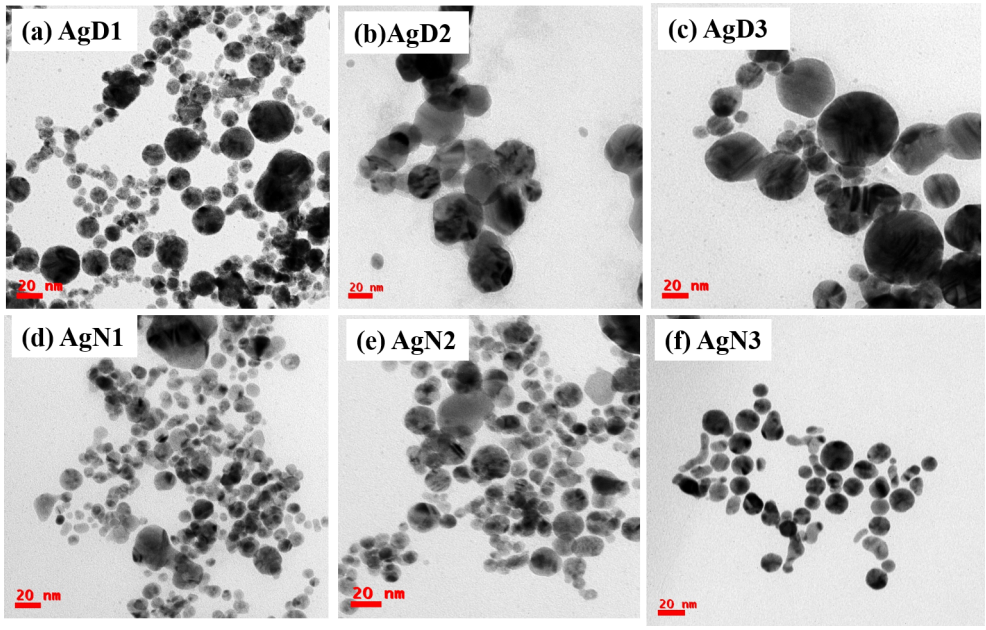

Figure 2: TEM images of Ag NPs: (a) AgD1, (b) AgD2, (c) AgD3, (d) AgN1, (e) AgN2, and (f) AgN3.

8.4 ± 0.4 nm at 355 nm, 13.3 ± 0.5 nm at 532 nm, and 16.5 ± 0.5 nm at 1064 nm, respectively. The size distributions are provided in Supporting Information File 1, Figure S1(d–f). The size of the NPs increases with increasing laser wavelength. It is worth mentioning that a reduction in NP size was noticed more in NPs produced in aqueous NaCl solution than in those fabricated in DW. The size reduction effect observed during ablation in aqueous NaCl solution can be attributed to Cl^- ions [55,57]. When a laser ablation process is conducted in the presence of NaCl, the ions in the solution can strongly influence nucleation processes and growth in the generation of the NPs. The presence of electrostatic repulsion among charged NPs generated in an electrolyte solution reduces the average size of the NPs. Rehbock et al. [21] pointed out the size reduction in Au NPs from 30 nm at 3 µM to 7 nm at 500 µM in the presence of aqueous NaCl solution during the ablation. He et al. [58] demonstrated that at higher NaCl (10 mM) concentrations, ZnO NPs exhibited coalescence, increasing NPs size in comparison to those obtained in DW.

In Figure 3, TEM images depicting as-synthesized Au NPs under different incident laser wavelengths (i.e., (a) 355, (b) 532, and (c) 1064 nm) in DW are shown. At 355 nm, a distinctive nanochain morphology linking spherical NPs was evident, contrasting with the separated spherical morphology. The prevalent interaction at 355 nm with the liquid phase was more influential than the NP production, resulting in particles with fragmented shapes [6]. This could be accredited to the more vital interaction of the lower wavelength with the liquid than with the submerged solid target. During ablation, the maximum energy dedicated to the formerly generated NPs resulted in further fragmentation of NPs and fusion rather than in target ablation. This phenomenon led to lower NP production at 355 nm compared to that at 532 and 1064 nm laser wavelengths, this was also reflected in the absorption spectra. Consequently, there is a tendency for NP agglomeration and chain formation, which is evident from the TEM pictures depicted in Figure 3. As the wavelength increases, ablation becomes more efficient, breaking the chains and creating smaller, separated spherical NPs. The mean sizes of the NPs synthesized at the three selected wavelengths are estimated to be approximately 9.5 ± 0.1 nm at 355 nm, 15.6 ± 0.1 nm at 532 nm, and 19.7 ± 0.7 nm at 1064 nm. The size distributions are provided in Supporting Information File 1, Figures S2(a)–(c). Notably, the mean diameter of NPs is smaller when generated at lower wavelengths compared to those produced at higher wavelengths.

Figure 3 displays TEM images depicting the synthesis of Au NPs under different laser wavelengths: (d) 355, (e) 532, and (f) 1064 nm in aqueous NaCl solution. Furthermore, the presence of NaCl in the surrounding medium significantly influences NP size, leading to size reduction. The mean sizes of the NPs in the presence of NaCl are estimated as 7.0 ± 0.5 nm at 355 nm, 11.4 ± 0.6 nm at 532 nm, and 12.6 ± 0.1 nm at 1064 nm. The size distributions are provided in Supporting Information File 1, Figures S2(d)–(f). This size reduction aligns with the observed behavior of nanochains at lower wavelengths and separated NPs at higher wavelengths. Figure 4 shows TEM

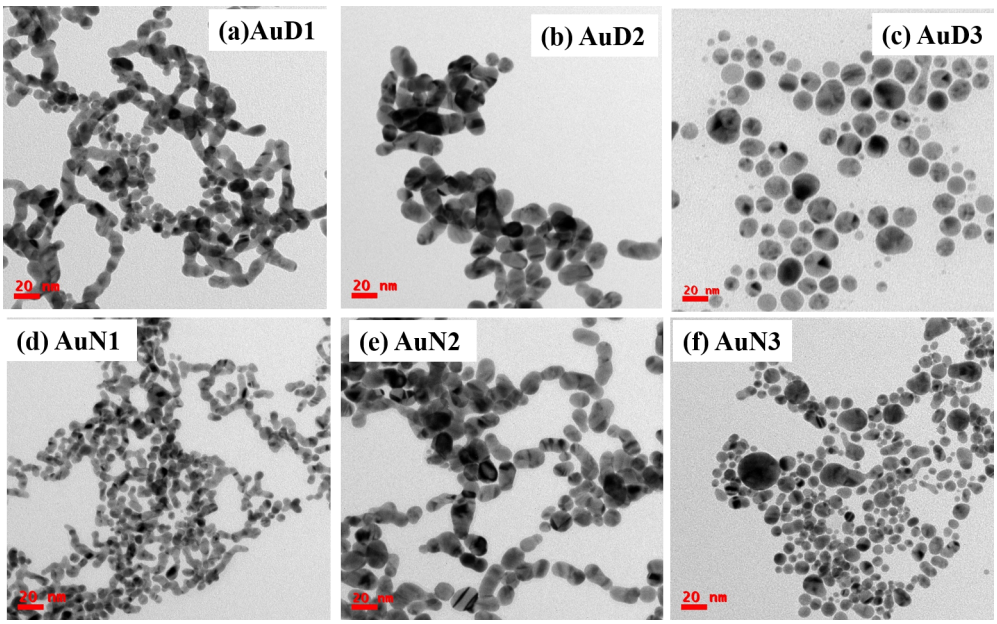

Figure 3: TEM images of Au NPs: (a) AuD1, (b) AuD2, (c) AuD3, (d) AuN1, (e) AuN2, and (f) AuN3.

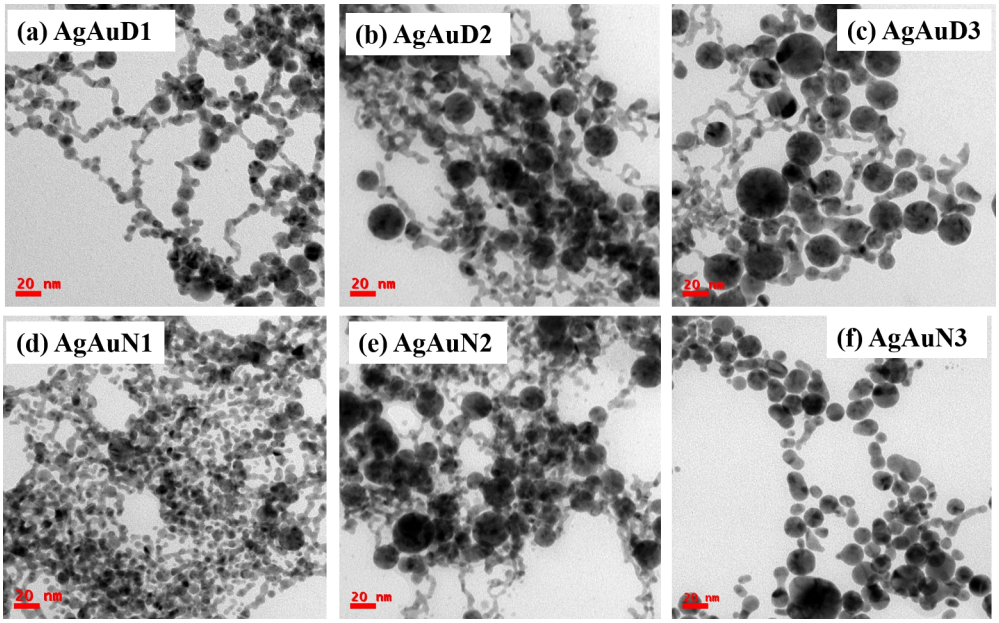

Figure 4: TEM images of Ag/Au NPs: (a) AgAuD1, (b) AgAuD2, (c) AgAuD3, (d) AgAuN1, (e) AgAuN2, and (f) AgAuN3.

images of Ag/Au alloy NPs under different laser wavelengths: (a,d) 355, (b,e) 532, and (c,f) 1064 nm in DW and aqueous NaCl solution, respectively. The mean sizes of the NPs in DW and NaCl are 24.9 ± 3.3 and 15.2 ± 0.2 nm at 355 nm, 12.7 ± 1 and 8.2 ± 0.3 nm at 532 nm, and 6.5 ± 0.1 and 5.8 ± 0.1 nm at 1064 nm, respectively. The NP size distributions are provided in Supporting Information File 1, Figure S3.

The variation in the sizes of Ag, Au, and Ag/Au NPs obtained in DW and aqueous NaCl solution at different wavelengths during the LASiS process is illustrated in Figure 5. It is noted that the NP size increased while the laser wavelength was increased. Size reduction was observed when the aqueous NaCl solution was used as a surrounding medium instead of other liquids (DW). In this case, the size increases with an increasing

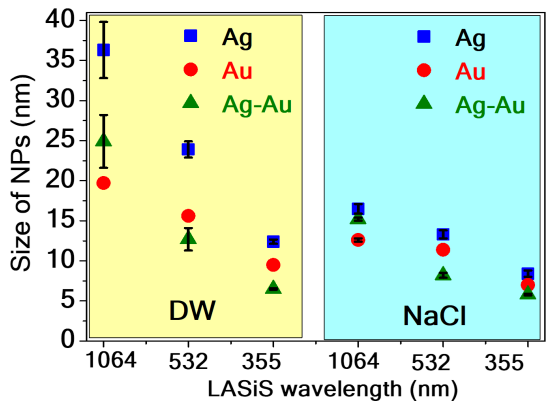

Figure 5: The variation in sizes of NPs at different wavelengths and environments. The left panel displays the size variation for Ag, Au, and Ag/Au in DW, while the right panel illustrates size variation in an aqueous NaCl solution.

wavelength. The diameters of colloids prepared at a laser wavelength of 1064 nm in DW are greater than 20 nm. However, NPs obtained in an aqueous NaCl solution at a laser wavelength of 355 nm showed nanochain features with diameters smaller than 10 nm.

Topographical studies of filter paper-loaded nanoparticles

The morphology and distribution of ps laser-fabricated NPs on filter paper were investigated using FESEM. The FESEM images reported in Figure 6 depict a filter paper surface grafted with Ag NPs, categorized as: (a) AgDW1, (b) AgD2, (c) AgD3, (d) AgN1, (e) AgN2, and (f) AgN3. Similarly, a FP loaded with Ag/Au NPs is illustrated in Figure 7, categorized as: (a) AgAuD1, (b) AgAuD2, (c) AgAuD3, (d) AgAuN1, (e) AgAuN2, and (f) AgAuN3. It is evident from the FESEM images that the concentrations of loaded NPs were different,

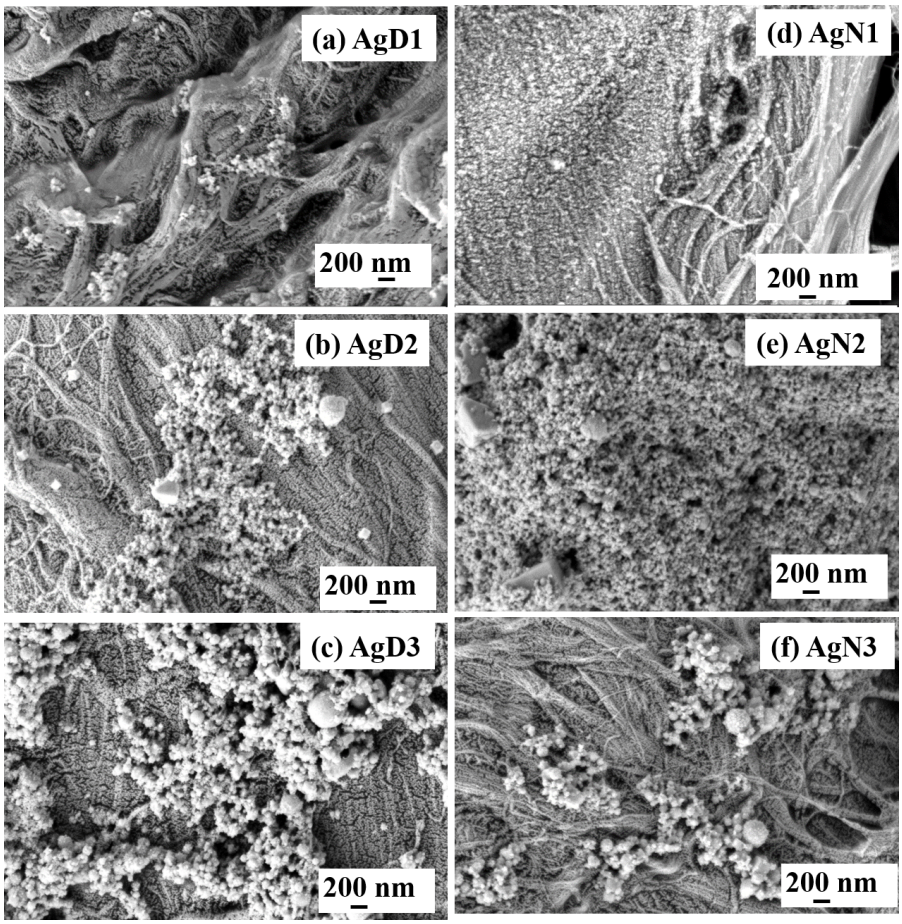

Figure 6: Panels (a)–(c) display FESEM images of a filter paper loaded with Ag NPs obtained in DW: (a) AgD1, (b) AgD2, and (c) AgD3. Panels (d)–(e) display FESEM images of a filter paper loaded with Ag NPs obtained in aqueous NaCl solution: (d) AgN1, (e) AgN2, and (f) AgN3 at wavelengths of 355, 532, and 1064 nm, respectively.

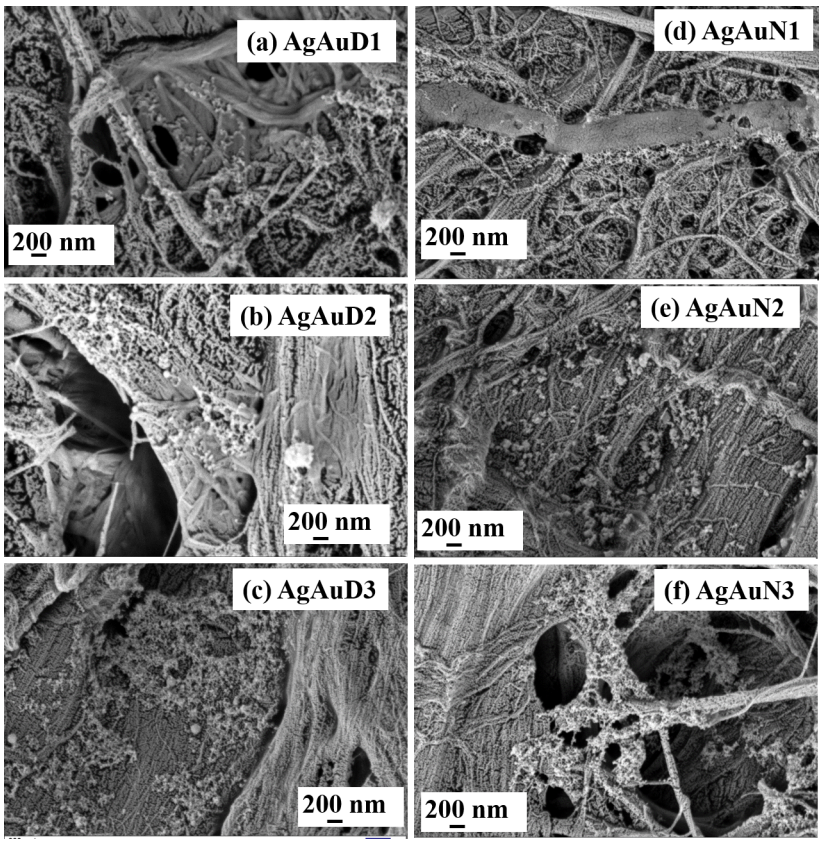

Figure 7: Panels (a)–(c) display FESEM images of a filter paper loaded with Ag/Au NPs obtained in DW: (a) AgAuD1, (b) AgAuD2, and (c) AgAuD3. Panels (d)–(e) display FESEM images of a filter paper loaded with Ag NPs obtained in aqueous NaCl solution: (d) AgAuN1, (e) AgAuN2, and (f) AgAuN3 at a wavelength of 355, 532, and 1064 nm, respectively.

possibly due to the differences in their loading and the effect of NPs yield obtained at different laser wavelengths. Furthermore, recorded FESEM-EDX data confirms the occurrence of Ag, Au, Na, Cl, C, and O elements on the FP-AgAuN3 substrate, provided in Supporting Information File 1, Figure S4. To confirm the presence of Ag and Au in alloy NPs, an EDX mapping investigation was conducted on AgAuD3 NPs coated on a Si substrate. The color map image of a single alloy NP with a squared area was represented in Supporting Information File 1, Figure S5. It is evident from the figure that individual NPs encompassed both Ag and Au elements. The detailed mechanism underlying the formation of alloy NPs was elucidated in our previous study [44]. Earlier studies suggested that the NP yield gradually increases with increasing laser wavelength. Notably, we could achieve a higher yield of NPs at higher wavelengths, resulting in a higher concentration of NPs on the filter paper surface. Additionally, larger NPs were observed at higher wavelengths than at lower wavelengths, which is also evident from TEM image analysis, as discussed above. A similar trend was noticed in the case of Au NP distribution on FP, as detailed in Supporting Information File 1, Figure S6.

SERS measurements from filter paper-loaded nanoparticles

Initially, a portable Raman spectrometer with a fixed excitation wavelength of 785 nm was employed, demonstrating the superior performance of flexible SERS substrates by depositing all the synthesized NPs onto a filter paper. This combination offers practical real-time onsite application capabilities, allowing for immediate and nondestructive analysis in the field, making it ideal for rapid screening and preliminary investigations. The portable spectrometer is user friendly, compact, and the lightweight design ensures minimal sample preparation and ease of transport, providing flexibility in diverse application scenarios. To capitalize on the advantages of a flexible substrate in the sensing field, filter paper was chosen as a base to host laser-ablated NPs [59]. The SERS performance of NP-loaded paper-based SERS substrates was assessed by choosing malachite green (MG) as a Raman reporter molecule. The SERS spectra reported in Figure 8a–c illustrate the prominent Raman bands of MG at a 1 nM concentration recorded from filter paper loaded with NPs, namely, Ag, Au, and Au NPs in DW and aqueous NaCl solution fabricated at three different wavelengths: 1064,

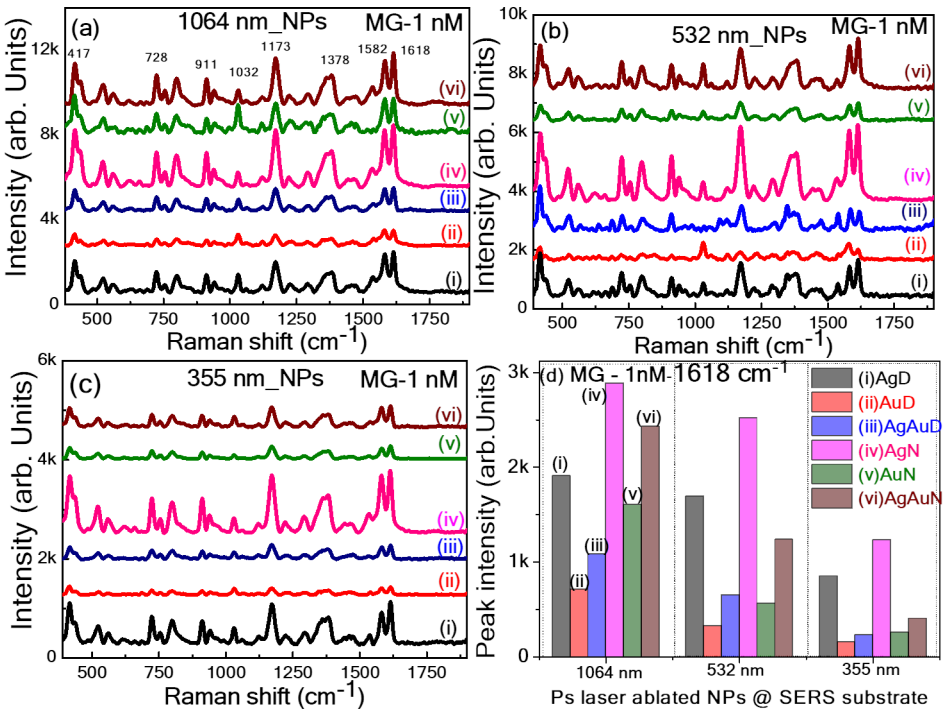

Figure 8: The SERS spectra of MG (1 nM) using filter paper loaded with ps laser ablated NPs (i) AgD, (ii) AuD, (iii) AgAuD, (iv) AgN, (v) AuN, and (vi) AgAuN at (a) 1064, (b) 532, and (c) 355 nm, (d) Intensity histogram of the prominent SERS peak at 1618 cm^{-1} (using a portable Raman spectrometer at an excitation wavelength of 785 nm).

532, and 355 nm. Figure 8d displays the intensity variation of a prominent 1618 cm^{-1} MG peak recorded from all substrates. The location of Raman peaks of MG noticed in our study coincides with the studies demonstrated earlier [60]. The leading characteristic bands found at 1618 cm^{-1} are assigned to phenyl-N and C–C stretching.

Similarly, SERS investigations were extended to detect the pesticide molecule thiram (10 μM) on all Ag, Au, and Ag/Au NP-loaded filter paper substrates. The obtained data is provided in Supporting Information File 1, Figures S7a–S7c using LASiS at 1064, 532, and 355 nm, respectively. All peaks align well with previous reports. The central characteristic peak at 1368 cm^{-1} was considered for evaluating performance, as illustrated in the performance histogram shown in Supporting Information File 1, Figure S7d. Further, similar studies are continued with methyl salicylate as a Raman reporter. Figure 9a–c present the SERS spectra of methyl salicylate (1 mM) collected from filter paper loaded NPs substrates obtained at laser wavelengths of (a) 1064, (b) 532, and (c) 355 nm. Figure 9d shows the Raman intensity variation of the central characteristic peak at 808 cm^{-1}. From the SERS measurements, we could point out that the filter paper grafted with Ag NPs was achieved in aqueous NaCl solution, demonstrating superior enhancement of AgAu alloy and Au NPs fabricated in DW and NaCl loaded on filter paper. Notably, the FP loaded with AgN3 NPs demonstrated superior SERS enhancement among all Ag NP-based substrates. This can be attributed to several factors, including (i) the plasmonic performance of Ag, (ii) a large number of NPs loaded onto the filter paper (resulting in a high yield of NPs at 1064 nm), (iii) the presence of ions from NaCl which can lead to ion-enhanced SERS effects [37,46,61].

The investigations further focused on assessing the stability of a SERS substrate over 60 days. We carried out systematic SERS measurements on different days, and their SERS intensities are compared concerning the days for the substrates, namely AgD3, AgAuD3, AuD3, AgN3, AgAuN3, and AuN3. The evolution of signal intensities over the 60 days is graphically depicted in Figure 10a and Figure 10b, revealing distinctive decay patterns of MG and thiram on the 7th, 15th, 30th, and 60th days. Notably, freshly prepared (on the first day) SERS substrates such as AgD3 and AgN3 exhibited prominent enhancement in Raman signals compared with other substrates, while AuD3 and AuN3 substrates displayed the lowest SERS signal. Decay percentages were calculated to assess the substrate performance. Figure 10c and Figure 10d visually represent the decay percentages over time. On the 30th day, Ag NPs SERS performance decreased by 95%, while Au NPs exhibited variations from ≈10% (7th day) to ≈35% (60th day).

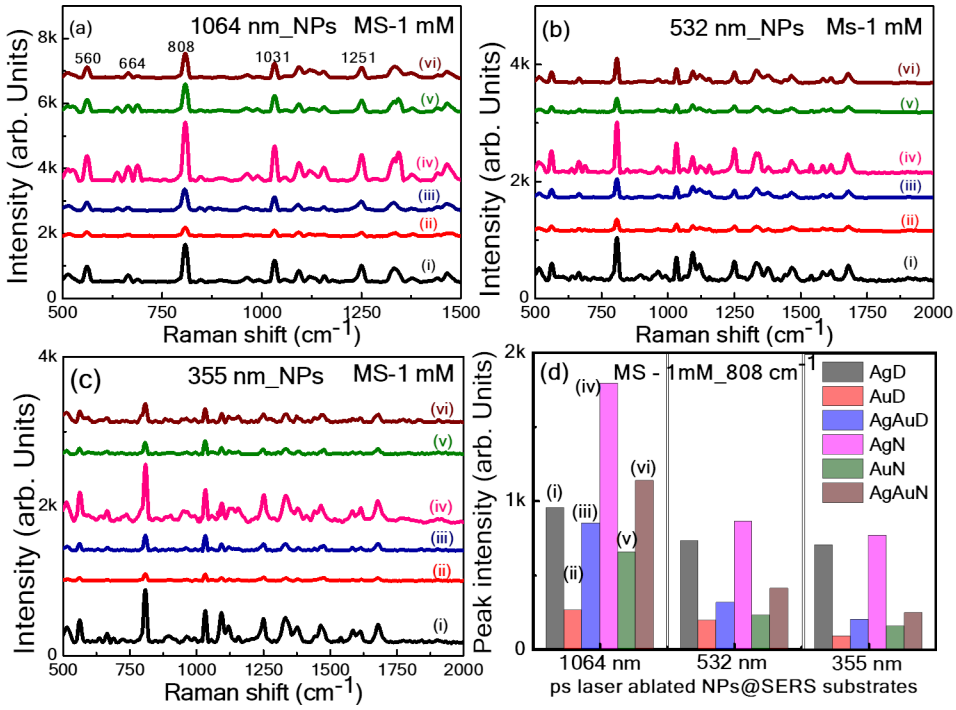

Figure 9: The SERS spectra of methyl salicylate (1 mM) using filter paper loaded with ps laser-ablated Ag, Au, and Ag/Au NPs in DW and aqueous NaCl solution at (a) 1064, (b) 532, and (c) 355 nm. (d) Intensity histogram of the prominent peak at 808 cm^{-1} from all 18 different FP substrates (using portable Raman spectrometer at an excitation of 785 nm).

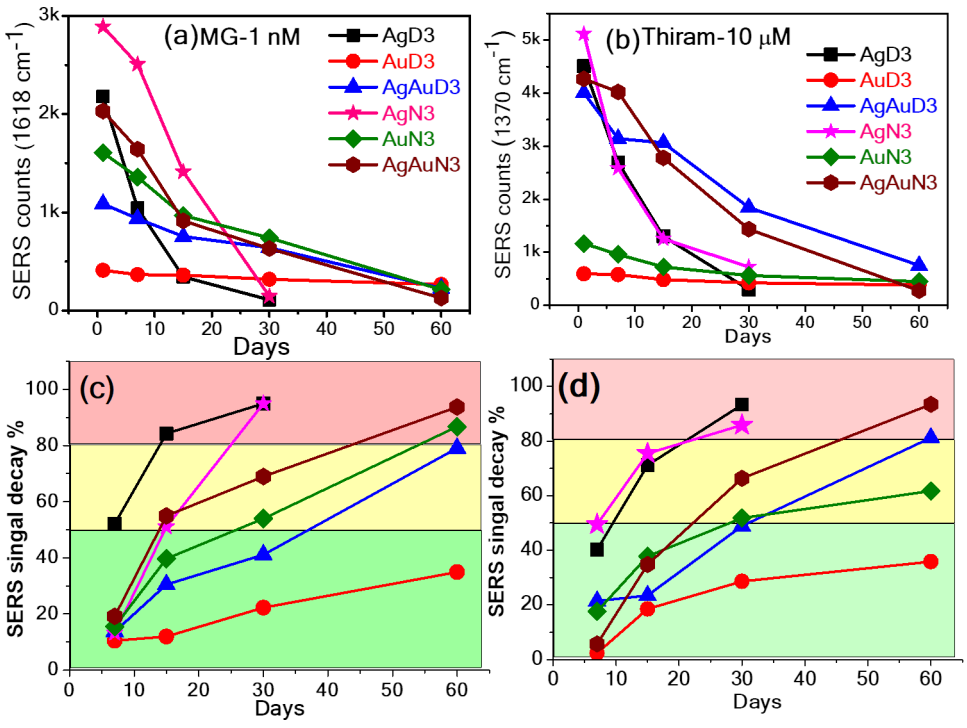

Figure 10: Stability of paper-based SERS substrates: (a) MG (1 nM) and (b) thiram (10 μM). Prominent peak intensity variation (c) and (d) % signal decay as a function of number of days (up to 60) using AgD3, AgAuD3, AuD3, AgN3, AgAuN3, AuN3 NPs loaded filter paper.

The graphical representation of categorized substrates into three areas based on decay percentages (i.e., green for up to 50%, yellow for 50–80%, and pink for 80–100%) are shown in Figure 10. Substrates, namely AuD3, AgAuD3, AuN3, and AgAuN3 remained stable in the yellow region for up to one month. Notably, the AuD3 substrate showed consistent performance with a decay percentage of 35% over 60 days. Ag/Au alloy NPs often display better properties than those of pure Ag and Au counterparts. Combining Ag and Au can lead to superior plasmonic properties derived from Ag, improved stability attributed to Au, and increased SERS efficiency, making them particularly advantageous for long-term applications with heightened sensitivity. These enhancements are due to synergistic effects, where the integrated properties of the metals surpass those of the individual elements. In the initial days, the presence of NaCl led to an increase in the SERS signal; however, over a longer duration, the NPs in DW showed better SERS intensity than those in aqueous NaCl solution. Jiang et al. [62] investigated the SERS performance of Ag NPs in detecting CV molecules. They found that bare Ag NPs exhibited diminishing performance over three weeks. However, a substrate composed of single atomic layer nanocellulose–Ag NP hybrids maintained nearly constant performance for 35 days. Zhang et al. [63] reported that after undergoing vacuum storage for seven days, the SERS intensity of CV at 1620 cm^{-1} detected on AgNP-120@BNC did not significantly decrease. The SERS intensity of CV detected on the AgNP-120@BNC substrate remained at 91% of its original intensity after seven days of vacuum storage.

Effect of Raman excitation wavelength on SERS measurements

The enhanced stability of AuD3 NPs loaded on filter paper regarding SERS performance was further investigated, particularly in hazardous chemical molecules such as methyl salicylate (1 mM) and dimethyl methyl phosphonate (1 mM). Methyl salicylate and dimethyl methyl phosphonate are critical chemical warfare agent (CWA) simulants, posing a significant threat to global security. Detecting these molecules is essential for security reasons, and various detection methods are currently under investigation [64-67]. One promising method for practical application is using flexible SERS substrates as sensing platforms [68].

This study explored the impact of different Raman excitation wavelengths, specifically 325, 532, and 633 nm. The prominent peaks of MS (810 cm^{-1}) and DMMP (710 cm^{-1}) molecules were observed in all cases, shown in Figure 11a and Figure 11b,

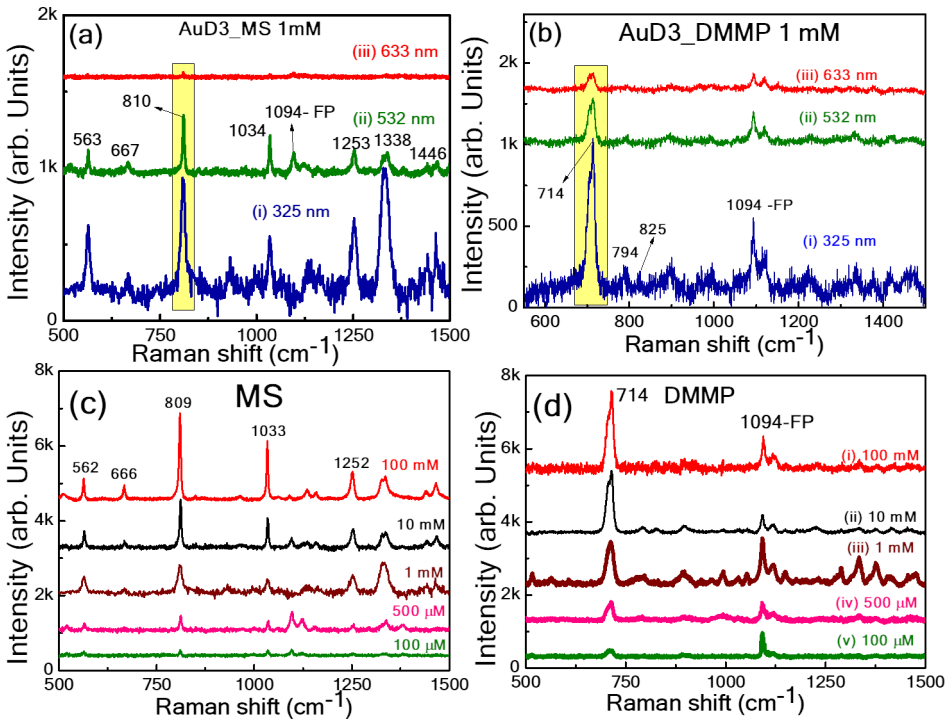

Figure 11: The SERS spectra of (a) MS (1 mM) and (b) DMMP (1 mM) at different Raman laser excitations: 633, 532, and 325 nm. Concentration-dependent SERS spectra of (c) MS (100 mM to 100 µM) and (d) DMMP (100 mM to 100 µM) at an excitation of 325 nm using the AuD3 substrate.

respectively. The peak at 810 cm^{-1} is due to the stretching vibration of C–H [69], and the peak at 710 cm^{-1} for DMMP is due to the combined vibrational mode, including the symmetrical stretching of the two single P–O bonds and the P–C bond [70]. The peak positions and their assignment of MS and DMMP are provided in Supporting Information File 1, Tables S8 and S9, respectively. Li et al. [69] detected MS (10^{-4} M) by SERS using a Raman excitation of 532 nm. Huang et al. [70] described the identification of DMMP (1 g/L) residues from an irregular surface using Ag NPs grafted cotton swabs via simple swabbing with a laser excitation of 532 nm. Lafuente et al. [71] also reported the detection of DMMP (1.2 ppm V) in the vapor phase using Glass_Ag_Au NPs, 3D fractal microstructure substrates developed by corner lithography and anisotropic wet etching of silicon using the 785 nm as the Raman excitation. When UV excitation was utilized during the measurements, the Raman peak intensities were notably higher for both MS and DMMP molecules at 124 and 152 ppm. This can be attributed to the resonance absorption of these molecules with laser excitation, which increased Raman signal intensity. The reproducibility of the substrate at these different wavelengths in detecting MS was also verified by collecting Raman spectra from more than 15 different locations. The obtained relative standard deviations (RSDs) were 20%, 10%, and 9% for Raman excitations at 633, 532, and 325 nm, respectively. The calculated histograms are provided in Supporting Information File 1, Figure S10a–c.

The sensitivity of the optimized FP SERS substrate was further examined at 325 nm with various concentrations of MS and DMMP ranging from 100 mM to 100 μM, as depicted in Figure 11c and Figure 11d. The leading prominent peaks of MS at 809 cm^{-1} and DMMP at 714 cm^{-1} were observed at the lowest concentration of 100 μM. The reproducibility of the SERS substrate was also examined with the DMMP molecule at a concentration of 500 μM at 15 different locations on the substrate. The histogram showing the most prominent intensity variation yielded an RSD of ≈6%, as shown in Supporting Information File 1, Figure S10d. Aligholizadeh et al. [72] detected DMMP using a handheld Raman spectrometer with an excitation of 785 nm, and the analytes were measured in a liquid-phase solution. The limit of detection (LOD) achieved for DMMP was 9 mM. Chang et al. [67] utilized a combination of cotton swabs with a Ag NP substrate along with a smartphone application to detect DMMP. They detected DMMP at a concentration of 1g/L (≈8 mM) using a Raman excitation of 532 nm. Wang and co-workers [73] developed a novel method using thin water film confinement to enhance Raman detection of weakly interacting nerve agent simulants, such as DMMP (mM), on SERS substrates using a Raman excitation of 633 nm. Li et al. [74] detected, using a portable Raman device at an excitation of 785 nm, DMMP at a concentration of 100 mg/kg (800 μM) utilizing a Au@ZrO_2 substrate.

Conclusion

In conclusion, this study delved into the impact of different laser wavelengths (355, 532, and 1064 nm) on the variation of morphological features and yields of colloids obtained through the ablation of Ag, Au, and $Ag_{50}Au_{50}$ targets conducted in a medium of DW and aqueous NaCl solution using a picosecond laser. Our findings demonstrated that the irradiation laser wavelengths of the UV region are more beneficial to produce smaller NPs due to the fragmentation effects. Conversely, the wavelengths lying in the NIR region are the ideal choice to obtain high ablation yield due to the low absorption by previously generated NPs. Furthermore, NPs sizes were smaller at lower irradiation laser wavelengths than those obtained at higher laser wavelengths. The subsequent development of flexible SERS substrates, utilizing the diverse NPs produced, showcased the superior performance of substrates containing NPs generated at the 1064 nm wavelength, characterized by enhanced yield and larger particle size. However, Au NPs in DW demonstrated optimal long-term stability, maintaining their SERS signal integrity for up to 60 days. Further, chemical warfare simulant MS and DMMP detection using a 325 nm Raman laser (UV resonance) demonstrated superior performance.

Supporting Information

Supporting Information File 1

Additional figures and tables.
[https://www.beilstein-journals.org/bjnano/content/supplementary/2190-4286-15-86-S1.pdf]

Acknowledgements

We acknowledge the School of Physics, University of Hyderabad for absorption and FESEM facilities and the School of Chemistry for the TEM facility. We sincerely thank the late Dr. Anik K. Razdan, LASTEC, India, for providing the DMMP sample. We thank the Director of ACRHEM for the fruitful discussions. We acknowledge the support of Dr. Bikash Ghose, HEMRL, Pune, for critical discussions and comments.

Funding

SSBM acknowledges the SERB, India, for the NPDF funding (PDF/2023/000958/PMS). VRS acknowledges IoE-UoH through a project funded by the Institute of Eminence (#UOH/IOE/RC1/RC1-20-016). VRS also acknowledges the financial support from DRDO, India [#ERIP/ER/1501138/M/01/319/D(R&D)].

Conflict of Interest

The authors declare no conflicts of interest.

Author Contributions

Sree Satya Bharati Moram: data curation; formal analysis; investigation; methodology; validation; writing – original draft; writing – review & editing. Chandu Byram: data curation; formal analysis; investigation; writing – original draft; writing – review & editing. Venugopal Rao Soma: conceptualization; formal analysis; methodology; project administration; resources; supervision; validation; writing – original draft; writing – review & editing.

ORCID® iDs

Sree Satya Bharati Moram - https://orcid.org/0000-0001-5147-7819
Venugopal Rao Soma - https://orcid.org/0000-0001-5361-7256

Data Availability Statement

All data that supports the findings of this study is available in the published article and/or the supporting information to this article.

References

1. Jamkhande, P. G.; Ghule, N. W.; Bamer, A. H.; Kalaskar, M. G. *J. Drug Delivery Sci. Technol.* **2019,** *53,* 101174. doi:10.1016/j.jddst.2019.101174
2. Johny, J.; Kamp, M.; Prymak, O.; Tymoczko, A.; Wiedwald, U.; Rehbock, C.; Schürmann, U.; Popescu, R.; Gerthsen, D.; Kienle, L.; Shaji, S.; Barcikowski, S. *J. Phys. Chem. C* **2021,** *125,* 9534–9549. doi:10.1021/acs.jpcc.1c02138
3. Ziefuss, A.; Barcikowski, S.; Zhigilei, L. V. *Sci. China: Phys., Mech. Astron.* **2022,** *65,* 274201. doi:10.1007/s11433-022-1909-6
4. Nadarajah, R.; Barcikowski, S.; Gökce, B. *Opt. Express* **2020,** *28,* 2909–2924. doi:10.1364/oe.28.002909
5. Shugaev, M. V.; Wu, C.; Armbruster, O.; Naghilou, A.; Brouwer, N.; Ivanov, D. S.; Derrien, T. J.-Y.; Bulgakova, N. M.; Kautek, W.; Rethfeld, B.; Zhigilei, L. V. *MRS Bull.* **2016,** *41,* 960–968. doi:10.1557/mrs.2016.274
6. Shih, C.-Y.; Shugaev, M. V.; Wu, C.; Zhigilei, L. V. *Phys. Chem. Chem. Phys.* **2020,** *22,* 7077–7099. doi:10.1039/d0cp00608d
7. Dittrich, S.; Barcikowski, S.; Gökce, B. *Opto-Electron. Adv.* **2021,** *4,* 200072. doi:10.29026/oea.2021.200072
8. Khairani, I. Y.; Lin, Q.; Landers, J.; Salamon, S.; Doñate-Buendía, C.; Karapetrova, E.; Wende, H.; Zangari, G.; Gökce, B. *Nanomaterials* **2023,** *13,* 227. doi:10.3390/nano13020227
9. Fazio, E.; Gökce, B.; De Giacomo, A.; Meneghetti, M.; Compagnini, G.; Tommasini, M.; Waag, F.; Lucotti, A.; Zanchi, C. G.; Ossi, P. M.; Dell'Aglio, M.; D'Urso, L.; Condorelli, M.; Scardaci, V.; Biscaglia, F.; Litti, L.; Gobbo, M.; Gallo, G.; Santoro, M.; Trusso, S.; Neri, F. *Nanomaterials* **2020,** *10,* 2317. doi:10.3390/nano10112317
10. Hupfeld, T.; Stein, F.; Barcikowski, S.; Gökce, B.; Wiedwald, U. *Molecules* **2020,** *25,* 1869. doi:10.3390/molecules25081869
11. Baladi, A.; Mamoory, R. S. Study on wavelength and energy effects on pulsed laser ablation synthesis of aluminum nanoparticles in ethanol. In *2009 Fifth International Conference on MEMS NANO, and Smart Systems,* IEEE, 2009; pp 218–221. doi:10.1109/icmens.2009.43
12. Horn, I.; Guillong, M.; Günther, D. *Appl. Surf. Sci.* **2001,** *182,* 91–102. doi:10.1016/s0169-4332(01)00465-2
13. Landstrom, L.; Boman, M.; Heszler, P. Size distribution and characterization of tungsten nanoparticles generated by laser-assisted chemical vapor deposition and pulsed laser ablation. In *Properties of Metal Nanostructures,* Halas, N. J., Ed.; SPIE, 2002. doi:10.1117/12.451578
14. Mortazavi, S. Z.; Parvin, P.; Reyhani, A.; Golikand, A. N.; Mirershadi, S. *J. Phys. Chem. C* **2011,** *115,* 5049–5057. doi:10.1021/jp1091224
15. Schwenke, A.; Wagener, P.; Nolte, S.; Barcikowski, S. *Appl. Phys. A: Mater. Sci. Process.* **2011,** *104,* 77–82. doi:10.1007/s00339-011-6398-9
16. Fromme, T.; Reichenberger, S.; Tibbetts, K. M.; Barcikowski, S. *Beilstein J. Nanotechnol.* **2024,** *15,* 638–663. doi:10.3762/bjnano.15.54
17. Satya Bharati, M. S.; Chandu, B.; Rao, S. V. *RSC Adv.* **2019,** *9,* 1517–1525. doi:10.1039/c8ra08462a
18. Compagnini, G.; Messina, E.; Puglisi, O.; Nicolosi, V. *Appl. Surf. Sci.* **2007,** *254,* 1007–1011. doi:10.1016/j.apsusc.2007.07.177
19. Zhang, D.; Lau, M.; Lu, S.; Barcikowski, S.; Gökce, B. *Sci. Rep.* **2017,** *7,* 40355. doi:10.1038/srep40355
20. Maximova, K.; Aristov, A.; Sentis, M.; Kabashin, A. V. *Nanotechnology* **2015,** *26,* 065601. doi:10.1088/0957-4484/26/6/065601
21. Rehbock, C.; Jakobi, J.; Gamrad, L.; van der Meer, S.; Tiedemann, D.; Taylor, U.; Kues, W.; Rath, D.; Barcikowski, S. *Beilstein J. Nanotechnol.* **2014,** *5,* 1523–1541. doi:10.3762/bjnano.5.165
22. Amendola, V.; Amans, D.; Ishikawa, Y.; Koshizaki, N.; Scirè, S.; Compagnini, G.; Reichenberger, S.; Barcikowski, S. *Chem. – Eur. J.* **2020,** *26,* 9206–9242. doi:10.1002/chem.202000686
23. Coviello, V.; Forrer, D.; Amendola, V. *ChemPhysChem* **2022,** *23,* e202200136. doi:10.1002/cphc.202200136
24. Menéndez-Manjón, A.; Schwenke, A.; Steinke, T.; Meyer, M.; Giese, U.; Wagener, P.; Barcikowski, S. *Appl. Phys. A: Mater. Sci. Process.* **2013,** *110,* 343–350. doi:10.1007/s00339-012-7264-0
25. Amendola, V.; Scaramuzza, S.; Carraro, F.; Cattaruzza, E. *J. Colloid Interface Sci.* **2017,** *489,* 18–27. doi:10.1016/j.jcis.2016.10.023
26. Jakobi, J.; Menéndez-Manjón, A.; Chakravadhanula, V. S. K.; Kienle, L.; Wagener, P.; Barcikowski, S. *Nanotechnology* **2011,** *22,* 145601. doi:10.1088/0957-4484/22/14/145601
27. Abdul Amir, H. A. A.; Fakhri, M. A.; Alwahib, A. A.; Salim, E. T.; Alsultany, F. H.; Hashim, U. *Mater. Sci. Semicond. Process.* **2022,** *150,* 106911. doi:10.1016/j.mssp.2022.106911
28. Srikanth, S.; Dudala, S.; Jayapiriya, U. S.; Mohan, J. M.; Raut, S.; Dubey, S. K.; Ishii, I.; Javed, A.; Goel, S. *Sci. Rep.* **2021,** *11,* 9750. doi:10.1038/s41598-021-88068-z
29. Pereira, P. F. S.; de Paula e Silva, A. C. A.; da Silva Pimentel, B. N. A.; Pinatti, I. M.; Simões, A. Z.; Vergani, C. E.; Barreto-Vieira, D. F.; da Silva, M. A. N.; Miranda, M. D.; Monteiro, M. E. S.; Tucci, A.; Doñate-Buendía, C.; Mínguez-Vega, G.; Andrés, J.; Longo, E. *Sci. Rep.* **2022,** *12,* 8118. doi:10.1038/s41598-022-11902-5
30. Zheng, Q.; Fu, Y.-c.; Xu, J.-q. *Procedia Eng.* **2010,** *7,* 179–184. doi:10.1016/j.proeng.2010.11.027
31. Zhang, D.; Pu, H.; Huang, L.; Sun, D.-W. *Trends Food Sci. Technol.* **2021,** *109,* 690–701. doi:10.1016/j.tifs.2021.01.058

32. Bharati, M. S. S.; Soma, V. R. *Opto-Electron. Adv.* **2021,** *4,* 210048. doi:10.29026/oea.2021.210048
33. Bharathi, M. S. S.; Byram, C.; Banerjee, D.; Sarma, D.; Barkakaty, B.; Soma, V. R. *Bull. Mater. Sci.* **2021,** *44,* 103. doi:10.1007/s12034-021-02402-9
34. Niu, F.; Hu, Y.; LeKarz, S.; Lu, W. *J. Vac. Sci. Technol., A* **2024,** *42,* 022406. doi:10.1116/6.0003352
35. Viriyakitpattana, N.; Rattanabut, C.; Lertvachirapaiboon, C.; Pimalai, D.; Bamrungsap, S. *ACS Omega* **2024,** *9,* 10099–10109. doi:10.1021/acsomega.3c05966
36. Verma, M.; Naqvi, T. K.; Tripathi, S. K.; Kulkarni, M. M.; Dwivedi, P. K. *Environ. Technol. Innovation* **2021,** *24,* 102033. doi:10.1016/j.eti.2021.102033
37. Khan, G. A.; Demirtaş, O. Ö.; Bek, A.; Bhatti, A. S.; Ahmed, W. *Vib. Spectrosc.* **2022,** *120,* 103359. doi:10.1016/j.vibspec.2022.103359
38. Pagano, R.; Ottolini, M.; Valli, L.; Bettini, S.; Giancane, G. *Colloids Surf., A* **2021,** *624,* 126787. doi:10.1016/j.colsurfa.2021.126787
39. Quynh Trang, T. N.; Phuong Trinh, N. T.; Gia Bao, N. T.; Thu, V. T. H. *J. Sci.: Adv. Mater. Devices* **2023,** *8,* 100597. doi:10.1016/j.jsamd.2023.100597
40. Mai, Q. D.; Nguyen, H. A.; Dinh, N. X.; Thu Thuy, N. T.; Tran, Q. H.; Thanh, P. C.; Pham, A.-T.; Le, A.-T. *Talanta* **2023,** *253,* 124114. doi:10.1016/j.talanta.2022.124114
41. Lan, L.; Hou, X.; Gao, Y.; Fan, X.; Qiu, T. *Nanotechnology* **2020,** *31,* 055502. doi:10.1088/1361-6528/ab4f11
42. Kumar, A.; Santhanam, V. *Anal. Chim. Acta* **2019,** *1090,* 106–113. doi:10.1016/j.aca.2019.08.073
43. Xie, J.; Li, L.; Khan, I. M.; Wang, Z.; Ma, X. *Spectrochim. Acta, Part A* **2020,** *231,* 118104. doi:10.1016/j.saa.2020.118104
44. Byram, C.; Rathod, J.; Moram, S. S. B.; Mangababu, A.; Soma, V. R. *Nanomaterials* **2022,** *12,* 2150. doi:10.3390/nano12132150
45. Lee, C. H.; Tian, L.; Singamaneni, S. *ACS Appl. Mater. Interfaces* **2010,** *2,* 3429–3435. doi:10.1021/am1009875
46. Moram, S. S. B.; Byram, C.; Shibu, S. N.; Chilukamarri, B. M.; Soma, V. R. *ACS Omega* **2018,** *3,* 8190–8201. doi:10.1021/acsomega.8b01318
47. Smirnov, N. A.; Kudryashov, S. I.; Rudenko, A. A.; Nastulyavichus, A. A.; Ionin, A. A. *Laser Phys. Lett.* **2022,** *19,* 026001. doi:10.1088/1612-202x/ac46ab
48. Zhang, J.; Claverie, J.; Chaker, M.; Ma, D. *ChemPhysChem* **2017,** *18,* 986–1006. doi:10.1002/cphc.201601220
49. Dittrich, S.; Streubel, R.; McDonnell, C.; Huber, H. P.; Barcikowski, S.; Gökce, B. *Appl. Phys. A: Mater. Sci. Process.* **2019,** *125,* 432. doi:10.1007/s00339-019-2704-8
50. Naser, H.; Alghoul, M. A.; Hossain, M. K.; Asim, N.; Abdullah, M. F.; Ali, M. S.; Alzubi, F. G.; Amin, N. *J. Nanopart. Res.* **2019,** *21,* 249. doi:10.1007/s11051-019-4690-3
51. W. Shukri, W. N.; Bidin, N.; Affandi, S.; Bohari, S. P. *J. Teknol.* **2016,** *78,* 267–270. doi:10.11113/jt.v78.7530
52. Solati, E.; Mashayekh, M.; Dorranian, D. *Appl. Phys. A: Mater. Sci. Process.* **2013,** *112,* 689–694. doi:10.1007/s00339-013-7812-2
53. Khairani, I. Y.; Mínguez-Vega, G.; Doñate-Buendía, C.; Gökce, B. *Phys. Chem. Chem. Phys.* **2023,** *25,* 19380–19408. doi:10.1039/d3cp01214j
54. Solati, E.; Dorranian, D. *J. Cluster Sci.* **2015,** *26,* 727–742. doi:10.1007/s10876-014-0732-2
55. Bae, C. H.; Nam, S. H.; Park, S. M. *Appl. Surf. Sci.* **2002,** *197–198,* 628–634. doi:10.1016/s0169-4332(02)00430-0
56. Naderi-Samani, H.; Shoja Razavi, R.; Mozaffarinia, R. *Mater. Chem. Phys.* **2023,** *305,* 128001. doi:10.1016/j.matchemphys.2023.128001
57. Procházka, M.; Mojzeš, P.; Štěpánek, J.; Vlčková, B.; Turpin, P.-Y. *Anal. Chem. (Washington, DC, U. S.)* **1997,** *69,* 5103–5108. doi:10.1021/ac970683+
58. He, C.; Sasaki, T.; Usui, H.; Shimizu, Y.; Koshizaki, N. *J. Photochem. Photobiol., A* **2007,** *191,* 66–73. doi:10.1016/j.jphotochem.2007.04.006
59. Cao, Y.; Sun, Y.; Yu, R.-J.; Long, Y.-T. *Microchim. Acta* **2024,** *191,* 8. doi:10.1007/s00604-023-06086-2
60. Byram, C.; Moram, S. S. B.; Soma, V. R. *Analyst* **2019,** *144,* 2327–2336. doi:10.1039/c8an01276h
61. Bibi, A.; Pant, U.; Tate, J.; Hill, D.; Cao, C. *Proc. SPIE* **2023,** *12430,* 1243012. doi:10.1117/12.2650251
62. Jiang, J.; Zou, J.; Wee, A. T. S.; Zhang, W. *Sci. Rep.* **2016,** *6,* 34599. doi:10.1038/srep34599
63. Zhang, S.; Xu, J.; Liu, Z.; Huang, Y.; Jiang, S. *Cellulose* **2022,** *29,* 9865–9879. doi:10.1007/s10570-022-04871-5
64. Pan, Y.; Yan, C.; Gao, X.; Yang, J.; Guo, T.; Zhang, L.; Wang, W. *Microsyst. Nanoeng.* **2024,** *10,* 4. doi:10.1038/s41378-023-00627-8
65. Saya, L.; Ratandeep; Arya, B.; Rastogi, K.; Verma, M.; Rani, S.; Sahu, P. K.; Singh, M. R.; Singh, W. R.; Hooda, S. *Talanta* **2024,** *272,* 125785. doi:10.1016/j.talanta.2024.125785
66. Christesen, S. D. *Appl. Spectrosc.* **1988,** *42,* 318–321. doi:10.1366/0003702884428220
67. Chang, C.-S.; Wang, J.-C.; Wu, K.-H. *Vib. Spectrosc.* **2023,** *127,* 103566. doi:10.1016/j.vibspec.2023.103566
68. Lafuente, M.; De Marchi, S.; Urbiztondo, M.; Pastoriza-Santos, I.; Pérez-Juste, I.; Santamaría, J.; Mallada, R.; Pina, M. *ACS Sens.* **2021,** *6,* 2241–2251. doi:10.1021/acssensors.1c00178
69. Li, Y.; Li, Q.; Wang, Y.; Oh, J.; Jin, S.; Park, Y.; Zhou, T.; Zhao, B.; Ruan, W.; Jung, Y. M. *Spectrochim. Acta, Part A* **2018,** *195,* 172–175. doi:10.1016/j.saa.2018.01.073
70. Huang, W.-C.; Chen, H.-R. *Molecules* **2023,** *28,* 520. doi:10.3390/molecules28020520
71. Lafuente, M.; Berenschot, E.; Tiggelaar, R.; Mallada, R.; Tas, N.; Pina, M. *Micromachines* **2018,** *9,* 60. doi:10.3390/mi9020060
72. Aligholizadeh, D.; Tewala, Y.; Langford, K.; Hondrogiannis, N.; Chikkaraddy, R.; Devadas, M. S. *Vib. Spectrosc.* **2023,** *129,* 103616. doi:10.1016/j.vibspec.2023.103616
73. Wang, J.; Duan, G.; Liu, G.; Li, Y.; Chen, Z.; Xu, L.; Cai, W. *J. Hazard. Mater.* **2016,** *303,* 94–100. doi:10.1016/j.jhazmat.2015.10.022
74. Li, T.-J.; Wen, B.-Y.; Zhang, Y.-J.; Zhang, L.; Li, J.-F. *J. Raman Spectrosc.* **2022,** *53,* 1386–1393. doi:10.1002/jrs.6373

BEILSTEIN JOURNAL OF NANOTECHNOLOGY

Fabrication of hafnium-based nanoparticles and nanostructures using picosecond laser ablation

Abhishek Das[1], Mangababu Akkanaboina[2], Jagannath Rathod[3], R. Sai Prasad Goud[1], Kanaka Ravi Kumar[1], Raghu C. Reddy[4], Ratheesh Ravendran[4], Katia Vutova[5], S. V. S. Nageswara Rao[*1,6] and Venugopal Rao Soma[*1,3]

Full Research Paper

Open Access

Address:
[1]School of Physics, University of Hyderabad, Hyderabad 500046, Telangana, India, [2]Department of Physics, Banaras Hindu University, Varanasi 221005, Uttar Pradesh, India, [3]Advanced Centre of Research in High Energy Materials (ACRHEM), DRDO Industry Academia – Centre of Excellence (DIA-COE), University of Hyderabad, Hyderabad 500046, Telangana, India, [4]Centre for Materials for Electronics Technology (C-MET), IDA Phase III, Cherlapalli, HCL (P.O.), Hyderabad 500 051, Telangana, India, [5]Institute of Electronics, Bulgarian Academy of Sciences, 72, Tzarigradsko Shosse, 1784, Sofia, Bulgaria and [6]Centre for Advanced Studies in Electronics Science and Technology (CASEST), University of Hyderabad, Hyderabad 500046, Telangana, India

Email:
S. V. S. Nageswara Rao[*] - svnsp@uohyd.ac.in;
Venugopal Rao Soma[*] - soma_venu@uohyd.ac.in

* Corresponding author

Keywords:
hafnium; laser ablation in liquids; nanofibres; nanoparticles; nanostructures

Beilstein J. Nanotechnol. **2024,** *15,* 1639–1653.
https://doi.org/10.3762/bjnano.15.129

Received: 01 August 2024
Accepted: 02 December 2024
Published: 18 December 2024

This article is part of the thematic issue "Energetic ions and photons for engineering nanomaterials".

Associate Editor: X. Song

Abstract

This work presents a unique and straightforward method to synthesise hafnium oxide (HfO_2) and hafnium carbide (HfC) nanoparticles (NPs) and to fabricate hafnium nanostructures (NSs) on a Hf surface. Ultrafast picosecond laser ablation of the Hf metal target was performed in three different liquid media, namely, deionised water (DW), toluene, and anisole, to fabricate HfO_2 and HfC NPs along with Hf NSs. Spherical HfO_2 NPs and nanofibres were formed when Hf was ablated in DW. Hf ablated in toluene and anisole demonstrated the formation of core–shell NPs of HfC with a graphitic shell. All NPs exhibited novel optical reflectance properties. Reflectance measurements revealed that the fabricated NPs had a very high and broad optical absorption throughout the UV–vis–NIR range. The NPs synthesised in toluene exhibited the best absorption. The successful fabrication of Hf NSs with the formation of laser-induced periodic surface structures (LIPSS) with low spatial frequency (LSFL) and high spatial frequency (HSFL) orthogonal to each other was also demonstrated. The LSFL and HSFL both exhibited quasi-periodicity. This work presents a simple way to fabricate HfO_2 and HfC NPs and provides insight into their morphological and optical characteristics paving way for their applications in future.

Introduction

Hafnium (Hf) is a tetravalent transition metal with compounds showing excellent thermal and optical properties [1-4]. Hf and its alloys are used in nuclear reactors because of their large neutron absorption cross sections and high melting points [5]. They are also used in submarines because of their corrosion resistance [6,7]. The high refractoriness of some Hf compounds [2,4] allows them to be used in high-temperature alloys and ceramics. Hf compounds are widely used in microelectronics because of their high dielectricity values [2]. In recent years, NPs derived from Hf have gained significant interest in biomedical fields because of their superior optical and thermal properties [8] compared to bulk Hf. HfO_2 is a wide-bandgap (5.68 eV) material with a high dielectric constant (≈25) [9,10]. HfC has a very high melting point (≈3900 °C) and ranks among the hardest materials, with a Vickers hardness value exceeding 20 GPa [4,11]. The properties vary substantially depending on size and morphology [1]. Recently, interest has risen regarding synthesis and study of Hf-based NPs. Depending on the morphology, chemical composition, and quantum confinement effects, NPs can exhibit novel properties, making them applicable for large-spectrum usage [12,13]. Thus, synthesizing the desired morphology is essential for a given application. Generally, practical techniques for obtaining nanomaterials are sol–gel method, chemical and physical vapour deposition, hydrothermal method, ball milling, grinding, lithography, etching, and laser ablation [14-18]. The morphology determines the electrical and optical properties, which can vary depending on the synthesis technique [19]. Among the methods mentioned above, laser ablation in liquids (LAL) is a clean and single-step synthesis method used for obtaining nanomaterials from a bulk source [11,16-18,20]. It produces NPs of high purity with minimal or no unwanted by-products [11,17,21], thus making it a valuable candidate for green synthesis [21,22].

In the LAL method, a high-energy ultrashort pulsed laser (nanosecond, picosecond, or femtosecond) is focused on the surface of the target material immersed in a liquid medium. The target material absorbs the pulse energy via the electrons. It transfers it to the lattice, which expulses the surface material as a plasma plume confined because of the pressure created by the surrounding liquid [16,20,23,24]. A cavitation bubble is formed as the energy is transferred to the surrounding liquid from the decaying plasma because of the existing temperature differences between the liquid and the plasma plume, leading to the emergence of a vapour layer with a volume equivalent to the plasma plume [16,20,23,24]. The cavitation bubble collapses because of cyclic expansion and shrinkage, releasing nanoparticles into the surrounding liquid. The formed nanoparticles stay in the liquid as colloidal suspensions or can agglomerate to form a precipitate [6,16,20,23-27]. LAL provides flexibility regarding the choice of the liquid medium surrounding the target, from a single pure medium to a mixture of liquid media, with a range of target types such as powder, pellets, and well-defined structures and shapes [16,20]. The choice of the liquid medium can significantly affect morphology and chemical composition of the obtained NPs. The high energy of the laser pulses sometimes causes a reaction between the surrounding liquid medium and ablated target molecules, which may lead to the formation of unusual or non-equilibrium nanodimensional products [25,26,28,29]. Only few works on the laser ablation of Hf in liquid media have been reported in the literature. In our earlier reports, HfO_2 nanoparticles, nanoribbons, and nanofibres were synthesised by ablating HfO_2 pellets utilising femtosecond laser pulses at 800 nm [10,30]. A bulk Hf target was also ablated in another work using nanosecond laser pulses in different liquids to synthesise oxides and carbides [11,31]. In one of our earlier works [10], we performed femtosecond ablation and reported the formation of colloidal hafnium oxide NPs and nanoribbons in deionised water. The average sizes of NPs and nanoribbons were 13.5–18.0 and 10–20 nm, respectively. Further, we also reported that monoclinic and hexagonal phases were observed at higher input pulse energies. We believe these correspond to HfO_2 and Hf_6O, respectively. Further, in [10], we did not explore the formation of surface nanostructures on Hf after ablation. Therefore, the current study intends to understand the role of input pulse duration (picosecond pulses used here) and the surrounding liquid medium on the laser-ablated Hf-based NPs and NSs. Three different solvents, deionised water (DW; inorganic and oxygen-containing), toluene (organic and oxygen-free), and anisole (organic and oxygen-containing), have been chosen as ablation media. The Hf target was ablated with a picosecond laser in these three solvents to make three different colloidal solutions of Hf-based NPs. The optical, morphological, and physical properties of the obtained Hf-based NPs were studied in detail. The morphology of the ablated Hf surface in the three liquids was also investigated.

Experimental

Materials

Hf sponge was produced by metallurgical operations involving solvent extraction, briquetting, carbochlorination, Kroll reduction and vacuum distillation. The sponge samples were further refined by consolidation and refining under vacuum ($3–6 \times 10^{-5}$ mbar) using an electron beam melting furnace having a beam power of 60 kW (ELIT 60) at an accelerating voltage of 24 kV in a water-cooled crucible with feeding mechanism and an extraction system [32]. All operations were conducted at the Centre for Materials for Electronics Technology

(CMET), Hyderabad. These Hf sponges, cut and polished to 10 mm × 10 mm × 2 mm, were used as ablation targets. The pristine target had the crystal structure of hexagonal $HfO_{0.25}$, as confirmed by X-ray diffraction (XRD) data (see Figure 1a). The elemental composition (Hf: 73.68%, O: 26.32%) was determined by energy-dispersive X-ray spectroscopy (EDX, Figure 1b). Distilled water with a resistivity of more than 18 MΩ·cm was obtained from a Millipore system. Toluene and anisole (spectroscopic grade) were obtained from Sigma-Aldrich and used as received.

Synthesis of nanoparticles and nanostructures

A linearly polarised picosecond laser [Nd:YAG, M/s EKSPLA] with a pulse duration of ≈30 ps, a repetition rate of ≈10 Hz, a wavelength of ≈1064 nm, and a pulse energy of ≈16.3 mJ (determined from previous experiments [33] and optimised using multiple ablation trials followed by detailed characterization studies) was used for the fabrication of the NPs and NSs. The ablation was performed in three different liquids, that is, DW, toluene, and anisole. As illustrated in Figure 2, the incoming

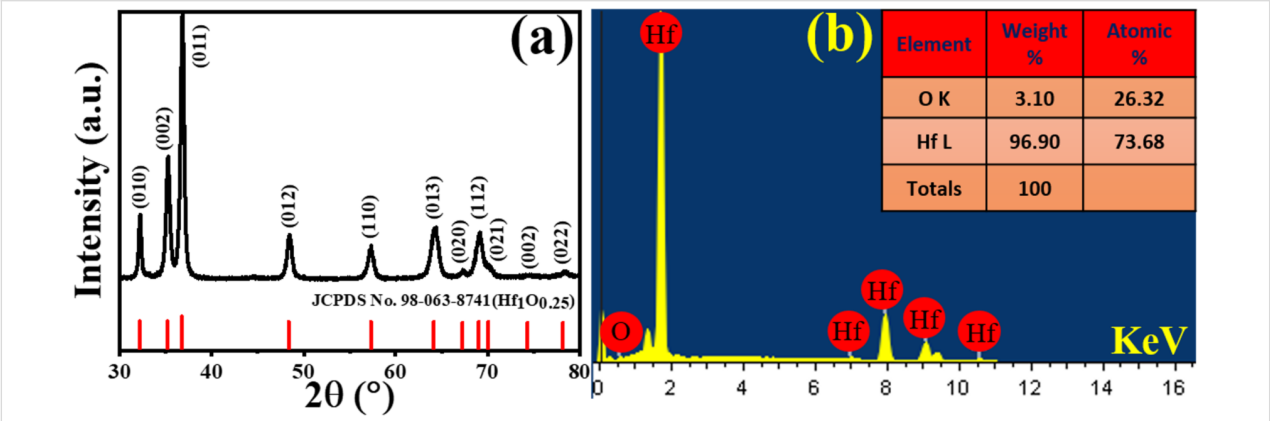

Figure 1: (a) XRD data and (b) EDX data of pristine Hf target.

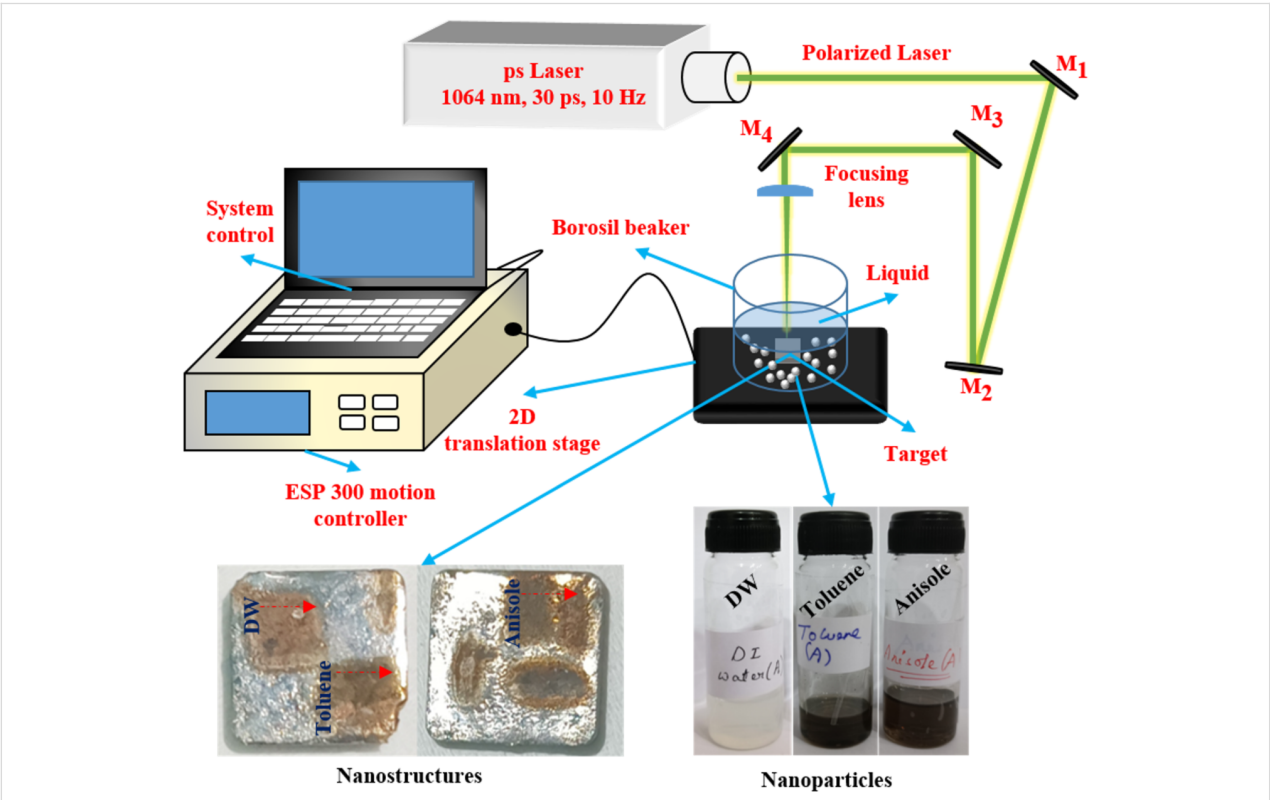

Figure 2: Schematic representation of the experimental setup used for picosecond LAL of a Hf target (M_n represents mirrors).

laser beam was focused vertically on the Hf target in a liquid-filled glass cell using a plano-convex lens (f = 80 mm). The liquid surface was about 5 mm above the target surface. Raster scanning was performed at a speed of 0.1 mm/s to ablate an area of 5 × 5 mm^2. This resulted in Hf surface nanostructures and Hf NPs forming in the surrounding liquid. A gradual colour change of the liquids initially confirmed the formation of Hf-based NPs; DW turned from transparent to turbid white, while toluene and anisole turned from transparent to black (Figure 2). The obtained NPs and NSs were labelled as described in Table 1, according to the liquid in which they were ablated, and subsequently characterised through different methods.

Table 1: Labelling of the NPs and NSs according to the liquid media used.

Liquids used	NPs	NSs
DW	HfNPs-D	HfNSs-D
toluene	HfNPs-T	HfNSs-T
anisole	HfNPs-A	HfNSs-A

Characterization techniques

The synthesised NPs were drop-cast on carbon-coated copper grids to record transmission electron microscopy (TEM) images and selected area electron diffraction (SAED) patterns using a FEI Tecnai G2 S-Twin operating at 200 kV. Further, these NPs were drop-cast on cleaned Si substrates, and their morphology was analysed using field-emission scanning electron microscopy (FESEM); the composition was determined by EDX attached to the FESEM (Carl Zeiss Smart SEM ULTRA 55). Reflectivity was investigated using a UV–vis–NIR spectrometer (PerkinElmer Lambda 750). For photoluminescence (PL) measurements, a Horiba LabRAM HR Evolution (Excitation: 325 nm, Lens: 40×, spot size: 1 µm) was used. Image J software was used to extract spatial periodicities and to generate 2D fast Fourier transform images (2D FFT) of the Hf surface structures.

Results and Discussion

Nanoparticles

Figure 3 shows TEM images, the corresponding particle size distributions, and the SAED patterns of NPs obtained in DW (Figure 3a–c), toluene (Figure 3d–f), and anisole (Figure 3g–i). The TEM image corresponding to HfNPs in DW shows the formation of nanofibres of diameters ranging from 5 to 65 nm along with spherical NPs (marked with red dashed circles, Figure 3a). The formation of nanofibres is consistent with our earlier observations for HfO_2 ablation in DW [10,30]. Further, the TEM images corresponding to Hf NPs in toluene and anisole (Figure 3d,g) illustrate the formation of spherical particles only. The majority of the NPs had a size distribution in the ranges of 5–40 nm in DW and 5–20 nm in toluene and anisole, respectively, as shown in Figure 3b, Figure 3e, and Figure 3h, respectively. The SAED patterns shown in Figure 3c,f,i indicate that the NPs were polycrystalline. The planes shown in Figure 3c for HfNPs-D were found to be (203), (103), (102), and (002) corresponding to orthogonal hafnium oxide HfO_2 (ICDD: 98-008-7456). In contrast, HfNPs-T (Figure 3f) and HfNPs-A (Figure 3i) exhibited the (111), (002), (022), and (113) planes corresponding to hafnium carbide HfC [ICDD: 98-018-5992]. The observation of HfO_2 in DW and HfC in toluene and anisole can be attributed to chemical interactions between the ablated Hf atoms and the liquid medium.

Careful observation of high-resolution TEM images revealed the formation of core–shell structures for the particles obtained in anisole and toluene (Figure 4b,c). In contrast, we did not notice such a structure in the case of NPs fabricated in DW (Figure 4a). Shell-like structures in Figure 4b and Figure 4c are indicated with red arrows. These structures are multilayered carbon shells around the NPs. Similar formations were noticed in other studies where carbon-rich liquids were used [34-36]. The d-spacing of the carbon shells was determined from the zoomed images in Figure 5. It was estimated to be ≈0.34 nm, confirming the outer shell to be made of graphite [37-39].

A similar analysis was conducted on the nanofibre-like structures formed when Hf was ablated in DW. Figure 6 shows nanofibres (Figure 6a) and NPs (Figure 6c) formed in DW, together with the corresponding SAED patterns (Figure 6b and Figure 6d, respectively). A difference can be seen between the crystallinity of the nanofibres and that of the NPs. Figure 6b shows that the nanofibres are perfectly polycrystalline. In contrast, in Figure 6d, the presence of diffused rings for HfNPs-D indicates a mix of amorphous and polycrystalline phases in the NPs. The formation of HfO_2 NPs in DW along with nanofibres and the observed crystallinity patterns can be explained by considering the decomposition of the surrounding H_2O molecules due to the laser energy [23,24,40]. This leads to the reaction of oxygen with Hf^{4+} ions in the plasma plume formed during the ablation [16,20,23,24,41], leading to the formation of hafnium oxide vapour as the plasma decays. As the pressure of the surrounding liquid exceeds the vapour pressure exerted by HfO_2, the cavitation bubble collapses, and the vapour rushes through the liquid in the form of a jet [23,24,41]. The lower temperature of the surrounding liquid leads to the formation of nuclei [23,42,43] with random crystallographic orientation, which grow to form crystals [43-45]. These crystals coalesce to form a polycrystalline structure [43,46]. As the vapour rushes out as a jet, these polycrystals assemble [43,47] linearly to form

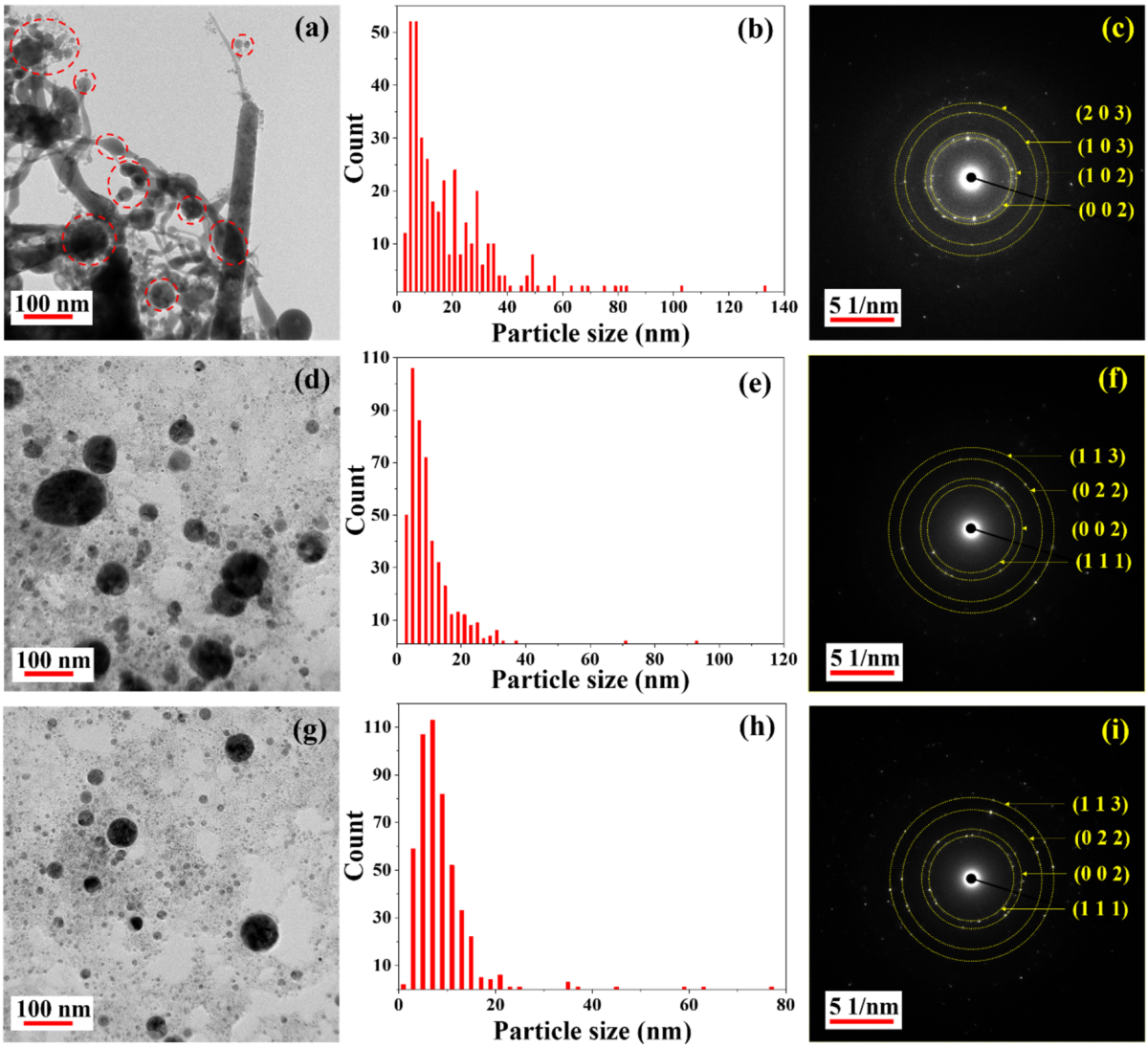

Figure 3: TEM images, particle size distributions, and SAED patterns of laser-ablated NPs in (a–c) DW, (d–f) toluene, and (g–i) anisole.

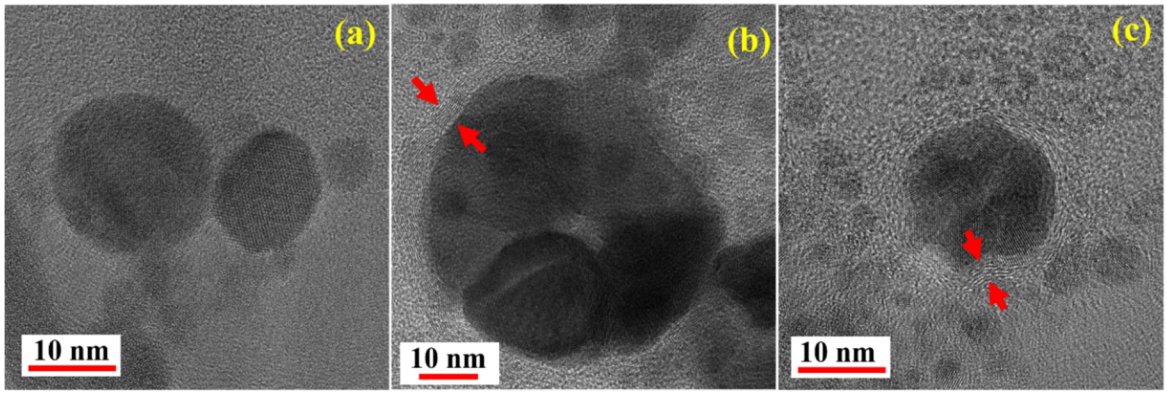

Figure 4: High-resolution TEM images of laser-ablated NPs in (a) DW, (b) toluene, and (c) anisole.

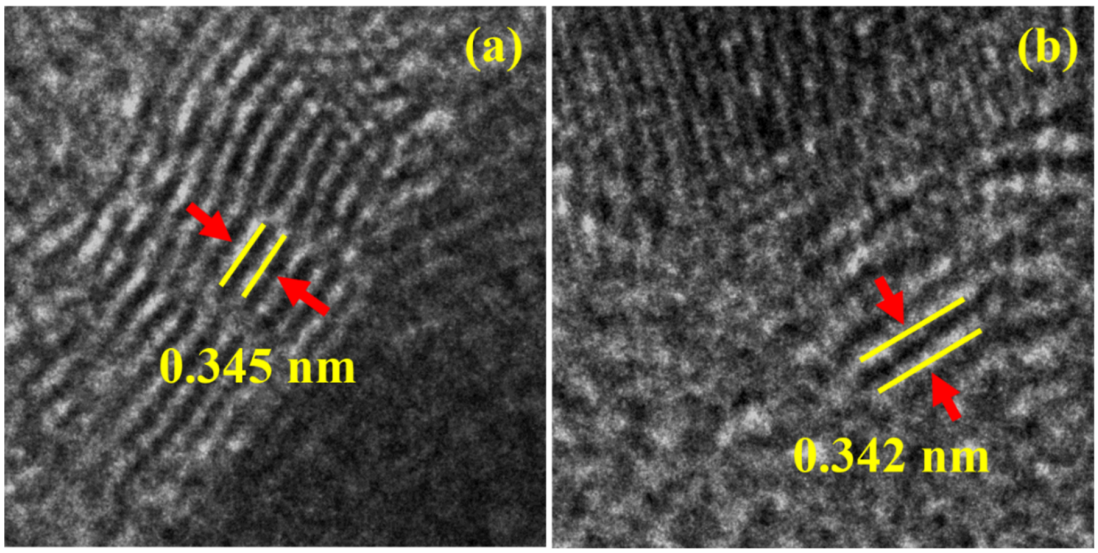

Figure 5: Zoomed TEM images of the shell-like structures shown in Figure 4b and Figure 4c for (a) toluene and (b) anisole (the d-spacings of the outer shells are indicated with yellow lines).

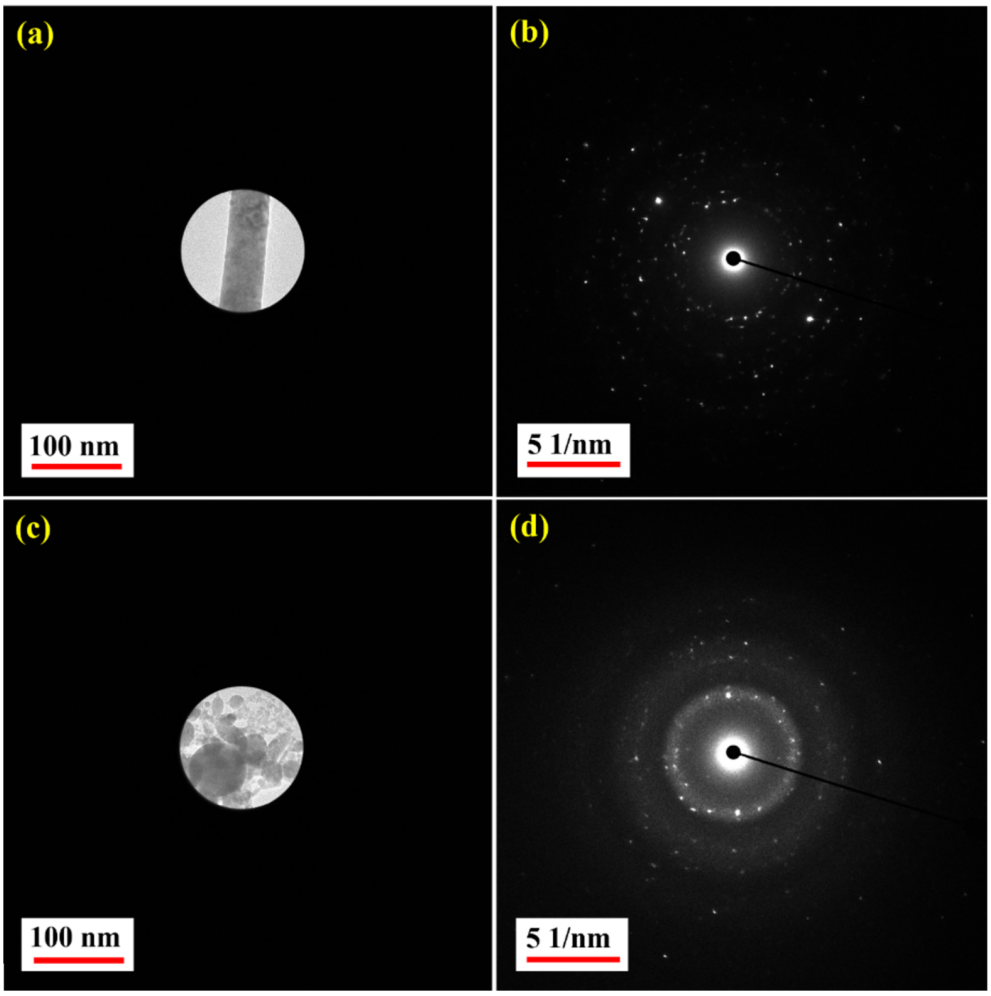

Figure 6: SAED measurement locations and patterns for (a, b) nanofibres and (c, d) NPs obtained in DW.

nanofibres. The formation of these nanofibres seems to depend upon laser parameters such as pulse duration, repetition rate, wavelength, and pulse energy, as is evident from earlier reports [11,18,31], where no such nanofibre formation is reported. However, the formation of nanofibres has been reported in [10,30]. Due to Brownian motion [48], some nuclei and crystals escape from the jet flow and agglomerate [43,47,48], leading to the formation of nanoparticles [43]. Some of these nuclei with abundant hafnium oxide molecules around grow like crystals [45,48]. The agglomeration [47] of such crystals leads to the observed polycrystalline state in the NPs [43,46]. The formation of the observed amorphous NPs is due to the suppression of nucleation [43,49]. Thus, a mix of amorphous and polycrystalline structures in NPs obtained in DW is seen. The formation of these HfO_2 NPs and nanofibres is responsible for the turbid white colour observed after ablation in DW.

Earlier reports on Hf ablation in toluene [11,31] did not discuss the formation of graphite shells around HfC NPs. The formation of polycrystalline HfC core–shell NPs with graphite shells similar to [36] in toluene and anisole can be explained by the possible reaction of carbon from decomposed surrounding liquid with Hf^{4+} ions in the plasma plume [20,23,24,40]. As the plasma plume decays, its space is occupied by HfC vapour. The pressure difference due to the surrounding liquid causes the cavitation bubble to collapse; thus, the vapour rushes through the liquid and forms polycrystals, similar to the above case of HfO_2 [16,20,23,24,41,43]. The decomposed surrounding liquid has a carbon-rich environment. As the polycrystals grow, they also act as a nucleus for carbon atoms to self-assemble [27,50], forming graphite layers and, eventually, core–shell NPs of different sizes. This formation of graphite layers might prevent the formation of fibres. As no hafnium oxide was observed, it can be stated that oxygen in the plasma from $HfO_{0.25}$ did not react with Hf^{4+}. This can be explained through the fact that the carbon-rich environment near the plasma shifts the reaction equilibrium in favour of the formation of HfC [23,24,51,52]. Thus, the O^{2+} ions do not react with the Hf^{4+} ions. The O^{2+} ions can react with C or escape the liquid as O_2. The black colour observed in toluene and anisole after ablation is due to the formation of HfC core–shell NPs and the decomposition of the surrounding liquid [27,39,53]. The formation of carbides by LAL in aromatic solvents was reported previously with transition metals such as iron and cobalt [54-56]. Kanitz et al. [55] have reported the formation of pure (i.e., with a clean surface) iron nanoparticles when the target was ablated with femtosecond pulses (5 kHz repetition rate, though) in different solvents. They observed that the choice of the surrounding liquid environment allowed them to tune the properties of the iron-based NPs, for example, the generation of iron oxides or carbides. In the present case, the surrounding liquid possibly had a huge influence on the formation of carbides. For a given Hf target (regarding purity and surface roughness), the ablation products depend critically on the surrounding liquid, input pulse duration, input pulse energy, and the number of pulses incident on the sample.

Figure 7 illustrates the EDX data for the particles synthesised in DW, toluene, and anisole. The EDX spectra of HfNPs-D confirm the presence of hafnium and oxygen (Figure 7a). The observed atomic percentages are 73.86 atom % oxygen and 26 atom % Hf (Figure 7a). The composition tables for HfNPs-T (Figure 7b) and for HfNPs-A (Figure 7c) show the presence of carbon and hafnium. The high fraction of C indicates the formation of the graphitic shell around HfC NPs in both toluene and anisole.

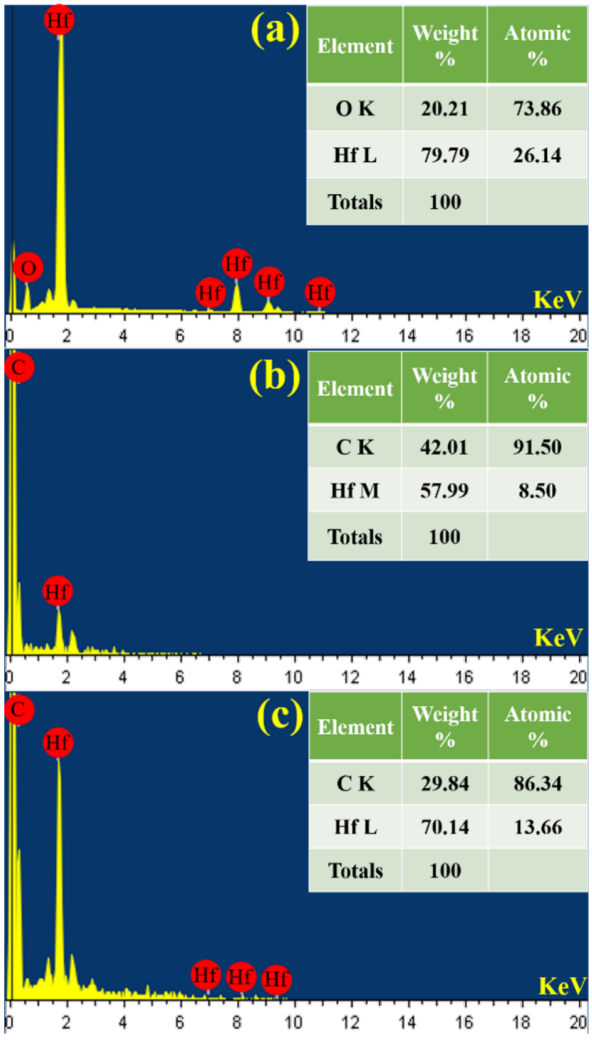

Figure 7: EDX spectra and elemental composition of (a) HfNPs-D, (b) HfNPs-T, and (c) HfNPs-A.

Figure 8 shows the reflectance data of a pristine Si substrate compared to a Si substrate coated with HfNPs-D, HfNPs-T, and HfNPs-A under three different angles of incidence (30°, 45°, and 60°) taken in the wavelength range from 250 to 1200 nm. The black curve corresponds to the reflectance spectrum of the reference pristine Si sample; the red curve is HfNPs-T, the blue curve is HfNPs-A, and the green curve is HfNPs-D. The values of the reflectance and reduction in the UV (λ = 250 nm) and the NIR (λ = 1200 nm) spectral regions of the NPs under different angles of incidence are summarised in Table 2. Based on the data, it can be concluded that Hf NPs show a very high and wide optical absorption from UV to NIR. HfNPs-T especially show exceptional performance compared to other NPs with far superior and stable optical absorption compared to similar HfC NPs synthesised in our earlier work [31]. With an increase in angle, a reduction in absorption was observed for HfNPs-D, HfNPs-T, and HfNPs-A. A decrease in absorption was also observed with an increase in wavelength at a constant angle. The deviation in the spectral pattern of HfNPs-T and HfNPs-A could be due to the presence of oxygen in the polycrystalline lattice of HfNPs-A. The additional oxygen in anisole compared to toluene might have been included in the NPs' polycrystalline structure during NP formation. We can confirm that the oxygen from anisole has not reacted with the Hf^{4+} ions as no oxide compound was found in the SAED data of HfNPs-A (Figure 3i) as compared to HfNPs-T (Figure 3f). Thus, the extra oxygen in anisole is likely to be present as an impurity in the polycrystalline structure of the NPs in HfNPs-A and may affect the optical properties of the NPs.

Figure 9a–c shows the PL emission spectra of the NPs laser-ablated in DW, toluene, and anisole, respectively. Emission peaks were observed for each of the NPs (Figure 9). The presence of emission peaks indicates the presence of defects in the

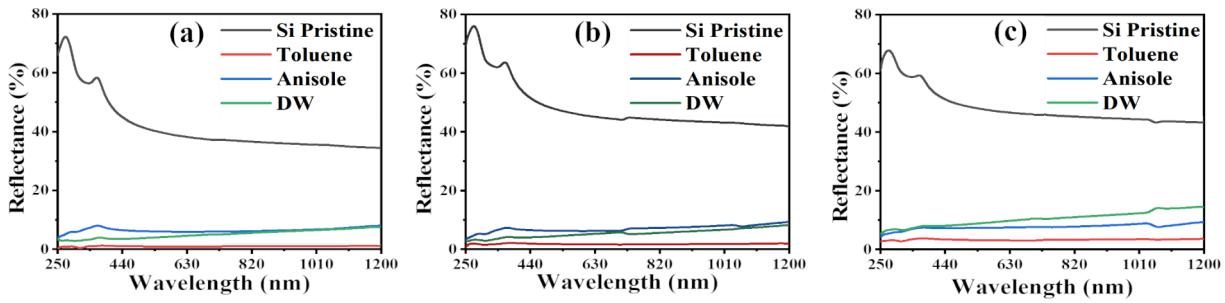

Figure 8: Reflectance spectra of NPs drop-cast on Si substrates measured under different incident angles: (a) 30°, (b) 45°, and (c) 60°. The black curve is the reflectance spectrum of the reference Si substrate; the red, blue, and green curves represent Hf NPs synthesised in in toluene, anisole, and DW, respectively.

Table 2: Reflectance and reduction in reflection in the UV and NIR regions of the NPs under different angles of incidence (θ).

θ		UV (λ = 250 nm)	NIR (λ = 1200 nm)
		reflectance (%) (reduction of reflectance)	reflectance (%) (reduction of reflectance)
30°	Si (pristine)	66.71% (–)	34.56% (–)
	HfNPs-D	3.35% (94.97%)	7.83% (77.34%)
	HfNPs-T	0.72% (98.92%)	1.11% (96.78%)
	HfNPs-A	3.35% (94.97%)	7.83% (77.34%)
45°	Si (pristine)	70.26% (–)	41.94% (–)
	HfNPs-D	3.28% (95.33%)	8.23% (80.37%)
	HfNPs-T	0.92% (98.69%)	1.87% (95.54%)
	HfNPs-A	3.28% (95.33%)	9.41% (77.56%)
60°	Si (pristine)	61.43% (–)	43.39% (–)
	HfNPs-D	5.45% (91.12%)	14.55% (66.46%)
	HfNPs-T	2.81% (95.42%)	3.66% (91.56%)
	HfNPs-A	4.27% (93.05%)	9.55% (77.99%)

NPs [57]. The defects may be due to impurities in the lattice structure, possibly in the form of oxygen contamination, or imperfect crystallinity of the graphitic layer or the NPs themselves. Further detailed PL studies are essential to understand the origin of the observed emission peaks.

Nanostructures

Figure 10 illustrates the NS fabrication with picosecond LAL by raster scanning the Hf target. The figure also depicts the LSFL and HSFL formed on the target during the scanning process. The LAL technique is versatile since the NPs and NSs

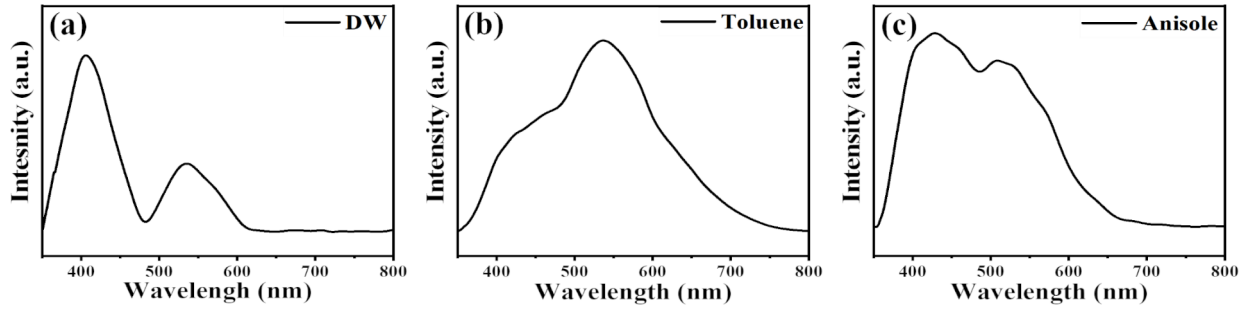

Figure 9: PL spectra of NPs laser-ablated in (a) DW, (b) toluene, and (c) anisole.

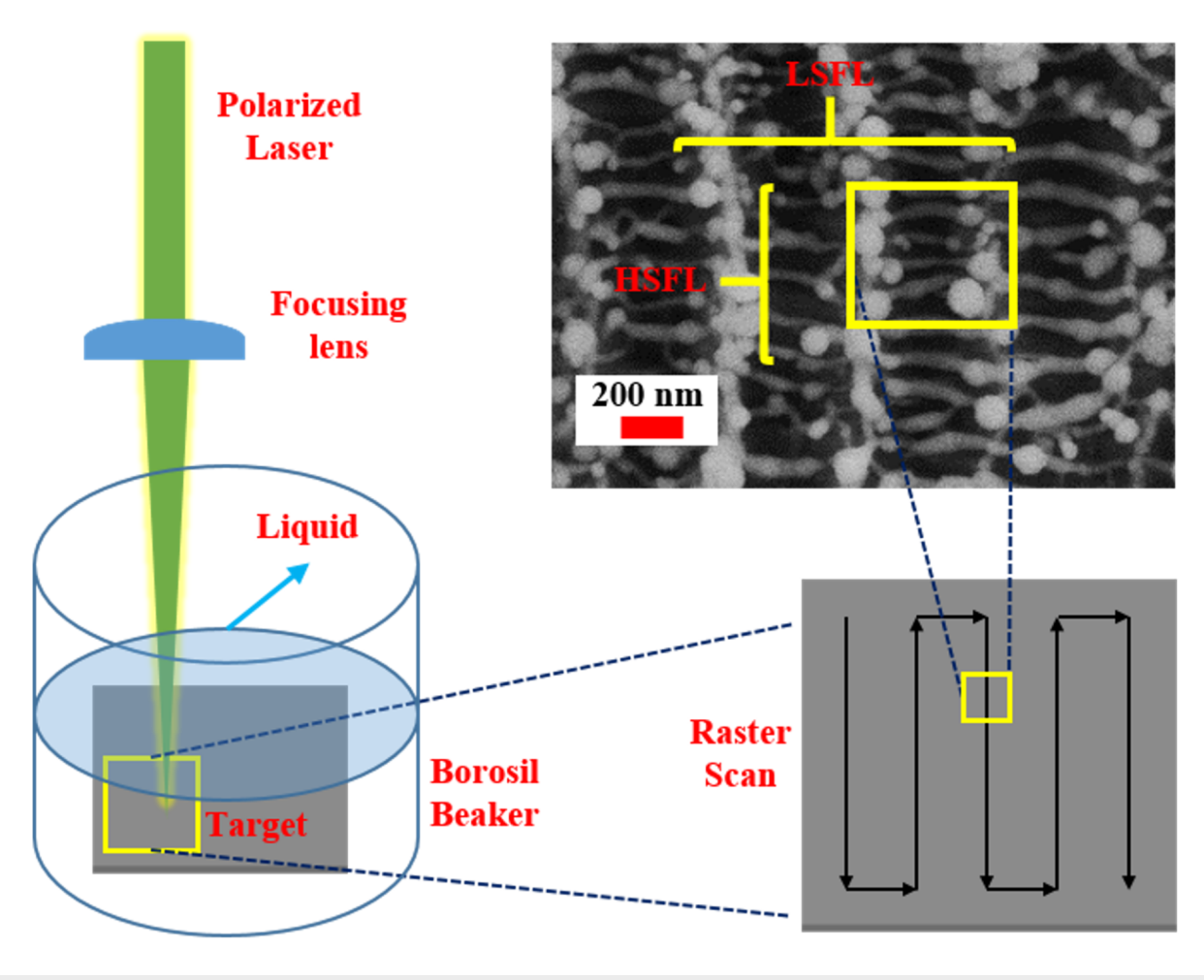

Figure 10: Schematic of the NS fabrication by raster scanning the sample, resulting in LSFL and HSFL formation.

are obtained simultaneously in a single experiment, which is impossible with any other lithographic technique (laser-based or otherwise). However, the patterning of the target will influence the obtained NPs and NSs since the number of pulses incident on a particular surface area will vary with different scanning/writing conditions. Scanning parameters (e.g., speed of the stage or spot size of the laser) can be varied to achieve an optimum size of the NPs and NSs. The simultaneous formation of HSFL and LSFL on the Hf target during LAL was observed in all liquids. The LSFL structures were oriented parallel to the laser scanning direction, and the HSFL structures were formed in the depressions of the LSFL with a direction perpendicular to the direction of the laser scan.

Similar observations regarding the formation of LSFL and HSFL with orthogonal directionality and the plausible mechanisms behind their formation are discussed in an earlier work [58]. Figure 11 shows FESEM images of the laser-ablated NSs and 2D FFTs of LSFL with spatial periodicity for HfNSs-D, HfNSs-T, and HfNSs-A analysed using ImageJ software. Based on the data analysis, it can be concluded that the structures are quasi-periodic and have a sub-wavelength periodicity of $\lambda_L/2$ or greater (λ_L is the laser wavelength). The quasi-periodicity values indicated as *D* in Figure 11b,d,f were 498 ± 40 nm for HfNSs-D, 519 ± 30 nm for HfNSs-T, and 505 ± 64 nm for HfNSs-A. On further inspection of the FESEM images of the NSs, the formation of HSFL was observed. Figure 12

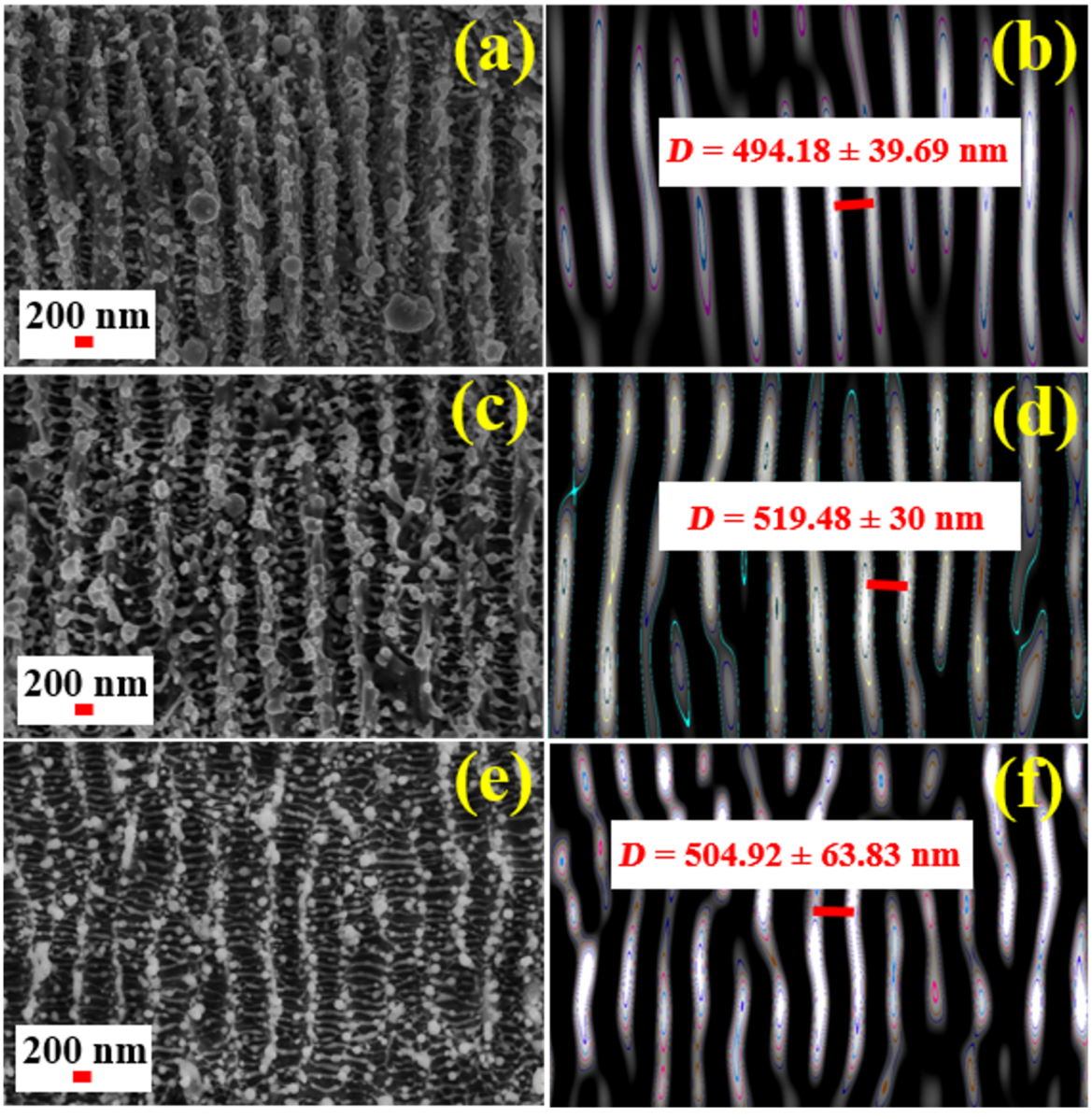

Figure 11: FESEM image and inverse FFTs of LSFL with spatial periodicity on laser-ablated NSs in (a, b) DW, (c, d) toluene, and (e, f) anisole.

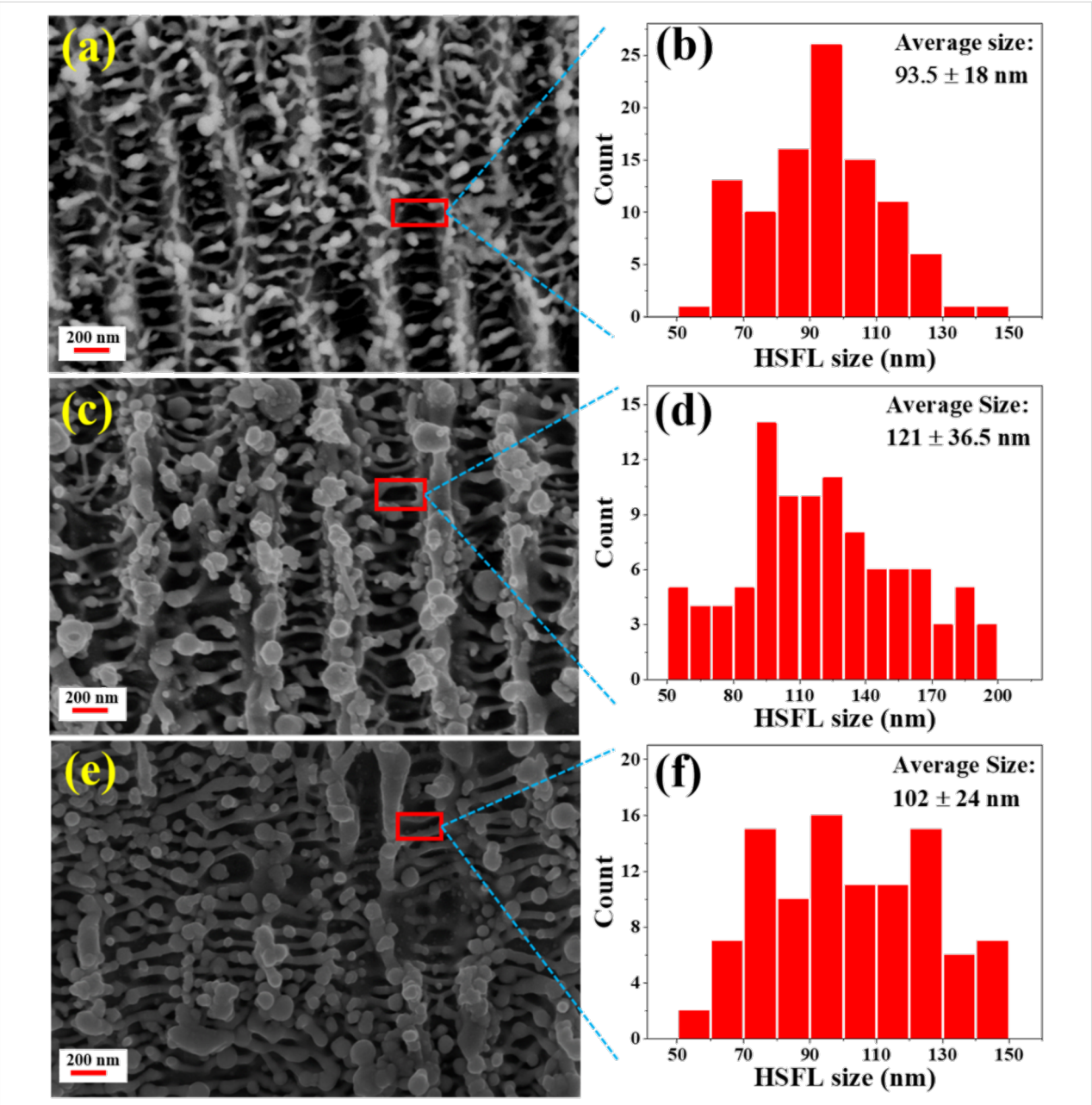

Figure 12: FESEM image and HSFL size distribution of NSs laser-ablated in (a, b) DW, (c, d) toluene, and (e, f) anisole.

shows FESEM images of the HSFLs and the corresponding distribution of their feature size in HfNSs-D, HfNSs-T, and HfNSs-A.

The structures show sub-wavelength quasi-periodicity. The observed HSFL had an average feature size between $\lambda_L/11$ and $\lambda_L/8$ for all NSs. The feature size for HfNSs-D ranged from 50 to 150 nm, with an average feature size of 94 ± 18 nm, that of HfNSs-T ranged from 50 to 200 nm, with an average feature size of 121 ± 37 nm, and that of HfNSs-A ranged from 50 to 150 nm with an average feature size of 102 ± 24 nm.

Figure 13 shows the relationship between the refractive index (η) of the liquid used during ablation and the corresponding spatial periodicity for LSFL and HSFL. The spatial periodicity was observed to increase from HfNSs-D ($\eta^{DW} \approx 1.33$ [59]) to HfNSs-T ($\eta^{toluene} \approx 1.49$ [60]) and to decrease again for HfNSs-A ($\eta^{anisole} \approx 1.51$ [61,62]). The values are summarised in Table 3. The observable HFSL size appears to be independent on λ_L [63], instead the HSFL size depends on laser parameters such as fluence, energy dose, and pulse duration [64]. Re-deposition and re-solidification of the ablated NPs on NSs were also observed, which matches with observation in an earlier re-

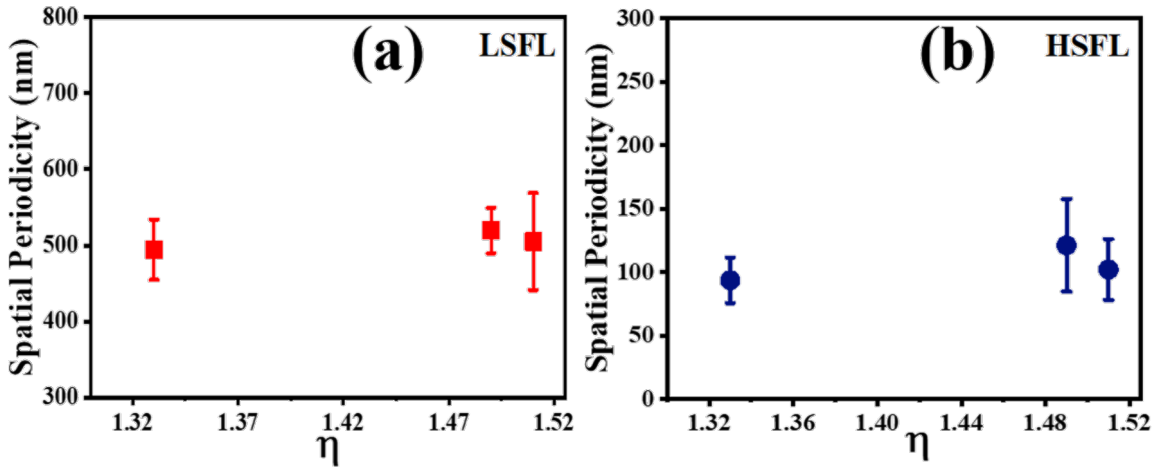

Figure 13: Spatial periodicity of (a) LSFL and (b) HSFL as function of the refractive index.

Table 3: Spatial periodicity of LSFL and HSFL in NSs as funcition of the refractive index of the liquid used for ablation.

Liquids used	Refractive index (η)	NSs	LSFL (nm)	HSFL (nm)
DW	≈1.33	HfNSs-D	498 ± 40	94 ± 18
toluene	≈1.49	HfNSs-T	519 ± 30	121 ± 37
anisole	≈1.51	HfNSs-A	505 ± 64	102 ± 24

ported work [65] for titanium ablation. These properties make Hf metal suitable for laser patterning of sub-wavelength-size structures, and the choice of the liquid for LAL enables the variation of feature size. We have used linearly polarised light in the present study. The orientation of the LIPSS depends on the polarization and rotates with the input polarization. The available literature on LIPSS suggests that there will be no changes in the spacing or other morphological features except the orientation of the LIPSS with respect to the polarisation. Combined with the picosecond laser's high precision processing and industrial scalability, Hf is a potential material for sophisticated design patterning [66].

Conclusion

The current study shows the successful single-step fabrication of HfO_2 NPs and nanofibres in DW and HfC core–shell NPs with multilayered graphitic shells in toluene and anisole via LAL of Hf metal. The obtained NPs exhibit a broad size distribution. Most NPs had a diameter between 5 and 20 nm. The HfNPs-D, HfNPs-T, and HfNPs-A NPs were found to be polycrystalline. The oxygen in anisole was found to be inert during ablation and was possibly incorporated as impurity in HfNPs-A. The HfO_2 nanofibres were also found to be polycrystalline, with diameters ranging from 5 to 65 nm. The NPs showed very high and broad optical absorption throughout the UV–vis–NIR range. The maximum absorption was observed at 30° at UV (λ = 250 nm) for HfNPs-T with just 0.72% reflection. The absorption decreases in HfNPs-D, HfNPs-T, and HfNPs-A with an increase in wavelength and angle of incidence. The NPs are suitable for application in optical devices requiring high and stable optical absorption throughout the UV–vis–NIR range. The successful fabrication of Hf NSs with the formation of LIPSS, LSFL and orthogonal HSFL, was also demonstrated. The LSFL and HSFL both showed quasi-periodicity. The spatial periodicity of LSFL and HSFL first increased and then decreased with respect to the refractive index of the liquid used during ablation. This form of data is highly valuable to optimise the feature sizes during laser patterning in standard ablation liquids. The study will be extended to other metallic targets and more liquids to create a more comprehensive report.

Acknowledgements

We acknowledge the School of Physics, the Central Facility for Nanotechnology (CNF), the Advanced Centre of Research in High Energy Materials (ACRHEM; now DIA-CoE, University of Hyderabad), and the School of Chemistry for providing access to the necessary instruments.

Funding

Funding is provided by IOE, UoH, and ACRHEM/DRDO. Mangababu acknowledges financial support from CSIR India (for SRF) and IOE BHU (for RJP PDF). S.V.S Nageswara Rao DST PURSE, UGC-SAP-DRS-1, CASEST, and SOP for financial support and CFN, UGC-NRC Venugopal Rao Soma thanks DRDO, India for financial support through ACRHEM [#ERIP/ER/1501138/M/01/319/D(R&D)]. We thank IOE and UOH for their financial support [Ref. No. UOH/IOE/RC1/RC1- 20-016].

Author Contributions

Abhishek Das: data curation; formal analysis; investigation; writing – original draft; writing – review & editing. Mangababu Akkanaboina: formal analysis; project administration; writing – original draft; writing – review & editing. Jagannath Rathod: formal analysis; project administration; writing – original draft. R. Sai Prasad Goud: data curation; investigation; writing – original draft. Kanaka Ravi Kumar: data curation; investigation; writing – original draft; writing – review & editing. Raghu C. Reddy: formal analysis; resources; writing – original draft. Ratheesh Ravendran: conceptualization; formal analysis; resources; writing – review & editing. Katia Vutova: formal analysis; resources; writing – original draft. S. V. S. Nageswara Rao: conceptualization; project administration; resources; supervision; writing – original draft; writing – review & editing. Venugopal Rao Soma: conceptualization; methodology; project administration; resources; supervision; validation; writing – original draft; writing – review & editing.

ORCID® iDs

Abhishek Das - https://orcid.org/0009-0000-4557-4882
R. Sai Prasad Goud - https://orcid.org/0000-0003-1533-0582
Kanaka Ravi Kumar - https://orcid.org/0000-0001-7066-9509
Katia Vutova - https://orcid.org/0000-0002-1300-2369
Venugopal Rao Soma - https://orcid.org/0000-0001-5361-7256

Data Availability Statement

Data generated and analyzed during this study is available from the corresponding author upon reasonable request.

Preprint

A non-peer-reviewed version of this article has been previously published as a preprint: https://doi.org/10.3762/bxiv.2024.55.v1

References

1. Wan, Y.; Zhou, X. *RSC Adv.* **2017,** *7,* 7763–7773. doi:10.1039/c6ra26663k
2. Araiza, J. d. J.; Álvarez-Fraga, L.; Gago, R.; Sánchez, O. *Materials* **2023,** *16,* 5331. doi:10.3390/ma16155331
3. Bokhonov, B. B.; Dudina, D. V. *Ceram. Int.* **2017,** *43,* 14529–14532. doi:10.1016/j.ceramint.2017.07.164
4. Zagorac, J.; Schön, J. C.; Matović, B.; Butulija, S.; Zagorac, D. *Crystals* **2024,** *14,* 340. doi:10.3390/cryst14040340
5. Ulybkin, A.; Rybka, A.; Kovtun, K.; Kutny, V.; Voyevodin, V.; Pudov, A.; Azhazha, R. *Nucl. Eng. Technol.* **2019,** *51,* 1964–1969. doi:10.1016/j.net.2019.06.007
6. Zhang, J.; Claverie, J.; Chaker, M.; Ma, D. *ChemPhysChem* **2017,** *18,* 986–1006. doi:10.1002/cphc.201601220
7. Cotton, S. A. *Annu. Rep. Prog. Chem., Sect. A: Inorg. Chem.* **2008,** *104,* 145. doi:10.1039/b716569m
8. Skrodzki, D.; Molinaro, M.; Brown, R.; Moitra, P.; Pan, D. *ACS Nano* **2024,** *18,* 1289–1324. doi:10.1021/acsnano.3c08917
9. Aktas, S.; Caglar, M. *Mater. Sci. Eng., B* **2024,** *308,* 117587. doi:10.1016/j.mseb.2024.117587
10. Dhanunjaya, M.; Byram, C.; Vendamani, V. S.; Rao, S. V.; Pathak, A. P.; Rao, S. V. S. N. *Appl. Phys. A: Mater. Sci. Process.* **2019,** *125,* 74. doi:10.1007/s00339-018-2366-y
11. Lopez, O.; Magaña, A.; Zhang, J.; Mehrabi, H.; Hunter, B. M. *ACS Appl. Nano Mater.* **2024,** *7,* 5085–5092. doi:10.1021/acsanm.3c05879
12. Khan, I.; Saeed, K.; Khan, I. *Arabian J. Chem.* **2019,** *12,* 908–931. doi:10.1016/j.arabjc.2017.05.011
13. Scher, J. A.; Elward, J. M.; Chakraborty, A. *J. Phys. Chem. C* **2016,** *120,* 24999–25009. doi:10.1021/acs.jpcc.6b06728
14. Kumar, S.; Bhushan, P.; Bhattacharya, S. Fabrication of Nanostructures with Bottom-up Approach and Their Utility in Diagnostics, Therapeutics, and Others. In *Environmental, Chemical and Medical Sensors. Energy, Environment, and Sustainability;* Bhattacharya, S.; Agarwal, A.; Chanda, N.; Pandey, A.; Sen, A., Eds.; Springer: Singapore, 2018; pp 167–198. doi:10.1007/978-981-10-7751-7_8
15. Abid, N.; Khan, A. M.; Shujait, S.; Chaudhary, K.; Ikram, M.; Imran, M.; Haider, J.; Khan, M.; Khan, Q.; Maqbool, M. *Adv. Colloid Interface Sci.* **2022,** *300,* 102597. doi:10.1016/j.cis.2021.102597
16. Balachandran, A.; Sreenilayam, S. P.; Madanan, K.; Thomas, S.; Brabazon, D. *Results Eng.* **2022,** *16,* 100646. doi:10.1016/j.rineng.2022.100646
17. Byram, C.; Moram, S. S. B.; Banerjee, D.; Beeram, R.; Rathod, J.; Soma, V. R. *J. Opt. (Bristol, U. K.)* **2023,** *25,* 043001. doi:10.1088/2040-8986/acbc31
18. Pugachevskii, M. A.; Panfilov, V. I. *J. Appl. Spectrosc.* **2014,** *81,* 640–643. doi:10.1007/s10812-014-9982-x
19. Kolahalam, L. A.; Kasi Viswanath, I. V.; Diwakar, B. S.; Govindh, B.; Reddy, V.; Murthy, Y. L. N. *Mater. Today: Proc.* **2019,** *18,* 2182–2190. doi:10.1016/j.matpr.2019.07.371
20. Fazio, E.; Gökce, B.; De Giacomo, A.; Meneghetti, M.; Compagnini, G.; Tommasini, M.; Waag, F.; Lucotti, A.; Zanchi, C. G.; Ossi, P. M.; Dell'Aglio, M.; D'Urso, L.; Condorelli, M.; Scardaci, V.; Biscaglia, F.; Litti, L.; Gobbo, M.; Gallo, G.; Santoro, M.; Trusso, S.; Neri, F. *Nanomaterials* **2020,** *10,* 2317. doi:10.3390/nano10112317
21. Altuwirqi, R. M.; Albakri, A. S.; Al-Jawhari, H.; Ganash, E. A. *Optik (Munich, Ger.)* **2020,** *219,* 165280. doi:10.1016/j.ijleo.2020.165280
22. Banerjee, D.; Moram, S. S. B.; Byram, C.; Rathod, J.; Jena, T.; Podagatlapalli, G. K.; Soma, V. R. *Appl. Surf. Sci.* **2021,** *569,* 151070. doi:10.1016/j.apsusc.2021.151070
23. Xiao, J.; Liu, P.; Wang, C. X.; Yang, G. W. *Prog. Mater. Sci.* **2017,** *87,* 140–220. doi:10.1016/j.pmatsci.2017.02.004
24. Aliofkhazraei, M., Ed. *Handbook of Nanoparticles;* Springer International Publishing: Cham, Switzerland, 2016. doi:10.1007/978-3-319-15338-4

25. D'Urso, L.; Spadaro, S.; Bonsignore, M.; Santangelo, S.; Compagnini, G.; Neri, F.; Fazio, E. *EPJ Web Conf.* **2018,** *167,* 04008. doi:10.1051/epjconf/201816704008
26. Fazio, E.; Santoro, M.; Lentini, G.; Franco, D.; Guglielmino, S. P. P.; Neri, F. *Colloids Surf., A* **2016,** *490,* 98–103. doi:10.1016/j.colsurfa.2015.11.034
27. Yang, S.; Zeng, H.; Zhao, H.; Zhang, H.; Cai, W. *J. Mater. Chem.* **2011,** *21,* 4432. doi:10.1039/c0jm03475d
28. Zhang, D.; Wada, H. Laser Ablation in Liquids for Nanomaterial Synthesis and Applications. In *Handbook of Laser Micro- and Nano-Engineering;* Sugioka, K., Ed.; Springer: Cham, 2021; pp 1481–1515. doi:10.1007/978-3-030-63647-0_30
29. Kuladeep, R.; Jyothi, L.; Prakash, P.; Mayank Shekhar, S.; Durga Prasad, M.; Narayana Rao, D. *J. Appl. Phys.* **2013,** *114*. doi:10.1063/1.4852976
30. Mangababu, A.; Sianglam, C.; Chandu, B.; Avasthi, D. K.; Rao, S. V.; Motapothula, M.; Rao, S. V. S. N. *J. Electron. Mater.* **2021,** *50,* 1742–1751. doi:10.1007/s11664-020-08610-z
31. Semaltianos, N. G.; Friedt, J.-M.; Chassagnon, R.; Moutarlier, V.; Blondeau-Patissier, V.; Combe, G.; Assoul, M.; Monteil, G. *J. Appl. Phys.* **2016,** *119*. doi:10.1063/1.4951740
32. Vutova, K.; Vassileva, V.; Ratheesh, R.; Reddy, R. C.; Kumar, A. *J. Phys.: Conf. Ser.* **2023,** *2443,* 012013. doi:10.1088/1742-6596/2443/1/012013
33. Mangababu, A.; Sai Prasad Goud, R.; Byram, C.; Rathod, J.; Banerjee, D.; Rao Soma, V.; Nageswara Rao, S. V. S. *Appl. Surf. Sci.* **2022,** *589,* 152802. doi:10.1016/j.apsusc.2022.152802
34. Zhang, D.; Zhang, C.; Liu, J.; Chen, Q.; Zhu, X.; Liang, C. *ACS Appl. Nano Mater.* **2019,** *2,* 28–39. doi:10.1021/acsanm.8b01541
35. De Bonis, A.; Curcio, M.; Santagata, A.; Galasso, A.; Teghil, R. *Nanomaterials* **2020,** *10,* 145. doi:10.3390/nano10010145
36. De Bonis, A.; Santagata, A.; Galasso, A.; Laurita, A.; Teghil, R. *J. Colloid Interface Sci.* **2017,** *489,* 76–84. doi:10.1016/j.jcis.2016.08.078
37. Lavakusa, B.; Mohan, B. S.; Prasad, P. D.; Belachew, N.; Basavaiah, K. *Int. J. Adv. Res.* **2017,** *5,* 405–412. doi:10.21474/ijar01/3526
38. Moosa, A. A.; Abed, M. S. *Turk. J. Chem.* **2021,** *45,* 493–519. doi:10.3906/kim-2101-19
39. Davari, S. A.; Gottfried, J. L.; Liu, C.; Ribeiro, E. L.; Duscher, G.; Mukherjee, D. *Appl. Surf. Sci.* **2019,** *473,* 156–163. doi:10.1016/j.apsusc.2018.11.238
40. Baimler, I. V.; Lisitsyn, A. B.; Gudkov, S. V. *Front. Phys.* **2020,** *8,* 1–6. doi:10.3389/fphy.2020.620938
41. Venkatakrishnan, K.; Vipparty, D.; Tan, B. *Opt. Express* **2011,** *19,* 15770. doi:10.1364/oe.19.015770
42. Wang, C. X.; Liu, P.; Cui, H.; Yang, G. W. *Appl. Phys. Lett.* **2005,** *87,* 201913. doi:10.1063/1.2132069
43. Karatutlu, A.; Barhoum, A.; Sapelkin, A. Theories of Nanoparticle and Nanostructure Formation in Liquid Phase. In *Emerging Applications of Nanoparticles and Architecture Nanostructures;* Barhoum, A.; Makhlouf, A. S. H., Eds.; Elsevier, 2018; pp 597–619. doi:10.1016/b978-0-323-51254-1.00020-8
44. Thanh, N. T. K.; Maclean, N.; Mahiddine, S. *Chem. Rev.* **2014,** *114,* 7610–7630. doi:10.1021/cr400544s
45. Singh, M. R.; Ramkrishna, D. *Chem. Eng. Sci.* **2014,** *107,* 102–113. doi:10.1016/j.ces.2013.11.047
46. Gránásy, L.; Pusztai, T.; Börzsönyi, T.; Warren, J. A.; Douglas, J. F. *Nat. Mater.* **2004,** *3,* 645–650. doi:10.1038/nmat1190
47. Vollath, D. *Beilstein J. Nanotechnol.* **2020,** *11,* 854–857. doi:10.3762/bjnano.11.70
48. Durán-Olivencia, M. A.; Otálora, F. *J. Cryst. Growth* **2013,** *380,* 247–255. doi:10.1016/j.jcrysgro.2013.06.035
49. Liang, S.-X.; Zhang, L.-C.; Reichenberger, S.; Barcikowski, S. *Phys. Chem. Chem. Phys.* **2021,** *23,* 11121–11154. doi:10.1039/d1cp00701g
50. Pola, J.; Urbanová, M.; Bastl, Z.; Plzák, Z.; Šubrt, J.; Vorlíček, V.; Gregora, I.; Crowley, C.; Taylor, R. *Carbon* **1997,** *35,* 605–611. doi:10.1016/s0008-6223(97)00007-9
51. Glynn, P. D.; Reardon, E. J.; Plummer, L. N.; Busenberg, E. *Geochim. Cosmochim. Acta* **1990,** *54,* 267–282. doi:10.1016/0016-7037(90)90317-e
52. Shaymardanov, Z.; Shaymardanova, B.; Kulenova, N. A.; Sadenova, M. A.; Shushkevich, L. V.; Charykov, N. A.; Semenov, K. N.; Keskinov, V. A.; Blokhin, A. A.; Letenko, D. G.; Kuznetsov, V. V.; Sadowski, V. *Processes* **2022,** *10,* 2493. doi:10.3390/pr10122493
53. Feizi Mohazzab, B.; Jaleh, B.; Kakuee, O.; Fattah-alhosseini, A. *Appl. Surf. Sci.* **2019,** *478,* 623–635. doi:10.1016/j.apsusc.2019.01.259
54. Kwong, H. Y.; Wong, M. H.; Leung, C. W.; Wong, Y. W.; Wong, K. H. *J. Appl. Phys.* **2010,** *108,* 034304. doi:10.1063/1.3457216
55. Kanitz, A.; Hoppius, J. S.; del Mar Sanz, M.; Maicas, M.; Ostendorf, A.; Gurevich, E. L. *ChemPhysChem* **2017,** *18,* 1155–1164. doi:10.1002/cphc.201601252
56. Amendola, V.; Riello, P.; Meneghetti, M. *J. Phys. Chem. C* **2011,** *115,* 5140–5146. doi:10.1021/jp109371m
57. Gilliland, G. D. *Mater. Sci. Eng., R* **1997,** *18,* 99–399. doi:10.1016/s0927-796x(97)80003-4
58. Kirichenko, N. A.; Barmina, E. V.; Shafeev, G. A. *Phys. Wave Phenom.* **2018,** *26,* 264–273. doi:10.3103/s1541308x18040027
59. Mitra, S. K.; Dass, N.; Varshneya, N. C. *J. Chem. Phys.* **1972,** *57,* 1798–1799. doi:10.1063/1.1678479
60. Debenham, M.; Dew, G. D. *J. Phys. E* **1981,** *14,* 544–545. doi:10.1088/0022-3735/14/5/004
61. Al-Jimaz, A. S.; Al-Kandary, J. A.; Abdul-latif, A.-H. M.; Al-Zanki, A. M. *J. Chem. Thermodyn.* **2005,** *37,* 631–642. doi:10.1016/j.jct.2004.09.021
62. Al-Kandary, J. A.; Al-Jimaz, A. S.; Abdul-Latif, A.-H. M. *J. Chem. Eng. Data* **2006,** *51,* 99–103. doi:10.1021/je0502546
63. Vlahou, M.; Fraggelakis, F.; Manganas, P.; Tsibidis, G. D.; Ranella, A.; Stratakis, E. *Nanomaterials* **2022,** *12,* 623. doi:10.3390/nano12040623
64. Nathala, C. S. R.; Ajami, A.; Ionin, A. A.; Kudryashov, S. I.; Makarov, S. V.; Ganz, T.; Assion, A.; Husinsky, W. *Opt. Express* **2015,** *23,* 5915. doi:10.1364/oe.23.005915
65. Dar, M. H.; Kuladeep, R.; Saikiran, V.; Desai, N. R. *Appl. Surf. Sci.* **2016,** *371,* 479–487. doi:10.1016/j.apsusc.2016.03.008
66. Rivera, L. P.; Munoz-Martin, D.; Chávez-Chávez, A.; Morales, M.; Gómez-Rosas, G.; Molpeceres, C. *Mater. Sci. Eng., B* **2021,** *273,* 115393. doi:10.1016/j.mseb.2021.115393

BEILSTEIN JOURNAL OF NANOTECHNOLOGY

Performance optimization of a microwave-coupled plasma-based ultralow-energy ECR ion source for silicon nanostructuring

Joy Mukherjee[1], Safiul Alam Mollick[2], Tanmoy Basu[3] and Tapobrata Som[*1,4]

Full Research Paper

Open Access

Address:
[1]SUNAG Laboratory, Institute of Physics, HBNI, Sachivalaya Marg, Bhubaneswar - 751 005, India, [2]Rabindra Mahavidyalaya, University of Burdwan, Hooghly, West Bengal, 712 401, India, [3]Centre for Quantum Engineering, Research and Education, TCG Centers for Research and Education in Science and Technology, Kolkata, West Bengal, 700 091, India and [4]Homi Bhabha National Institute, Training School Complex, Anushaktinagar, Mumbai - 400 085, India

Email:
Tapobrata Som[*] - tsomiop@gmail.com

* Corresponding author

Keywords:
optimization of ion current; surface topography; TEM; ultralow-energy ECR-based ion source; UV–vis spectroscopy

Beilstein J. Nanotechnol. **2025,** *16,* 484–494.
https://doi.org/10.3762/bjnano.16.37

Received: 22 November 2024
Accepted: 06 March 2025
Published: 31 March 2025

This article is part of the thematic issue "Energetic ions and photons for engineering nanomaterials".

Guest Editor: D. K. Avasthi

Abstract

This paper presents a comprehensive optimization of key parameters for generating ion beams in a microwave-coupled plasma-based ultralow-energy electron cyclotron resonance ion source, generally used for nanostructuring solid surfaces. The investigation focuses on developing, accelerating, and extracting Ar ions from a magnetron-coupled plasma cup utilizing a three-grid ion extraction composed of molybdenum. The study systematically examines the dependence of ion beam current on critical parameters, such as gas pressure, magnetron power, extraction voltage, and ion energies. The Gaussian nature of the beam profile is scrutinized and elucidated within the context of grid extraction-based ion sources. Plasma physics principles are employed to interpret the observed variations in the beam current with various parameters. The optimized beam current is used to investigate the inert ion-induced nanopatterning of silicon surfaces, at various ion fluences and incidence angles. The pre- and post-bombardment changes in optical properties, resulting from nanopatterned surfaces, are investigated using UV–vis reflectivity measurements and correlated with the dimensions of the nanopatterns. This manuscript highlights the potential applications arising from these findings, emphasizing the transformative impact of nanopatterning through low-energy inert ions.

Introduction

Ion sources serve as fundamental components in numerous scientific and industrial applications and play a crucial role in generating charged particles. Various systems harness energetic ions for diverse purposes, spanning material science, high-energy physics, medical applications, and agricultural science [1-5]. Presently, energetic ions find application in various sur-

face treatments such as nanopatterning, sputter etching, and controlled defect formation [6,7]. Particularly, ultralow-energy ion beams are exceptionally valuable for the precise modification of 2D layers [8] and ion-induced nanopatterning of semiconductor surfaces [9]. Over the past few decades, ion-induced nanopatterning and nanoscale functionalization have garnered significant interest, owing to their broad applications in DNA origami [10], tuning of wettability [11] and electrical and magnetic anisotropy [12,13], isolated dot formation [1], nanoscale plasmonic arrays [14], and field emission [15]. Thus, ion sources generate enormous possibilities for material modifications both physically and chemically. Further, there are diverse ion production mechanisms. The fundamental process of producing ions is the collision of atoms with ions or electrons, which may be either elastic or inelastic. In elastic collisions, the internal energy of the colliding particles does not change. Ionization, stripping, electron capture, and excitation of atoms due to collisions are examples of inelastic collisions. Free electrons colliding with atoms also produce ions. Electrons in the gas are heated by the inductively coupled method and then acquire enough energy to generate a plasma. Because of several drawbacks, such as Townsend discharge [16], these sources are not used nowadays. Compact broad-beam ion sources are widely used in scientific laboratories to generate ions. Depending upon the mechanism of production of various ions using gaseous plasma, the ion sources can be classified in direct current (DC)-operated ion sources, radio frequency discharge ion sources, and microwave-based electron cyclotron resonance (ECR) ion sources, as well as electron bombardment, charge exchange, and laser-driven ion sources [17,18]. In the past few decades, DC ion sources were commonly used [19-21]. These DC ion sources consist of a hot cathode or filament, which is not appropriate in cases of reactive gas discharge; hence, their lifetime is limited [22,23]. Moreover, the beam current produced by those ion sources is not suitable for modern-day applications. In material science as well as surface science applications, the ion source should be mobile and adaptable to the vacuum system, having a longer lifetime. Further, the ion source should produce a relatively high beam current (i.e., capable of forming a high density of plasma) with lower maintenance. To address this challenge, ECR-based ion sources were developed [24,25]. ECR ion sources are one of the most preferred ion sources for the easy production of ions with different energies and charge states. Since the discharge is maintained in the quartz cup via a strong electric field generated in the cavity, the ECR-based ion sources equipped with microwave cavities neither contain any filament nor any type of electrode [26]. The high plasma density within a quartz cup is confined by solenoid magnets surrounding it, creating a multicusp magnetic field. However, careful attention is required for the microwave coupling to the plasma cup to minimize the reflections of microwave power. Mechanical adjustments to the resonator length and waveguide are made to ensure minimal reflection. Additionally, maintaining the necessary magnetic field strength is crucial for sustaining the plasma. The ion source's compact design is user-friendly and capable of producing a high beam current density using single- or multigrid extraction systems [27,28]. The extracted beam current is influenced by magnetron power, gas pressure, and extraction voltage. Furthermore, the beam current varies with different ion energies [29,30].

This article focuses on optimizing the beam current generated by a cost-effective microwave-based ECR ion source and the subsequent development of nanoscale patterns on the surface of silicon. The relationship between the beam current and various parameters is extensively examined and elucidated. Experimental parameters, spanning from plasma generation to ion beam extraction, are systematically optimized for the study of low-energy Ar-ion-induced nanostructures on silicon. The dependence of the extracted ion beam on gas pressure, magnetron power, and extraction grid voltage is documented for different ion energies. Additionally, the manuscript establishes the relationship between ion beam current and ion energy. Irradiation of p-type single crystal Si(100) surfaces at off-normal angles (60° and 72.5°) with 450 eV Ar ions results in the formation of well-defined nanoscale ripple patterns. The prominence of ripple structures increases with prolonged irradiation time, while bombardment at 72.5° with the same ion beam parameters leads to the coarsening of nanostructures. Cross-sectional transmission electron microscopy (TEM) measurements confirm the formation of nanostructures as observed from atomic force microscopy (AFM) images. The thickness of the amorphous thin layer is in good agreement with Monte Carlo simulations (SRIM) [31]. The article further investigates and explains the optical response (by UV–vis spectrometry) of the nanopatterned surfaces depending on the dimensions of the nanopatterns (i.e., wavelength and rms roughness). The potential applications of such nanopatterned silicon surfaces are highlighted. This article underscores the versatility of an optimized broad-beam ultralow-energy ion source, specifically in the context of optimization of inert Ar-ion beam and subsequent ion-induced silicon nanopatterning.

The TEM used for this work is a FEI Tecnai G2 12 Twin model, which operates at a voltage range of 20–120 kV. It employs a LaB_6 emitter as the electron source and offers a line resolution of 0.2 nm with a maximum eccentric tilt angle of ±70°. Sample preparation for cross sectional TEM measurement involved mechanically grinding the substrate into a circular disk with a diameter of 3 mm and a thickness of approximately 100 μm. The disk was then subjected to dimpling to

achieve uniform thinning. To further reduce the thickness to less than 40 μm at the center, ion milling was performed. This ultrathin central region was used for detailed TEM analysis.

Description of the Ion Source

Figure 1 illustrates the block diagram of the magnetron-coupled ultralow-energy ECR ion source (Plasma Gen-II, Tectra GmbH, Germany). The schematic representation in Figure 1 elucidates the process of extracting an ultralow-energy ion beam. A magnetron is connected to the ceramic Al_2O_3 plasma cup via a waveguide. The gas inlet system facilitates the filling of the plasma cup with gas through a capillary tube. The intense electric field generated by the magnetron induces gas breakdown (discharge), leading to the formation of a highly intense plasma. The produced plasma is confined and sustained by a permanent magnet positioned near the plasma cup. For the extraction and focusing of the beam, a gridded electrostatic einzel lens is employed. The shape and size of the beam are contingent on the extraction voltage applied at the grid and the corresponding ion energy. The directed beam impacts the silicon target kept in ultrahigh vacuum (UHV) within the target chamber. A Faraday cup, connected to a multimeter, measures the beam current, and the corresponding ion fluence is expressed in terms of irradiation time. The sample holder located in a UHV chamber is connected to a five-axes (x, y, z, θ, φ) manipulator (PREVAC Technologies) system, offering movement and rotation in all possible directions. The sample is transferred to the ion source using a load-lock system.

The cross-sectional view of the setup is shown in Figure 2. The type of magnetron-coupled ion source used here was first developed by Anton and coworkers [25]. The ion source is fitted in the cylindrical cavity of the UHV target chamber. The inner diameter of the plasma cup is around 52 mm. The cup is surrounded by water-cooled NdFeB magnets, which produce a multi-cusp field to confine the plasma. The 2.45 GHz magnetron microwave source is attached to the back side of the ion source, as shown in Figure 2. The dimension of the cylindrical resonator (waveguide) is chosen in such a way that it can produce maximum beam current. To generate plasma in the plasma cup, a gas is inserted into it through a capillary tube attached to the gas cylinder (reservoir). A pressure of 10^{-4} mbar is maintained for sustaining plasma by adjusting a needle valve attached to the gas reservoir. The entire length of the ion source is around 130 cm. The extraction of ion beams is accomplished by a three-grid ion optics system, as seen in Figure 2. The extraction voltage is applied to the grid to enable the extraction of an intense beam with different diameters. The circular perfection of the beam shape is evident from observations on the front plate attached to the UHV chamber. In this configuration, the beam current, specific to a given ion energy, can be finely adjusted based on magnetron power, working pressure, and extraction voltage. Additionally, the beam current is influenced by the extracted ion energy and the position of the target. Hence, a comprehensive investigation into the intricate relationship between ion current and the mentioned parameters emerges as a compelling topic in the current scientific context.

Beam Extraction Grid

Grid 1 (anode)

The anode, in contact with the plasma within the isolated plasma cup, serves to shift the plasma potential. By applying a voltage (e.g., +500 V) to the anode, the plasma potential is elevated to +500 V (plus the intrinsic plasma potential). When the sample is maintained at ground potential, the positive ions within the plasma are accelerated towards the sample with an energy approximately equal to the applied voltage.

Grid 2 (extractor)

This grid is employed to control the divergence of the ion beam. A negative voltage is applied to the extractor grid, creating an electric field that influences ion trajectories. Additionally, a small negative field can extend from the extractor grid into the positively charged plasma region. This increases the ion extrac-

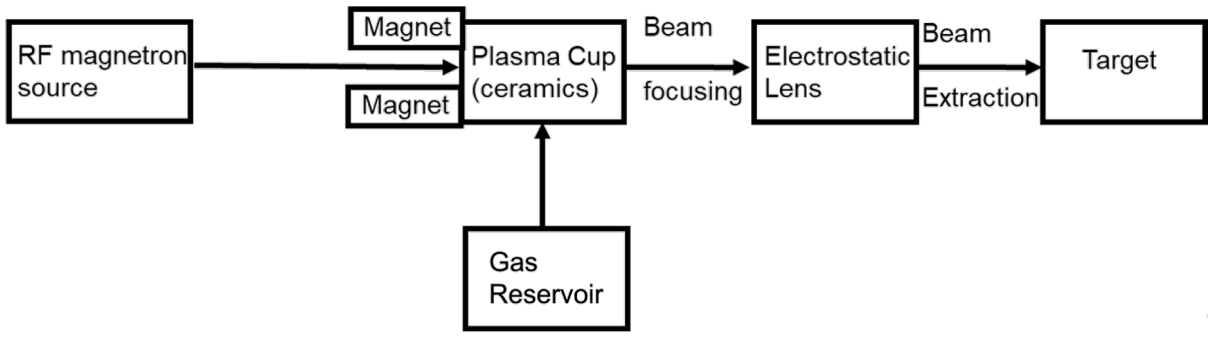

Figure 1: Block diagram of the components of the high-vacuum plasma ion source.

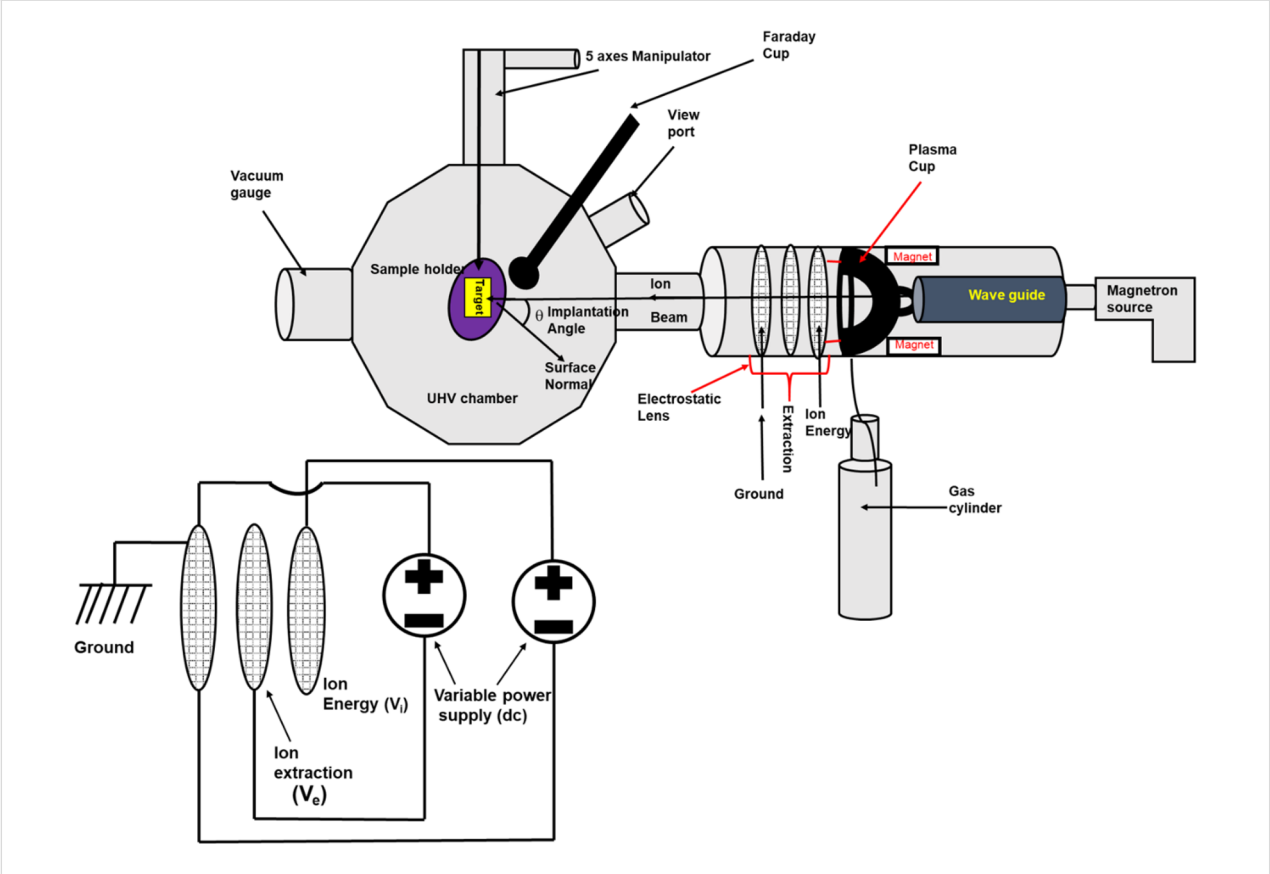

Figure 2: Cross-sectional schematic view of the microwave-coupled ultralow-energy ion beam system.

tion efficiency by enhancing the electric field gradient and enlarging the effective extraction volume.

Grid 3 (grounded grid)

The third grid is maintained at ground potential and is particularly effective for operations involving very-low-energy ions. This grid enables ions to decelerate and traverse a field-free region near the source, ensuring minimal perturbations to the ion beam and facilitating precise ion transport.

Results and Discussion

Optimization of ion current through various plasma parameters

The variation of beam current with gas pressure and magnetron power for different ion energies are investigated and presented in Figure 3. Figure 3a–c demonstrates that the beam current decays almost exponentially with the increase in gas pressure. The ion current is maximum at a gas pressure of 1.5×10^{-4} mbar, regardless of the ion energy. It is also evident that for the same gas pressure, the beam current is maximum for the highest ion energy. At low gas pressure, the mean free path of gas molecules is larger because of the lower density of gas molecules, which allows the produced ions to traverse a longer distance without collision. This increases the ionization efficiency, and hence, with fewer collisions, the probability for recombination of the ions is very low. Consequently, a large number of ions are extracted, intensifying the beam current. The entire phenomenon can be summarized through the equation $\lambda = (\sigma \cdot n)^{-1}$, where λ is the mean free path of the ions, σ is the recombination cross section, and n is the density of the ions inside the plasma [32-34]. The mean free path of the ions, determined by the recombination cross section and density of plasma, plays a key role in quantifying the ion current.

Further, the conversion of the gas to plasma is governed by a magnetron source; therefore, the ion current or plasma density depends on magnetron power. To understand that, the variation of ion current with microwave power is recorded at different gas pressure and ion energies, as presented in Figure 3d–f. In general, the plasma density (n) depends on the microwave frequency (ω) as $n = E_{RF}\omega^2/\varepsilon$, where E_{RF} is the microwave power and ε is the minimum energy required for ion–electron pair generation [32]. The magnitude of ε is different for different gases. It is evident from Figure 3d,e that up to a critical microwave power, no plasma is formed, resulting in a zero beam current.

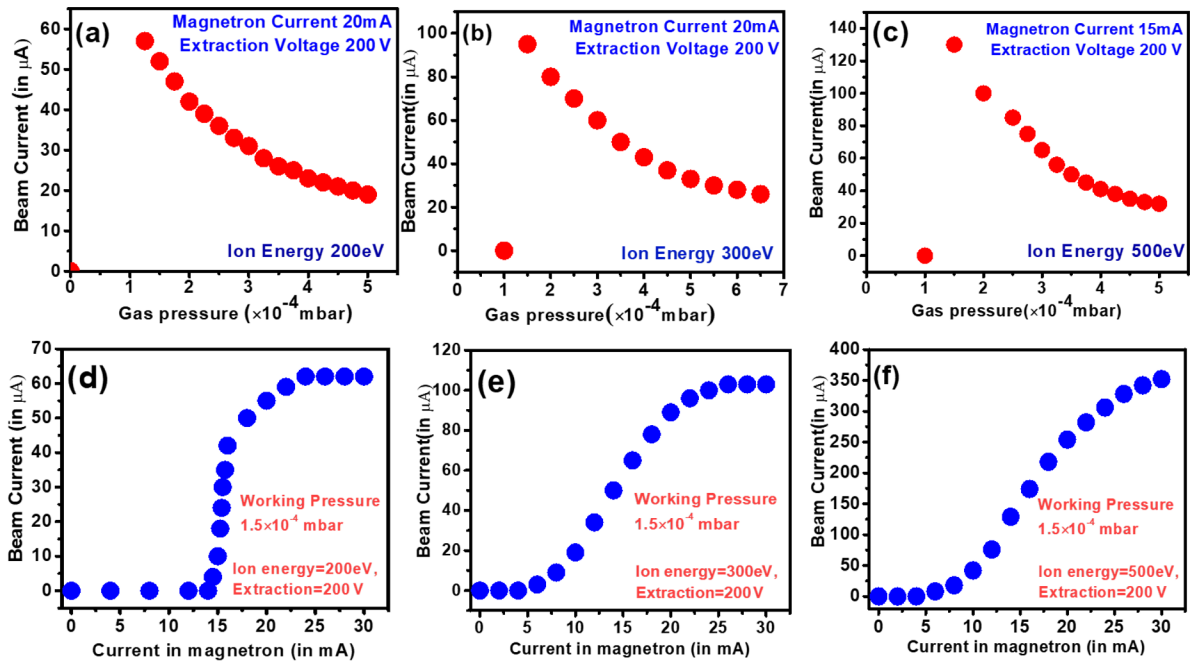

Figure 3: Variation of beam current with (a–c) gas pressure and (d–f) magnetron power for different ion energies.

With the increase of magnetron power beyond ε, the beam current increases almost linearly with the input magnetron power since n is directly proportional to E_{RF}. The beam current reaches saturation at a specific microwave power level, which varies based on the ion energy. (Figure 3d–f). Further, the cutoff power also depends on the ion energy. At low ion energies, the microwave power required for generating a plasma is high. With higher ion energies, the microwave power required for ion–electron pair generation decreases.

The Ar-ion beam is extracted via a three-grid ion optics system [35-37]. The beam current and the beam profile depend on the potential applied at the grid and the target. The change in beam current with the ion extraction voltage recorded for different ion energies is presented in Figure 4a–c. Initially, the beam current increases linearly with the applied extraction voltage since more ions are extracted at higher extraction voltages. Regardless of the ion energy, the beam current is maximum at an extraction voltage of 400 V. With further increases in extraction voltage, the beam current decreases rapidly. Beyond this threshold of 400 V, the increased extraction voltage induces significant defocusing of the ion beam. This highlights the critical role of the extraction voltage in maintaining beam coherence. Generally, the extraction voltage is kept fixed to maintain the shape of the beam, essential for uniform irradiation of samples.

The dependence of beam current on the ion energy is given in Figure 4d. The beam current increases almost linearly with increasing ion energy at a fixed extraction voltage and microwave power. For a particular ion energy, lowering the extraction voltage also results in a lowering of beam current as observed from the above Figure 4a–c. Therefore, to maintain a proper beam shape and adequate beam current, the extraction voltage and ion energy are to be precisely optimized. Further, the variation of beam current with the target position, known as the beam profile, is also presented in Figure 4e. The beam profile is Gaussian for concave grid beam extraction optics.

Nanostructuring on Si surface by 450 eV Ar-ion bombardment

The morphological evolution of Si after the off-normal bombardment with 450 eV Ar ions at different incidence angles and for various irradiation times is investigated using AFM in tapping mode. Si cantilevers with tip radii of 10 nm were employed, with scan rate of 1 μm/s and a fixed scan size of 5 μm × 5 μm. Quantitative analysis of the surface topography was conducted using WSxM software. Figure 5 presents the surface morphology of the Si surface after Ar-ion bombardment at different incidence angles. The arrow on the right-hand side indicates the direction of the ion beam concerning the surface normal. The irradiation of the silicon surface at an angle of 55° leads to no changes in surface morphology (Figure 5a). However, at an ion incidence angle of 58°, changes in surface morphology begin to appear, although no prominent ripple structure is observed (Figure 5b). In contrast, the bombardment of the Si surface for 1 h at an angle of 60° leads to the formation of

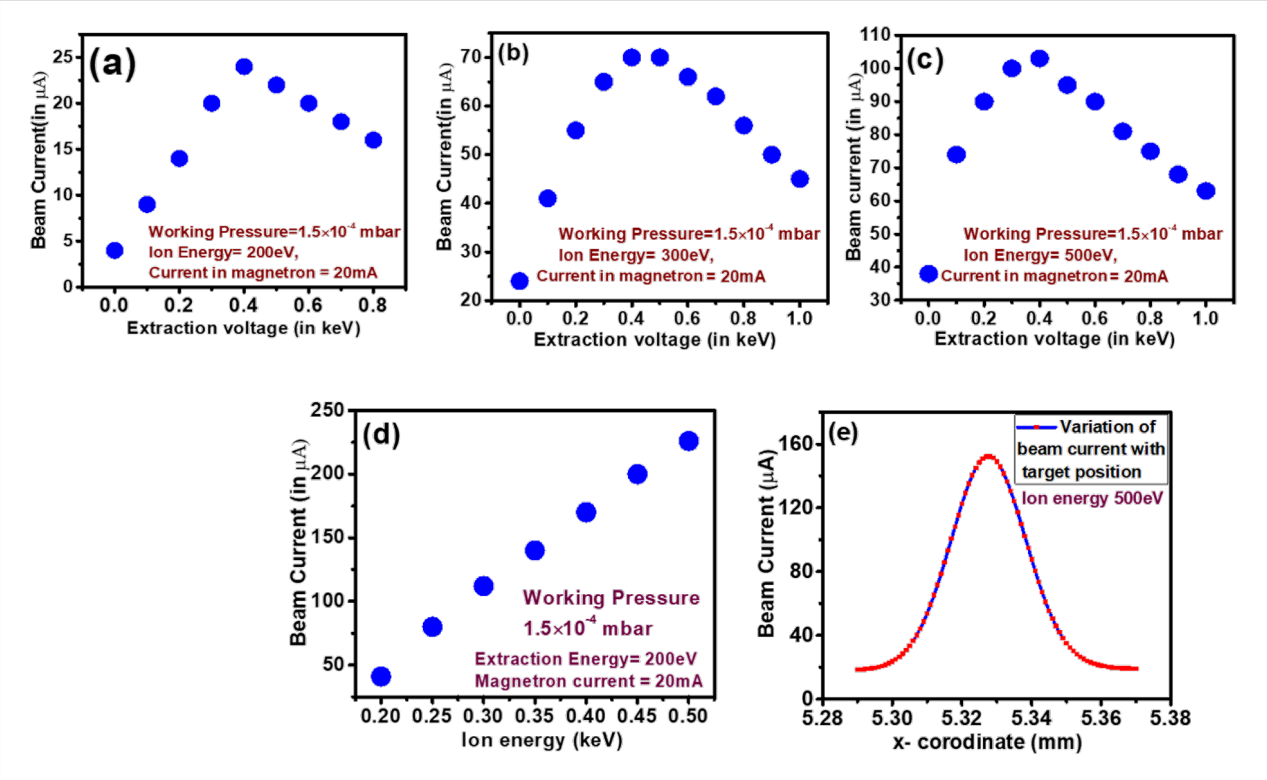

Figure 4: Variation of (a–c) beam current with ion extraction voltage at different ion energy; (d) beam current as function of the ion energy; (e) beam current as function of the target position.

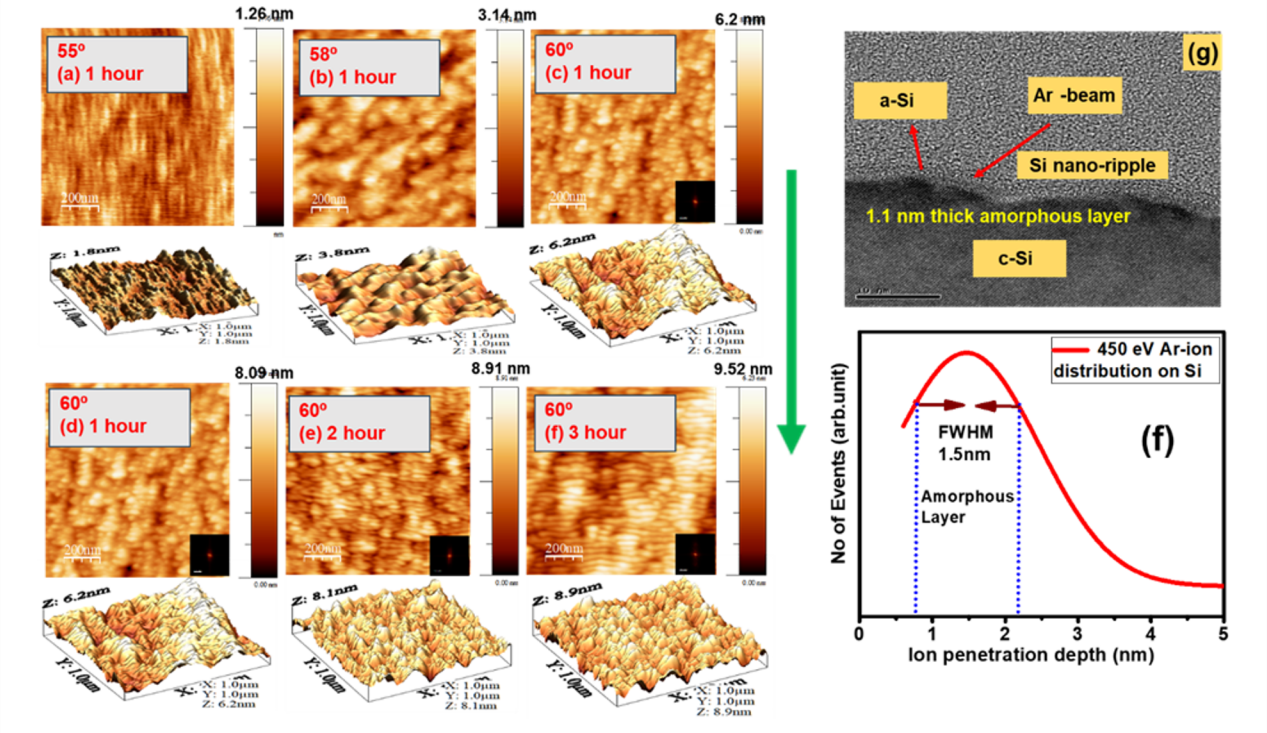

Figure 5: AFM image (2D and 3D) of the evolution of surface morphology after 450 eV Ar-ion bombardment at different incidence angles and irradiation times. The arrow indicates the ion beam direction.

a well-defined nanoscale ripple pattern as observed in Figure 5c. The growth of the ripple becomes more prominent with the increase in bombardment time, that is, the amplitude of the ripples grows.

To visualize the growth of the ripples, 3D AFM images are presented along with 2D images. The ripple height increases with bombardment time. Fast Fourier transform (FFT) images of the nanopatterned surface are inset in the lower right corner of each image. In the present case, the fluence is represented by irradiation time. The quality and the growth of the nanostructures are quantitatively discussed in Figure 6, where variations of ripple wavelength, rms roughness, and power spectral density are discussed.

Figure 5g shows the cross-sectional TEM image after 450 eV Ar-ion bombardment of the Si surface at an angle of 60° for a time of 3 h. The presence of Ar-ion-induced surface corrugation in terms of ripple-like nanostructures is evidenced in Figure 5g. Although the amplitude of the ripples is not large, the observed ripple wavelength of around 31 nm from the TEM image is consistent with that of AFM data (Figure 6e). However, in addition to the ripple-like nanostructures, an ultrathin amorphous layer is formed because of the Ar-ion bombardment. The thickness of the amorphous layer is around 1.5 nm, which is consistent with the penetration depth of the Ar ions (1.2 nm) estimated by Monte Carlo simulations (Figure 5f) [31]. Therefore, the topographical image is consistent with the cross-sectional image, indicating a clear signature of ripple-like nanostructure formation.

Figure 6a–c shows the variation of the surface profile of the AFM images shown in Figure 5. The height profile is direct evidence of the variation of ripple amplitude with irradiation time. The increase in ripple height with irradiation time is shown in Figure 6a–c. Further, the fluctuation in ripple height or ampli-

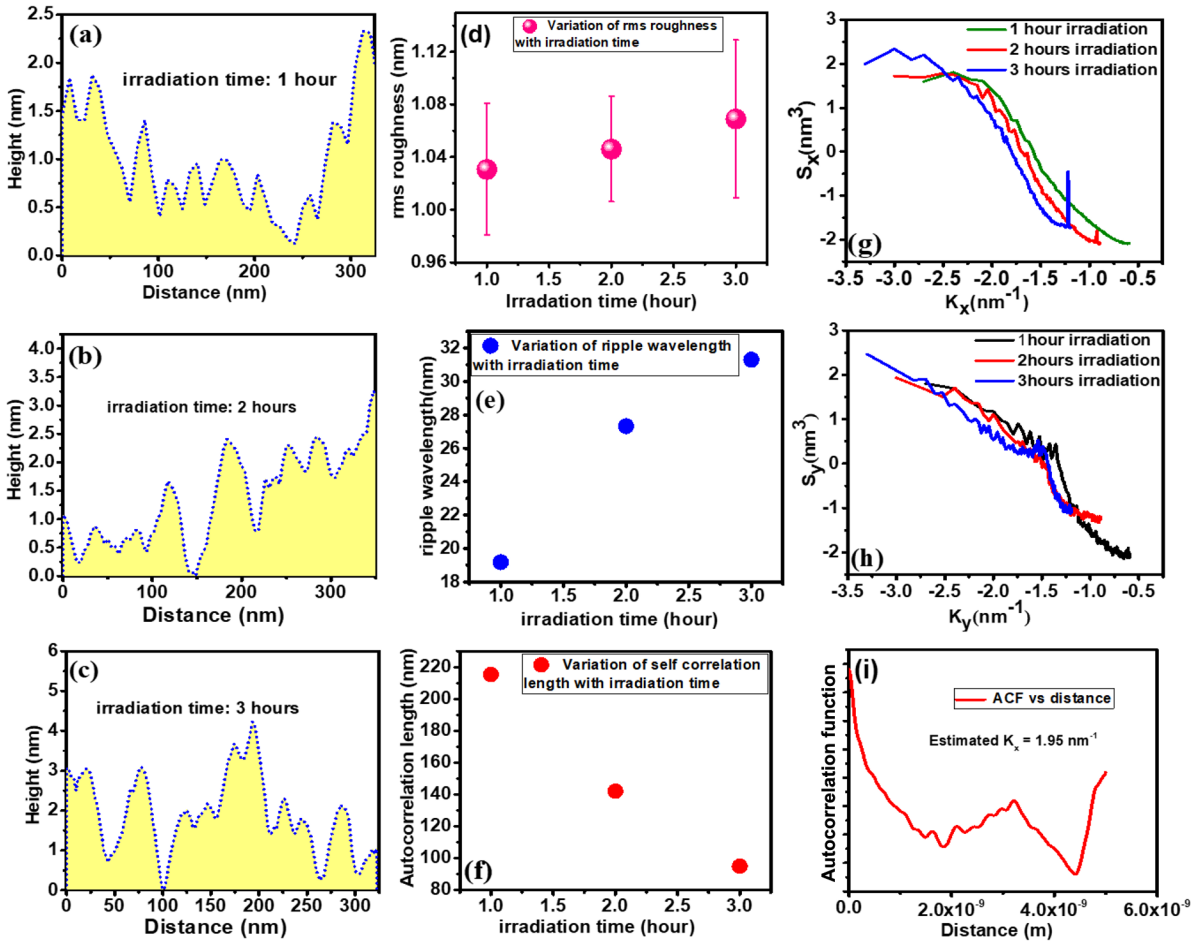

Figure 6: Variation of (a–c) surface height modulation of the nanopatterned silicon surface; (d) ripple wavelength and (e) rms roughness as function of the irradiation time. Variation of power spectral density of the nanopatterned silicon surface in (g) parallel and (h) perpendicular direction. (f) Variation of autocorrelation length with irradiation time. (i) Variation of the autocorrelation function with distance.

tude, generally termed as rms roughness, is also investigated in Figure 6d. The rms roughness increases linearly with the irradiation time (i.e., fluence). Further, the ordering of the nanostructure with bombardment time, examined in terms of ripple wavelength, is presented in Figure 6e. The ripple wavelength increases as the bombardment time increases from 1 to 2 h. With a further increment in irradiation time, the change of ripple wavelength is negligible, that is, a saturation of ripple wavelength is observed. The degree of similarity between two spatial morphologies is generally quantified by the autocorrelation length, as presented in Figure 6f. The autocorrelation length decreases with bombardment time. This indicates that less ordered ripple structures develop with higher irradiation times. To understand the growth of the ripple structure, the power spectral density factor along the parallel and perpendicular direction of the developed ripples is presented in Figure 6g,h. The prominent peak present in Figure 6g indicates the development of the ripple structure along the x direction (parallel) with a particular wavevector (k_x). The absence of a ripple wavevector in the perpendicular direction is evidenced in Figure 6h. The estimated k_x from the autocorrelation function (Figure 6i) is almost consistent with the one obtained from the power spectral density (Figure 6g). Thus, 450 eV Ar-ion bombardment on Si leads to the formation of well-defined parallel ripples at off-normal incidence.

Figure 7 illustrates the surface topography after 450 eV Ar-ion bombardment of the silicon surface at an angle of 72.5° as function of the bombardment time. 3D AFM images are presented along with 2D surface topography images. Generally, the transformation of well-defined nanoripples into nanofacets is expected at such near-grazing-incidence irradiation [38]. In the present case, although no prominent nanofacet formation is observed, a clear signature of the transformation of ripple structures into nanofacets is seen. After a sufficiently large bombardment time (10 h), nanofacet-like structures with larger dimensions develop, although the facets are not well organized. It is also evident that the rms roughness increases with bombardment time.

Surface nanostructuring by energetic ion bombardment is a consequence of ion-beam-induced off-normal (60° and 72.5°) sputtering of surface atoms and their consecutive redistribution [9,39,40]. During ion bombardment, the unequal radius of curvature of the surface leads to unequal deposition of energy at different points on the surface, which results in unequal sputtering at those points. This generates surface instabilities, and consequently, the surface atoms are redistributed to stabilize the surface. These two effects jointly trigger nanopattern formation on the surface. A first theoretical model was proposed by Bradley and Harper [41], based on curvature-dependent sputtering of surface and near-surface atoms. Later, Carter and Vishnyakov introduced the concept of redistribution of surface atoms [42]. Several experiments have been carried out to understand other factors that contribute to nanopattern formation, such as preferential and differential sputtering [6,43], the role of

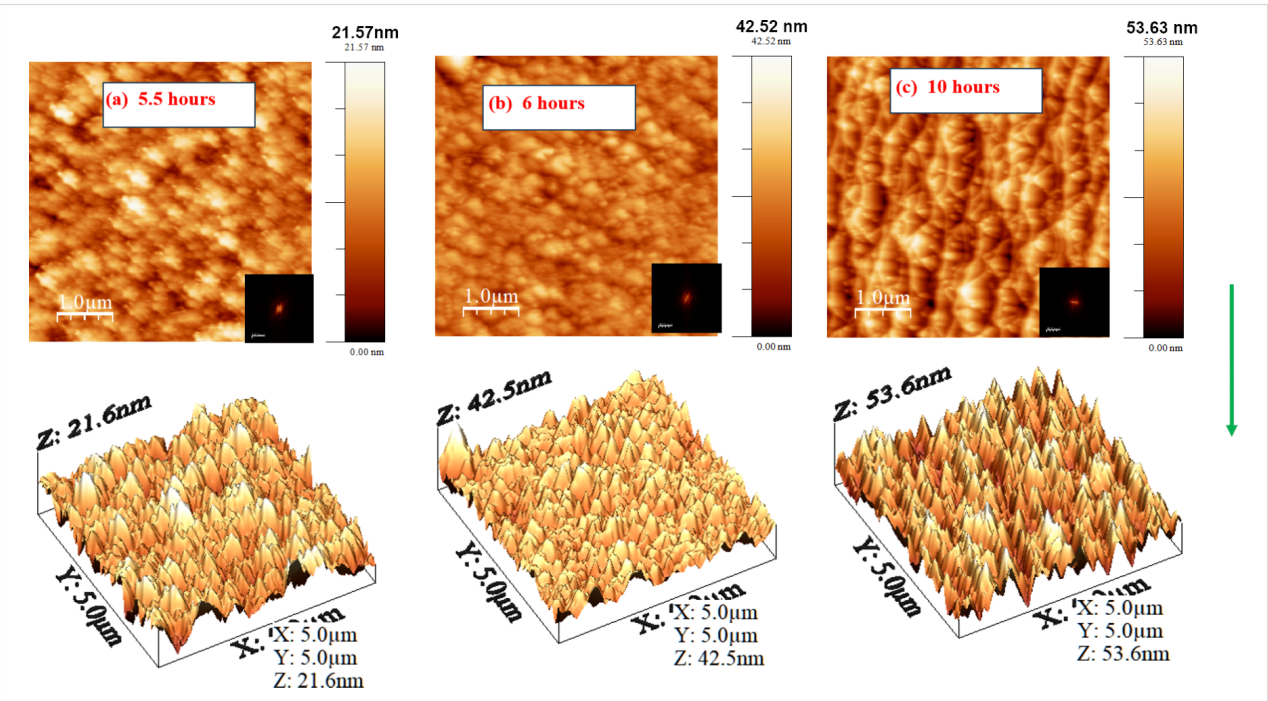

Figure 7: AFM images (2D and 3D) of the evolution of nanostructures on the Si surface with irradiation time at an angle of 72.5°.

surface and beam impurities, and the effect of chemical compound formation and compound ion irradiation [44,45]. In cases of ultralow-energy ion bombardment, the rate of sputtering is lower compared to medium-energy ion bombardment; therefore, in this case, mass redistribution of the surface atoms plays a key role. There is no reaction between the inert Ar ions and the Si atoms, ensuring the absence of a chemical aspect of pattern formation. However, the native silicon oxide layer is partially sputtered. This is also a key factor in generating surface instabilities. The surface morphology largely varies due to different extents of near-surface mass transport by the surface-confined ion-enhanced viscous flow [46]. Here, up to an ion incidence angle of 58°, the surface becomes unstable under 450 eV Ar-ion bombardment. Due to sputtering, a well-defined ripple formation is found after 1 h of 450 eV Ar-ion bombardment. With the increase in bombardment time, more silicon and oxygen atoms are sputtered. Due to the presence of the ripples, the surface becomes anisotropic. The consequence of such an anisotropic nature of the surface is investigated and discussed in the upcoming section.

Application of nanopatterned Si surface

The optical response of pristine and Ar-ion-induced nanopatterned silicon surfaces are investigated through UV–vis reflectivity measurements and presented in Figure 8. Figure 8a depicts the change in reflectivity of the silicon surface due to the presence of nanopatterns. With the increase of bombardment time, reflectivity decreases drastically. The change in reflectivity with respect to rms roughness and ripple wavelength is shown in Figure 8b. It is clear from Figure 8b, that the reflectivity decreases with the increase in ripple wavelength. In general, the presence of nanopatterns on the surface reduces the reflection of UV–visible light because of light trapping by multiple reflections [47-49]. Ar-ion bombardment for 3 h leads to the development of a well-defined nanopattern on the silicon surface; hence, the reflectivity becomes minimal compared to the other two surfaces that were irradiated for shorter periods of time. The change in reflectivity depends on the change in the electronic structure as well as surface topography of the material. A change in electronic structure can be related to changes in chemical nature, impurity incorporation on the surface, and amorphization of the surface. Inert Ar causes no chemical modifications of the silicon surface. Also there are no implanted Ar ions on the silicon surface (Figure 5g), particularly in this lower-energy regime. Therefore, in the present case, the amorphization due to ion beam sputtering and the nanostructure formation change the electronic density of the material, causing a lowering in reflectivity. The tailoring of the reflectivity by developing nanostructures is widely applicable for anti-reflective coatings and photovoltaic device applications [50,51].

The formation of nanostructures on the silicon surface by inert-ion bombardment is a consequence of ion-induced instabilities on the surface by the interplay between sputtering and mass redistribution of surface atoms [52,53]. During ion bombardment, the sputtering of the native silicon oxide layer along with that of bulk silicon takes place. The rate of sputtering of silicon oxide and the elemental silicon is different, which leads to instabilities during bombardment and the development of nanopatterns on the surface. Further, the exposure of the nanopatterned silicon surface to air during optical measurement ensures the formation of non-uniform silicon oxide on the nanopatterned silicon surface. Additionally, the post-bombardment growth of silicon oxide on nanopatterned silicon leads to site-dependent growth of native oxide, which is useful for producing hysteresis in surface current–voltage characteristic measure-

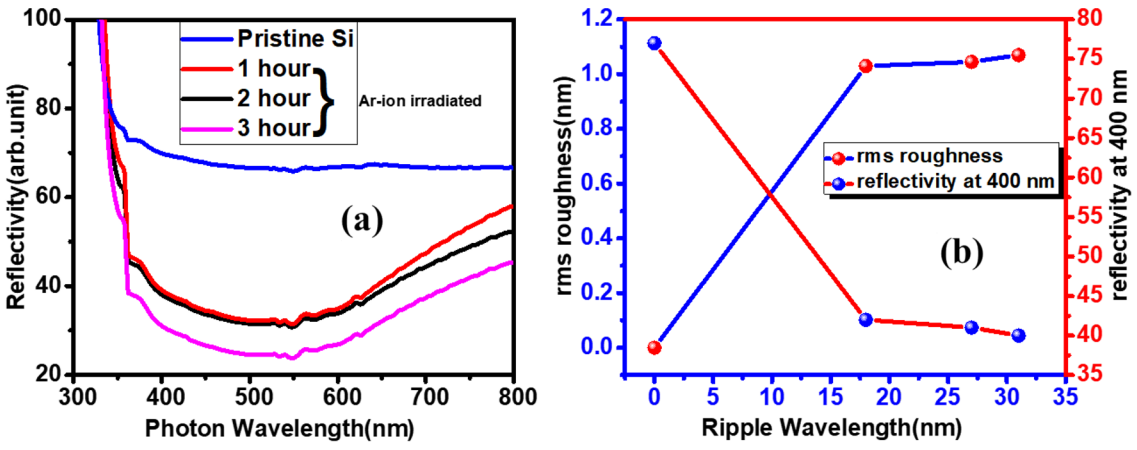

Figure 8: (a) UV–vis spectra of pristine and nanopatterned surfaces, (b) variation of rms roughness and reflectivity with ripple wavelength.

ments [50,51]. The preferential spatial formation of silicon oxide changes the reflectivity. Also, nanopatterned silicon surfaces can be an alternative for memory devices.

Conclusion

In this manuscript, the intricacies of an ultralow-energy magnetron-based electron cyclotron resonance (ECR) ion source are studied systematically by exploring optimal parameters to achieve stable and intense beam currents. The cost-effectiveness and versatility of this ion source make it particularly noteworthy, offering a practical solution for generating reasonable beam currents. The ion source operates within an ultrahigh-vacuum environment, rendering it valuable for both implantation and deposition processes. Our meticulous investigation of the ECR ion source lays the groundwork for ion beam-induced nanostructuring and layer-wise material modification, affording precise control over ion penetration depth and fluence. The manuscript emphasizes an intriguing alternative perspective by highlighting the in-depth optimization of the ion source and inert ion-induced nanopatterning as a viable approach for antireflective coatings. This study not only advances our understanding of ECR-based ion sources but also opens avenues for innovative applications in nanotechnology and materials science.

Acknowledgements

The authors are thankful to Dr. Rupam Mandal for valuable discussion.

Author Contributions

Joy Mukherjee: conceptualization; data curation; formal analysis; investigation; methodology; software; visualization; writing – original draft; writing – review & editing. Safiul Alam Mollick: investigation; visualization. Tanmoy Basu: data curation; investigation; supervision; visualization; writing – review & editing. Tapobrata Som: conceptualization; funding acquisition; investigation; methodology; resources; supervision; validation; visualization; writing – review & editing.

ORCID® iDs

Joy Mukherjee - https://orcid.org/0000-0002-5387-2617
Safiul Alam Mollick - https://orcid.org/0000-0002-0985-8914

Data Availability Statement

Data generated and analyzed during this study is available from the corresponding author upon reasonable request.

Preprint

A non-peer-reviewed version of this article has been previously published as a preprint: https://doi.org/10.3762/bxiv.2024.67.v1

References

1. Bhowmick, S.; Mukherjee, J.; Satpati, B.; Karmakar, P. *Appl. Surf. Sci.* **2022,** *578,* 152079. doi:10.1016/j.apsusc.2021.152079
2. Barofsky, D. F. *Braz. J. Phys.* **1999,** *29,* 432–439. doi:10.1590/s0103-97331999000300006
3. Gambino, N.; Myalsky, S.; Adler, L.; De Franco, A.; Ecker, F.; Guidoboni, G.; Kurfürst, C.; Penescu, L.; Pivi, M.; Schmitzer, C.; Strasik, I.; Wastl, A. *J. Instrum.* **2019,** *14,* C05017. doi:10.1088/1748-0221/14/05/c05017
4. Gammino, S. Ion Sources for Medical Applications. In *CERN Yellow Reports: School Proceedings,* CERN, 2017; pp 59–70. doi:10.23730/cyrsp-2017-001.59
5. Satoh, K.; Oono, Y. *Quantum Beam Sci.* **2019,** *3,* 11. doi:10.3390/qubs3020011
6. Mukherjee, J.; Bhowmik, D.; Mukherjee, M.; Satpati, B.; Karmakar, P. *J. Appl. Phys.* **2020,** *127,* No. 145302. doi:10.1063/1.5144960
7. Mukherjee, J.; Bhowmik, D.; Bhattacharyya, G.; Satpati, B.; Karmakar, P. *J. Phys.: Condens. Matter* **2022,** *34,* 135001. doi:10.1088/1361-648x/ac4937
8. de Lima, L. H.; Cun, H. Y.; Hemmi, A.; Kälin, T.; Greber, T. *Rev. Sci. Instrum.* **2013,** *84,* 126104. doi:10.1063/1.4848936
9. Norris, S. A.; Aziz, M. J. *Appl. Phys. Rev.* **2019,** *6,* 011311. doi:10.1063/1.5043438
10. Teshome, B.; Facsko, S.; Keller, A. *Nanoscale* **2014,** *6,* 1790–1796. doi:10.1039/c3nr04627c
11. Bhowmik, D.; Karmakar, P. *Surf. Coat. Technol.* **2020,** *385,* 125369. doi:10.1016/j.surfcoat.2020.125369
12. Mollick, S. A.; Singh, R.; Kumar, M.; Bhattacharyya, S.; Som, T. *Nanotechnology* **2018,** *29,* 125302. doi:10.1088/1361-6528/aaaa74
13. Parida, B. K.; Kundu, A.; Hazra, K. S.; Sarkar, S. *Appl. Phys. A: Mater. Sci. Process.* **2021,** *127,* No. 972. doi:10.1007/s00339-021-05117-0
14. Kasani, S.; Curtin, K.; Wu, N. *Nanophotonics* **2019,** *8,* 2065–2089. doi:10.1515/nanoph-2019-0158
15. Saini, M.; Singh, R.; Sooraj, K. P.; Basu, T.; Roy, A.; Satpati, B.; Srivastava, S. K.; Ranjan, M.; Som, T. *J. Mater. Chem. C* **2020,** *8,* 16880–16895. doi:10.1039/d0tc03862h
16. Dwyer, J. R.; Uman, M. A. *Phys. Rep.* **2014,** *534,* 147–241. doi:10.1016/j.physrep.2013.09.004
17. Averkin, S. N.; Ershov, A. P.; Orlikovsky, A. A.; Rudenko, K. V.; Sukhanov, Y. N. *Russ. Microelectron.* **2003,** *32,* 292–300. doi:10.1023/a:1025569917849
18. Scrivens, R. *arXiv* **2014,** No. 1404.0918. doi:10.48550/arxiv.1404.0918
19. Abdel Rahman, M. M.; Abdel Salam, F. W.; Soliman, B. A. *J. Phys.: Conf. Ser.* **2022,** *2304,* 012011. doi:10.1088/1742-6596/2304/1/012011
20. Gaus, A. D.; Htwe, W. T.; Brand, J. A.; Gay, T. J.; Schulz, M. *Rev. Sci. Instrum.* **1994,** *65,* 3739–3745. doi:10.1063/1.1144500
21. Schmor, W. P. A review of polarized ion sources. In *Proceedings Particle Accelerator Conference,* IEEE, 1996. doi:10.1109/pac.1995.504814
22. Angra, S. K.; Kumar, P.; Dongaonkar, R. R.; Bajpai, R. P. *Pramana* **2000,** *54,* 763–769. doi:10.1007/s12043-000-0121-2
23. Asmussen, J. *J. Vac. Sci. Technol., A* **1989,** *7,* 883–893. doi:10.1116/1.575815
24. Schmidt, A. A.; Offermann, J.; Anton, R. *Thin Solid Films* **1996,** *281-282,* 105–107. doi:10.1016/0040-6090(96)08586-0

25. Anton, R.; Wiegner, T.; Naumann, W.; Liebmann, M.; Klein, C.; Bradley, C. *Rev. Sci. Instrum.* **2000,** *71,* 1177–1180. doi:10.1063/1.1150420
26. Bhowmick, S.; Mukherjee, J.; Naik, V.; Karmakar, P. *Vacuum* **2023,** *215,* 112348. doi:10.1016/j.vacuum.2023.112348
27. Runkel, S.; Hohn, O.; Schmidt, L.; Stiebing, K. E.; Schmidt-Böcking, H.; Schempp, A.; Becker, R. *Rev. Sci. Instrum.* **1998,** *69,* 721–723. doi:10.1063/1.1148561
28. Pugachev, D. K.; Bogomolov, S. L.; Bondarchenko, A. E.; Berestov, K. I.; Kuzmenkov, K. I.; Efremov, A. A.; Loginov, V. N.; Mironov, V. E.; Protasov, A. A. *Phys. Part. Nucl. Lett.* **2024,** *21,* 331–336. doi:10.1134/s1547477124700213
29. Mironov, V.; Runkel, S.; Stiebing, K. E.; Hohn, O.; Schmidt, L.; Schmidt-Böcking, H.; Schempp, A.; Shirkov, G. *Rev. Sci. Instrum.* **2001,** *72,* 3826–3828. doi:10.1063/1.1400149
30. Jardin, P.; Farabolini, W.; Gaubert, G.; Pacquet, J. Y.; Drobert, T.; Cornell, J.; Barue, C.; Canet, C.; Dupuis, M.; Flambard, J.-L.; Lecesne, N.; Leherissier, P.; Lemagnen, F.; Leroy, R. *Nucl. Instrum. Methods Phys. Res., Sect. B* **2003,** *204,* 377–381. doi:10.1016/s0168-583x(02)01980-8
31. Ziegler, J. F.; Ziegler, M. D.; Biersack, J. P. *Nucl. Instrum. Methods Phys. Res., Sect. B* **2010,** *268,* 1818–1823. doi:10.1016/j.nimb.2010.02.091
32. Ohtsu, Y. Physics of High-Density Radio Frequency Capacitively Coupled Plasma with Various Electrodes and Its Applications. In *Plasma Science and Technology - Basic Fundamentals and Modern Applications;* Jelassi, H.; Benredjem, D., Eds.; IntechOpen: Rijeka, Croatia, 2019. doi:10.5772/intechopen.78387
33. Chu, P. K.; Qin, S.; Chan, C.; Cheung, N. W.; Ko, P. K. *IEEE Trans. Plasma Sci.* **1998,** *26,* 79–84. doi:10.1109/27.659535
34. Ghosh, S. N.; Dhungel, S. K.; Yoo, J.; Gowtham, M.; Yi, J.; Bora, D. *J. Korean Phys. Soc.* **2006,** *48,* 908–913.
35. Yang, Y. R.; Fu, S. H.; Ding, Z. F. *AIP Adv.* **2022,** *12,* No. 055325. doi:10.1063/5.0082813
36. Fournier, P.; Lisi, N.; Meyer, C.; Scrivens, R.; Ostroumov, P. Experimental Characterisation of Gridded Electrostatic Lens (GEL) Low Energy Beam Transport (LEBT) for the Laser Ion Source (LIS) and Effect of a Wire Grid on the Extraction Electrode. 1999; https://cds.cern.ch/record/2849783 (accessed March 5, 2025).
37. Dudin, S. V.; Rafalskyi, D. V. *Eur. Phys. J. D* **2011,** *65,* 475–479. doi:10.1140/epjd/e2011-20402-y
38. Deka, A.; Barman, P.; Mukhopadhyay, M. K.; Bhattacharyya, S. R. *Surf. Interfaces* **2021,** *25,* 101242. doi:10.1016/j.surfin.2021.101242
39. Jain, I. P.; Agarwal, G. *Surf. Sci. Rep.* **2011,** *66,* 77–172. doi:10.1016/j.surfrep.2010.11.001
40. Datta, D. P.; Garg, S. K.; Basu, T.; Satpati, B.; Hofsäss, H.; Kanjilal, D.; Som, T. *Appl. Surf. Sci.* **2016,** *360,* 131–142. doi:10.1016/j.apsusc.2015.10.133
41. Bradley, R. M.; Harper, J. M. E. *J. Vac. Sci. Technol., A* **1988,** *6,* 2390–2395. doi:10.1116/1.575561
42. Carter, G.; Vishnyakov, V. *Phys. Rev. B* **1996,** *54,* 17647–17653. doi:10.1103/physrevb.54.17647
43. Kumar, M.; Datta, D. P.; Basu, T.; Garg, S. K.; Hofsäss, H.; Som, T. *J. Phys.: Condens. Matter* **2018,** *30,* 334001. doi:10.1088/1361-648x/aad1b8
44. Basu, T.; Datta, D. P.; Som, T. *Nanoscale Res. Lett.* **2013,** *8,* 289. doi:10.1186/1556-276x-8-289
45. Basu, T.; Mohanty, J. R.; Som, T. *Appl. Surf. Sci.* **2012,** *258,* 9944–9948. doi:10.1016/j.apsusc.2012.06.054
46. Vorathamrong, S.; Panyakeow, S.; Ratanathammaphan, S.; Praserthdam, P. *AIP Adv.* **2019,** *9,* No. 025318. doi:10.1063/1.5084344
47. Mennucci, C.; Muhammad, M. H.; Hameed, M. F. O.; Mohamed, S. A.; Abdelkhalik, M. S.; Obayya, S. S. A.; Buatier de Mongeot, F. *Appl. Surf. Sci.* **2018,** *446,* 74–82. doi:10.1016/j.apsusc.2018.02.186
48. Garnett, E.; Yang, P. *Nano Lett.* **2010,** *10,* 1082–1087. doi:10.1021/nl100161z
49. Amalathas, A. P.; Alkaisi, M. M. *Micromachines* **2019,** *10,* 619. doi:10.3390/mi10090619
50. Mousavi, B. K.; Mousavu, A. K.; Busani, T.; Zadeh, M. H.; Brueck, S. R. J. *J. Appl. Math. Phys.* **2019,** *07,* 3083–3100. doi:10.4236/jamp.2019.712217
51. Zang, K.; Jiang, X.; Huo, Y.; Ding, X.; Morea, M.; Chen, X.; Lu, C.-Y.; Ma, J.; Zhou, M.; Xia, Z.; Yu, Z.; Kamins, T. I.; Zhang, Q.; Harris, J. S. *Nat. Commun.* **2017,** *8,* 628. doi:10.1038/s41467-017-00733-y
52. Madi, C. S.; Anzenberg, E.; Ludwig, K. F.; Aziz, M. J. *Phys. Rev. Lett.* **2011,** *106,* 066101. doi:10.1103/physrevlett.106.066101
53. Chan, W. L.; Chason, E. *J. Appl. Phys.* **2007,** 101. doi:10.1063/1.2749198

License and Terms

BEILSTEIN JOURNAL OF NANOTECHNOLOGY

Ar^+ implantation-induced tailoring of RF-sputtered ZnO films: structural, morphological, and optical properties

Manu Bura, Divya Gupta, Arun Kumar and Sanjeev Aggarwal*

Full Research Paper

Open Access

Address:
Department of Physics, Kurukshetra University, Kurukshetra, 136119, India

Email:
Sanjeev Aggarwal* - saggarwal@kuk.ac.in

* Corresponding author

Keywords:
AFM; diffuse reflectance; GXRD; polycrystalline; ZnO films

Beilstein J. Nanotechnol. **2025,** *16,* 872–886.
https://doi.org/10.3762/bjnano.16.66

Received: 28 January 2025
Accepted: 16 May 2025
Published: 11 June 2025

This article is part of the thematic issue "Energetic ions and photons for engineering nanomaterials".

Guest Editor: V. R. Soma

Abstract

Radio frequency-sputtered zinc oxide films are implanted with 30 keV Ar^+ ions at various fluences ranging from 1×10^{15} to 2×10^{16} ions·cm^{-2}. Raman spectra reveal the presence of the E_2 (low), E_2 (high), and A_1 (LO) Raman modes in pristine and implanted ZnO films. A gradual fall and rise in peak intensity of, respectively, the E_2 (high) and A_1 (LO) Raman modes is observed with increases in ion fluence. However, the E_2 (low) mode broadens and merges completely with disorder-induced broad band at higher fluences. Moreover, the deconvolution of the A_1 (LO) Raman peak affirms the presence of defect-related Raman modes in the implanted samples. A gradual reduction in crystallinity of the implanted ZnO films with increasing ion fluence is observed in grazing incidence angle X-ray diffraction patterns. Atomic force microscopy images show grain size reduction and a fall in the surface roughness value of films after implantation. The implantation-induced structural modifications are further correlated with the variation in diffuse reflectance, Urbach energy, and optical bandgap. The low reflectance values of implanted films assure their suitability as transparent windows and anti-reflective coating in various optoelectronic devices.

Introduction

Zinc oxide has emerged as a promising material for device fabrication in different fields, namely, spintronics, nanoelectronics, and photonics [1,2]. It possesses a wide bandgap of 3.37 eV [3] and has a large exciton binding energy of about 60 meV [4], which assures the stability of ZnO film-based devices such as liquid crystal displays [5], solar cells [6], and light-emitting diodes [7]. There are numerous methods for synthesizing ZnO films, including pulsed laser deposition, spray pyrolysis, radio frequency (RF) sputtering, and sol–gel techniques. Here RF sputtering is preferred over other methods because it provides high deposition rates and uniform growth of films with good reproducibility [4]. The physical properties of grown ZnO films

can be tuned by altering various growth parameters and employing post-deposition treatments such as ion implantation and thermal annealing.

Ion implantation has proven a versatile tool to control material properties by inducing damage and introducing defects in the host matrix in a controlled manner [8]. It offers the advantage of controlling the amount of energy transferred to the host system by selecting the desired ion energy, mass, and fluence [9]. Different types of lattice vacancies, defects, and interstitials are induced through the interaction between energetic ions and the host material, resulting in structural modification and thus alteration in lattice dynamics of the host material [10].

The implantation-induced disorder can be qualitatively examined using Raman spectroscopy, which is a well-established and non-destructive method to determine crystal structure, lattice defects, and dynamics. Since ZnO is a polar semiconductor, the phonon–electron interaction produces longitudinal optical (LO) phonon modes, whose long-range behavior considerably affects the efficacy of optoelectronic devices [11]. Thus, a detailed study of the evolution of phonon modes is needed to utilize implanted ZnO films effectively in such devices. The activation of Raman modes in implanted films depends on various implantation parameters, namely, ion energy, mass, and fluence.

The origin of these optical phonon modes is ascribed to the formation of oxygen vacancies, which are supposed to be electron carriers in ZnO. Therefore, the evolution of the A_1 (LO) mode acts as indirect evidence of a rise in carrier concentration, which can in turn alter the optical bandgap. Moreover, the presence of foreign ions in the ZnO film lattice can create an impact on its surface roughness and particle size.

Previous reports available discuss the implantation-induced optical longitudinal phonon symmetry in ZnO films using heavy ions with high energy and low implantation fluences [12-15]. Singh et al. [12] observed the evolution of symmetry-forbidden and A_1 (LO) modes in 120 MeV Au^{9+} ion-irradiated ZnO films. Ying et al. [13] described an A_1 (LO) mode in the Raman spectra of energy-dependent and dose-dependent krypton ion-implanted ZnO film after varying the fluence in the range from 5×10^{13} to 2.5×10^{15} ions·cm^{-2}. Gupta et al. [14] have investigated the activation of the A_1 (LO) mode and the production of a broad band at the lower Raman shift side in ZnO films implanted with 300 keV argon and 1.2 MeV xenon ions with varying fluence from 1×10^{14} to 3×10^{15} ions·cm^{-2}. Gautam et al. [15] reported the presence of an A_1 (LO) Raman mode and a disorder-induced band at low wavenumbers in cadmium-doped zinc oxide films irradiated using 120 MeV Ag^{9+} and 80 MeV O^{6+} ions at fluences of 1×10^{13} and 3×10^{13} ions·cm^{-2}.

Further, few studies [16,17] reported the emergence of optical longitudinal phonon symmetry in ZnO films implanted at lower ion beam energies. Zhiguang et al. [16] have observed the appearance of a longitudinal phonon mode in 80 keV nitrogen ion-implanted ZnO films at different fluences. Kennedy et al. [17] have reported enhancement in the disordered phase and an A_1 (LO) mode in 23 keV co-implanted (H^+ and N^+ ions) ZnO films. But in these two above-quoted reports nitrogen ions were used for implantation. Nitrogen ions act as n-type doping and can alter the stoichiometry of ZnO films, which is not desirable in certain optoelectronic devices [10,11]. Hence, we have used Ar^+ ions for implantation, which produce less lattice distortions than nitrogen ions. This is because argon ions are heavier and larger than nitrogen ions.

Also, in the above-quoted studies the authors did not study the effect of the evolution of longitudinal optical A_1 (LO) and symmetry-disallowed Raman modes on the surface morphological and optical characteristics (Urbach energy and optical bandgap). In fact, in the existing literature, there are barely any studies that have addressed the impact of the evolution of A_1 (LO) modes on surface morphology and optical properties in low-energy regimes, although the variation in surface parameters and optical characteristics can significantly impact the applicability of ZnO films in semiconductors, spintronics, solar cells, and green energy industries [3,18].

This motivated us to investigate the emergence of Raman longitudinal optical modes and their correlation with morphological and optical properties using low-energy Ar^+ beams in ZnO films. Here, argon ions were chosen because of the inert nature, which means that any changes in properties of the implanted ZnO films are attributed solely to implantation-induced effects.

In the present study, ZnO films were implanted with 30 keV Ar^+ at fluences varying from 1×10^{15} to 2×10^{16} ions·cm^{-2}. Surface variables (roughness and particle size), structural variables (crystallite size and dislocation density), and optical properties (diffuse reflectance, Urbach energy, and optical bandgap) were studied in response to a rise in ion fluence. The ion implantation-induced lattice disorder and lattice damage as functions of the ion fluence were studied in terms of displacement produced per atom in the host lattice calculated using TRIM simulations [19] and were correlated with changes in Urbach energy. The films are versatile in developing high-performance electro-optical and spintronic devices [18].

Experimental

ZnO films are grown on a quartz substrate (1×1 cm^2) using a ZnO (99.99%) target (2″ diameter and 3 mm thickness) in a radio frequency (RF) sputtering system. The quartz substrate is

ultrasonically cleaned using acetone and, finally, isopropyl alcohol before the experiment. The sputtering chamber is pumped to a base pressure of 1.2×10^{-6} Torr; then a mixture of nitrogen and argon gas is introduced into the sputtering chamber with flows of 1.8 and 10.0 sccm, respectively. When the pressure inside the chamber has stabilized, the sputtering power is set to a value of 80 W. The sputtering is performed at a pressure of 1.8×10^{-5} Torr at room temperature with a deposition rate of 0.4–0.5 Å·s^{-1}. A spectroscopic ellipsometer is used to calculate the thickness of the pristine ZnO films. An appropriate physical model is designed and fitted using different ellipsometry parameters to obtain the least root mean square error. The thickness of the as-grown ZnO films was found to be around 296 ± 6 nm. Moreover, the thickness of ZnO films calculated using cross-sectional FESEM images was of the same order as the thickness calculated from spectroscopic ellipsometry (Figure 1).

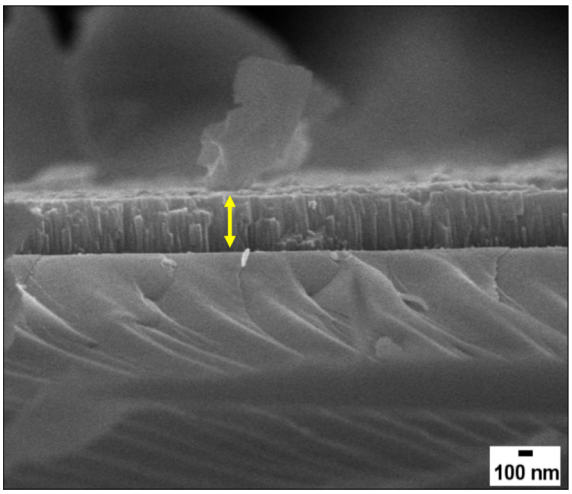

Figure 1: Cross-sectional FESEM images of pristine ZnO film. Here yellow arrow represents the thickness of grown film.

After deposition, films are implanted with 30 keV Ar^+ ions at different fluences of 1×10^{15}, 5×10^{15}, 1×10^{16}, and 2×10^{16} Ar^+ cm^{-2} using the 200 kV ion accelerator facility at Ion Beam Centre, Kurukshetra University. The implantation is carried out at normal incidence for all fluences. The electronic energy loss of 30 keV Ar^+ ions in ZnO films is 18.73 eV·Å^{-1}, while the nuclear energy loss is 9.610×10^3 eV·Å^{-1}, calculated using SRIM-2008 [19]. The projected range of 30 keV Ar^+ ions in the ZnO lattice is 25.9 ± 13.7 nm.

The crystalline structure is studied using a Bruker AXS D8 Advance X-ray diffractometer operating in grazing incidence geometry using Cu Kα radiation (λ = 1.5406 Å). The scans are obtained at an incidence angle of 0.5°. The Raman spectra of ZnO films before and after implantation are recorded at room temperature using a WITec alpha300 RA Raman spectrometer under excitation with a 532 nm solid-state diode laser operated at 10 mW. The topography of the films is examined using atomic force microscopy (AFM) with a Bruker Multimode 8 instrument. The surface morphology of pristine and implanted films is further studied using field-emission scanning electron microscopy (FESEM) along with energy dispersive X-ray spectroscopy (EDS). Cross-sectional images are also obtained to evaluate the thickness of ZnO film. The optical properties of pristine and implanted ZnO films are investigated using a Shimadzu UV–visible–NIR spectrophotometer (UV-3600Plus) employed with Integrating Sphere Assembly (ISR-603) in the wavelength range of 200–800 nm.

Results and Discussion

Structural analysis

Grazing incidence X-ray diffraction

The grazing incidence X-ray diffraction (GXRD) patterns of pristine ZnO and argon-implanted ZnO films at various ion fluences are depicted in Figure 2. The coexistence of two diffraction peaks (Figure 2) depicts the polycrystalline nature of films. The diffraction peaks centered at 2θ values of 34.23° and 62.59° corresponding to (002) and (103) planes, respectively, confirm the wurtzite structure (JCPDS No. 36-1451) of pristine samples (Figure 2a) [20]. The intense peak centered at 2θ = 34.23° indicates the growth of samples along the *c* axis, that is, in the [002] direction, which has the lowest surface energy. The existence of a peak related to the (103) planes can be attributed to the presence of intrinsic defects in the films [21,22]. The presence of the same diffraction peaks in the GXRD pattern of implanted samples (Figure 2b–e) suggests the occurrence of identical crystal structures after implantation.

To study the effect of implanted ions on the structure of the films, the more intense (002) peak is further analyzed. The intensity of the peak reduces with increasing ion fluence, revealing a reduction in crystallinity. This is due to argon ion implantation-induced lattice damage. Yet, even at the highest fluence, complete amorphization is not detected.

ZnO films were implanted with 30 keV Ar^+ ions. The energy used here was a low energy; also, argon is lighter than zinc. Because of this, the irradiation did not cause a significant shift in peak positions with increasing ion fluence, but it is observable. The shift in peak position and the variation in peak intensity of the (002) peak at 34.41° with increase in ion fluence is given in Figure 3 and Table 1.

For more detailed information regarding the structural evolution of implanted ZnO films, the crystallite size (*D*), micro-

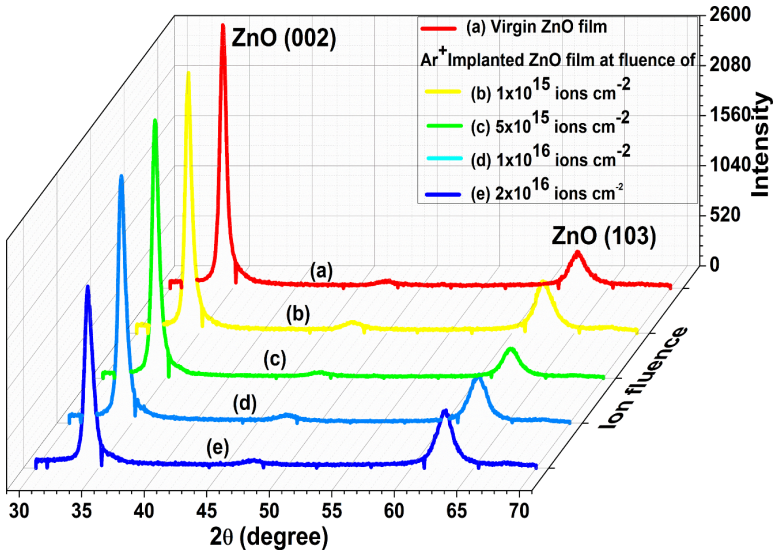

Figure 2: GXRD pattern of pristine and Ar^+-implanted ZnO films at various fluences.

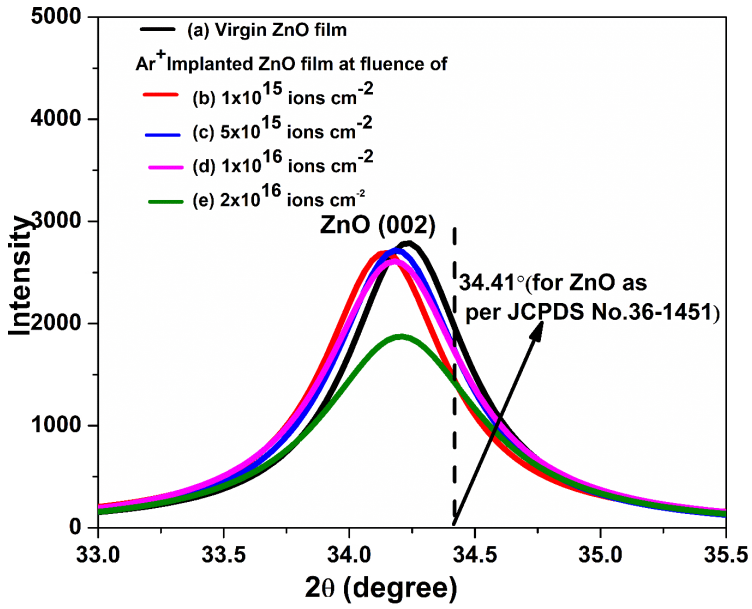

Figure 3: Shift in peak position of the (002) peak centered at 34.23° for all samples. 34.41° is the Bragg angle of the (002) reflection as per JCPDS No. 36-1451.

Table 1: Variation in peak position, intensity, and shift in peak position of the (002) peak centered at 34.23° with increase in ion fluence.

Ion fluence (ions·cm^{-2})	2θ (°) from literature	2θ (°) in present work	Peak intensity	Shift in peak position (°)
pristine	34.41	34.23	2781	−0.18
1×10^{15}	–	34.14	2654	−0.27
5×10^{15}	–	34.18	2735	−0.23
1×10^{16}	–	34.18	2612	−0.23
2×10^{16}	–	34.20	1887	−0.21

strain (ε), and dislocation density (δ) values are calculated from the (002) peaks using the following equations [23]:

$$D = \frac{0.9\lambda}{\beta\cos\theta}, \quad (1)$$

$$\varepsilon = \frac{\beta}{4\tan\theta}, \quad (2)$$

$$\delta = \frac{1}{D^2}. \quad (3)$$

In the above relations, λ is the wavelength of the incident Cu Kα radiation (1.5406 Å), β represents the full-width at half maximum (FWHM), and θ is the peak position. The variation in values of these parameters is shown in Table 2.

The crystallite size of the pristine sample is found to be 14.42 ± 0.35 nm. It decreases slowly with the rise in implantation fluence and achieves a value of 10.97 ± 0.47 nm at the highest ion fluence due to a reduced crystallinity of the implanted films. Moreover, argon atoms can reside on substitutional sites of the ZnO lattice, which causes strain in the implanted layers; thus, the microstrain values increase with fluence [24]. Strain in implanted ZnO films arises primarily from lattice mismatch, which is due to the difference in thermal expansion coefficients between film and substrate. Also, when argon ions are implanted into the ZnO lattice, they create defects and dislocations. This creates lattice strain, which increases with ion fluence. The size and type of the implanted ions, as well as the dose, can affect the amount of strain introduced [24]. It is observed that dislocation density values increase with the rise in implantation fluence, which can be attributed to the fact that an enormous amount of energy is transferred to the lattice when the ion beam travels through the sample quickly, which generates dislocations.

Raman spectroscopy

Figure 4 reveals the Raman spectra of pristine and 30 keV argon-implanted ZnO films at various fluences. The spectrum

Table 2: Variation in FWHM, crystallite size *D*, dislocation density δ, and microstrain ε of pristine and Ar^+-implanted ZnO films at various fluences.

Ion fluence (ions·cm^{-2})	2θ (°)	FWHM (°)	Crystallite size (*D*) (nm)	Dislocation density (δ) (10^{16} m^{-2})	Microstrain (ε) (10^{-3})
pristine	34.23	0.577	14.42 ± 0.35	0.48	8.16
1 × 10^{15}	34.14	0.588	14.16 ± 0.47	0.49	8.33
5 × 10^{15}	34.18	0.618	13.46 ± 0.44	0.55	8.75
1 × 10^{16}	34.18	0.669	12.45 ± 0.45	0.64	9.47
2 × 10^{16}	34.20	0.759	10.97 ± 0.47	0.83	10.73

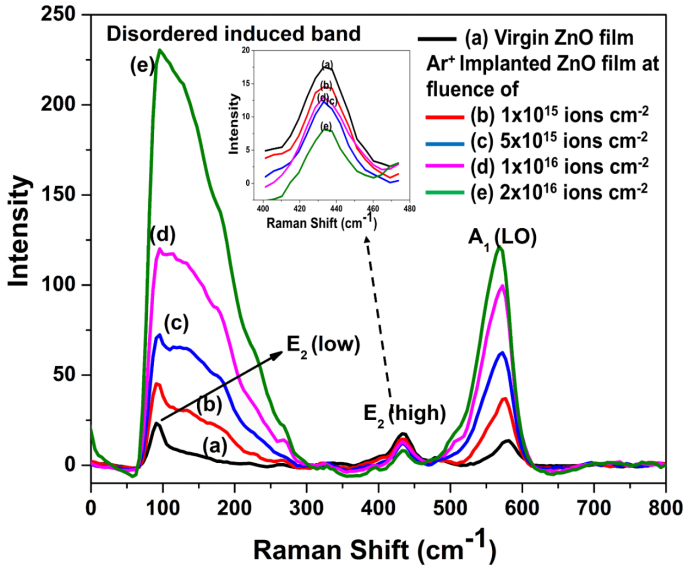

Figure 4: Raman spectra of (a) pristine and Ar^+-implanted ZnO films at various fluences of (b) 1 × 10^{15}, (c) 5 × 10^{15}, (d) 1 × 10^{16}, and (e) 2 × 10^{16} ions·cm^{-2} with inset representing the peak related to the E_2 (high) mode.

of the pristine film (Figure 4a) show peaks at 96, 433, and 577 cm^{-1}, which correspond to E_2 (low), E_2 (high), and A_1 (LO) modes of ZnO respectively. The prominent peaks corresponding to E_2 (low) and E_2 (high) are characteristic peaks related to the wurtzite crystal structure of ZnO, which points toward the good crystallinity of our films.

Moreover, the presence of the A_1 (LO) and E_2 (high) modes indicates the growth of the film along the *c* axis, which is also confirmed using GXRD. The intensity of the peak related to the A_1 (LO) mode is relatively weak in the pristine film (Figure 4a). The A_1 (LO) mode evolves because of defects present in the film in the form of oxygen vacancies, zinc interstitials, and their complexes. For the case of ZnO films implanted at 1×10^{15} ions·cm^{-2} fluence (Figure 4b), the intensity of the E_2 (low) and A_1 (LO) modes increases, while the peak intensity of the E_2 (high) modes decreases. Besides this, a broad band started to appear around 104 to 200 cm^{-1}, which is assigned as a disorder-induced band due to lattice disorder induced by ion implantation [14]. With further increase in fluence to 5×10^{15} ions·cm^{-2} (Figure 4c), phonon modes corresponding to A_1 (LO) symmetry intensify, and those corresponding to E_2 (high) weaken. Also, the peak related to the E_2 (low) mode starts to merge with the disorder-induced broad band. At 1×10^{16} ions·cm^{-2} fluence (Figure 4d), the peak related to the E_2 (low) mode merges completely with the disorder-induced broad band, while the phonon mode corresponding to A_1 (LO) symmetry intensifies and the intensity of the phonon mode referred to as E_2 (high) decreases. Last, at the highest fluence (Figure 4e), the intensity of disorder-induced broad band surpasses the phonon mode related to A_1 (LO) symmetry, and the peak intensity related to the E_2 (high) phonon mode diminishes. The decrease in intensity of the E_2 (high) phonon peak can be attributed to the evolution of defects in the oxygen (O^{2-}) sublattice due to energy deposition via ion implantation. This is also correlated with enhancement in the intensity of the disorder-induced band and a decrease in crystallinity along the *c* axis as depicted by GXRD.

Furthermore, for a better understanding of the evolution of defects with implantation, position and FWHM of the peak corresponding to the A_1 (LO) phonon mode of all samples is displayed in Table 3. It is observed that for all the samples, the A_1 (LO) phonon mode exhibits softening and broadening with the rise in argon ion fluence from 1×10^{15} to 2×10^{16} ions·cm^{-2}. It is well known that a shift of the peak position of phonon modes occurs because of strain present in the film. The broadening of peaks occurs because of the fast decay of phonons or an anharmonic process due to damage [25]. One can determine the phonon lifetime from the Raman spectra using the energy–time uncertainty equation [25]:

$$\Delta E \cdot \tau = h/2\pi \tag{4}$$

$$\frac{1}{\tau} = \frac{\Delta E \cdot 2\pi}{h} = \frac{hc \cdot 2\pi \cdot \Delta\bar{\nu}}{h} = 2\pi c \Delta\bar{\nu}$$

Here $\Delta\bar{\nu}$ represents Raman shift, which is of the order of the FWHM (Γ) of the Raman mode; thus, the lifetime is determined employing the following relation [25]:

$$\frac{1}{\tau} = 2\pi c \Gamma. \tag{5}$$

The lifetime related to the phonon is calculated using Equation 5 and summarized in Table 3; the values are of the order of picoseconds and match well with the literature [26,27]. It is found that the lifetime of the A_1 (LO) mode is becoming shorter with the rise in argon ion fluence, which can be correlated with the emergence of the defect-induced band. Moreover, phonon softening relates to tensile stress, while phonon stiffening relates to compressive stress. Thus, all argon ion-implanted ZnO films show phonon softening, which indicates that tensile stress is produced in the films with an increase in argon ion fluence. This can be ascribed to expansion in volume due to implanted ions since argon ions are inert in nature, which

Table 3: Variation in the position of peak and FWHM corresponding to the A_1 (LO) mode, phonon lifetime, and number of displacements produced per atom (dpa) as a function of ion fluence.

Ion fluence (ions·cm^{-2})	Peak position (cm^{-1}) of A_1 (LO) mode	FWHM (cm^{-1}) of A_1 (LO) mode	Lifetime (τ) picoseconds	dpa
pristine	577	38.2	0.138	–
1×10^{15}	569	46.6	0.113	0.45
5×10^{15}	565	49.3	0.107	2.25
1×10^{16}	564	49.8	0.106	4.51
2×10^{16}	562	50.9	0.104	9.03

prevents them from reacting with host ions. This leads to the accumulation of inert ions at the interstitial sites of ZnO, which produces stress in the material [14].

Additionally, it is observed that the intensity of the disorder-induced band rises with the rise in Ar^+ fluence. This is attributed to the fact that ion implantation produces lattice disorder or lattice damage, which is studied in terms of the fluence of implanted ions and displacements produced per atom (dpa) in the host matrix through implantation [28]. The value of dpa can be calculated via TRIM simulations using the following relation [14]:

$$\text{dpa} = \frac{\text{Fluence}\left(\text{ions}/\text{cm}^2\right)\times\left(\text{vacancies}/\text{ion-Å}\right)\times 10^8\left(\text{Å}/\text{cm}\right)}{\text{atomic density of host material}\left(\text{atoms}/\text{cm}^3\right)} \quad (6)$$

The above equation depicts the number of vacancies created per ion per angstrom, which can be calculated from TRIM simulations as shown in Figure 5. For ZnO, the atomic density value is 8.30×10^{22} atoms/cm^3, and the displacement energy for both zinc and oxygen is 56 eV.

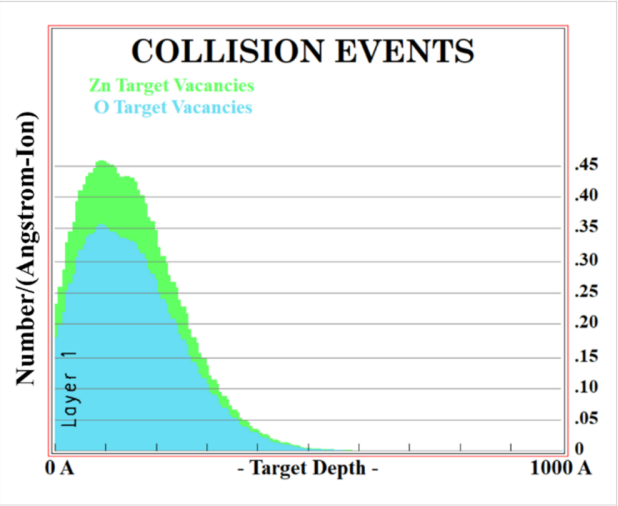

Figure 5: Number of zinc and oxygen vacancies created by the argon ion beam in the ZnO target calculated using TRIM simulations.

It is to be noticed from Table 3 that dpa increases with increases in argon ion fluence. Thus, the rise in intensity of the disorder-induced band can be ascribed to an increase in dpa, which leads to lattice disorder [14].

The peak corresponding to the A_1 (LO) mode of implanted samples is deconvoluted as shown in Figure 6. This type of scattering from the K–M point of the Brillouin zone is symmetrically forbidden. Gupta et al. [14] have also reported such behavior of the A_1 (LO) Raman mode in 300 keV argon ion-implanted ZnO films. Mondal et al. [29] and Li et al. [30] have ascribed these peaks centered at 577 and 554 cm^{-1} to oxygen vacancies and zinc interstitials, respectively. Moreover, the peak related to the A_1 (LO) mode both at the Γ and K–M points of the Brillouin zone shows softening and broadening with increasing argon ion fluence. Also, enhancement in peak intensity of both the peaks reveals the increases in lattice defects with increasing ion fluence.

Morphological analysis

Atomic force microscopy

The surface morphology of pristine and 30 keV Ar^+ ion-implanted ZnO films is studied using AFM. Figure 7 represents 2D and 3D AFM images at the scale 2 μm × 2 μm of the pristine film (Figure 7a) and films implanted at four different fluences, viz. 1×10^{15} (Figure 7b), 5×10^{15} (Figure 7c), 1×10^{16} (Figure 7d), and 2×10^{16} ions cm^{-2} (Figure 7e).

All the images have been analyzed using Nanoscope analysis software provided with the AFM to determine the particle size and surface root mean square (RMS) roughness values for different implanted samples. The results are shown in Table 4.

The pristine sample exhibits a surface RMS roughness of 6.92 ± 0.22 nm. After implantation, the RMS roughness decreases to about 3.58 ± 0.31 nm at the highest fluence, indicating smoothening of the films. The particle size is found to decrease from 74.41 ± 0.71 nm (pristine) to 53.78 ± 0.89 nm (highest fluence). The decrease in particle size and RMS roughness can be ascribed to the rearrangement of surface atoms due to the elastic collisions. This leads to the evolution of small ZnO particles due to the breaking of clusters by the transfer of energy from incident ions. Kahng et al. [31] presented a nonlinear theory that explains the mechanism of the evolution of nanostructures on ion beam-implanted surfaces at normal incidence. According to this theory, in the early stages, sputtering leads to the formation of tiny wavy perturbations induced via instabilities created by the ion beam. These instabilities are followed by a surface relaxation process, which leads to the smoothening of the surface and is also mentioned as negative surface tension by others [32,33]. This process causes the breaking of larger structures into smaller ones. Thus, one can tune the surface morphology of films using an inert ion beam through a competition between surface diffusion and ion erosion processes [34,35].

Field-emission scanning electron microscopy

The surface morphology of pristine and 30 keV argon-implanted ZnO films was also studied by FESEM. Figure 8 shows the FESEM images of pristine and implanted films. To

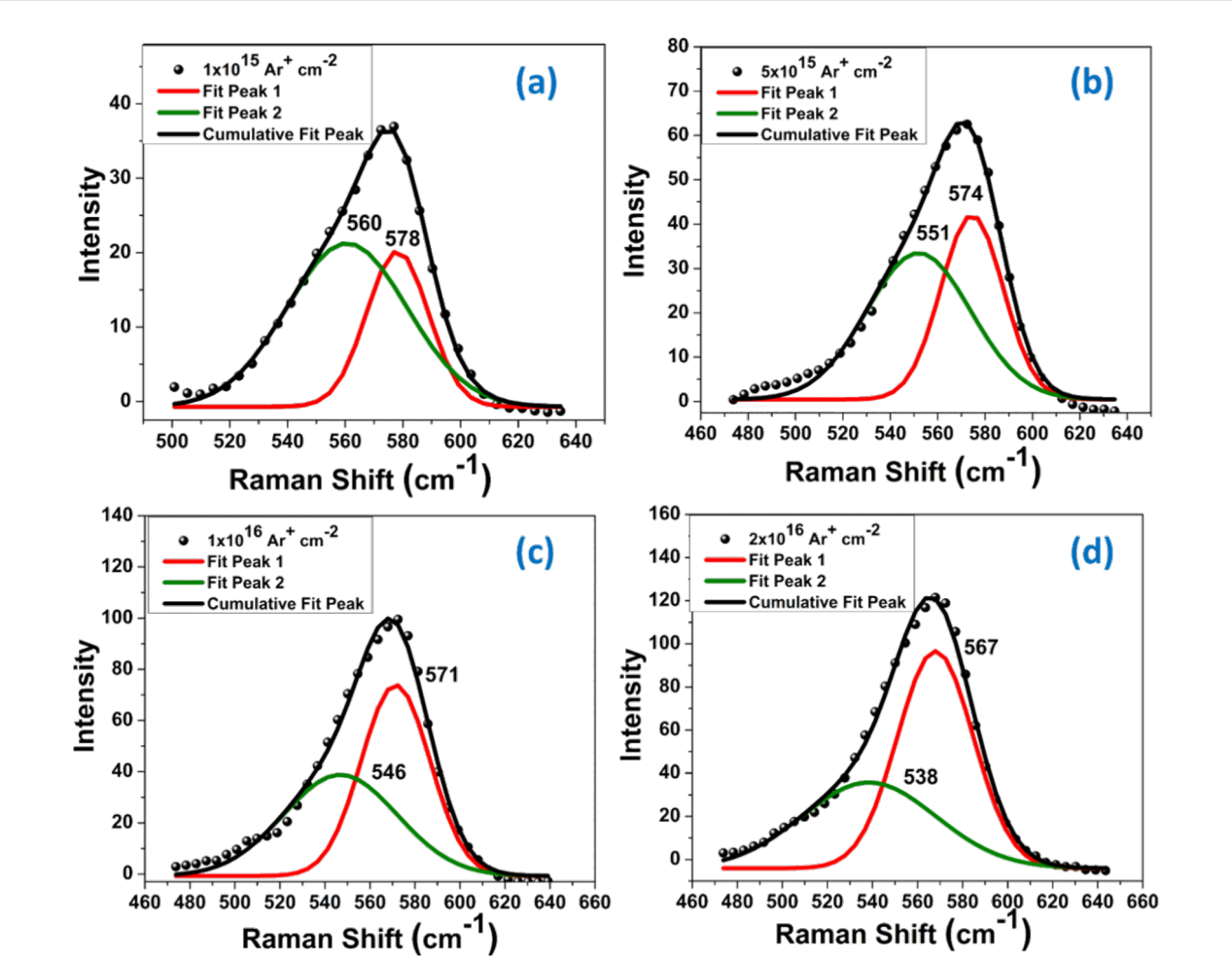

Figure 6: Deconvolution of the A_1 (LO) Raman peak of ZnO films implanted at various fluences of (a) 1 × 10^{15}, (b) 5 × 10^{15}, (c) 1 × 10^{16}, and (d) 2 × 10^{16} ions·cm^{-2}.

deduce the change in surface RMS roughness and grain size of films after implantation, FESEM images have been processed with Image J software [36] and the results are given in Table 5.

It is observed from Figure 8 that average grain size and surface RMS roughness reduce with ion fluence. As the implantation dose of argon ions increases, the RMS roughness decreases from 17.8 ± 0.33 to 11.8 ± 0.68 because of inverse coarsening and fragmentation of nanostructures, leading to the smoothening of films. According to Paramanik et al. [33], surface smoothening can be associated with a decrease in the crystallinity of films. At high fluences, the density of electronic excitation increases, and covalent bonds in the lattice are weakened. This leads to relaxation, which causes surface smoothening. The stoichiometry of pristine and implanted samples evaluated using EDS analysis are shown in Table 6. Because of the native oxide layer on the Si substrate, the oxygen content contains contributions from both SiO_2 and ZnO. The variations in grain size and RMS roughness of ZnO films with increase in ion fluence follow the same trend in AFM and FESEM analyses, but with different magnitudes. This is because of the greater sensitivity of AFM closer to the surface, while FESEM measures further inside the sample.

Optical analysis

Figure 9 shows diffuse reflectance spectra of pristine and implanted ZnO films at different Ar^+ ion fluences. The reflectance spectra of all the samples exhibit oscillating behavior, which can be attributed to interference phenomena due to differences in film refractive index and substrate refractive index.

This behavior of the spectra indicates the formation of smooth and uniform films on the quartz substrate [37]. The spectra of all samples show a sudden rise in reflectance above 370 nm, which represents the ZnO fundamental absorption edge. With

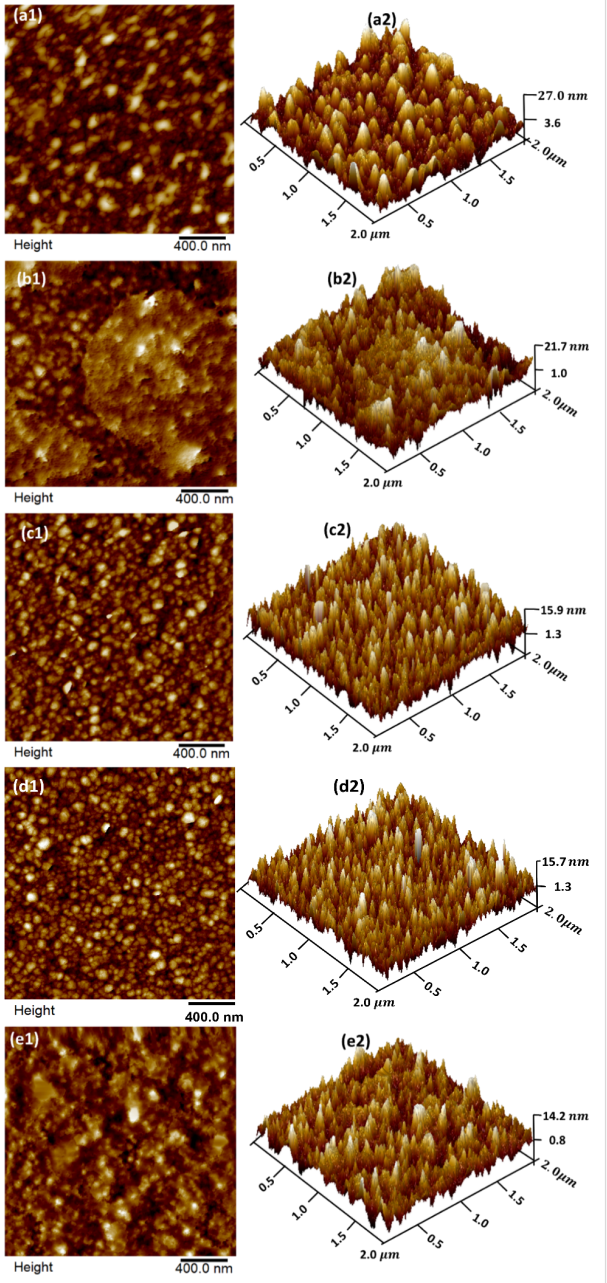

Figure 7: 2D and 3D AFM images of pristine (a1, a2) and Ar^+-implanted ZnO films at fluences 1×10^{15} (b1, b2), 5×10^{15} (c1, c2), 1×10^{16} (d1, d2), and 2×10^{16} ions·cm^{-2} (e1, e2).

the increase in argon ion fluence, the diffuse reflectance was found to decrease, which is related to the decrease in the surface RMS roughness also reported in AFM analysis. Thus, implanted ZnO films can be employed as an antireflection coating in optoelectronic devices [38].

The diffuse reflectance of the films can be used to calculate the associated Kubelka–Munk function, which is equivalent to the absorption spectra [39,40]. This paves the way to calculate the optical bandgap of the implanted films. The Kubelka–Munk function $F(R)$ is determined employing diffuse reflectance by the following relation [41]:

$$F(R) = \frac{(1-R)^2}{2R} = \frac{\alpha}{s}. \quad (7)$$

Here R is the diffuse reflectance of the samples; s and α correspond to scattering and absorption coefficients, respectively. The scattering coefficient does not depend on the wavelength. Thus, $F(R)$ becomes proportional to α. It has been observed that with the rise in ion fluence, $F(R)$ of the films increases (Figure 10). This points towards the degradation of the crystal quality of ZnO films with disordering of atoms and defects in the films. This causes an increased absorption of UV and visible light. Moreover, additional peaks are observed, centered at around 450 and 650 nm, which are ascribed to the presence of defects like oxygen vacancies, oxygen interstitials, zinc vacancies, and zinc interstitials. The defects lead to the formation of sub-bandgap levels [42,43]. Further, the peak positions of these absorption peaks shift towards shorter wavelengths with an increase in ion fluence, which is coherent with a decrease in particle size. This depicts the effect of the surface morphology on the optical response of implanted films [44]. The intensity of these absorption peaks rises with the increase in ion fluence, which points towards an increase in defects as described in GXRD and Raman studies.

The optical bandgap (E_g) values of samples have been estimated employing Tauc's relation [45]:

Table 4: Variations of particle size and surface RMS roughness values of pristine and Ar^+-implanted ZnO films as functions of ion fluence.

Fluence (ions·cm^{-2})	Particle size (nm)	RMS roughness (nm)
pristine	74.41 ± 0.71	6.92 ± 0.22
1×10^{15}	63.00 ± 0.25	5.88 ± 0.67
5×10^{15}	60.50 ± 0.42	4.14 ± 0.16
1×10^{16}	55.85 ± 0.30	4.08 ± 0.19
2×10^{16}	53.78 ± 0.89	3.58 ± 0.31

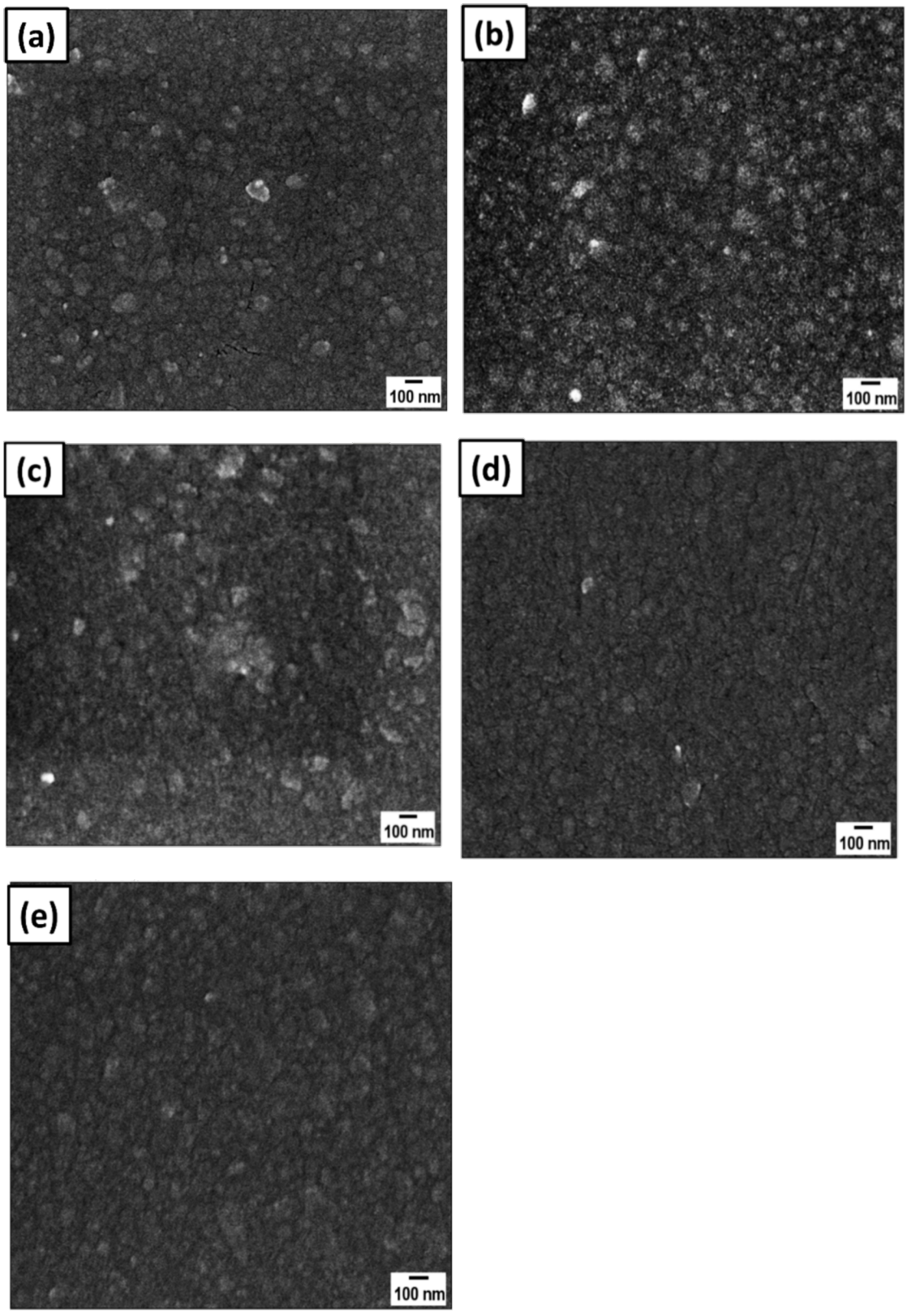

Figure 8: FESEM images of pristine (a) and Ar^+-implanted ZnO films at fluences of (b) 1×10^{15}, (c) 5×10^{15}, (d) 1×10^{16}, and (e) 2×10^{16} ions·cm^{-2}.

Table 5: Variation in grain size and RMS roughness of pristine and implanted ZnO films.

Fluence (ions cm^{-2})	Average grain size (nm)	RMS roughness (nm)
pristine	63.24 ± 2.98	17.7 ± 0.43
1 × 10^{15}	51.53 ± 1.58	16.8 ± 0.23
5 × 10^{15}	43.80 ± 3.08	15.5 ± 0.58
1 × 10^{16}	38.58 ± 0.67	12.6 ± 0.28
2 × 10^{16}	25.22 ± 2.91	11.8 ± 0.68

Table 6: EDS analysis of the pristine ZnO film and the film with the highest implanted dose.

Fluence (ions·cm^{-2})	O content (atom %)	Si content (atom %)	Zn content (atom %)	Ar content (atom %)
pristine	48.8	27.7	25.5	–
2 × 10^{16}	47.2	28.7	23.8	0.3

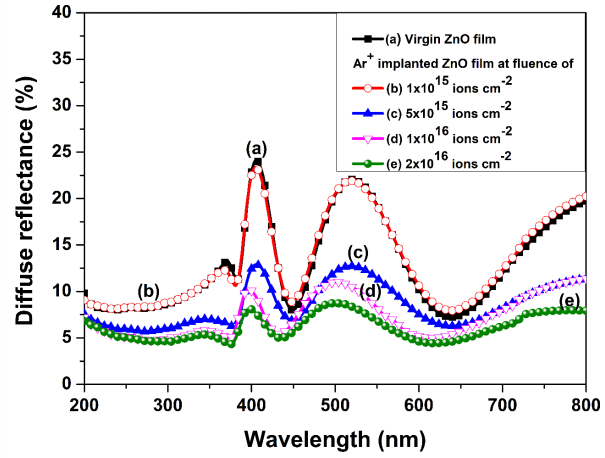

Figure 9: Diffuse reflectance spectra of (a) pristine and Ar$^+$-implanted ZnO films at various fluences, viz. (b) 1 × 10^{15}, (c) 5 × 10^{15}, (d) 1 × 10^{16}, and (e) 2 × 10^{16} ions·cm^{-2}.

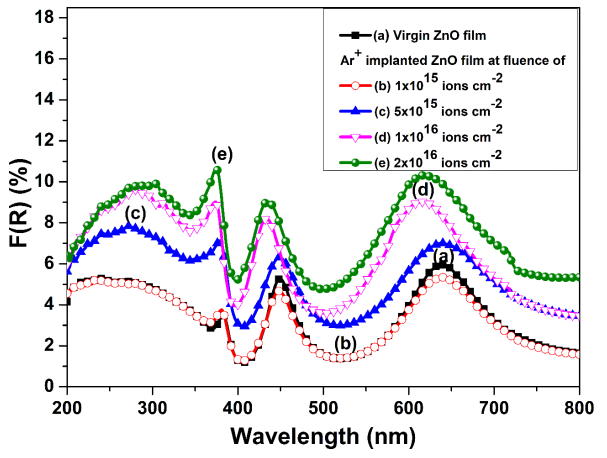

Figure 10: Kubelka–Munk function $F(R)$ related to (a) pristine and Ar$^+$-implanted ZnO films at various fluences, viz. (b) 1 × 10^{15}, (c) 5 × 10^{15}, (d) 1 × 10^{16}, and (e) 2 × 10^{16} ions·cm^{-2}.

$$(\alpha h\nu)^n = C\left(h\nu - E_g\right), \tag{8}$$

where α and $h\nu$ are absorption coefficient and photon energy, respectively, C represents constant, and n elucidates the transition type (n is 2/3 for forbidden direct, 2 for allowed direct, 1/3 for forbidden indirect, and 1/2 for allowed indirect transitions). The above equation has been evaluated regarding all possible n values. It is observed that for the present study, n = 2 holds good. Also, α is proportional to $F(R)$, which modifies Equation 8 to:

$$\left(F(R)\cdot h\nu\right)^2 \propto \left(h\nu - E_g\right). \tag{9}$$

Extrapolation of the linear region of the $(h\nu\cdot F(R))^2$ versus $(h\nu)$ plot to the energy axis is used to find optical bandgap values. Figure 11 depicts the different bandgap values, out of which the highest value of the bandgap values in each plot indicate the fundamental bandgap value, while the other three values represent sub-bandgap absorptions due to defects.

The optical bandgap values decrease after implantation from 3.29 ± 0.05 eV to 2.89 ± 0.04 eV with the rise in ion fluence. This is assigned to the emergence of defect-trapping levels between valence band and conduction band [46]. These trapping levels can be acceptor level or donor levels present at the top of the valence band or at the bottom of the conduction band, respectively. This results in a decrease in the energy separation

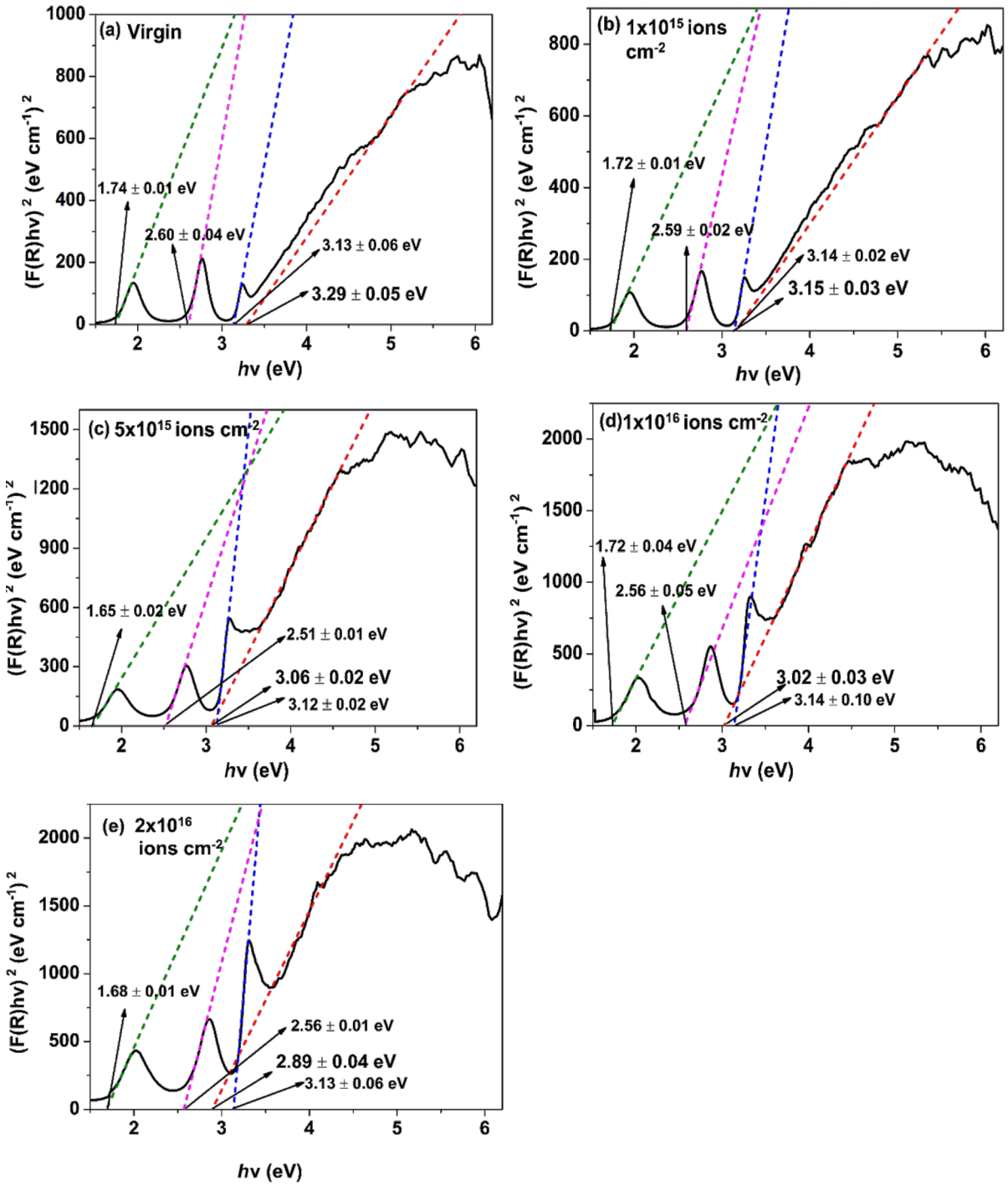

Figure 11: Tauc's plot of (a) pristine and Ar^+-implanted ZnO films at various fluences, viz. (b) 1 × 10^{15}, (c) 5 × 10^{15}, (d) 1 × 10^{16}, and (e) 2 × 10^{16} ions·cm^{-2}.

between the valence band and the conduction band. Also, the sub-bandgap values decrease with increase in ion fluence as shown in Figure 11. Generally, implanted ions lead to the production of point defects, which act as trapping centers and affect the optical absorption [47].

Thus, a progressive decrement in bandgap values with increasing fluence is ascribed to lattice disorder due to argon ion implantation. Moreover, we have observed higher reductions of optical bandgap values than other earlier studies using low-energy ion beams [3,12]. Thus, low-energy argon ion implanta-

tion of ZnO films provides us with an approach to fabricate advanced materials having smoother surfaces, lower particle sizes, lower bandgap, and higher absorption in the UV region. This amplifies the data storage capacity and energy efficiency of ZnO films [13].

The implantation-induced structural disorder is reflected in terms of Urbach energy, which is defined as the band tail energy and can be calculated using the Urbach edge rule. Near the band edges, the absorption coefficient varies exponentially with photon energy [45]:

$$\alpha(\lambda) = \alpha_0 \exp\frac{h\nu}{E_0}. \quad (10)$$

Here, α_0 represents a constant, α is the absorption coefficient, and E_0 stands for the Urbach energy, which is calculated by taking the inverse of the slope of the plot between $\ln(\alpha(\lambda))$ and photon energy ($E = h\nu$). Since α is proportional to $F(R)$, the plot of $\ln(F(R))$ versus E is employed to estimate Urbach energy. The dependence of $\ln(F(R))$ on E for pristine and implanted ZnO films at various fluences is shown in Figure 12.

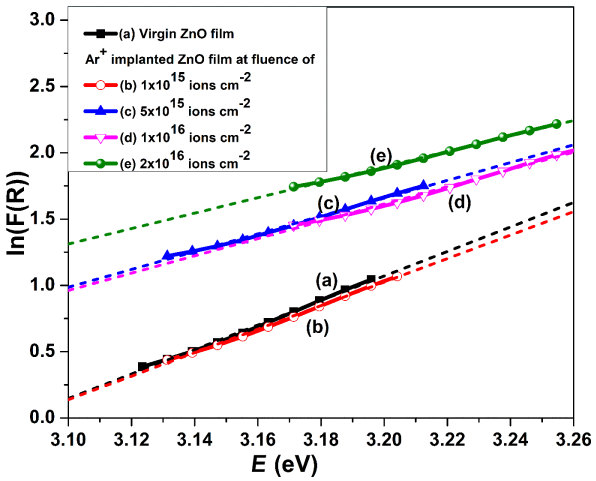

Figure 12: Plot of $\ln(F(R))$ versus E for (a) pristine and Ar^+-implanted ZnO films at various fluences, viz. (b) 1×10^{15}, (c) 5×10^{15}, (d) 1×10^{16}, and (e) 2×10^{16} ions·cm^{-2}.

The value of Urbach energy for pristine and implanted ZnO films at fluences of 1×10^{15}, 5×10^{15}, 1×10^{16}, and 2×10^{16} ions·cm^{-2} rises from 0.10 to 0.17 eV as shown in Figure 13. The increase in Urbach energy and decrease in optical bandgap (Figure 13) with the rise in argon ion fluence can be ascribed to implantation-induced structural disorder, which is coherent with GXRD and Raman analysis.

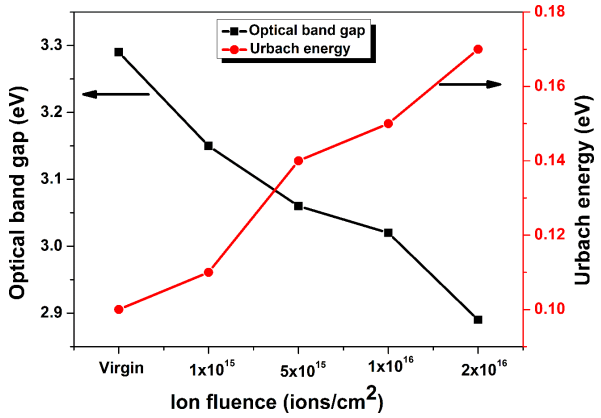

Figure 13: Variation in optical bandgap and Urbach energy values of pristine and 30 keV Ar^+-implanted ZnO films at various fluences.

Correlations

This anomalous behavior of Raman modes can be attributed to the fact that the incorporation of lattice defects and disorder by energetic ions leads to translational symmetry loss. This results in the breaking of the wave vector $k = 0$ selection rule required for Raman scattering from different parts of the Brillouin zone. Thus, scattering occurs from the whole Brillouin zone [48]. This can be correlated with the diminishing of the E_2 (high) mode, enhancement in the disorder band (101–200 cm^{-1}), and broadening of the symmetry-disallowed A_1 (LO) Raman mode at the K–M point of the Brillouin zone at higher fluences. Moreover, AFM studies reveal grain size reduction leading to the enhancement in the density of grain boundaries. This generates an intrinsic electric field, which in turn evolves Raman optical modes [49]. Further, the fall in intensity of the E_2 (high) mode is corroborated with GXRD studies, which revealed a decrease of the (002) peak and an increase in lattice strain along the c axis with increasing argon ion fluence. Besides this, the lattice defects induce distortion in the lattice, which leads to a decrease in the bandgap and an increase in Urbach energy due to the formation of bands that accumulate the defects and an increase in carrier concentration in the form of oxygen vacancies. Therefore, the evolution of different Raman modes and softening of 15 cm^{-1} of the A_1 (LO) mode in implanted ZnO films can be ascribed to the phonon localization due to lattice defects, reduction in grain size, and structural strain.

Conclusion

ZnO films have been investigated before and after Ar^+ implantation to study the effect of ion fluence on various properties of the films. GXRD pattern reveals a decline in crystallinity along the c axis with the rise in ion fluence. Implanted ZnO films show the increase and decrease in intensity of A_1 (LO) and E_2 (high) Raman modes, respectively, with increasing argon ion

fluence. The E_2 (low) mode merges with a disorder-induced broad band at higher fluences. The peaks centered at 577 and 554 cm^{-1} in the deconvoluted spectrum of the A_1 (LO) mode in implanted films are ascribed to oxygen vacancies and zinc interstitials, respectively. The film implanted at the highest fluence exhibits the smoothest surface and lowest grain size, which boosts light absorption and lower reflection. The optical bandgap values of ZnO films declined from 3.29 to 2.89 eV. Thus, we conclude that low-energy ion beams open a wide perspective for controlling the structural and optical characteristics of ZnO films, which makes them potential candidates for integrated optoelectronic devices.

Funding

The authors are thankful to the Department of Science and Technology (DST), New Delhi, for providing financial support to establish Ion Beam Centre at Kurukshetra University. Further, authors acknowledge MHRD, Govt. of India for RUSA-2 funding to Kurukshetra University, Kurukshetra.

Conflict of Interest

The authors have no conflicts of interest.

Author Contributions

Manu Bura: conceptualization; investigation; methodology; visualization; writing – original draft. Divya Gupta: data curation; resources; visualization. Arun Kumar: formal analysis; investigation. Sanjeev Aggarwal: conceptualization; methodology; project administration; supervision; validation; writing – review & editing.

ORCID® iDs

Manu Bura - https://orcid.org/0000-0001-5311-7745
Divya Gupta - https://orcid.org/0000-0002-9879-8553
Sanjeev Aggarwal - https://orcid.org/0000-0002-0054-4679

Data Availability Statement

Data generated and analyzed during this study is available from the corresponding author upon reasonable request.

References

1. Fortunato, E. M. C.; Barquinha, P. M. C.; Pimentel, A. C. M. B. G.; Gonçalves, A. M. F.; Marques, A. J. S.; Martins, R. F. P.; Pereira, L. M. N. *Appl. Phys. Lett.* **2004,** *85,* 2541–2543. doi:10.1063/1.1790587
2. Nomura, K.; Ohta, H.; Takagi, A.; Kamiya, T.; Hirano, M.; Hosono, H. *Nature* **2004,** *432,* 488–492. doi:10.1038/nature03090
3. Hariwal, R. V.; Malik, H. K.; Negi, A.; Asokan, K. *Appl. Surf. Sci. Adv.* **2022,** *7,* 100189. doi:10.1016/j.apsadv.2021.100189
4. Hammad, A. H.; Abdel-wahab, M. S.; Vattamkandathil, S.; Ansari, A. R. *Phys. B (Amsterdam, Neth.)* **2018,** *540,* 1–8. doi:10.1016/j.physb.2018.04.017
5. Jagadish, C.; Pearton, S. *Zinc Oxide Bulk, Thin Films and Nanostructures: Processing, Properties, and Applications;* Elsevier: Oxford, UK, 2011. doi:10.1016/b978-0-08-044722-3.x5000-3
6. Krebs, F. C.; Thomann, Y.; Thomann, R.; Andreasen, J. W. *Nanotechnology* **2008,** *19,* 424013. doi:10.1088/0957-4484/19/42/424013
7. Willander, M.; Nur, O.; Zhao, Q. X.; Yang, L. L.; Lorenz, M.; Cao, B. Q.; Zúñiga Pérez, J.; Czekalla, C.; Zimmermann, G.; Grundmann, M.; Bakin, A.; Behrends, A.; Al-Suleiman, M.; El-Shaer, A.; Che Mofor, A.; Postels, B.; Waag, A.; Boukos, N.; Travlos, A.; Kwack, H. S.; Guinard, J.; Le Si Dang, D. *Nanotechnology* **2009,** *20,* 332001. doi:10.1088/0957-4484/20/33/332001
8. Nastasi, M.; Mayer, J. W.; Wang, Y. *Ion Beam Analysis: Fundamentals and Applications;* CRC Press: Boca Raton, FL, USA, 2014. doi:10.1201/b17310
9. Krishna, R.; Agarwal, D. C.; Avasthi, D. K. *Radiat. Eff. Defects Solids* **2021,** *176,* 145–166. doi:10.1080/10420150.2021.1891065
10. Kumar, V.; Prakash, J.; Pathak, D.; Sharma, D. P.; Purohit, L. P.; Swart, H. C. *Chem. Eng. J. Adv.* **2023,** *15,* 100501. doi:10.1016/j.ceja.2023.100501
11. Balkanski, M.; Morhange, J. F.; Kanellis, G. *J. Raman Spectrosc.* **1981,** *10,* 240–245. doi:10.1002/jrs.1250100148
12. Singh, F.; Singh, R. G.; Kumar, V.; Khan, S. A.; Pivin, J. C. *J. Appl. Phys.* **2011,** *110,* 083520. doi:10.1063/1.3651638
13. Ying, M.; Saeedi, A. M. A.; Yuan, M.; Zhang, X.; Liao, B.; Zhang, X.; Mei, Z.; Du, X.; Heald, S. M.; Fox, A. M.; Gehring, G. A. *J. Mater. Chem. C* **2019,** *7,* 1138–1145. doi:10.1039/c8tc05929b
14. Gupta, H.; Joshi, K.; Gautam, S. K.; Singh, R. G.; Singh, F. *Vacuum* **2020,** *181,* 109598. doi:10.1016/j.vacuum.2020.109598
15. Gautam, N.; Gupta, H.; Kapoor, A.; Singh, F. *Phys. B (Amsterdam, Neth.)* **2019,** *570,* 13–18. doi:10.1016/j.physb.2019.05.043
16. Zhiguang, W.; Hang, Z.; Kongfang, W.; Jianrong, S.; Cunfeng, Y.; Tielong, S.; Yizhun, M.; Lilong, P.; Yabin, Z. *Nucl. Instrum. Methods Phys. Res., Sect. B* **2011,** *269,* 837–841. doi:10.1016/j.nimb.2010.12.084
17. Kennedy, J.; Sundrakannan, B.; Katiyar, R. S.; Markwitz, A.; Li, Z.; Gao, W. *Curr. Appl. Phys.* **2008,** *8,* 291–294. doi:10.1016/j.cap.2007.10.018
18. Decremps, F.; Pellicer-Porres, J.; Saitta, A. M.; Chervin, J.-C.; Polian, A. *Phys. Rev. B* **2002,** *65,* 092101. doi:10.1103/physrevb.65.092101
19. Ziegler, J. F.; Ziegler, M. D.; Biersack, J. P. *Nucl. Instrum. Methods Phys. Res., Sect. B* **2010,** *268,* 1818–1823. doi:10.1016/j.nimb.2010.02.091
20. Bui, Q. C.; Salem, B.; Roussel, H.; Mescot, X.; Guerfi, Y.; Jiménez, C.; Consonni, V.; Ardila, G. *J. Alloys Compd.* **2021,** *870,* 159512. doi:10.1016/j.jallcom.2021.159512
21. Mondal, P. *Opt. Mater. (Amsterdam, Neth.)* **2019,** *98,* 109476. doi:10.1016/j.optmat.2019.109476
22. Lim, W. C.; Singh, J. P.; Kim, Y.; Song, J.; Chae, K. H.; Seong, T.-Y. *Vacuum* **2021,** *183,* 109776. doi:10.1016/j.vacuum.2020.109776
23. Cullity, B. D. *Elements of X-Ray Diffraction;* Addison-Wesley Publishing: Reading, MA, USA, 1956.
24. Popović, M.; Novaković, M.; Mitrić, M.; Zhang, K.; Bibić, N. *Int. J. Refract. Met. Hard Mater.* **2015,** *48,* 318–323. doi:10.1016/j.ijrmhm.2014.09.026
25. Bergman, L.; Alexson, D.; Murphy, P. L.; Nemanich, R. J.; Dutta, M.; Stroscio, M. A.; Balkas, C.; Shin, H.; Davis, R. F. *Phys. Rev. B* **1999,** *59,* 12977–12982. doi:10.1103/physrevb.59.12977

26. Kumar, V.; Singh, F.; Ntwaeaborwa, O. M.; Swart, H. C. *Appl. Surf. Sci.* **2013,** *279,* 472–478. doi:10.1016/j.apsusc.2013.04.145
27. Locker, D. R.; Meese, J. M. *IEEE Trans. Nucl. Sci.* **1972,** *19,* 237–242. doi:10.1109/tns.1972.4326839
28. Manjón, F. J.; Mari, B.; Serrano, J.; Romero, A. H. *J. Appl. Phys.* **2005,** *97,* 053516. doi:10.1063/1.1856222
29. Mondal, A.; Pal, S.; Sarkar, A.; Bhattacharya, T. S.; Das, A.; Gogurla, N.; Ray, S. K.; Kumar, P.; Kanjilal, D.; Devi, K. D.; Singha, A.; Chattopadhyay, S.; Jana, D. *Mater. Sci. Semicond. Process.* **2018,** *80,* 111–117. doi:10.1016/j.mssp.2018.02.026
30. Li, C.; Lv, J.; Yao, S.; Hu, J.; Liang, Z. *Nucl. Instrum. Methods Phys. Res., Sect. B* **2013,** *295,* 11–15. doi:10.1016/j.nimb.2012.10.010
31. Kahng, B.; Jeong, H.; Barabási, A.-L. *Appl. Phys. Lett.* **2001,** *78,* 805–807. doi:10.1063/1.1343468
32. Facsko, S.; Dekorsy, T.; Koerdt, C.; Trappe, C.; Kurz, H.; Vogt, A.; Hartnagel, H. L. *Science* **1999,** *285,* 1551–1553. doi:10.1126/science.285.5433.1551
33. Paramanik, D.; Majumder, S.; Sahoo, S. R.; Varma, S. *Def. Sci. J.* **2009,** *59,* 413–426. doi:10.14429/dsj.59.1541
34. Krishna, R.; Baranwal, V.; Katharria, Y. S.; Kabiraj, D.; Tripathi, A.; Singh, F.; Khan, S. A.; Pandey, A. C.; Kanjilal, D. *Nucl. Instrum. Methods Phys. Res., Sect. B* **2006,** *244,* 78–80. doi:10.1016/j.nimb.2005.11.015
35. Xu, M.; Teichert, C. *J. Appl. Phys.* **2004,** *96,* 2244–2248. doi:10.1063/1.1771476
36. Schneider, C. A.; Rasband, W. S.; Eliceiri, K. W. *Nat. Methods* **2012,** *9,* 671–675. doi:10.1038/nmeth.2089
37. Sreedharan, R. S.; Ganesan, V.; Sudarsanakumar, C. P.; Bhavsar, K.; Prabhu, R.; Mahadevan Pillai, V. P. P. *Nano Rev.* **2015,** *6,* 26759. doi:10.3402/nano.v6.26759
38. Hu, Y.-H.; Chen, Y.-C.; Xu, H.-J.; Gao, H.; Jiang, W.-H.; Hu, F.; Wang, Y.-X. *Engineering (Irvine, CA, U. S.)* **2010,** *2,* 973–978. doi:10.4236/eng.2010.212124
39. Köferstein, R.; Jäger, L.; Ebbinghaus, S. G. *Solid State Ionics* **2013,** *249–250,* 1–5. doi:10.1016/j.ssi.2013.07.001
40. Kara, K.; Şenadim Tüzemen, E.; Esen, R. *Turk. J. Phys.* **2014,** *38,* 238–244. doi:10.3906/fiz-1310-3
41. Gesesse, G. D.; Gomis-Berenguer, A.; Barthe, M.-F.; Ania, C. O. *J. Photochem. Photobiol., A* **2020,** *398,* 112622. doi:10.1016/j.jphotochem.2020.112622
42. Lin, B.; Fu, Z.; Jia, Y. *Appl. Phys. Lett.* **2001,** *79,* 943–945. doi:10.1063/1.1394173
43. Allabergenov, B.; Shaislamov, U.; Shim, H.; Lee, M.-J.; Matnazarov, A.; Choi, B. *Opt. Mater. Express* **2017,** *7,* 494–502. doi:10.1364/ome.7.000494
44. Jamil, H.; Dildar, I. M.; Ilyas, U.; Hashmi, J. Z.; Shaukat, S.; Sarwar, M. N.; Khaleeq-ur-Rahman, M. *Thin Solid Films* **2021,** *732,* 138796. doi:10.1016/j.tsf.2021.138796
45. Tauc, J. Optical Properties of Amorphous Semiconductors. *Amorphous and liquid semiconductors;* Springer: Boston, MA, USA, 1974; pp 159–220. doi:10.1007/978-1-4615-8705-7_4
46. Priyadarshini, P.; Das, S.; Alagarasan, D.; Ganesan, R.; Varadharajaperumal, S.; Sahoo, S.; Naik, R. *RSC Adv.* **2022,** *12,* 5012–5026. doi:10.1039/d2ra00097k
47. Chandramohan, S.; Kanjilal, A.; Sarangi, S. N.; Majumder, S.; Sathyamoorthy, R.; Som, T. *J. Appl. Phys.* **2009,** *106,* 063506. doi:10.1063/1.3224867
48. Manjón, F. J.; Syassen, K.; Lauck, R. *High Pressure Res.* **2002,** *22,* 299–304. doi:10.1080/08957950212798
49. Millot, M.; Tena-Zaera, R.; Munoz-Sanjose, V.; Broto, J.-M.; Gonzalez, J. *Appl. Phys. Lett.* **2010,** *96,* 152103. doi:10.1063/1.3387843

License and Terms

BEILSTEIN JOURNAL OF NANOTECHNOLOGY

Characterization of ion track-etched conical nanopores in thermal and PECVD SiO_2 using small angle X-ray scattering

Shankar Dutt*[1], Rudradeep Chakraborty[1], Christian Notthoff[1], Pablo Mota-Santiago[2], Christina Trautmann[3,4] and Patrick Kluth[1]

Full Research Paper

Open Access

Address:
[1]Department of Materials Physics, Research School of Physics, The Australian National University, Canberra ACT 2601, Australia, [2]ANSTO-Australian Synchrotron, Clayton VIC 3168, Australia, [3]GSI Helmholtzzentrum für Schwerionenforschung, Planckstr. 1, 64291 Darmstadt, Germany and [4]Technische Universtät Darmstadt, 64289 Darmtadt, Germany

Email:
Shankar Dutt* - shankar.dutt@anu.edu.au

* Corresponding author

Keywords:
etched ion tracks; SiO_2; small angle X-ray scattering (SAXS); swift heavy ion irradiation; track-etched nanopores

Beilstein J. Nanotechnol. **2025,** *16,* 899–909.
https://doi.org/10.3762/bjnano.16.68

Received: 19 February 2025
Accepted: 22 May 2025
Published: 12 June 2025

This article is part of the thematic issue "Energetic ions and photons for engineering nanomaterials".

Guest Editor: V. R. Soma

Abstract

Conical nanopores in amorphous SiO_2 thin films fabricated using the ion track etching technique show promising potential for filtration, sensing, and nanofluidic applications. The characterization of the pore morphology and size distribution, along with its dependence on the material properties and fabrication parameters, is crucial to designing nanopore systems for specific applications. Here, we present a comprehensive study of track-etched nanopores in thermal and plasma-enhanced chemical vapor-deposited (PECVD) SiO_2 using synchrotron-based small-angle X-ray scattering (SAXS). The nanopores were fabricated by irradiating the samples with 89 MeV, 185 MeV, and 1.6 GeV Au ions, followed by hydrofluoric acid etching. We present a new approach for analyzing the complex highly anisotropic two-dimensional SAXS patterns of the pores by reducing the analysis to two orthogonal one-dimensional slices of the data. The simultaneous fit of the data enables an accurate determination of the pore geometry and size distribution. The analysis reveals substantial differences between the nanopores in thermal and PECVD SiO_2. The track-to-bulk etching rate ratio is significantly different for the two materials, producing nanopores with cone angles that differ by almost a factor of two. Furthermore, thermal SiO_2 exhibits an exceptionally narrow size distribution of only 2–4%, while PECVD SiO_2 shows a higher variation ranging from 8% to 18%. The impact of different ion energies on the size of the nanopores was also investigated for pores in PECVD SiO_2 and shows only negligible influence. These findings provide crucial insights for the controlled fabrication of conical nanopores in different materials, which is essential for optimizing membrane performance in applications that require precise pore geometry.

Introduction

Solid-state nanopores have attracted significant attention in the past decade because of their broad applicability in a variety of areas including biosensing, micro/ultrafiltration, desalination, ion and molecular separation, dialysis, battery technologies, blue energy generation, and nanofluidics [1-33]. Conical nanopores are of particular interest because of the asymmetric ion transport resulting from their unique geometry [30,34-38].

Conical nanopores can be reproducibly fabricated at scale using the track-etch technology in a number of different materials [29,39]. This method involves irradiating the material with swift heavy ions to create long and narrow damaged regions along the paths of the ions known as "ion tracks". These ion tracks are more susceptible to chemical etching compared to the undamaged material, which can be exploited for the fabrication of nanopores with narrow size distribution [13,29,40]. The geometry of the resulting nanopores is determined by several factors, including the substrate material, the type and concentration of the etchant, the density of the material, and the type and energy of the ions used [13,29,40].

Track-etch technology has been used for the commercial fabrication of cylindrical nanopores in polymers for filtration applications [41-46]. Only recently we have adapted this technology to generate conical nanopores in silicon dioxide [29,30,40]. Amorphous silicon dioxide (SiO_2) has excellent chemical stability, well-understood surface chemistry, and compatibility with semiconductor processing, opening up new applications for track-etched nanopores in this material [30].

In this study, we report the characterization of track-etched nanopores in two types of silicon dioxide, namely, one produced by wet thermal oxidation of Si (thermal SiO_2) and another deposited by plasma-enhanced chemical vapor deposition (PECVD). Thermally grown SiO_2 is of high quality and stoichiometric, however, requires high temperatures for growth, and can only be grown on a Si substrate. PECVD, in contrast, allows for the deposition at much lower temperatures on many different substrates with control over the film properties, such as stoichiometry, density, refractive index, and residual stress. As these fabrication methods involve fundamentally different growth mechanisms, the resulting layers have different properties [47,48] and it can be expected that the track-etched nanopores also show different characteristics, including the track etching process itself. Understanding how the different fabrication methods influence the characteristics of ion track-etched nanopores is crucial to optimize their fabrication for specific applications. Here we focus on characterizing size, geometry, and size distribution of track-etched nanopores in thermal and PECVD SiO_2 as these parameters are critical for membrane performance in specific applications, including selectivity, throughput, and molecular capture.

Small-angle X-ray scattering (SAXS) has proven to be an invaluable tool for characterizing nanopore membranes, offering nondestructive analytical capabilities that yield statistical information of more than 10^6 pores [6,13,29,40]. With a beam size at the Australian Synchrotron of 250 μm × 23 μm, we measure ≈5.8×10^5 and ≈2.9×10^6 nanopores for samples irradiated with fluences of 1×10^8 and 5×10^8 ions/cm^2, respectively. Our previous work demonstrated the effectiveness of SAXS for studying conical nanopores in SiO_2, providing unprecedented precision in determining the pore morphologies [29,40]. The method involved fitting two-dimensional (2D) scattering patterns to a conical pore model utilizing a series of images with different tilts of the sample with respect to the incident X-ray beam, corresponding to the alignment of the parallel pores with the beam. Although highly accurate, this approach has two limitations, that is, the computational resources required for numerical calculation of intensity values for each pixel in the 2D fit and the challenge of incorporating size distribution analysis due to the computational complexity of applying distribution functions in a 2D fitting scenario. To address these limitations, we have developed a new approach that maintains the high precision of SAXS analysis while significantly reducing computational requirements and enabling the investigation of size distributions. This method involves analyzing and fitting one-dimensional (1D) sections of the SAXS patterns employing different form factors rather than performing 2D image fitting.

We implemented our new fitting method to investigate conical nanopores in the two different SiO_2 membrane materials. For nanopores in thermal SiO_2 we confirm that these results are consistent with our previous studies that employ 2D fitting and quantify the size distribution. Track-etched nanopores in PECVD-SiO_2 have not been studied before and revealed striking differences in the geometrical parameters due to a different track-to-bulk etching rate ratio and a wider size distribution.

Results and Discussions

Figure 1 shows plan-view scanning electron microscopy (SEM) images of nanopores fabricated in thermal (Figure 1a) and PECVD (Figure 1b) SiO_2 by etching ion tracks produced with 1.6 GeV Au ion irradiation (see Experimental and Theory section for details). Although both materials reveal conical nanopores, thermal SiO_2 exhibits more uniformly sized nanopores, while PECVD SiO_2 displays higher dispersity in pore dimensions (excluding overlapping pores). As an example,

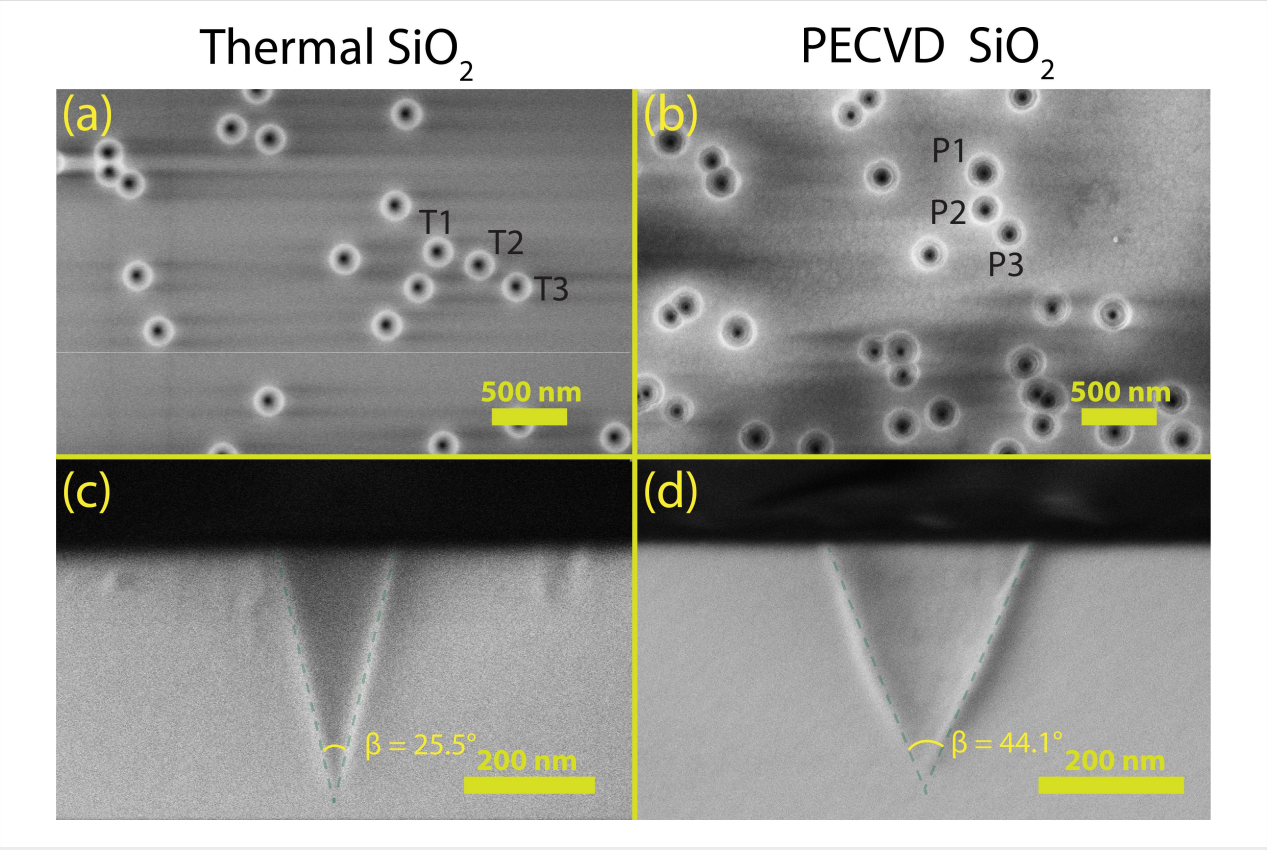

Figure 1: Plan-view (a, b) and cross-sectional (c, d) scanning electron microscopy images of nanopores in thermal (a, c) and PECVD (b, d) SiO_2. The thermal and PECVD SiO_2 thin films were irradiated with 1.6 GeV Au ions and subsequently etched in 3% HF for 8.5 min and 6 min respectively. The irradiation fluence was 5×10^8 ions/cm^2. The fluence was verified by counting nanopores in multiple SEM images, closely matching the expected values. The top-view images (a, b) highlight the circular pore openings, while the cross-sectional views (c, d) reveal conical pore geometry. The cone-angle (β) of the conical pores in thermal SiO_2 (c) is approximately 1.8 times less than that in PECVD SiO_2 (d).

three representative non-overlapping pores are highlighted in Figure 1a,b. Their average radius at the sample surface (T1, T2, and T3) are measured to be 100.3 ± 1.3, 103.2 ± 1.6, and 102.4 ± 2.6 nm, respectively, in thermal SiO_2. In contrast, the representative pores (P1, P2, and P3) in PECVD SiO_2 measure 127.2 ± 2.7, 112.3 ± 2.4, and 114.7 ± 1.6 nm, respectively. The uncertainty values result from challenges in precisely defining nanopore boundaries due to charging effects during SEM imaging (see Figure 1). To address this, four cross-sectional measurements were taken across each pore and averaged. The standard deviation of these measurements provides the reported uncertainty values. Although only three pores are shown, they illustrate the larger size variation in PECVD SiO_2 compared to the uniform pore size in thermal SiO_2. From SEM measurements, the standard deviation in the pore radius was measured to be ≈1.8 nm for thermal SiO_2 but ≈8 nm for PECVD SiO_2. The reader must note that, unless otherwise noted, the nanopore radius or size mentioned throughout this work refers specifically to the radius of the cone base. To overcome the limited sampling of pores in SEM imaging, we complemented the microscopy analysis with small-angle X-ray scattering, which provides statistically robust measurements, averaging over more than 10^7 pores during an experiment.

Cross-sectional SEM images (Figure 1c,d) reveal distinct differences in nanopore geometry between thermal and PECVD SiO_2. The full cone angle (β) in PECVD SiO_2 (≈44°) is approximately 1.8 times larger than in thermal SiO_2 (≈26°). As described in our track etching model [13], the cone angle depends only on the ratio of the track-etch rate to the bulk-etch rate. Hence, the different angles indicate different etch-rate ratios for PECVD and thermal SiO_2. This discrepancy is not unexpected because PECVD-deposited films typically differ in morphology, density, and stoichiometry compared to thermally grown SiO_2. The electronic energy loss (S_e) in the thermal and PECVD SiO_2 layers was calculated using the SRIM2008 code [49]. The average S_e values for thermal SiO_2 for 1.6 GeV, 185 MeV, and 89 MeV Au irradiation are 21.1, 16.6, and 12.1 keV/nm respectively, remaining almost constant throughout the film ($\Delta S_e \leq 0.5\%$). Similarly, the average S_e values for PECVD SiO_2 for 1.6 GeV, 185 MeV, and 89 MeV Au irradiation are 20.6, 16.3, and 11.8 keV/nm respectively, also with minimal varia-

tion across the film ($\Delta S_e \leq 0.5\%$). The calculations for PECVD SiO_2 thin films used values for the density and composition from our previous study [47]. In both layers, the projected ranges when irradiated with 185 and 89 MeV Au ions were ≈20 µm and ≈14 µm, respectively, whereas the projected ranges for thermal and PECVD SiO_2 irradiated with 1.6 GeV were calculated to be ≈87 µm and ≈9 µm, respectively. Given that both the projected ranges and stopping powers are comparable for thermal and PECVD SiO_2 layers, these parameters do not account for the observed differences in the shape of the fabricated nanopores.

To quantify the bulk etch rates, we measured the thickness etched from each film after etching in 3% HF for different defined time intervals. The thickness difference before and after etching was measured using ellipsometry, which revealed that thermal SiO_2 is etched at 15.6 ± 0.6 nm/min, while PECVD SiO_2 is etched at 34.3 ± 1.2 nm/min. Since the cone shape depends only on the ratio of track to bulk etch rate, the significantly different cone angles cannot be explained solely by the variation in bulk etch rates. Therefore, the track etch rate must also differ between the two types of SiO_2. Using our track etching model [13] and the measured pore radii, we estimate track etch rates of 69 ± 3 nm/min for thermal and 90 ± 6 nm/min for PECVD SiO_2, respectively.

While the scanning electron microscopy images reveal the variation in nanopore size for PECVD SiO_2 compared to thermal SiO_2, as well as differences in nanopore morphology, these images do not provide robust statistical information and are prone to measurement errors. Cross-sectional SEM imaging provides limited statistical reliability as the probability of cleaving directly through a nanopore's central axis is extremely low. This sampling bias introduces significant uncertainties in dimensional measurements and makes it challenging to obtain robust structural information about the nanopores. Figure 2 shows a representative 2D scattering pattern obtained from conical nanopores in thermal SiO_2. This image represents the simultaneous measurement of approximately 10^7 parallel nanopores, tilted by ≈20° with respect to the X-ray beam. Although fitting the entire image can give precise information on the nanopore size and cone angle, fitting the size distribution is computationally too expensive [29]. Our new approach of fitting the scattering intensities uses two orthogonal 1D cuts of the scattering image (Figure 2). This analysis preserves the high precision of SAXS analysis while substantially reducing computational demands and enabling investigation of the size distributions. Figure 2 highlights the regions selected for horizontal and vertical cuts. The resulting scattering intensity profiles (vertical cut: orange and horizontal cut: blue) from these cuts are shown on the right-hand side of Figure 2. The intensity values obtained at different tilt angles were fitted as described below.

Figure 3 presents 2D scattering images for thermal (Figure 3a) and PECVD (Figure 3b) SiO_2. As indicated by the yellow arrows in Figure 3a, clear secondary scattering features can be observed in thermal SiO_2, indicative for a low dispersity in nanopore dimensions. In contrast, these features are absent in PECVD SiO_2. We ascribe this effect to the variation in

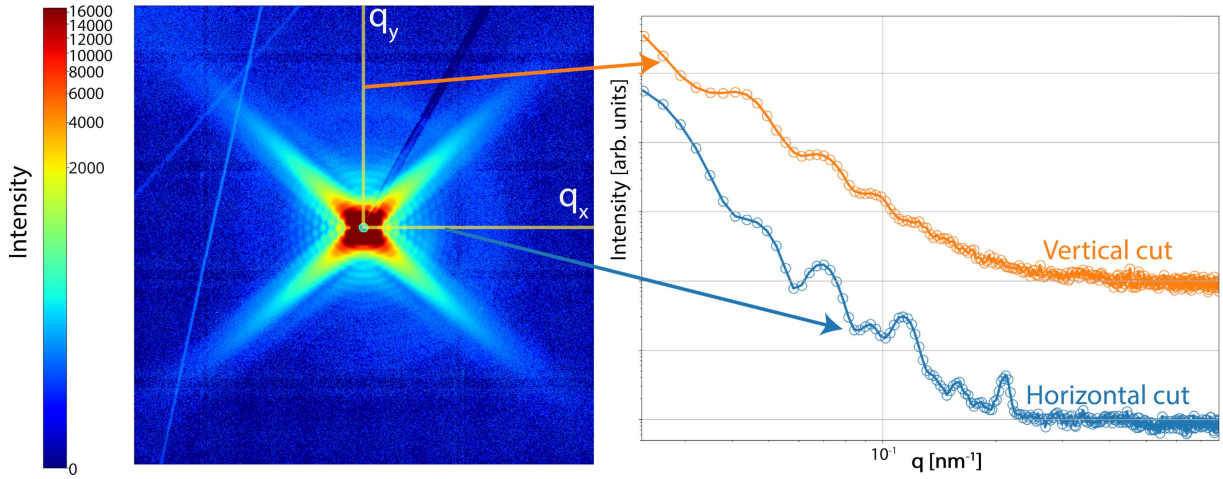

Figure 2: Representative two-dimensional scattering pattern (left) from conical nanopores in thermal SiO_2 illustrating the regions used for horizontal (blue) and vertical (orange) cuts. The sample was irradiated with 1.6 GeV Au ions and etched for 15 mins in 3% HF. Measurements were performed with a tilt angle of the surface normal of ≈20° with respect to the X-ray beam. The corresponding one-dimensional intensity profiles (right) are shown as a function of the magnitude of the scattering vector $\vec{q}$.

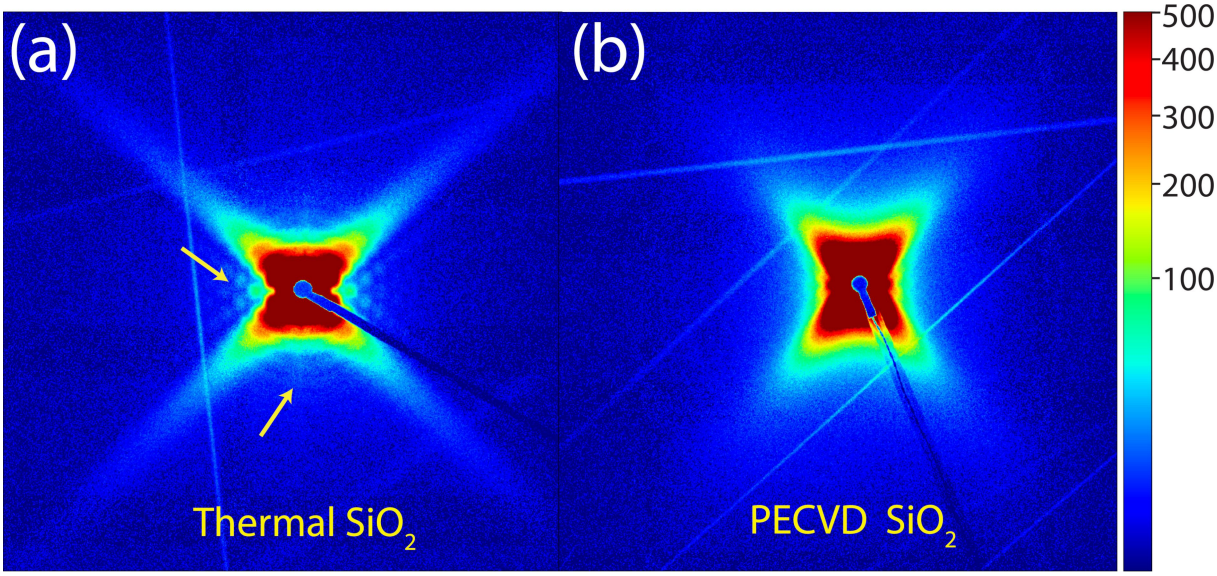

Figure 3: Two-dimensional small-angle X-ray scattering (SAXS) patterns of conical nanopores in thermal (a) and PECVD (b) SiO_2 produced from irradiation of thin film samples with 1.6 GeV Au ions and etching with 3% HF, shown using the same intensity-contrast scale. The arrows in (a) highlight secondary scattering features that are more pronounced in thermal SiO_2 than in the PECVD sample, consistent with a higher polydispersity of pore sizes in the latter.

nanopore size, as each pore generates a slightly different scattering intensity, effectively smearing out the secondary features. Furthermore, the absence of secondary features makes it difficult to fit the SAXS data using our 2D fitting model [29].

The scattering intensities from vertical and horizontal cuts of 2D SAXS images were analyzed for both PECVD and thermal SiO_2 samples using the methodology detailed in the Experimental and Theory section. Figure 4 presents the experimental data and the corresponding model fits, where Figure 4a,b represents data from nanopores in thermal SiO_2 and Figure 4c,d shows data from nanopores in PECVD SiO_2. Horizontal cuts are shown in Figure 4a,c, while vertical cuts at various tilt angles are shown in Figure 4b,d. The fitting models demonstrate excellent agreement with the experimental data across all scattering curves. Both samples were irradiated with 1.6 GeV Au ions and subsequently etched in 3% HF. For comparative analysis, we selected samples with similar nanopore radii: Thermal SiO_2 (etched for 12 min) yielded pores of average radius 141.3 nm, while PECVD SiO_2 (etched for 7 min) produced pores of average radius 154.2 nm. The PECVD samples exhibited nanopores of high quality, with a size distribution of ≈8.3%. While this size distribution is narrow compared to many nanopore systems [50], thermal SiO_2 nanopores show an even narrower size distribution of only ≈2.1%. The higher dispersity observed in PECVD-based nanopores could be the result of defects or localized variations in material properties. While thermal SiO_2 typically exhibits high homogeneity in local material properties, factors such as the etching process and the ion irradiation energy straggling may introduce an effective narrow size distribution of pores. Although we apply a Schulz–Zimm distribution to model the nanopore radius, as described in the Experimental and Theory section, this distribution strongly correlates with variations in the cone angle. We can thus ascribe the polydispersity directly to the variation of the cone angles as well. The influence of size distribution on the scattering patterns is evident upon detailed examination. The horizontal cut intensities from thermal SiO_2 nanopores reveal six to eight distinct oscillations, whereas PECVD SiO_2 displays a maximum of four oscillations. Furthermore, the reduced peak-to-trough amplitude in oscillations resulting from nanopores in PECVD SiO_2 corroborates the broader size distribution obtained from our fitting analysis. The reduced number of oscillations in PECVD SiO_2 1D scattering intensity corresponds to the absence of secondary scattering features in the 2D scattering image as described above.

Figure 5 presents the evolution of half cone angle (Figure 5a), percentage polydispersity (Figure 5b), and nanopore radius (Figure 5c) as a function of etching time for nanopores in PECVD and thermal SiO_2 irradiated with Au ions at different energies. The analysis reveals distinct differences between the two types of SiO_2. Nanopores in PECVD SiO_2 exhibit on an average ≈1.8 times larger cone angles compared to the pores in thermal SiO_2. Moreover, the size distribution of nanopores, quantified by the polydispersity values (Figure 5b), are higher

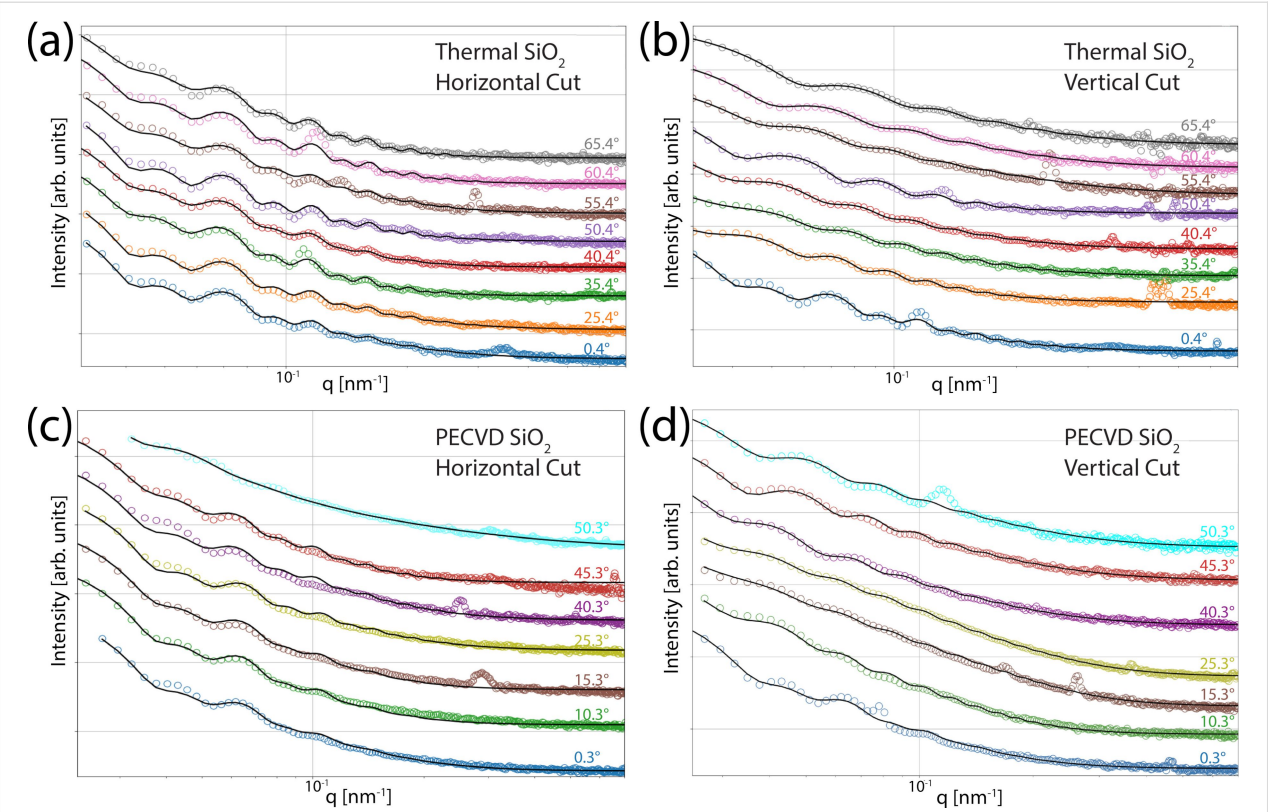

Figure 4: One-dimensional SAXS profiles of ion-irradiated thermal (a, b) and PECVD (c, d) SiO_2, extracted along the horizontal (a, c) and vertical (b, d) directions. Each pattern corresponds to a different tilt angle (labels in degrees), offset vertically for clarity. The solid lines denote model fits based on conical and core-transition models.

(≈8–18%) in PECVD SiO_2 compared to (≈2–4%) in thermal SiO_2. We note that compared to many other systems, the pore size homogeneity in thermal SiO_2 is exceptional. In PECVD SiO_2 samples, nanopores fabricated using 185 MeV Au ion irradiation show slightly larger cone angles compared to those created with 89 MeV and 1.6 GeV Au ions. This variation may result from sample-to-sample difference that can arise from the PECVD deposition processes, as the samples originated from different deposition runs. The 185 MeV-fabricated nanopores also exhibited the highest polydispersity, underscoring the variability in PECVD film characteristics. The validity of our analysis is supported by multiple cross-validation measures. The cone angle values derived from 1D fits for thermal SiO_2 not only agree well with those obtained from the established 2D fitting model [29] but also correspond well with the cross-sectional SEM images. Furthermore, polydispersity values determined by SAXS correlate strongly with the estimates from scanning electron microscopy analysis. It is important to emphasize that SAXS analysis provides a statistically robust characterization of polydispersity, radius, and cone angle values by sampling over 10^6 nanopores – a population size unattainable through microscopy analysis. A linear fit of the nanopore radius versus etching time yielded radial etching rates of 21.1 ± 0.8, 21.1 ± 0.2, and 22.1 ± 0.2 nm/min for PECVD SiO_2 nanopores fabricated using 1.6 GeV, 185 MeV, and 89 MeV Au ions, respectively. In contrast, thermal SiO_2 exhibited a lower radial etching rate of 11.9 ± 0.1 nm/min. Using these values in conjunction with our track etching model [13], we calculated track etching rates of 85 ± 10, 87 ± 5, and 91 ± 6 nm/min for the respective PECVD samples, while thermal SiO_2 showed a track etching rate of 68 ± 4 nm/min. These track etching rates agrees well with the values calculated using radii from SEM images and employing our track etching model.

Conclusion

In this study, we performed a comparative analysis of conical nanopores fabricated in thermal and PECVD SiO_2 using ion track etching employing SEM and SAXS. Our findings reveal substantial differences in the track etching rate and the bulk etching rate between these materials, which in turn affect the nanopore geometry. Nanopores in PECVD SiO_2 exhibit cone angles approximately 1.8 times larger than those in thermally grown SiO_2 – a variation attributable to differences in material density, composition, and stoichiometry between the two oxide types. Furthermore, thermal SiO_2 demonstrates remarkable homogeneity (polydispersity ≈2–4%) compared to PECVD

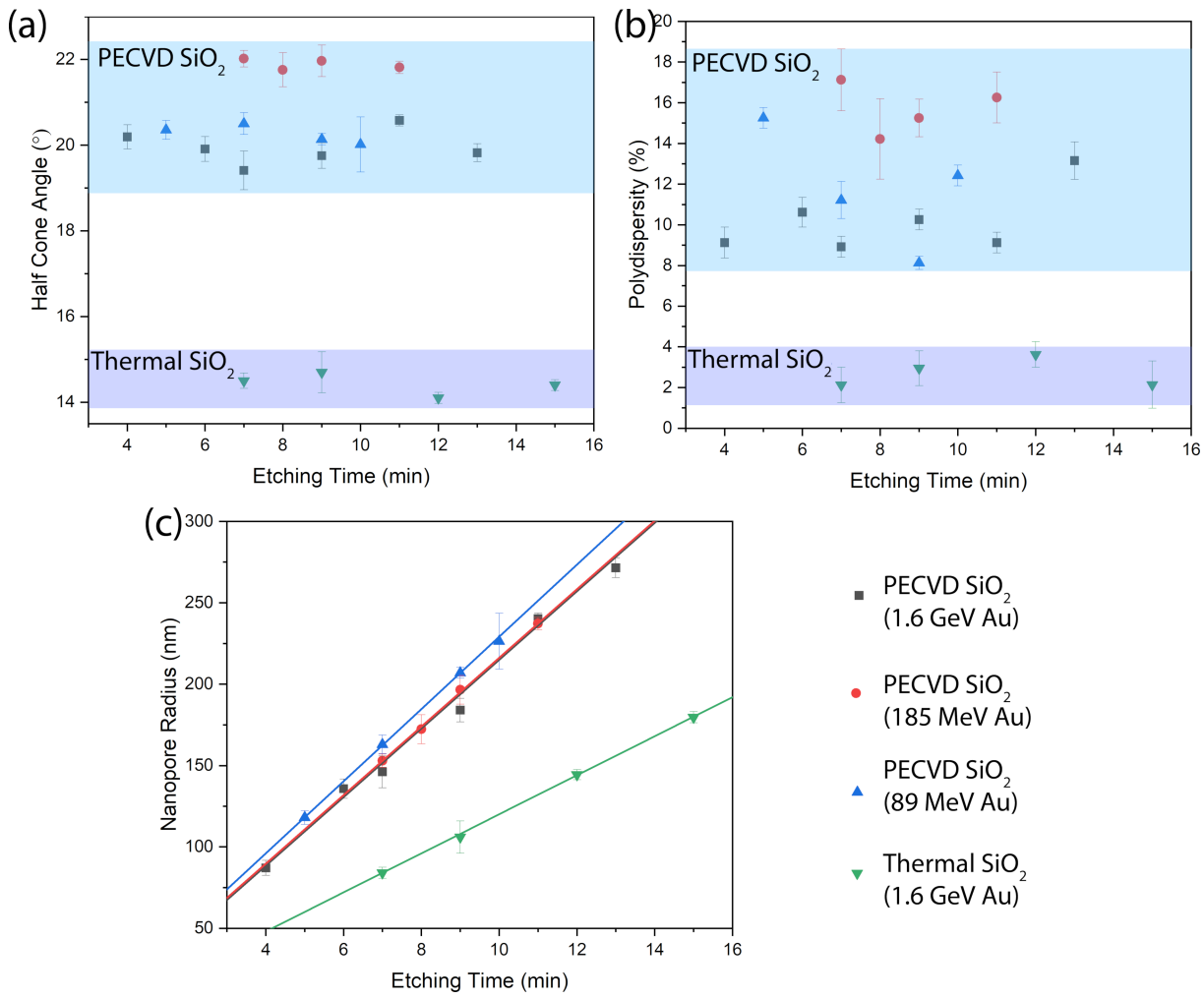

Figure 5: Half cone angle (a), percentage polydispersity (b), and nanopore radius (c) as functions of etching time for conical nanopores in thermal and PECVD SiO_2, irradiated with Au ions at different energies. The shaded regions in (a) and (b) highlight approximate parameter ranges for thermal versus PECVD SiO_2. In (c), solid lines represent linear fits to the data.

SiO_2 (polydispersity ≈8–18%). Although PECVD SiO_2 nanopores show broader size distributions, these values still represent a significant improvement over existing nanoporous systems reported in the literature [50] as the pore distributions can exceed 50% in existing systems. The use of different SiO_2 compositions allows for tuning of the pore geometry, which can have a significant influence on performance in different applications [35,51-53].

The new analytical methodology developed and employed in this study marks a pronounced advancement in conical nanopore characterization. This approach enables reliable assessment of size distributions while maintaining high precision in the determination of nanopore shape, thereby facilitating a detailed investigation of the relationships between fabrication conditions and resultant pore characteristics. The ability to quantify the size distribution with high accuracy is particularly valuable, as size uniformity often plays a crucial role in the performance of nanopore-based applications.

Experimental and Theory

Nanopore formation in thermal and PECVD SiO_2

We utilized two types of amorphous silicon dioxide samples. The first type consisted of 1 µm thick thermally grown SiO_2 on ⟨100⟩ Si substrates (300 µm thickness), obtained commercially from WaferPro Ltd, USA. The second type comprised PECVD-deposited SiO_2 films (≈1.1 µm thick) grown on a 300 µm thick, polished ⟨100⟩ Si substrates using an Oxford Plasmalab 100 PECVD system. PECVD deposition was performed at 650 °C with gas flow rates of 16 sccm SiH_4, 980 sccm N_2, and 14 sccm

NH_3. Ellipsometry measurements employing a Tauc–Lorentz model revealed a deposition rate of ≈36.6 nm/min.

Both sample types were irradiated with Au ions of 1.6 GeV at the UNILAC accelerator (GSI Helmholtzzentrum für Schwerionenforschung GmbH, Germany). Additionally, the PECVD SiO_2 samples were irradiated with 89 and 185 MeV Au ions at the 14UD accelerator (Heavy Ion Accelerator Facility, Australian National University). The irradiation fluences ranged from 1×10^8 to 5×10^8 ions·cm^{-2}, ensuring minimal overlap between ion tracks and resulting nanopores [13,54,55].

To convert the ion tracks into nanopores, the samples were etched at room temperature in 3% hydrofluoric acid for varying durations. The etching process was stopped by removing samples from the etchant followed by three successive rinses in de-ionized water, each lasting 30 s, after which the samples were air dried. The scanning electron microscopy images of the nanopores were obtained using a FEI Verios 460 microscope. For cross-sectional images, the samples were cleaved and imaged vertically.

Small angle X-ray scattering

Transmission small angle X-ray scattering (SAXS) measurements were conducted at the SAXS/WAXS beamline at the Australian Synchrotron, Melbourne, with a photon energy of 12 keV. The samples were measured as is, and the Si substrate was not removed before SAXS measurements. The sample-to-detector distances ranged between 7.2 and 7.6 m. Data collection was performed using Pilatus 1M and Pilatus 2M detectors during different measurement cycles. A silver behenate (AgBeh) standard was used to calibrate both the sample-to-detector distance and beam center positions. Exposure times ranged from 2 to 10 s, with samples mounted on a three-axis goniometer for precise alignment with the incident X-ray beam. Detailed information regarding alignment, tilts, measurements, geometry, and 2D analysis procedures can be found in our previous works [29,40].

The 2D scattering patterns were converted into 1D scattering intensities through horizontal and vertical cuts (along q_x and q_y, respectively) originating from the center of the beamstop. We selected the cut with minimal interference from the Kossel line by comparing the symmetric positive and negative values q_x and q_y relative to the center of the beam. These cuts were obtained through azimuthal integration along the masked region (see Figure 2). To preserve the accuracy of polydispersity measurements without averaging interference effects, the cuts were kept as narrow as practicable. For analysis of the vertical cut, we employed our previously reported cone model [29], where the form factor is given by:

$$f_{2\mathrm{D}}\left(q_r,q_z\right)=C\int_0^L J_1\left(r_z,q_r\right)\frac{r_z}{q_r}\exp\left(-i,z,q_z\right)\mathrm{d}z. \quad (1)$$

Here, $f_{2D}(q_r,q_z)$ represents the form factor assuming rotational symmetry along the Z axis of the conical nanopores, L is the length of the conical nanopores, J_1 denotes the first-order Bessel function, and C accounts for electron density contrast and other constant parameters. The radial component of the scattering vector ($\vec{q}$), denoted as q_r, is given by $\sqrt{q_x^2+q_y^2}$. For the vertical cut analysis, we set $q_x = 0$, which reduces q_r to q_y. This formulation captures the scattering amplitude for conical objects while accounting for the radius variation along the Z axis. The horizontal cut analysis was performed setting $q_y = 0$. Equation 1 then reduces to a "core transition" model, previously detailed in our work [21,56]. This model incorporates a constant core radius (fixed to the ion track radius determined by SAXS [13,47,57]) with a linear density transition region. The corresponding form factor is expressed as:

$$f_{\mathrm{CT}}\left(q_r,q_z\right)=4\pi\frac{\sin\left(q_z l\right)}{q_z}\frac{\pi}{\left(q_r\right)^2}\times\begin{bmatrix}-R_{\mathrm{C}}J_1\left(R_{\mathrm{C}}q_r\right)H_0\left(R_{\mathrm{C}}q_r\right)\\+\left(R_{\mathrm{C}}+R_{\mathrm{T}}\right)J_1\left(\left(R_{\mathrm{C}}+R_{\mathrm{T}}\right)q_r\right)H_0\left(\left(R_{\mathrm{C}}+R_{\mathrm{T}}\right)q_r\right)\\+R_{\mathrm{C}}J_0\left(R_{\mathrm{C}}q_r\right)H_1\left(R_{\mathrm{C}}q_r\right)\\-\left(R_{\mathrm{C}}+R_{\mathrm{T}}\right)J_0\left(\left(R_{\mathrm{C}}+R_{\mathrm{T}}\right)q_r\right)H_1\left(\left(R_{\mathrm{C}}+R_{\mathrm{T}}\right)q_r\right)\end{bmatrix}, \quad (2)$$

where R_{C} represents the fixed core radius matching the ion track radius, R_{T} denotes the transition region thickness, and $H_u(z)$ represents the Struve function given by:

$$H_u\left(z\right)=\left(\frac{z}{2}\right)^{u+1}\sum_{m=0}^{\infty}\frac{\left(-1\right)^m\left(\frac{z}{2}\right)^{2m}}{\Gamma\left(m+\frac{3}{2}\right)\Gamma\left(m+u+\frac{3}{2}\right)}. \quad (3)$$

To measure the distribution of the nanopore sizes, we implemented a narrow Schulz–Zimm distribution [13,21,47,56]. Readers are referred to these works for detailed information on the implementation of polydispersity. The fits are performed using a custom C- and Python-based code that employs a non-linear least-squares algorithm. To correct for background scattering originating from the, among others, air and the substrate, we employ a q-dependent background [26] as it is not feasible to extract and subtract the background explicitly for these materials systems.

We fit the horizontal cuts to determine the nanopore radii and the corresponding size distribution. The oscillations in the scattering intensity along the horizontal cuts remain the same as a

function of the tilt angle between cone axis and X-ray beam, making it impossible to extract direct information about the cone angles. In contrast, the scattering intensities in the vertical cuts vary with the tilt angle and provide information on the cone angle of the nanopores. As the cone angle and tilt angle are highly correlated, fitting just a single vertical cut produces large uncertainties mainly because of the challenges in accurately determining the experimental tilt angle [29,40]. Therefore, we acquire scattering images at multiple tilt angles and fit the resulting scattering intensities simultaneously.

Our overall fitting strategy proceeds as follows. For each sample, first, we fit the scattering intensities from individual horizontal cuts obtained at different tilt angles to obtain initial estimates of nanopore radii. Next, multiple horizontal cuts originating from different tilt angles are fitted together to refine the radius values and determine size dispersity more accurately. We then used these refined values as starting points for simultaneously fitting multiple vertical cuts, treating the tilt angle as a variable to account for the imperfect alignment of the cones with the incoming X-rays. It should be noted that the difference in different tilt angles is fixed and known for different experiments. Finally, we combine both horizontal and vertical cuts in a single simultaneous fit, constraining the radius and the cone angle to the same values.

Acknowledgements

Part of the research was undertaken at the SAXS/WAXS beamline at the Australian Synchrotron, part of ANSTO, and we thank the beamline scientists for their technical assistance. We also acknowledge access to the NCRIS (National Collaborative Research Infrastructure Strategy) supported Heavy-Ion Accelerator facility (the 14UD accelerator) at the Australian National University. The results presented here are based on a UMAT experiment that was carried out on the UNILAC X0 beamline at the GSI Helmholtz Center for Heavy Ion Research, Darmstadt (Germany) in the frame of FAIR Phase-0. This work used the ACT node of the NCRIS-enabled Australian National Fabrication Facility (ANFF-ACT).

Funding

The authors acknowledge financial support from the Australian Research Council (ARC) under the ARC Discovery Project Scheme.

Author Contributions

Shankar Dutt: conceptualization; formal analysis; investigation; methodology; software; visualization; writing – original draft. Rudradeep Chakraborty: formal analysis; investigation. Christian Notthoff: investigation; methodology; software; writing – review & editing. Pablo Mota-Santiago: investigation; writing – review & editing. Christina Trautmann: investigation; writing – review & editing. Patrick Kluth: conceptualization; funding acquisition; investigation; methodology; supervision; visualization; writing – review & editing.

ORCID® iDs

Shankar Dutt - https://orcid.org/0000-0002-6814-070X
Pablo Mota-Santiago - https://orcid.org/0000-0002-1537-4318
Christina Trautmann - https://orcid.org/0000-0001-7058-6340
Patrick Kluth - https://orcid.org/0000-0002-1806-2432

Data Availability Statement

Data generated and analyzed during this study is available from the corresponding author upon reasonable request.

Preprint

A non-peer-reviewed version of this article has been previously published as a preprint: https://doi.org/10.48550/arXiv.2502.14118

References

1. Xue, L.; Yamazaki, H.; Ren, R.; Wanunu, M.; Ivanov, A. P.; Edel, J. B. *Nat. Rev. Mater.* **2020,** *5,* 931–951. doi:10.1038/s41578-020-0229-6
2. He, Y.; Tsutsui, M.; Zhou, Y.; Miao, X.-S. *NPG Asia Mater.* **2021,** *13,* 48. doi:10.1038/s41427-021-00313-z
3. Yeh, H.-C.; Chang, C.-C.; Yang, R.-J. *Phys. Rev. E* **2015,** *91,* 062302. doi:10.1103/physreve.91.062302
4. Zhao, X.; Qin, H.; Tang, M.; Zhang, X.; Qing, G. *TrAC, Trends Anal. Chem.* **2024,** *173,* 117658. doi:10.1016/j.trac.2024.117658
5. Wanjiya, M.; Zhang, J.-C.; Wu, B.; Yin, M.-J.; An, Q.-F. *Desalination* **2024,** *578,* 117441. doi:10.1016/j.desal.2024.117441
6. Dutt, S.; Apel, P.; Lizunov, N.; Notthoff, C.; Wen, Q.; Trautmann, C.; Mota-Santiago, P.; Kirby, N.; Kluth, P. *J. Membr. Sci.* **2021,** *638,* 119681. doi:10.1016/j.memsci.2021.119681
7. Dutt, S.; Karawdeniya, B. I.; Bandara, Y. M. N. D. Y.; Afrin, N.; Kluth, P. *Anal. Chem. (Washington, DC, U. S.)* **2023,** *95,* 5754–5763. doi:10.1021/acs.analchem.3c00023
8. Wei, X.; Penkauskas, T.; Reiner, J. E.; Kennard, C.; Uline, M. J.; Wang, Q.; Li, S.; Aksimentiev, A.; Robertson, J. W. F.; Liu, C. *ACS Nano* **2023,** *17,* 16369–16395. doi:10.1021/acsnano.3c05628
9. Meyer, N.; Abrao-Nemeir, I.; Janot, J.-M.; Torrent, J.; Lepoitevin, M.; Balme, S. *Adv. Colloid Interface Sci.* **2021,** *298,* 102561. doi:10.1016/j.cis.2021.102561
10. Siwy, Z. S.; Bruening, M. L.; Howorka, S. *Chem. Soc. Rev.* **2023,** *52,* 1983–1994. doi:10.1039/d2cs00894g
11. Varongchayakul, N.; Song, J.; Meller, A.; Grinstaff, M. W. *Chem. Soc. Rev.* **2018,** *47,* 8512–8524. doi:10.1039/c8cs00106e
12. Lu, W.; Cao, Y.; Qing, G. *Chem. – Asian J.* **2022,** *17,* e202200675. doi:10.1002/asia.202200675
13. Dutt, S.; Notthoff, C.; Wang, X.; Trautmann, C.; Mota-Santiago, P.; Kluth, P. *Appl. Surf. Sci.* **2023,** *628,* 157370. doi:10.1016/j.apsusc.2023.157370
14. Pan, J.; Xu, W.; Zhang, Y.; Ke, Y.; Dong, J.; Li, W.; Wang, L.; Wang, B.; Meng, B.; Zhou, Q.; Xia, F. *Nano Energy* **2024,** *132,* 110412. doi:10.1016/j.nanoen.2024.110412

15. Zhang, H.; Tian, Y.; Jiang, L. *Nano Today* **2016,** *11,* 61–81. doi:10.1016/j.nantod.2015.11.001
16. Mohammad, A. W.; Teow, Y. H.; Ang, W. L.; Chung, Y. T.; Oatley-Radcliffe, D. L.; Hilal, N. *Desalination* **2015,** *356,* 226–254. doi:10.1016/j.desal.2014.10.043
17. Calvo, J. I.; Bottino, A.; Capannelli, G.; Hernández, A. *J. Membr. Sci.* **2004,** *239,* 189–197. doi:10.1016/j.memsci.2004.02.038
18. Kanani, D. M.; Fissell, W. H.; Roy, S.; Dubnisheva, A.; Fleischman, A.; Zydney, A. L. *J. Membr. Sci.* **2010,** *349,* 405–410. doi:10.1016/j.memsci.2009.12.003
19. Dutt, S.; Shao, H.; Karawdeniya, B.; Bandara, Y. M. N. D. Y.; Daskalaki, E.; Suominen, H.; Kluth, P. *Small Methods* **2023,** *7,* 2300676. doi:10.1002/smtd.202300676
20. Li, N.; Yu, S.; Harrell, C. C.; Martin, C. R. *Anal. Chem. (Washington, DC, U. S.)* **2004,** *76,* 2025–2030. doi:10.1021/ac035402e
21. Wang, X.; Dutt, S.; Notthoff, C.; Kiy, A.; Mota-Santiago, P.; Mudie, S. T.; Toimil-Molares, M. E.; Liu, F.; Wang, Y.; Kluth, P. *Phys. Chem. Chem. Phys.* **2022,** *24,* 9345–9359. doi:10.1039/d1cp05813d
22. Sun, C.; Zhu, S.; Liu, M.; Shen, S.; Bai, B. *J. Phys. Chem. Lett.* **2019,** *10,* 7188–7194. doi:10.1021/acs.jpclett.9b02715
23. DesOrmeaux, J. P. S.; Winans, J. D.; Wayson, S. E.; Gaborski, T. R.; Khire, T. S.; Striemer, C. C.; McGrath, J. L. *Nanoscale* **2014,** *6,* 10798–10805. doi:10.1039/c4nr03070b
24. Wang, L.; Wang, Z.; Patel, S. K.; Lin, S.; Elimelech, M. *ACS Nano* **2021,** *15,* 4093–4107. doi:10.1021/acsnano.0c08628
25. Wang, X.; Luo, Y.; Huang, K.; Cheng, N. *Adv. Agrochem* **2022,** *1,* 3–6. doi:10.1016/j.aac.2022.08.002
26. Kiy, A.; Notthoff, C.; Dutt, S.; Grigg, M.; Hadley, A.; Mota-Santiago, P.; Kirby, N.; Trautmann, C.; Toimil-Molares, M. E.; Kluth, P. *Phys. Chem. Chem. Phys.* **2021,** *23,* 14231–14241. doi:10.1039/d1cp02063c
27. Rastgar, M.; Moradi, K.; Burroughs, C.; Hemmati, A.; Hoek, E.; Sadrzadeh, M. *Chem. Rev.* **2023,** *123,* 10156–10205. doi:10.1021/acs.chemrev.3c00168
28. Tsutsui, M.; Yoshida, T.; Yokota, K.; Yasaki, H.; Yasui, T.; Arima, A.; Tonomura, W.; Nagashima, K.; Yanagida, T.; Kaji, N.; Taniguchi, M.; Washio, T.; Baba, Y.; Kawai, T. *Sci. Rep.* **2017,** *7,* 17371. doi:10.1038/s41598-017-17443-6
29. Hadley, A.; Notthoff, C.; Mota-Santiago, P.; Dutt, S.; Mudie, S.; Carrillo-Solano, M. A.; Toimil-Molares, M. E.; Trautmann, C.; Kluth, P. *Phys. Rev. Mater.* **2020,** *4,* 056003. doi:10.1103/physrevmaterials.4.056003
30. Kiy, A.; Dutt, S.; Notthoff, C.; Toimil-Molares, M. E.; Kirby, N.; Kluth, P. *ACS Appl. Nano Mater.* **2023,** *6,* 8564–8573. doi:10.1021/acsanm.3c00960
31. Liu, Z.; Ma, L.; Zhang, H.; Zhuang, J.; Man, J.; Siwy, Z. S.; Qiu, Y. *ACS Appl. Mater. Interfaces* **2024,** *16,* 30496–30505. doi:10.1021/acsami.4c02078
32. Vlassiouk, I.; Apel, P. Y.; Dmitriev, S. N.; Healy, K.; Siwy, Z. S. *Proc. Natl. Acad. Sci. U. S. A.* **2009,** *106,* 21039–21044. doi:10.1073/pnas.0911450106
33. Dutt, S.; Karawdeniya, B.; Bandara, Y. M. N. D. Y.; Kluth, P. *Future Sci. OA* **2024,** *10,* 2340882. doi:10.2144/fsoa-2023-0226
34. Ma, C.; Yeung, E. S. *Anal. Chem. (Washington, DC, U. S.)* **2010,** *82,* 478–482. doi:10.1021/ac902487c
35. Balannec, B.; Ghoufi, A.; Szymczyk, A. *J. Membr. Sci.* **2018,** *552,* 336–340. doi:10.1016/j.memsci.2018.02.026
36. Zhang, Y.; Schatz, G. C. *J. Phys. Chem. Lett.* **2017,** *8,* 2842–2848. doi:10.1021/acs.jpclett.7b01137
37. Lin, C.-Y.; Combs, C.; Su, Y.-S.; Yeh, L.-H.; Siwy, Z. S. *J. Am. Chem. Soc.* **2019,** *141,* 3691–3698. doi:10.1021/jacs.8b13497
38. Duleba, D.; Dutta, P.; Denuga, S.; Johnson, R. P. *ACS Meas. Sci. Au* **2022,** *2,* 271–277. doi:10.1021/acsmeasuresciau.1c00062
39. Hellborg, R.; Whitlow, H. J.; Zhang, Y., Eds. *Ion Beams in Nanoscience and Technology;* Particle Acceleration and Detection; Springer: Berlin, Heidelberg, 2010. doi:10.1007/978-3-642-00623-4
40. Hadley, A.; Notthoff, C.; Mota-Santiago, P.; Hossain, U. H.; Kirby, N.; Toimil-Molares, M. E.; Trautmann, C.; Kluth, P. *Nanotechnology* **2019,** *30,* 274001. doi:10.1088/1361-6528/ab10c8
41. Apel, P. Y.; Dmitriev, S. N. *Adv. Nat. Sci.: Nanosci. Nanotechnol.* **2011,** *2,* 013002. doi:10.1088/2043-6262/2/1/013002
42. Apel, P. *Nucl. Instrum. Methods Phys. Res., Sect. B* **2003,** *208,* 11–20. doi:10.1016/s0168-583x(03)00634-7
43. Liu, F.; Wang, M.; Wang, X.; Wang, P.; Shen, W.; Ding, S.; Wang, Y. *Nanotechnology* **2019,** *30,* 052001. doi:10.1088/1361-6528/aaed6d
44. Hanot, H.; Ferain, E. *Nucl. Instrum. Methods Phys. Res., Sect. B* **2009,** *267,* 1019–1022. doi:10.1016/j.nimb.2009.02.011
45. Kaya, D.; Keçeci, K. *J. Electrochem. Soc.* **2020,** *167,* 037543. doi:10.1149/1945-7111/ab67a7
46. Price, P. B. *Radiat. Meas.* **2008,** *43,* S13–S25. doi:10.1016/j.radmeas.2008.04.002
47. Mota-Santiago, P.; Vazquez, H.; Bierschenk, T.; Kremer, F.; Nadzri, A.; Schauries, D.; Djurabekova, F.; Nordlund, K.; Trautmann, C.; Mudie, S.; Ridgway, M. C.; Kluth, P. *Nanotechnology* **2018,** *29,* 144004. doi:10.1088/1361-6528/aaabdb
48. Karouta, F.; Vora, K.; Tian, J.; Jagadish, C. *J. Phys. D: Appl. Phys.* **2012,** *45,* 445301. doi:10.1088/0022-3727/45/44/445301
49. Ziegler, J. F.; Ziegler, M. D.; Biersack, J. P. *Nucl. Instrum. Methods Phys. Res., Sect. B* **2010,** *268,* 1818–1823. doi:10.1016/j.nimb.2010.02.091
50. Sutariya, B.; Karan, S. *Sep. Purif. Technol.* **2022,** *293,* 121096. doi:10.1016/j.seppur.2022.121096
51. Ramírez, P.; Apel, P. Y.; Cervera, J.; Mafé, S. *Nanotechnology* **2008,** *19,* 315707. doi:10.1088/0957-4484/19/31/315707
52. Pietschmann, J.-F.; Wolfram, M.-T.; Burger, M.; Trautmann, C.; Nguyen, G.; Pevarnik, M.; Bayer, V.; Siwy, Z. *Phys. Chem. Chem. Phys.* **2013,** *15,* 16917–16926. doi:10.1039/c3cp53105h
53. Laohakunakorn, N.; Thacker, V. V.; Muthukumar, M.; Keyser, U. F. *Nano Lett.* **2015,** *15,* 695–702. doi:10.1021/nl504237k
54. Riedel, C.; Spohr, R. *Radiat. Eff.* **1979,** *42,* 69–75. doi:10.1080/10420157908201738
55. Kluth, P.; Schnohr, C. S.; Sprouster, D. J.; Byrne, A. P.; Cookson, D. J.; Ridgway, M. C. *Nucl. Instrum. Methods Phys. Res., Sect. B* **2008,** *266,* 2994–2997. doi:10.1016/j.nimb.2008.03.182
56. Dutt, S.; Apel, P.; Polezhaeva, O.; Kiy, A.; Afrin, N.; Notthoff, C.; Kirby, N.; Kluth, P. *Polymer* **2023,** *282,* 126133. doi:10.1016/j.polymer.2023.126133
57. Kluth, P.; Schnohr, C. S.; Pakarinen, O. H.; Djurabekova, F.; Sprouster, D. J.; Giulian, R.; Ridgway, M. C.; Byrne, A. P.; Trautmann, C.; Cookson, D. J.; Nordlund, K.; Toulemonde, M. *Phys. Rev. Lett.* **2008,** *101,* 175503. doi:10.1103/physrevlett.101.175503

BEILSTEIN JOURNAL OF NANOTECHNOLOGY

Focused ion beam-induced platinum deposition with a low-temperature cesium ion source

Thomas Henning Loeber*[1], Bert Laegel[1], Meltem Sezen[2], Feray Bakan Misirlioglu[2], Edgar J. D. Vredenbregt[3] and Yang Li[3]

Full Research Paper

Open Access

Address:
[1]Nano Structuring Center (NSC), Rheinland-Pfälzische Technische Universität Kaiserslautern-Landau (RPTU), P.O. Box 3049, D-67653, Kaiserslautern, Germany, [2]Sabanci University Nanotechnology Research and Application Center (SUNUM), 34956, Istanbul, Turkey and [3]Department of Applied Physics, Eindhoven University of Technology, P.O. Box 513, 5600 MB Eindhoven, The Netherlands

Email:
Thomas Henning Loeber* - loeber@physik.uni-kl.de

* Corresponding author

Keywords:
cesium ion source; cold atom ion source; focused ion beam (FIB); FIB-induced deposition (FIBID)

Beilstein J. Nanotechnol. **2025,** *16,* 910–920.
https://doi.org/10.3762/bjnano.16.69

Received: 27 February 2025
Accepted: 05 June 2025
Published: 16 June 2025

This article is part of the thematic issue "Energetic ions and photons for engineering nanomaterials".

Guest Editor: V. R. Soma

Abstract

In addition to precise milling, the deposition of material at a specific location on a sample surface is a frequently used process of focused ion beam (FIB) systems. Here, we report on the deposition of platinum (Pt) with a new kind of cesium (Cs) FIB, in which the cesium ions are produced by a low-temperature ion source. Platinum was deposited at different acceleration voltages and ion beam currents. Deposition rate, material composition, and electrical resistivity were examined and compared with layers deposited at comparable settings with a standard gallium (Ga) FIB. The deposition rate is found to depend linearly on the current density. The rate is comparable for Cs^+ and Ga^+ under similar conditions, but the deposit has lower Pt content for Cs^+. The electrical resistivity of the deposit is found to be higher for Cs^+ than for Ga^+ and decreasing with increasing acceleration voltage.

Introduction

The deposition of material at a certain spot on a sample surface is a powerful and useful feature of focused ion beam (FIB) systems. At first, the deposition was used for circuit editing and as a protection layer before milling. Nowadays, the process is more far-reaching, and three-dimensional magnetic or superconductive structures can be created [1-4]. Also, specific mechanical structures on atomic force microscopy (AFM) cantilevers can be made [5,6]. In the literature, four mechanisms are used to explain the complex process of focused ion beam-induced deposition (FIBID) [5,7]; the major role is played by the primary ion beam, together with a thermal heat spike, excited surface atoms (ESA), or secondary electrons (SE). According to Hlawacek et al. [8], the number of ESA is proportional to the nuclear stopping power, so for heavier ions this mechanism

dominates the deposition. The exact order, however, of which mechanism contributes how much to the deposition, for example, for cesium (Cs) ions, is beyond the scope of this paper since FIBID is rather complex and depends on a variety of parameters. Besides beam parameters such as acceleration voltage, beam current, ion dose, dwell time, and refresh time, precursor material and substrate have an influence on the effective deposition rate. Gallium (Ga^+) and helium (He^+) are the most often utilized ion species for FIBID [1,2,5].

Besides these standard FIB systems, new kinds of laser-cooled ion sources have been developed in the last few years. One strength of these ion sources, which are based on laser-cooled atoms, is that many elements unavailable with conventional sources can be used. At least 27 elements, including metals and non-metals, have successfully been laser-cooled [9]. Among these elements, rubidium (Rb) and Cs are more advanced with respect to source development because of their relatively low requirements regarding the cooling laser. Milling [10] as well as induced deposition of platinum (Pt) [11] and tungsten (W) [12] have been studied for a prototype FIB with an ultracold Rb^+source.

Further, a Cs^+ laser-cooled ion source (LoTIS) has been developed and characterized [13,14]. Like the Rb^+ source, the Cs^+ LoTIS has also been incorporated in a standard Ga FIB column. Loeber et al. have shown several advantages of the cold Cs^+ FIB in imaging [15] and milling [16] applications over standard Ga^+ FIBs. Compared to a standard Ga^+ FIB, the Cs^+ FIB can produce images with higher resolution and a larger depth of focus. Furthermore, the material contrast is greater in images acquired with Cs^+ compared to images acquired with Ga^+. For milling applications, Cs^+ can deliver more evenly etched pattern floors than Ga^+. With these benefits in applications established, microscopy and induced deposition studies help to establish more properties of the Cs^+ FIB. Given the similar sources and FIB column designs of Cs^+ and Rb^+ FIBs, it is useful to compare applications with these FIBs to understand the relative merits of ion sources based on alkali metals. Also, Cs^+ is a preferred species of ions over Ga^+ for secondary ion mass spectroscopy (SIMS) applications because Cs^+ can induce higher secondary ion yields for several elements such as carbon (C), oxygen (O), and hydrogen [17-19], which provides higher signal-to-noise ratios for SIMS analysis. A disadvantage of using Cs^+ is a possible surface modification [20-22]. One aspect of this paper is to show whether it is at all possible to deposit Pt with Cs^+ ions or whether surface modifications dominate [10].

This work presents FIBID experiments using a Cs^+ FIB in comparison to results of layer deposition induced by Rb^+ and Ga^+. Pt was deposited at different acceleration voltages and ion beam currents to evaluate the deposition rate and the electrical resistivity of the layers. To measure the grain structure as well as the material composition using energy-dispersive X-ray spectroscopy (EDS), lamellas for transmission electron microscopy (TEM) were prepared.

Experimental

The Ga^+ FIB is a ThermoFisher Helios NanoLab 650 and uses a gas injection system (GIS). ZeroK NanoTech Corporation has created commercially available Cs^+ FIB systems based on standard ion columns from ThermoFisher [23]. Both the Cs^+ and the Rb^+ FIB are equipped with a standard Pt GIS. The same precursor trimethylplatinum, $C_5H_4CH_3Pt(CH_3)_3$, was used for all FIBID-Pt experiments. The precursor was heated to 40 °C to create a gas flow through the GIS nozzle, with the exit of the nozzle kept about 100 µm above the sample surface. The chamber pressure of the Cs^+ and the Ga^+ FIB was about 5×10^{-7} mbar before deposition and 8×10^{-6} mbar during deposition. For Pt deposition, a beam step size of −150% of the beam diameter was used with an upper limit of 200 nm for the Cs FIBID to avoid, for example, any inhomogeneous ripple structures. The dwell time was always 200 ns.

For growth rate characterization, Pt layers with a length of 20 µm and a width of 1 µm were deposited on silicon (Si). The ion beam currents were changed, while the pattern size was kept constant. With the Cs^+ FIB, ion currents from 16 to 285 pA were used, so the current densities were between 0.9 and 14.2 $pA{\cdot}\mu m^{-2}$. The overall deposition time was kept constant at 2:30 min, and the ion dose was changed from 128 to 2138 $pC{\cdot}\mu m^{-2}$. The ions were accelerated with voltages of 2, 5, 8, and 16 kV, while the measured ion beam diameter changed with voltage and current from 32 to 445 nm.

With the Ga^+ FIB, patterns were deposited at ion beam currents ranging from 17 to 396 pA with current densities between 0.7 and 19.8 $pA{\cdot}\mu m^{-2}$. With a deposition time of 2:30 min, the ion dose is between 105 and 2970 $pC{\cdot}\mu m^{-2}$. The diameter of the ion beam is specified as ranging from 10 to 159 nm, changing with acceleration voltage (5, 8, 16, and 30 kV) and ion beam current. The actual thickness of each layer was measured with a standard cross section using the Ga^+ FIB. All scanning electron microscopy (SEM) images were taken with the NanoLab 650 dual beam system. All parameters of the FIBID for the growth rate measurements can be seen below in Table 2 in the Appendix section.

The electrical resistivity of Ga^+ and Cs^+ FIBID-Pt was measured via the Cr-on-glass standards mentioned in [11] using the sample design displayed below in Figure 8a. The pattern size was 35 µm by 1.5 µm. The deposition time was varied with

the ion beam current and the acceleration voltage to achieve a constant layer thickness of approximately 1000 nm. With the Ga^+ FIB, ion beam currents between 30 and 630 pA were used, so the current densities ranged from 0.9 to 8.4 pA·μm^{-2}. The deposition time was calculated between 4:42 and 24:24 min with ion doses ranging from 1254 to 2276 pC·μm^{-2}. With acceleration voltages of 8, 16, and 30 kV and the used ion beam currents, the beam diameter changes from 32 to 208 nm.

With the Cs^+ FIB, ion beam currents between 13 and 440 pA, corresponding to current densities between 0.4 and 8 pA·μm^{-2}, were utilized. The deposition time was between 3:05 and 16:11 min, and the total ion dose ranged between 717 and 1921 pC·μm^{-2}. Using acceleration voltages of 2, 5, 8, and 16 kV, the ion beam diameter changed from 25 to 460 nm. All deposition parameters are shown in Table 1. To calculate the resistivity of the deposits, the NanoLab 650 dual beam system was used to determine the length and the cross section of each deposited layer.

The TEM lamellas were prepared with a JEOL JIB 4601F FIB-SEM MultiBeam system. The sample characterization in terms of elemental composition and structure was done with a JEOL ARM 200F (S)TEM system equipped with an Oxford EDS detector.

Results and Discussion

Deposit surface

First, to reveal possible surface modifications, Pt layers were deposited with Cs^+ ions at 16, 8, 5, and 2 kV with a current density of 6 pA·μm^{-2} . Before deposition, a small part of the Si substrate was gently milled with the Cs^+ FIB at 16 kV, such that any native oxide and other contaminations were completely removed at this location. With that, the influence of oxygen molecules on the deposited layer can be excluded. The layers, which have a length of 40 μm and a width 1 μm, were deposited across the boundary between the bare Si and the Si with its native oxide intact.

A visual inspection with the SEM reveals surface bubbles on layers deposited at 2 and 5 kV (as shown in Figure 1a). No significant differences can be seen in the size or density of the bubbles when comparing depositions on Si (upper part) and Si with the native oxide layer (lower part). Similar to Rb^+ FIBID-Pt discussed in [11], these bubbles appear after exposure of the samples to air (during the short transfer from the Cs^+ FIB to the Ga^+ FIB) and are more numerous and larger at 2 kV than at 5 kV. At higher acceleration voltages, bubbles are not observed (see Figure 1b,c).

EDS measurements displayed in Figure 2 show that these bubbles mainly consist of Cs and O. This is also consistent with the observations reported in [11] on surface bubbles in Rb^+ FIBID-Pt.

The proposed mechanism for the formation of these bubbles is that elements of the Pt precursor trap the primary alkali metal ions when the chemical bonds of the precursor are not completely broken. With higher ion beam voltage, more bonds are broken and volatile elements including Cs^+ ions are sputtered from the surface and pumped away by the vacuum system. Also, Cs^+ ions with higher energies penetrate deeper into the material (see the "Stopping and Range of Ions in Matter" (SRIM) [24] simulations in Figure 3) and react less with the elements on the surface. Therefore, the surface bubbles diminish with higher acceleration voltages. This is why only 2 and 5 kV Cs^+ depositions lead to surface bubbles. Because the Pt layers deposited with Cs^+ ions at 2 kV are so sensitive to air exposure, the deposition rate and the resistivity measurements will mainly focus on layers deposited with acceleration voltages of 5, 8, and 16 kV.

Deposition rates

Deposition rates of Ga^+ and Cs^+ FIBID-Pt were measured using the dimensions of the cross sections determined via FIB cut and SEM imaging. The deposition rates of Pt on Si (shown in Figure 4) increase with increasing ion current density. This

Table 1: The deposition parameters are shown for the growth rate and the electrical resistivity measurements for both ion species.

		Acceleration voltage [kV]		Ion current [pA]		Beam size [nm]		Deposit area [μm^2]	Current density [pA·μm^{-2}]		Deposition time [min:s]		Ion dose [pC·μm^{-2}]	
Deposition for	Ion	from	to	from	to	from	to		from	to	from	to	from	to
growth rate	Ga	5	30	17	396	10	159	20	0.7	19.8	2:30		105	2970
	Cs	2	16	16	285	32	445	20	0.9	14.2	2:30		128	2138
resistivity	Ga	8	30	30	630	32	208	52.5	0.9	8.4	4:42	24:24	1254	2276
	Cs	2	16	13	440	25	460	52.5	0.4	8	3:05	16:11	717	1921

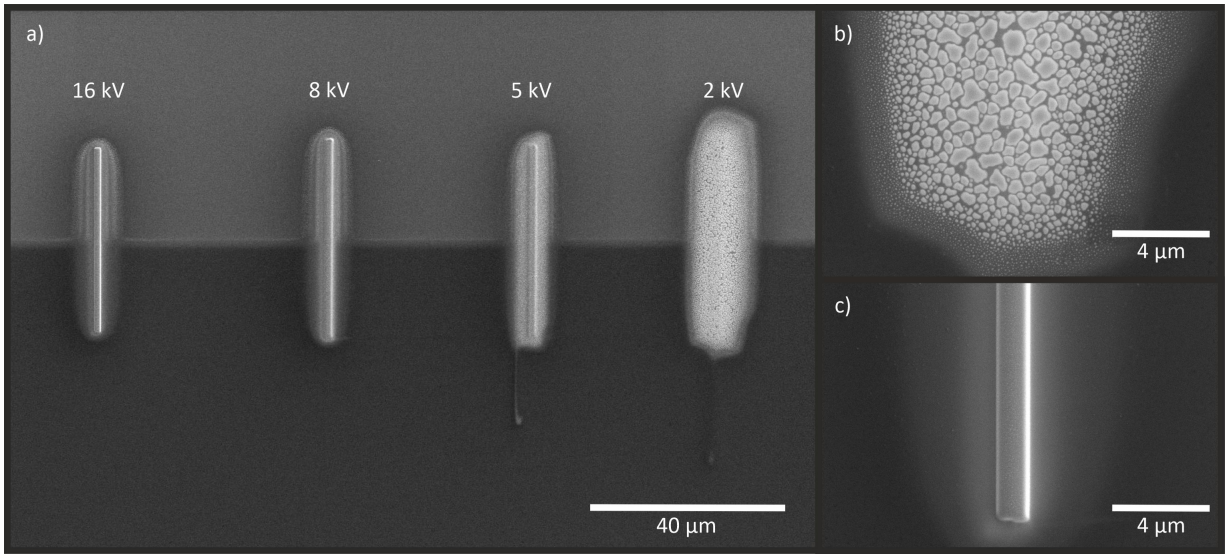

Figure 1: (a) SEM images of Pt deposited with Cs^+ ions at 16, 8, 5, and 2 kV on Si. The upper part of the image appears brighter because the native oxide of Si was removed before the deposition. The amount of surface bubbles increases with decreasing acceleration voltage, while no difference between Si and Si with oxide can be observed. (b) FIBID-Pt on Si with Cs^+ ions at 2 kV showing the highest amount of bubbles. (c) Pt deposited at 16 kV with no bubbles.

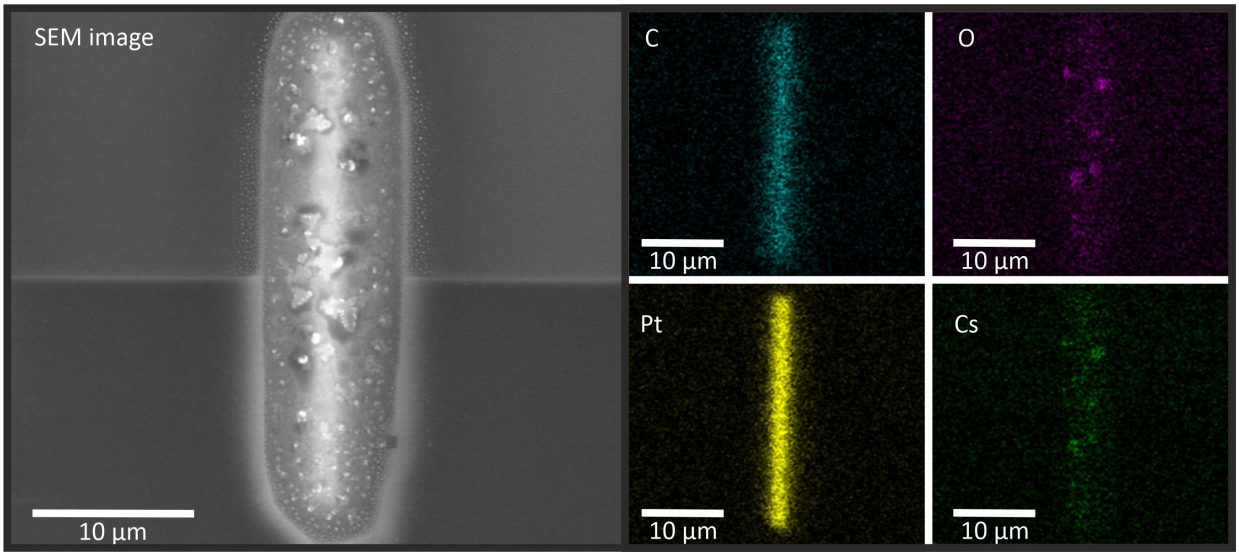

Figure 2: SEM and EDS analysis of a Pt layer deposited at 2 kV with Cs^+ ions. The SEM image shows an overview of the layer, while the other images depict the individual material distribution. The actual shape of the layer can be seen in the images of the Pt and C concentration, while the bubbles mainly consist of Cs and O. While the highest concentration of Pt and C can be found within the actual shape, the Cs and O distribution correspond to the bubble area in the SEM image.

applies to almost all voltages for Cs^+ as well as for Ga^+ ions. Only for Ga at 30 kV and a current density above 6 pA·µm^{-2}, the growth rate is lower than those for all other beam parameters. This is due to the fact that the sputter rate increases with beam current while the deposition rate is saturated due to the limited gas flow, which leads to an overall lower increase in growth rate with increasing current density. This agrees with previous findings for Ga^+ FIBID-Pt [25]. Also, for Cs^+ at 5 kV, the deposition rate is lower. A possible explanation might be the broader beam diameter, which increases for lower acceleration voltages (<5 kV) and higher ion beam currents (>200 pA). This leads to a lower current density in a beam spot compared to the current density at higher voltages for the same ion beam current. Thus, while the overall current density (ion beam current

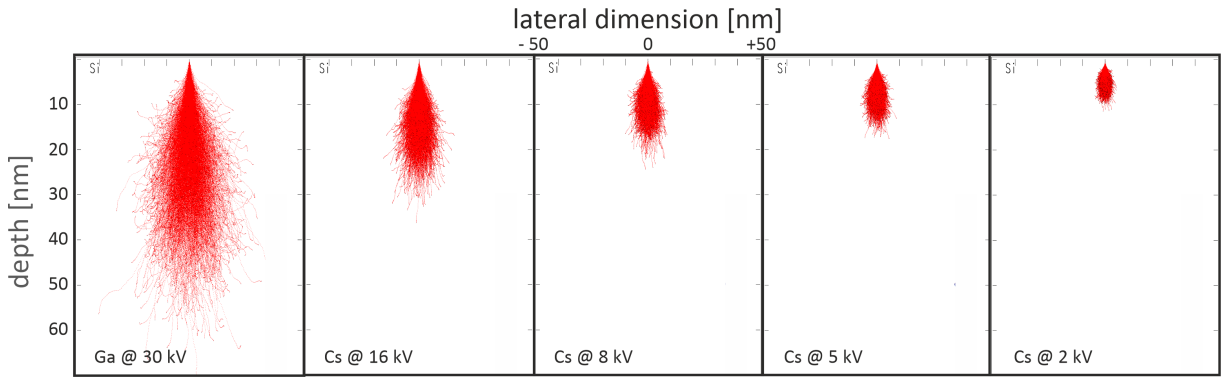

Figure 3: SRIM simulation showing the penetration of Ga^+ and Cs^+ ions into a Si substrate at different acceleration voltages. Cs^+ ions at a voltage of 2 and 5 kV remain much closer to the surface and can react more with the Pt precursor elements on the surface.

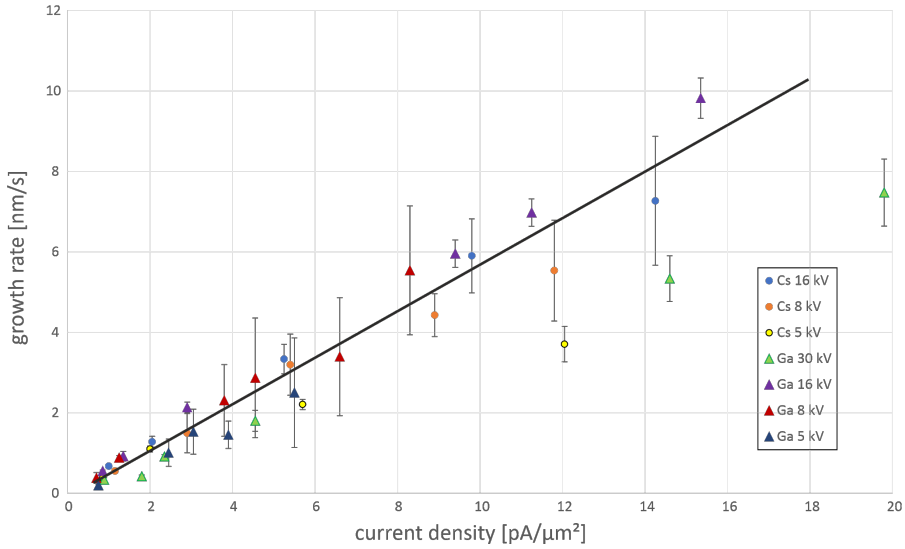

Figure 4: Pt growth rate vs ion current density for different acceleration voltages of Cs^+ and Ga^+ ions. As a guide to the eye, a line for the average growth rate is shown. With increasing current density, the growth rate increases. Only for Ga^+ ions at 30 kV and Cs^+ ions at 5 kV, the growth rates at higher current densities are much lower than the average.

per unit area of the pattern) is the same, the local density is lower, which could result in a lower growth rate. In the future, further measurements could be done with finer variations of the ion beam current starting at 100 pA and 5 kV to verify this assumption.

Composition and microstructure

Compositional data of the Cs^+ FIBID-Pt were calculated from the data provided by TEM-EDS analysis. An exemplary EDS map for 16 kV 54 pA Cs^+ FIBID-Pt is shown in Figure 5. The Si-rich region shown as the red area in the upper-right corner of the Si map corresponds to the Si substrate. Before the TEM sample preparation process, a C layer was deposited on top of the Cs^+ FIBID-Pt deposits using focused electron beam-induced deposition (FEBID). Therefore, a C-rich region exists in the lower-left corner of the C map. EDS spectra were taken at five points within the bulk deposit and then averaged to determine the chemical composition. Figure 6 displays these compositional data for C, O, Pt, and Cs with standard deviations of the average as uncertainties.

From the data shown in Figure 6, it follows that the Pt deposits created at 8 kV and 10 pA Cs^+ result in an atomic abundance ratio of C/O/Pt/Cs = 74:2.5:23:1. Compared to Rb^+ FIBID-Pt of similar beam energy, current, and ion dose (8.5 kV 7 pA Rb+ delivers C/O/Pt/Rb = 25:20:49:5, and 8.0 kV 8.5 pA Ga+ delivers C/O/Pt/Ga = 22:14:37:27) presented in [11], Cs^+ FIBID-Pt thus is found to have lower O, Pt, and Cs content and higher C content. This C content could be partially affected by the FEBID-C protective layer for the TEM sample. However,

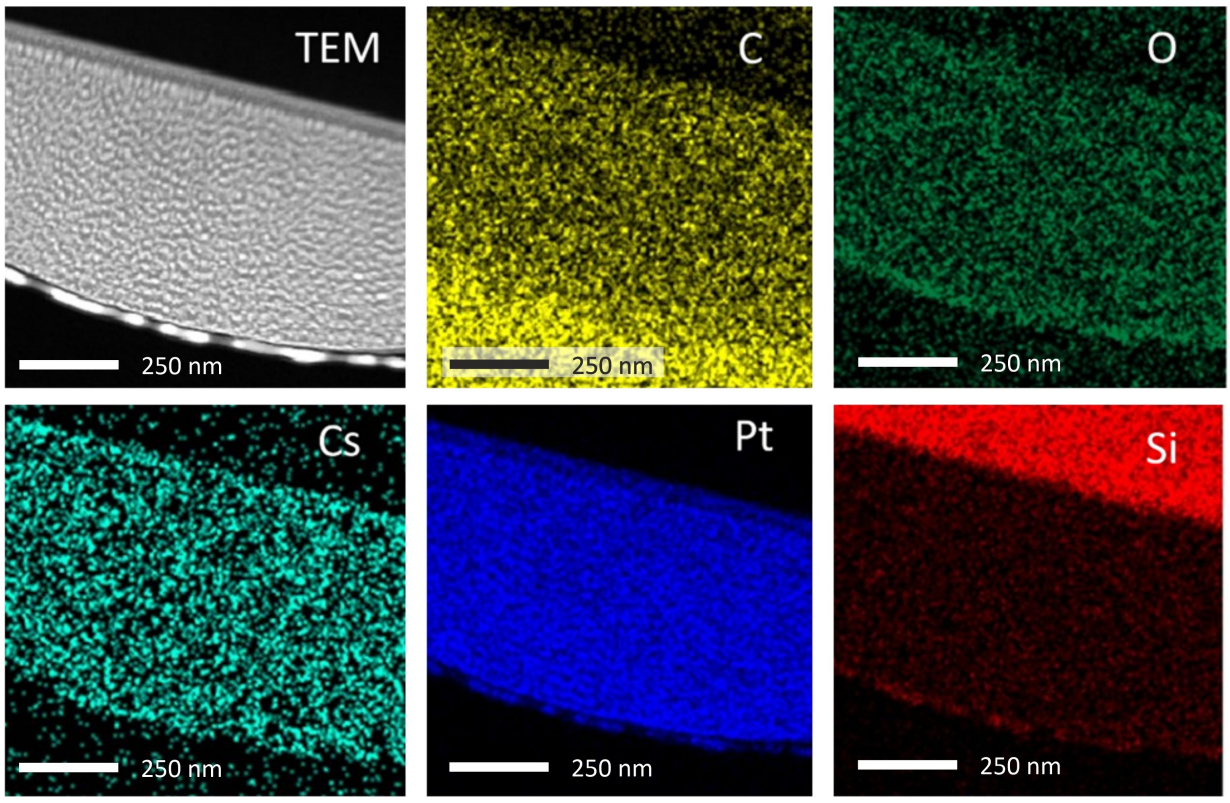

Figure 5: TEM-EDS mapping for the Pt deposit induced with 16 kV 54 pA Cs^+.

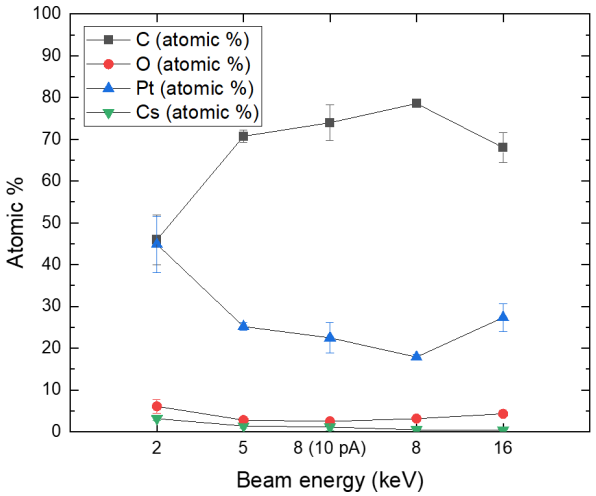

Figure 6: Cs^+-induced Pt composition data. Other than for the 8 kV 10 pA data, 54 pA was used for deposition with different beam energies.

the EDS data were reported without adjustment to the C% data because the 2 kV 54 pA Cs^+ FIBID-Pt included in Figure 6 exhibits much lower C% despite being on the same TEM lamella as the other deposits. In addition, very little Si% appears within the deposit area, which demonstrates the location sensitivity of TEM-EDS. This location sensitivity makes it likely that the FEBID-C protective layer is not the main contributor to the higher C% of Cs^+ FIBID-Pt. The composition of the Cs^+ FIBID-Pt stays mostly constant for beam energies above 2 kV. The 2 kV Cs^+ FIBID, being closer to Rb^+ FIBID-Pt in Pt% and C%, is an outlier compared to the FIBID under higher beam energies. The cause for the higher C% in Cs^+ FIBID-Pt remains unclear to the authors at this stage, however.

As with Rb^+ and Ga^+, Cs^+ FIBID-Pt also contains crystalline Pt grains embedded in a C-rich matrix, as shown in Figure 7. These bright-field TEM images were used for grain diameter measurements in the same way as done in [11]. In short, bright-field TEM images similar to those shown in Figure 7, but taken at two times higher magnification, were analyzed using the particle analyzer option provided by the image processing software ImageJ [26]. The Pt grains appear darker than the C matrix in the TEM images, thus allowing the grains to be counted by ImageJ. This software also provides the area of each grain counted, which we convert to an effective diameter by equating the area to that of a circular disk. Figure 7 shows that the average grain diameter grows from 1.9 to 5.8 nm when the beam energy increases from 2 to 16 kV. The increase in grain size with beam energy is visually obvious from the bright-field

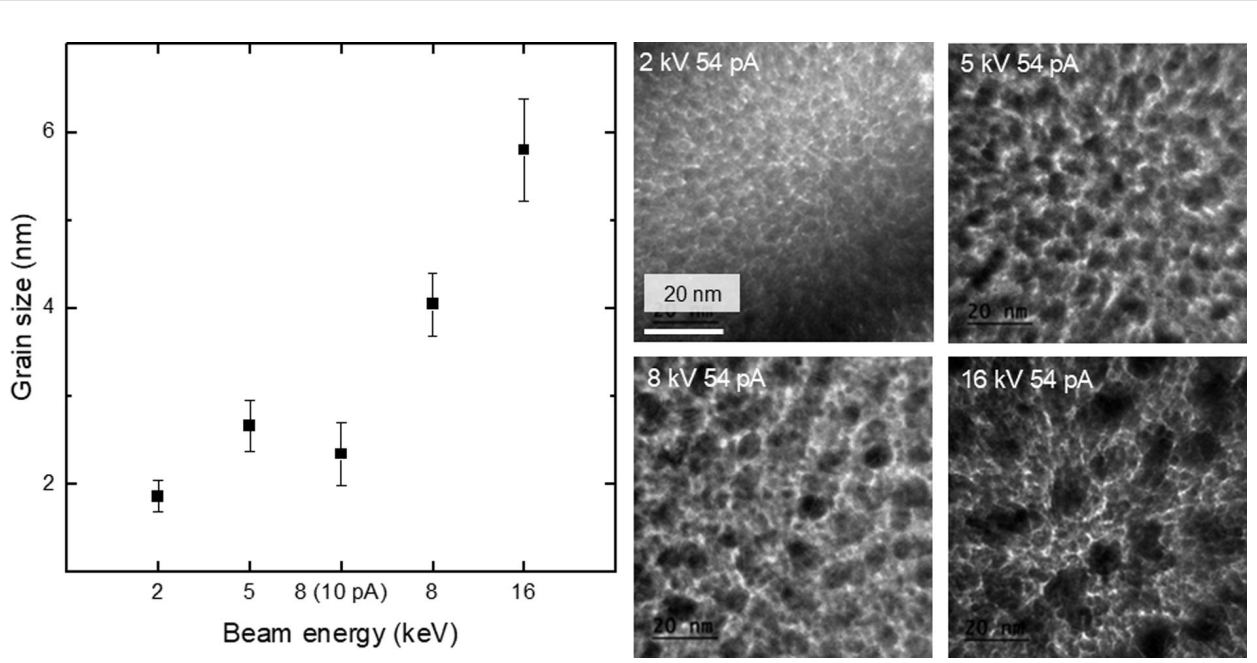

Figure 7: Bright-field images of Cs^+-induced Pt deposit and Pt grain size data for different acceleration voltages.

images shown in Figure 7. Previously, De Teresa et al. reported a 3.2 ± 0.8 nm grain diameter for 5 kV Ga^+ FIBID-Pt [25], which is similar to the 2.7 ± 0.3 nm grain diameter for 5 kV Cs^+ FIBID-Pt. The grain diameter of 5.8 nm at 16 kV Cs^+ FIBID-Pt is similar to the diameters of 8.5 kV Rb^+ and 8 kV Ga^+ FIBID-Pt. Thus, lower-energy Cs^+ creates deposits with finer grains. It is worth noting that the growth in grain diameter does not correlate with the EDS data, in which the composition remains nearly constant for above 2 kV Cs^+ FIBID-Pt.

Deposit resistivity

The electrical resistivity was measured with a four-point probe setup as shown in Figure 8a. The electric current was pushed trough the deposited layer using the two upper contacts, while the resulting voltage was measured between the two lower contacts to evaluate the resistivity R in the same way as in [11]. After these measurements were done, the area A of the cross section was determined with a FIB cut and SEM image (see Figure 8b). The length l between the contacts was about 14.6 µm, so the electrical resistivity can be calculated with $R = \rho l/A$ for each layer.

For each beam setting, the deposition time was calculated using the growth rate shown in Figure 4 in order to deposit Pt layers with a thickness of 1 µm. Because here the substrate is glass and not Si, charging effects can occur. In addition, the SE yields of

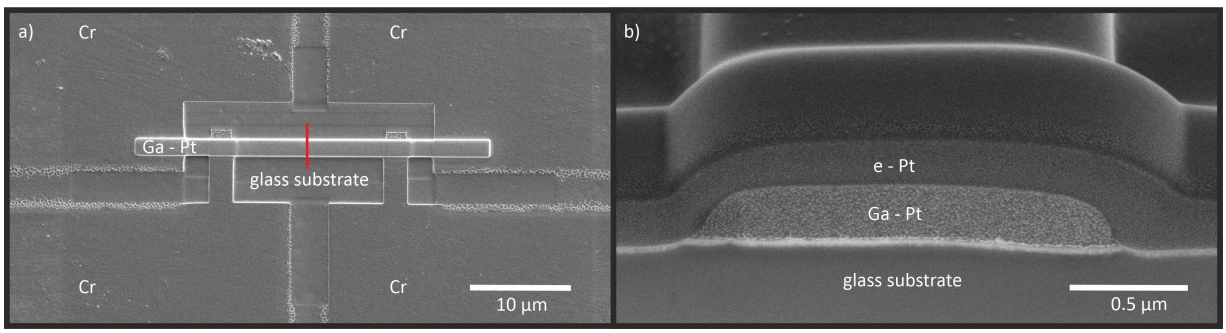

Figure 8: (a) Structure for the resistivity measurements consisting of four Cr electrodes and the 35 µm by 1.5 µm Ga-induced Pt deposit layer. The red line indicates the position of the cross section. (b) SEM image of this cross section. Before the FIB cut for the cross section measurement was done, an additional Pt layer was deposited with FEBID for protection.

amorphous SiO_2 and crystalline Si are different. Therefore the actual deposition rates and the estimated and real layer thickness differ. Overall, they vary from 300 to 1200 nm. Although in theory, the area of the cross section should not have an influence on the calculation of the specific resistivity, De Teresa et al. showed that there can be an impact [25,27]. Therefore, preliminary measurements were carried out to study the thickness dependence of the resistivity. With the Ga^+ FIB, Pt layers were deposited with an ion current density of 6 pA·µm^{-2} at a voltage of 30 kV. Only the deposition time and thus the layer thickness was varied. The results can be seen in Figure 9a. We find that layers thicker than 1 µm have a lower electrical resistivity compared to thinner ones by up to a factor of two in the range covered. We conclude that for our conditions, layer thickness does indeed have an influence on the resistivity of Ga^+ FIBID-Pt deposits.

Figure 9b contains measured resistivity results for Ga^+- and Cs^+-induced Pt deposits for different current densities and acceleration voltages. The resistivity of Cs^+ FIBID-Pt decreases with increasing primary ion beam energy. For 16 and 8 kV Cs^+ FIBID-Pt, the resistivity also decreases with higher Cs^+ ion current density. Only for 5 kV, the resistivity increases at higher beam currents. For all acceleration voltages used with

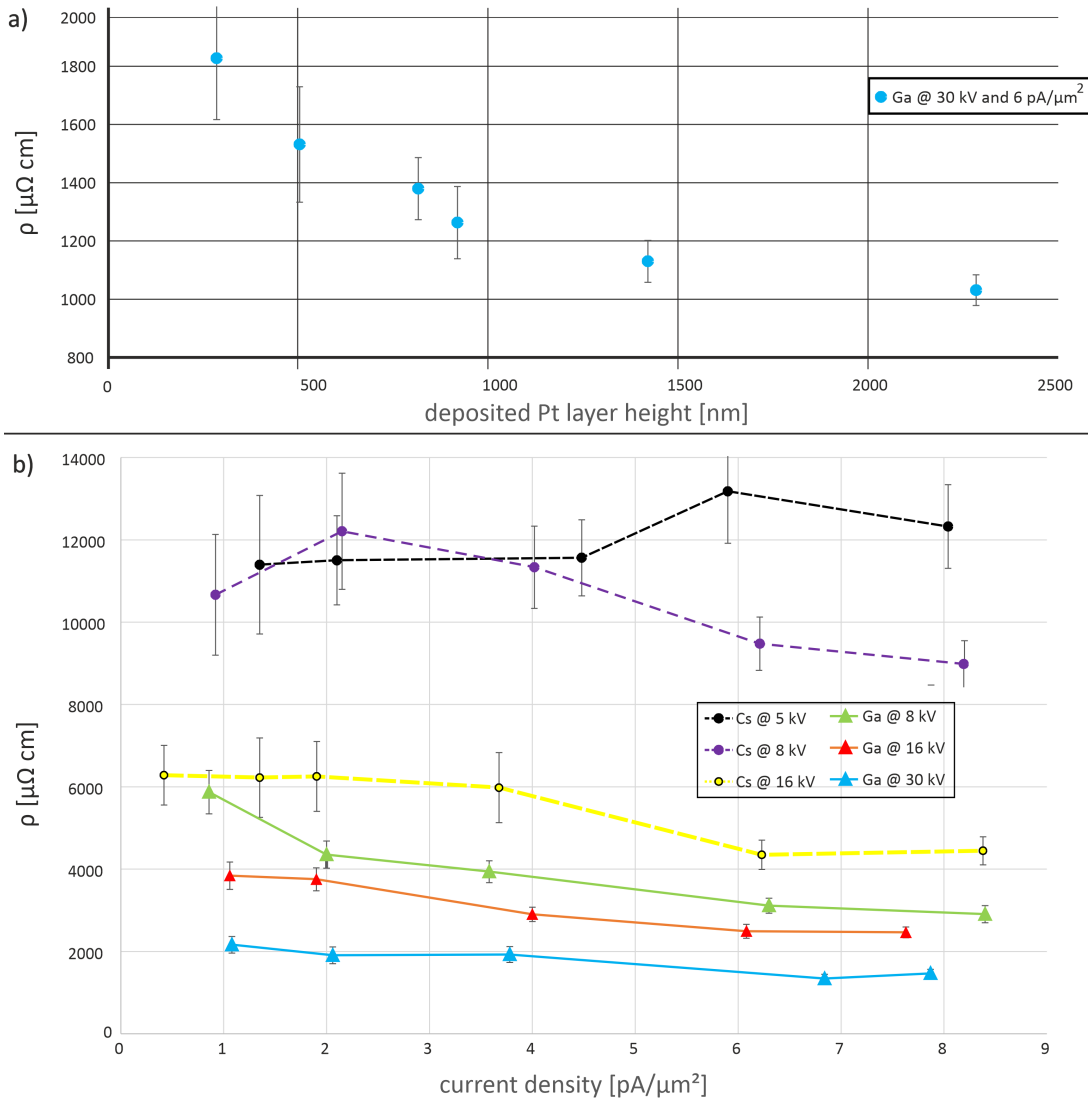

Figure 9: (a) Resistivity of Ga^+-induced Pt deposits using the same current density and acceleration voltage. Only the layer thickness was varied. Thicker layers have a lower electrical resistivity. (b) Resistivity vs current density for different acceleration voltages for Ga^+ and Cs^+ ions. With increasing acceleration voltage, the electrical resistivity decreases. Furthermore, the Ga^+ FIBID-Pt has a lower resistivity than the Cs^+ FIBID-Pt.

Ga^+ ions, that is, 30, 16, and 8 kV, the electrical resistivity decreases with increasing current density. At all voltages, the resistivity of Cs^+ FIBID-Pt is higher than that of Ga^+ FIBID-Pt. Only Pt deposited with Cs^+ ions at 16 kV has almost the same value as Ga^+ FIBID-Pt. The other voltages create layers with at least three times higher specific resistivity values.

The decrease in resistivity for Ga^+ FIBID-Pt with increasing ion current has already been reported [28] and is now verified in the measurements reported here. In particular, the Cs^+ FIBID-Pt layers deposited with a current density below 6 pA·μm^{-2} have a thickness below 1 μm. As shown in Figure 9a, this may lead to a higher electrical resistivity. The changes in resistivity are not immediately obvious from the chemical composition of the deposits. Speculation based on the microstructure provides a probable cause for this decreasing resistivity vs beam energy. Figure 7 shows that the average grain diameter grows from 1.9 to 5.8 nm when the beam energy increases from 2 to 16 kV. With larger grain diameters, the Pt-rich particles have larger surface areas in close contact. These larger surface areas help the current to flow more easily between the Pt deposits. Therefore, the deposit resistivity decreases despite a similar chemical composition. However, it is unclear why Cs^+ FIBID-Pt would have a higher resistivity than Ga^+ FIBID-Pt under similar beam conditions since the Cs^+ FIBID was observed to have the lowest O%, which should lead to a smaller resistivity. So this might be a combined effect of chemical composition and grain size. However, the acceleration voltage and the ion species seem to play a more dominant role than the ion current density for the electrical resistivity. Further studies are required to fully investigate the resistivity–microstructure dependency for FIBID-Pt.

To compare the Cs^+ and Rb^+ FIBID, Pt layers were deposited with the same beam settings, namely, a very low current density of about 0.2 pA·μm^{-2} at a voltage of 8 kV. The electrical resistivity of Cs^+ FIBID-Pt is $(3.2 \pm 0.4) \times 10^4$ μΩ·cm, which is about four times lower compared to Rb^+ FIBID-Pt with a resistivity of about $(12 \pm 4) \times 10^4$ μΩ·cm [11]. Also, one Pt layer was deposited with Cs^+ ions at 2 kV and a beam current density of 3.76 pA·μm^{-2}. Here the resistivity is $(3.4 \pm 0.3) \times 10^4$ μΩ·cm, which is three to five times higher compared to other Cs^+ induced Pt layers. We conclude that alkali metal ion beams operating at low current densities and acceleration voltages lead to high electrical resistivity of the Pt deposits.

Conclusion

In this paper, we show that it is possible to deposit Pt with a Cs^+ FIB. Growth rates were measured for Ga^+ and Cs^+ ions at different acceleration voltages. The rate mainly increases linearly with ion current density. Pt layers deposited with Cs^+ ions at 2 and 5 kV react with air and form bubbles. This similarity in the occurrence of surface bubbles between Cs^+ and Rb^+ may reveal a characteristic phenomenon of alkali metal ion-induced deposition. The electrical resistivity of the deposited Pt decreases with increasing acceleration voltage and is mostly independent of the ion current density. The Cs^+ FIBID-Pt has resistivity values between those of Ga^+ and Rb^+ FIBID-Pt, while having a lower Pt content. Lower current densities and acceleration voltages were found to lead to a higher electrical resistivity.

Appendix

Table 2 contains the complete set of parameters of the FIBID for the growth rate measurements.

Table 2: Complete set of parameters of the FIBID for the growth rate measurements.

Ion	Acceleration voltage [kV]	Ion current [pA]	Current density [pA·μm^{-2}]	Step size [nm]	Layer height [nm]	Growth rate [nm/s]	Volume per dose [μm^3/nC]
Cs	16	20	1.00	80	101	0.67	0.67
	16	41	2.05	100	192	1.28	0.62
	16	105	5.25	100	500	3.33	0.63
	16	196	9.80	100	885	5.90	0.60
	16	285	14.25	100	1090	7.27	0.51
	8	21	1.15	100	83	0.55	0.48
	8	62	2.90	100	224	1.49	0.51
	8	130	5.40	100	479	3.19	0.59
	8	220	8.90	150	664	4.43	0.50
	8	300	11.80	150	830	5.53	0.47
	5	17	0.85	100	57	0.38	0.45
	5	40	2.00	100	165	1.10	0.55
	5	114	5.70	200	331	2.21	0.39
	5	241	12.05	200	556	3.71	0.31

Table 2: Complete set of parameters of the FIBID for the growth rate measurements. (continued)

	30	17.8	0.89	24.5	58	0.39	0.43
	30	36	1.80	32.5	122	0.81	0.45
	30	47	2.35	40	157	1.05	0.45
	30	91	4.55	52.5	309	2.06	0.45
	30	292	14.60	95	885	5.90	0.40
	30	396	19.80	132.5	1225	8.17	0.41
	16	17	0.85	40	83	0.55	0.65
	16	27	1.35	50	138	0.92	0.68
	16	58	2.90	67.5	320	2.13	0.74
	16	188	9.40	187.5	893	5.95	0.63
	16	225	11.25	250	1046	6.97	0.62
Ga	16	307	15.35	250	1473	9.82	0.64
	8	14	0.70	55	57	0.38	0.54
	8	25	1.25	80	132	0.88	0.70
	8	76	3.80	145	346	2.31	0.61
	8	91	4.55	210	430	2.87	0.63
	8	132	6.60	220	509	3.39	0.51
	8	166	8.30	295	831	5.54	0.67
	5	15	0.75	100	29	0.19	0.26
	5	49	2.45	190	151	1.01	0.41
	5	61	3.05	232.5	229	1.53	0.50
	5	78	3.90	250	218	1.45	0.37
	5	110	5.50	397.5	375	2.50	0.45

Funding

This work is part of the project Next-Generation Focused Ion Beam (NWO-TTW16178) of the research program Applied and Engineering Sciences (TTW), which is (partly) financed by the Dutch Research Council (NWO). The authors are all members of the FIT4NANO COST Action CA19140.

ORCID® iDs

Thomas Henning Loeber - https://orcid.org/0000-0003-4697-1761

Data Availability Statement

Data generated and analyzed during this study is available from the corresponding author upon reasonable request.

Preprint

A non-peer-reviewed version of this article has been previously published as a preprint: https://doi.org/10.3762/bxiv.2025.12.v1

References

1. Alkemade, P. F. A.; Miro, H. *Appl. Phys. A: Mater. Sci. Process.* **2014,** *117,* 1727–1747. doi:10.1007/s00339-014-8763-y
2. Utke, I.; Hoffmann, P.; Melngailis, J. *J. Vac. Sci. Technol., B: Microelectron. Nanometer Struct.–Process., Meas., Phenom.* **2008,** *26,* 1197–1276. doi:10.1116/1.2955728
3. Gazzadi, G. C.; Mulders, J. J. L.; Trompenaars, P.; Ghirri, A.; Rota, A.; Affronte, M.; Frabboni, S. *Microelectron. Eng.* **2011,** *88,* 1955–1958. doi:10.1016/j.mee.2010.12.031
4. Orús, P.; Sigloch, F.; Sangiao, S.; De Teresa, J. M. *Nanomaterials* **2022,** *12,* 1367. doi:10.3390/nano12081367
5. Höflich, K.; Hobler, G.; Allen, F. I.; Wirtz, T.; Rius, G.; McElwee-White, L.; Krasheninnikov, A. V.; Schmidt, M.; Utke, I.; Klingner, N.; Osenberg, M.; Córdoba, R.; Djurabekova, F.; Manke, I.; Moll, P.; Manoccio, M.; De Teresa, J. M.; Bischoff, L.; Michler, J.; De Castro, O.; Delobbe, A.; Dunne, P.; Dobrovolskiy, O. V.; Frese, N.; Gölzhäuser, A.; Mazarov, P.; Koelle, D.; Möller, W.; Pérez-Murano, F.; Philipp, P.; Vollnhals, F.; Hlawacek, G. *Appl. Phys. Rev.* **2023,** *10,* 041311. doi:10.1063/5.0162597
6. Utke, I.; Michler, J.; Winkler, R.; Plank, H. *Micromachines* **2020,** *11,* 397. doi:10.3390/mi11040397
7. Chen, P.; Salemink, H. W. M.; Alkemade, P. F. A. *J. Vac. Sci. Technol., B: Microelectron. Nanometer Struct.–Process., Meas., Phenom.* **2009,** *27,* 2718–2721. doi:10.1116/1.3237147
8. Hlawacek, G.; Gölzhäuser, A., Eds. *Helium Ion Microscopy;* NanoScience and Technology; Springer International Publishing: Cham, Switzerland, 2016. doi:10.1007/978-3-319-41990-9
9. McClelland, J. J.; Steele, A. V.; Knuffman, B.; Twedt, K. A.; Schwarzkopf, A.; Wilson, T. M. *Appl. Phys. Rev.* **2016,** *3,* 011302. doi:10.1063/1.4944491
10. Xu, S.; Li, Y.; Vredenbregt, E. J. D. *J. Vac. Sci. Technol., B: Nanotechnol. Microelectron.: Mater., Process., Meas., Phenom.* **2022,** *40,* 042801. doi:10.1116/6.0001838

11. Li, Y.; Xu, S.; Sezen, M.; Misirlioglu, F. B.; Vredenbregt, E. J. D. *J. Vac. Sci. Technol., B: Nanotechnol. Microelectron.: Mater., Process., Meas., Phenom.* **2023,** *41,* 042803. doi:10.1116/6.0002609
12. Li, Y. Characterization and Application of an Ultracold Rubidium Focused Ion Beam. Ph.D. Thesis, Eindhoven University of Technology, Eindhoven, The Netherlands, 2023. https://research.tue.nl/files/313563364/20231215_Li_Y._hf.pdf
13. Knuffman, B.; Steele, A. V.; McClelland, J. J. *J. Appl. Phys.* **2013,** *114,* 044303. doi:10.1063/1.4816248
14. Steele, A. V.; Schwarzkopf, A.; McClelland, J. J.; Knuffman, B. *Nano Futures* **2017,** *1,* 015005. doi:10.1088/2399-1984/aa6a48
15. Li, Y.; Xu, S.; Loeber, T. H.; Vredenbregt, E. J. D. *Microsc. Microanal.* **2024,** *30,* 817–824. doi:10.1093/mam/ozae087
16. Loeber, T. Benefits of a Cs FIB with a low temperature ion source compared to a standard Ga FIB. https://www.zerok.com/assets/slides/Krakau2022.pdf (accessed Oct 1, 2023).
17. Storms, H. A.; Brown, K. F.; Stein, J. D. *Anal. Chem. (Washington, DC, U. S.)* **1977,** *49,* 2023–2030. doi:10.1021/ac50021a034
18. De Castro, O.; Audinot, J.-N.; Hoang, H. Q.; Coulbary, C.; Bouton, O.; Barrahma, R.; Ost, A.; Stoffels, C.; Jiao, C.; Dutka, M.; Geryk, M.; Wirtz, T. *Anal. Chem. (Washington, DC, U. S.)* **2022,** *94,* 10754–10763. doi:10.1021/acs.analchem.2c01410
19. Wirtz, T.; Migeon, H.-N. *Surf. Sci.* **2004,** *557,* 57–72. doi:10.1016/j.susc.2004.03.015
20. Priebe, A.; Michler, J. *Ultramicroscopy* **2019,** *196,* 10–17. doi:10.1016/j.ultramic.2018.09.008
21. Okumura, T.; Tamura, K.; Fujii, E.; Yamada, H.; Kogure, T. *Microscopy (Oxford, U. K.)* **2014,** *63,* 65–72. doi:10.1093/jmicro/dft045
22. Yoshigoe, A.; Shiwaku, H.; Kobayashi, T.; Shimoyama, I.; Matsumura, D.; Tsuji, T.; Nishihata, Y.; Kogure, T.; Ohkochi, T.; Yasui, A.; Yaita, T. *Appl. Phys. Lett.* **2018,** *112,* 021603. doi:10.1063/1.5005799
23. zeroK Nanotech, Cs FIB: Zero. https://www.zerok.com/products.html#FIBZERO_GOTO (accessed Aug 1, 2023).
24. Ziegler, J. F.; Ziegler, M. D.; Biersack, J. P. *Nucl. Instrum. Methods Phys. Res., Sect. B* **2010,** *268,* 1818–1823. doi:10.1016/j.nimb.2010.02.091
25. De Teresa, J. M.; Córdoba, R.; Fernandez-Pacheco, A.; Montero, O.; Strichovanec, P.; Ibarra, M. R. *J. Nanomater.* **2009,** 936863. doi:10.1155/2009/936863
26. ImageJ, Image processing and analysis in Java. https://imagej.net/ij/ (accessed April 11, 2025).
27. Fernández-Pacheco, A.; De Teresa, J. M.; Córdoba, R.; Ibarra, M. R. *Phys. Rev. B* **2009,** *79,* 174204. doi:10.1103/physrevb.79.174204
28. Telari, K. A.; Rogers, B. R.; Fang, H.; Shen, L.; Weller, R. A.; Braski, D. N. *J. Vac. Sci. Technol., B: Microelectron. Nanometer Struct.–Process., M eas., Phenom.* **2002,** *20,* 590–595. doi:10.1116/1.1458958

License and Terms

BEILSTEIN JOURNAL OF NANOTECHNOLOGY

Wavelength-dependent correlation of LIPSS periodicity and laser penetration depth in stainless steel

Nitin Chaudhary[1], Chavan Akash Naik[2], Shilpa Mangalassery[1], Jai Prakash Gautam[2] and Sri Ram Gopal Naraharisetty[*1]

Full Research Paper

Open Access

Address:
[1]School of Physics, University of Hyderabad, Gachibowli, Hyderabad, 500046, India and [2]School of Engineering Sciences and Technology, University of Hyderabad, 500046, India

Email:
Sri Ram Gopal Naraharisetty[*] - srgopal234@gmail.com

* Corresponding author

Keywords:
cross section of LIPSS; high spatial frequency LIPSS (HSFL); laser-induced periodic surface structures (LIPSS); low spatial frequency LIPSS (LSFL); maximum LIPSS; penetration depth

Beilstein J. Nanotechnol. **2025,** *16,* 1302–1315.
https://doi.org/10.3762/bjnano.16.95

Received: 10 February 2025
Accepted: 18 July 2025
Published: 11 August 2025

This article is part of the thematic issue "Energetic ions and photons for engineering nanomaterials".

Associate Editor: P. Leiderer

Abstract

This research paper delves into the exploration of laser-induced periodic surface structures (LIPSS) on a 100 µm thin stainless steel (SS) sheet. Through the application of laser irradiation with wavelengths spanning from 400 to 2400 nm, we systematically generate ladder-like LIPSS across a substantial area, incorporating LIPSS with both low spatial frequency (LSFL) and high spatial frequency (HSFL) simultaneously. Notably, the embedded LIPSS exhibit a linear relationship in the observed spatial periodicity of LSFL and HSFL with wavelengths up to 2000 nm, after which a decrease in periodicity is observed. By employing cross-sectional electron microscopy, we scrutinize the penetration depth of laser radiation or laser-affected zone, in the LIPSS-formed SS sheets, revealing a parallel trend with LSFL and HSFL spatial periodicity. Specifically, the penetration depth increases with wavelength up to 2000 nm, reaching a peak at approximately 13 µm, and subsequently decreases. This distinctive correlation underscores the role of plasma material reorganizational effects in LIPSS formation at higher wavelengths, presenting a new experimental observation to the existing literature. The findings enhance our comprehension of laser–material interactions and hold potential implications for surface engineering and material science applications.

Introduction

Nanostructuring on surfaces plays a pivotal role in governing surface properties, and laser-induced periodic surface structures (LIPSS) have emerged as a potent method for achieving nanoscale surface modifications. Over the past decade, LIPSS and laser ablation techniques for micro/nanostructuring have garnered significant attention due to their versatile applications. In particular, fabricating subwavelength structures using high-power pulsed lasers offers a flexible, single-step processing approach compatible with industry standards, making it a promising alternative to high-precision lithography techniques [1-3].

The utilization of short femtosecond laser pulses has proven instrumental in overcoming diffraction limit restrictions, enabling controlled fabrication of periodic subwavelength structures [4-9]. This controlled structuring offers a straightforward means to manipulate the functional and surface characteristics of substrates [10-13]. The applications span a broad spectrum, encompassing colorization control, self-cleaning surfaces, regulation of cell and bacterial films, antireflective surfaces, surface-enhanced Raman spectroscopy, reduction of friction and wear, fuel injection, and enhancement of tribological properties [14-30].

Extensive research efforts have been directed toward understanding LIPSS, encompassing systematic investigations on different metals, semiconductors, and polymers [9,12,31-39]. LIPSS characterized by ripple-like subwavelength periodic structures on a material's surface, are broadly classified into low spatial frequency LIPSS (LSFL) and high spatial frequency LIPSS (HSFL), based on their spatial periodicity (Λ) relative to the laser wavelength (λ). Typically in metal surfaces with high absorbance, the range of LSFL periodicity is $\lambda > \Lambda > \lambda/2$, oriented perpendicular to the incident polarization, and HSFL periodicities are much smaller and in the range of $\Lambda < \lambda/2$, orientated parallel to the incident polarization [40-45]. A recent review by Jörn Bonse and Stephan Gräf provides a comprehensive classification based on materials and associated theories [46].

Two primary classes of theories – electromagnetic and matter reorganization – have been proposed to explain LIPSS formation [46-48]. LSFL formation is often attributed to the interference between incoming electromagnetic radiation and surface electromagnetic waves and involves surface polaritons and surface plasmon polaritons (SPPs). These SPPs propagate along the interface of the two media in which the electron density coherently oscillates, coupled to both media. Usually, LIPSS formation is a multipulse phenomenon, as pulse after pulse create a different roughness on the surface or feedback mechanism to form certain SPP modes. The interference of incoming light with scattering from the SPP modes can lead to the modulation of the net localized energy distribution on the surface, and this field absorption is manifested as LIPSS on the surface. This process depends on several experimental factors, namely, incident wavelength, polarization, material dielectric, dielectric, fluence of the laser, pulse width, repetition rate, and number of pulses. These parameters result in different periodicities and aspect ratios, and corresponding theoretical predictions are not yet completely mature or framed. The formation of HSFL, however, remains an unrevealed phenomenon with theories ranging from twining [49] and self-organization [33] to second harmonic generation [11] and cavitation instability [23,50,51]. Despite numerous studies, the formation mechanism of HSFL and the reason for their shorter periodicity compared to the laser wavelength remain elusive. Our previous work addressed this gap by patterning a single line structure with laser irradiation wavelengths ranging from 400 to 2200 nm. From this, a linear trend in LIPSS characteristics was observed up to 2000 nm, and the threshold of the LIPSS formation was determined [52]. In the present work, we extend the LIPSS over a large area, instead of a single line, using 400 to 2400 nm laser irradiation. This enabled the examination of the cross-sectional zone where the cumulative effect of the laser irradiation occurs. We analyzed how these effects correlate with the incident laser wavelength.

The manuscript delves into the critical parameter of penetration depth, or laser-affected zone, and its impact on material processing efficiency using femtosecond laser pulses. The study reveals deviations from the expected behavior predicted by existing theories, showing a wavelength-dependent penetration depth on stainless steel. This finding challenges our understanding of how metal surfaces respond to incident wavelengths [53,54]. This work advances our comprehension of LIPSS structures and their applications, shedding new light on the interplay between incident wavelengths and surface interactions. The paper concludes by emphasizing the importance of optical properties, laser parameters, and material characteristics in determining penetration depth, thereby contributing to the broader understanding of light–material interactions.

Materials and Methods

Materials

A double-sided polished stainless steel surface (SS304) with a thickness of 100 μm was utilized. Before and after the laser treatment, these SS surfaces underwent ultrasonic rinsing with acetone for 10 min each, aiming to eliminate dust particles and other contaminants.

Experimental details

A commercially available Ti:sapphire femtosecond laser operating at an 800 nm central wavelength, with 75 fs pulse duration, 5.5 mJ/pulse energy, and a repetition rate of 1 kHz, was utilized for laser direct writing experiments. The fundamental part of the laser, providing 2.6 mJ/pulse, acted as the pump for an optical parametric amplifier (OPA), allowing for flexible tuning of the laser wavelength from 400 to 2400 nm. The TOPAS Prime optical parametric amplifier supplied by Light Conversion is used for this purpose. Subsequently, the laser beam was directed to ablate stainless steel following wavelength adjustments. To regulate the laser beam's final intensity at the sample, an ND variable filter (VF) was employed as

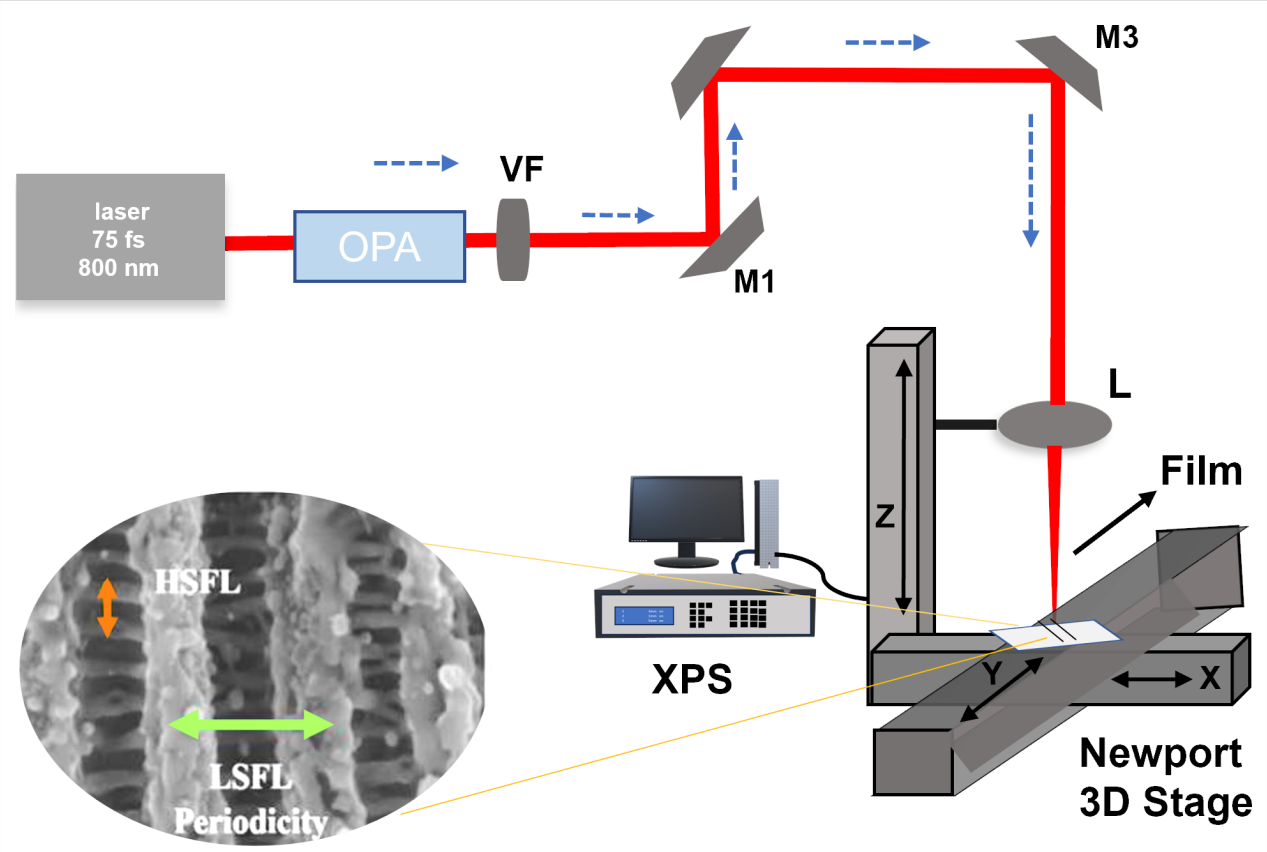

Figure 1: Depicts the experimental setup utilized in the fabrication process of laser-induced periodic surface structures (LIPSS). Critical components of this setup include the femtosecond laser, optical parametric amplifier (OPA), ND variable filter (VF), mirrors (M), three-axis stages (3D stages), and a convex lens (L) employed to focus the laser beam onto the surface precisely. The inset image shows the ladder-like LIPSS structures on the laser-patterned SS surface.

shown in Figure 1. For nanostructuring, a convex lens made of CaF_2 with a focal length of 5 cm was used to focus the laser beam. Precise sample positioning was achieved using a three-dimensional Newport stage with a resolution of 1 µm, controlled by an ESP motion controller, with all axes being computer-controlled.

In our previous work, we had generated LIPSS on stainless steel via single-line scanning [52]. In the present work to optimize the fabrication of large-area embedded LIPSS, a series of specimens were generated using four discrete laser scanning intervals, that is, 60, 50, 40, 30, and 20 µm. It involved a meticulous process to fine-tune laser parameters such as power, speed, and step size to attain the desired LIPSS pattern. Each incident wavelength required creating samples with varying scanning speeds, specifically, 0.2, 0.5, 0.8, and 1.5 mm/s, with the input laser beam power fixed at 20 mW. For each wavelength, four different step sizes and scanning speeds were explored. Table 1 below displays the optimal spatial periodicity of LIPSS structures obtained for each wavelength. In this work, we fabricated LIPSS over a large area 5 mm × 5 mm and optimization was carried out for best ladder-like structures over a large area. The size of the sample that one can make is limited by the scanning range of the three axis stages.

Electrolytic etching

The cross-sectional area of the laser-treated stainless steel samples underwent thorough polishing across their thickness using various grades of emery paper (3000, 4000, and 5000). Subsequently, alumina polishing was applied for 20 min to achieve a flawless mirror finish on the surface. A solution containing 10 g of oxalic acid in 100 mL of distilled water was employed for etching the stainless steel.

An external etching process was conducted to examine the surface morphology of the samples and precisely measure the depth to which the laser heat affected or penetrated the zone. Imaging was performed using an FEI NOVA NANO SEM 450 scanning electron microscope. External etching was executed using a DC power supply machine, applying a voltage of 10 kV. In this procedure, a steel plate served as the cathode and was submerged in the oxalic acid solution, while the steel sample

acted as the anode and was also immersed in the solution. Etching was carried out for 80 s to unveil the microstructure.

Characterization and measurements

High-resolution images of cross section and surface morphologies of the sample were obtained using a FESEM (Zeiss, Ultra 55). EDS was used to determine the elemental distribution on the bare and laser-treated surfaces. The periodicity in various locations on the FESEM images was determined using ImageJ software.

Results and Discussion

Introduction to embedded LIPSS to form ladder-like structures

The laser-induced ripples formed on surfaces typically exhibit two types of spatial periodicity, namely, LSFL and HSFL, which are generally produced at different laser fluence regimes. In most cases, the generation of LIPSS occurs at repetition rates of 100 kHz or less, where the sequence of successive pulses creates a feedback mechanism conducive to LIPSS formation. This results in pulse intervals of more than 10 μs, deemed sufficient for efficient heat conduction [55,56]. To achieve a clear formation of HSFL or LSFL, it is essential to optimize the laser direct writing (LDW) parameters, such as fluence, focusing, scanning speed, polarization, and repetition rate of the pulses. By tuning the LDW parameters, both LSFL and HSFL can be simultaneously formed on a metal surface [52]. In our previous work, we presented optimal laser parameters for the formation of ladder-like structures over a single line. In that study, the laser power/fluence was varying, and we used a fixed scanning speed of 0.2 mm/s. To cover larger areas, we need faster scanning speeds. In this work we used a fixed power for all the wavelengths and varied the scanning speed from 0.5 to 1.6 mm/s. The most important parameter for the formation of large-area LIPSS is the stepsize or line interval, which was optimized for each wavelength for the best ladder-like structures. This approach is more complex compared to single-line patterning as one has to attain structural uniformity across the entire surface [52].

A notable observation is that the periodicity of LIPSS increases when using laser wavelengths from 400 to 2000 nm, after which it decreases at both 2200 and 2400 nm irradiation. Naturally, as the photon energy decreases, the ability to ablate the material also decreases. The increase and decrease in the periodicity of large-area ladder-like LIPSS with changes in the wavelength of irradiation are explained in later sections.

The exact mechanism of LSFL formation and the reason for the shorter HSFL periods than the laser wavelength remains not fully understood, despite numerous studies on this topic. The most puzzling aspect of our current results is the decrease in the periodicity of LIPSS after irradiation with wavelengths beyond 2000 nm. Further experiments and theoretical studies are necessary to develop a precise model or understand the underlying mechanisms. In pursuit of this understanding, we monitored the formation of plasma and the depth of laser penetration inside the material for all wavelengths of femtosecond laser irradiations.

According to the plasmonic model, when the radiation is incident at a normal angle, the period of the resulting ripples can be determined using the equation [57-59]:

$$\Lambda = \frac{\lambda}{\left(\mathrm{Re}\sqrt{\frac{\varepsilon_d * \varepsilon_m}{\varepsilon_d + \varepsilon_m}} \right)},$$

where Λ is the ripple periodicity (LSFL spatial periodicity), λ is the incident wavelength, and ε_d and ε_m are the dielectric constants of the medium and metal, respectively. $\varepsilon_d = 1$ (dielectric constant of the medium) and $\varepsilon_m = (n + ik)^2$, n is the real part of the refractive index of the metal, and k is the coefficient of extinction. According to this model, the periodicity should exhibit an increasing trend with wavelength when there is no resonance. However, the experiments presented in this work show some anomalies.

The refractive index of stainless steel is $n = 1.580$, and the extinction coefficient is $k = 3.413$ at 500 nm [60]. The calculated ripple periodicity $\Lambda = 470$ nm is higher than most of the experimental values. This discrepancy may arise because the refractive index values of stainless steel are determined at room temperature, which might not be appropriate for metals heated with intense femtosecond laser pulses. The LIPSS period becomes smaller when the stainless steel surface is rougher as the roughness increases the real part of the refractive index at the metal–air interface [61].

Variation of LIPSS with varying laser power

The spatial periodicity of LIPSS varies under different experimental conditions. This section specifically examines how surface morphology and the periodicity of LSFL and HSFL change with varying power values while maintaining a fixed wavelength of 800 nm. Figure 2 illustrates the formation of LIPSS at 800 nm for different incident powers, that is, 20, 100, 200, and 400 mW. It is observed that, at the energy levels where LIPSS form, the spatial periodicity of LSFL undergoes slight variations, while the periodicity of HSFL remains relatively constant. However, as the power values increase, HSFL begin to deterio-

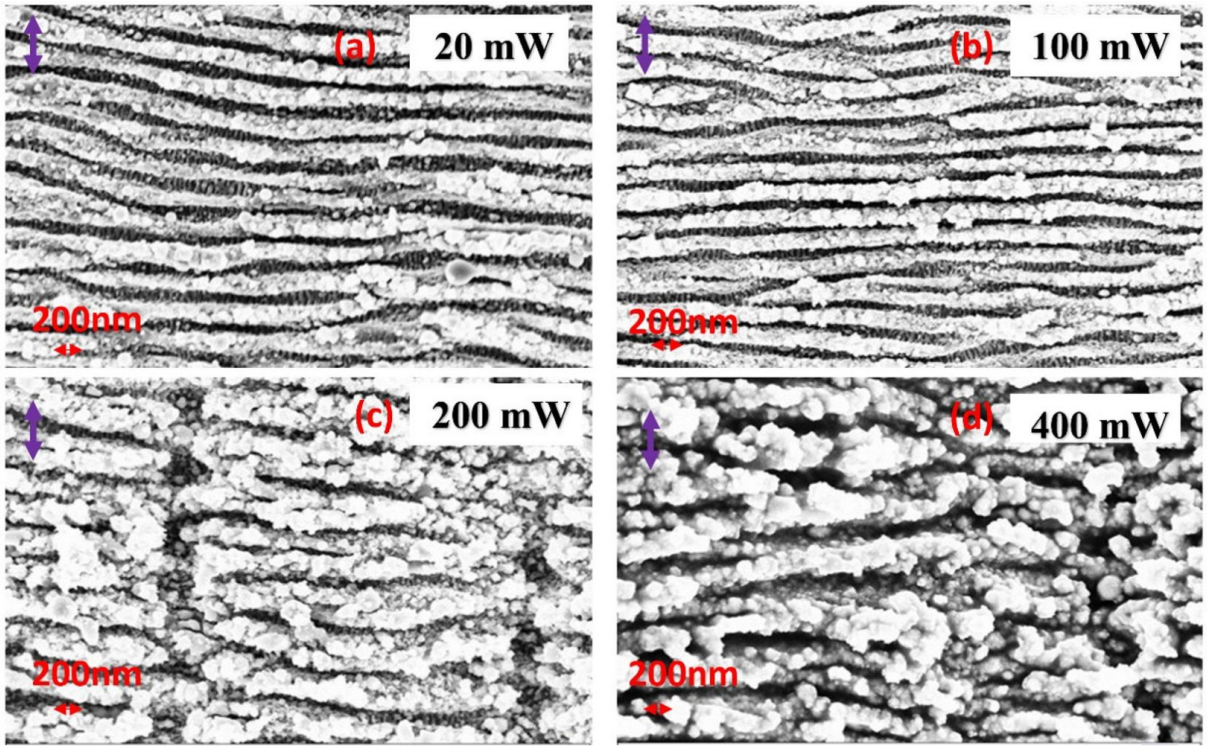

Figure 2: FESEM images of the surface after laser irradiation with the different incident laser powers: (a) 20 mW, (b) 100 mW, (c) 200 mW, and (d) 400 mW at 800 nm wavelength, 0.5mm/s scanning speed, and 60 µm scanning interval. The violet arrows show the polarization direction.

rate, and LSFL do not manifest uniformly across the surface, as depicted in Figure 2c,d. This increased power leads to more debris accumulation, resulting in inadequate formation of HSFL. Furthermore, with an increase in power, the surface cannot sustain LIPSS altogether. We kept the scanning speed constant at 0.5 mm/s here. Attaining a stable high power at all wavelengths from 400 to 2400 nm becomes difficult with our OPAs. In the following sections, we kept a constant power output of 20 mW for all wavelengths, while the fluence was changed for each wavelength. The optimization regarding LIPSS was performed by varying the scanning speed and the step size between the consecutive lines to generate large-area LIPSS for each irradiation wavelength.

Effect of scanning speed

The comparative analysis of LSFL and HSFL spatial periodicity with varying numbers of laser pulses per beam spot area is illustrated in Figure 3A for a laser wavelength of 2200 nm. When aiming to fabricate large-area LIPSS under a fixed incident laser wavelength, it becomes imperative to adjust both the scanning speed and interval carefully:

$$N = \frac{d \cdot f}{v}.$$

Here, N is number of effective laser pulses per beam spot area, f represents the repetition rate of the laser (1 kHz), d denotes the spot diameter at the focal point, and v signifies the scanning speed of the linear stage. As evidenced in Figure 3A, the spatial periodicity of both LSFL and HSFL remains consistent even with an increase in the number of effective laser pulses per beam spot area.

Considering that the spot diameter invariably expands with longer wavelengths, the laser-ablated area becomes more substantial in comparison to lower wavelengths. This phenomenon is crucial to note as it influences the fabrication of large-area LIPSS patterns. Perfect overlapping optimization becomes paramount in this process; any discrepancies in overlapping, whether excessive or insufficient, can lead to the destruction of LIPSS or incomplete patterning across the large surface area.

From the correlation between wavelength and spot diameter, the spot diameter of a focused laser beam increases with increasing wavelength due to the diffraction limit. Consequently, as you can see in Figure 3B, achieving optimal ladder-like structures across different wavelengths necessitates simultaneous adjustments in scanning speed and scanning interval. This coordinated approach ensures precise control over fabrication, resulting

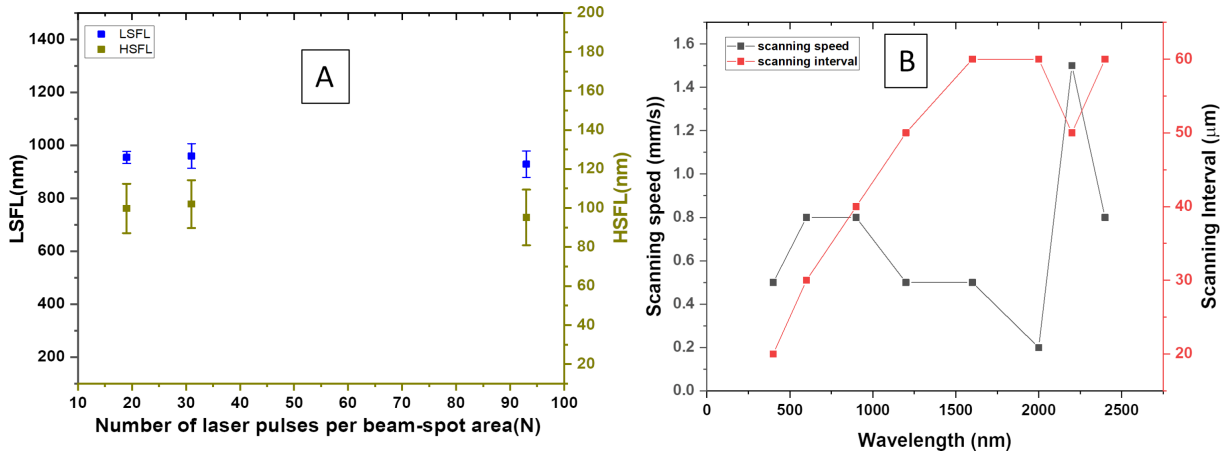

Figure 3: (A) Variations of spatial periodicity of LSFL and HSFL with the effective number of laser pulses per beam spot area on the incident wavelengths 2200 nm. (B) Scanning speed and scanning interval values for the best ladder-like structures with the incident wavelength.

in the desired LIPSS patterns on the target material surface over a large area limited by scanning stages.

Optimization of large-area LIPSS with the incident wavelength

As discussed in the previous section, several experimental LDW parameters influence the periodicity of the LIPSS. The scanning interval between successive lines plays an essential role in producing LIPSS on large areas of SS surfaces [33,47]. This section explains how the surface structures and spacing of LSFL and HSFL vary with exposure to wavelengths of 400, 600, 800, 1200, 1600, 2000, 2200, and 2400 nm at a constant laser power of 20 mW on a large area of stainless steel. The best ladder-like structures require optimal scanning speed and optimized step sizes between the successive laser lines, yielding clear and smooth ladder-like structures with embedded LSFL and HSFL for all the specified wavelengths over a larger area. The optimization process has been presented in detail in our previous work, where ladder-like LIPPS structures were observed over a single line [52]. In this work, we did not vary the average power of the incident beam for all wavelengths and kept it as a fixed parameter.

Figure 4 presents the surface morphologies, illustrating the periodic nature of ladder-like structures resulting from exposure to varying wavelengths under fixed laser power. The focused laser

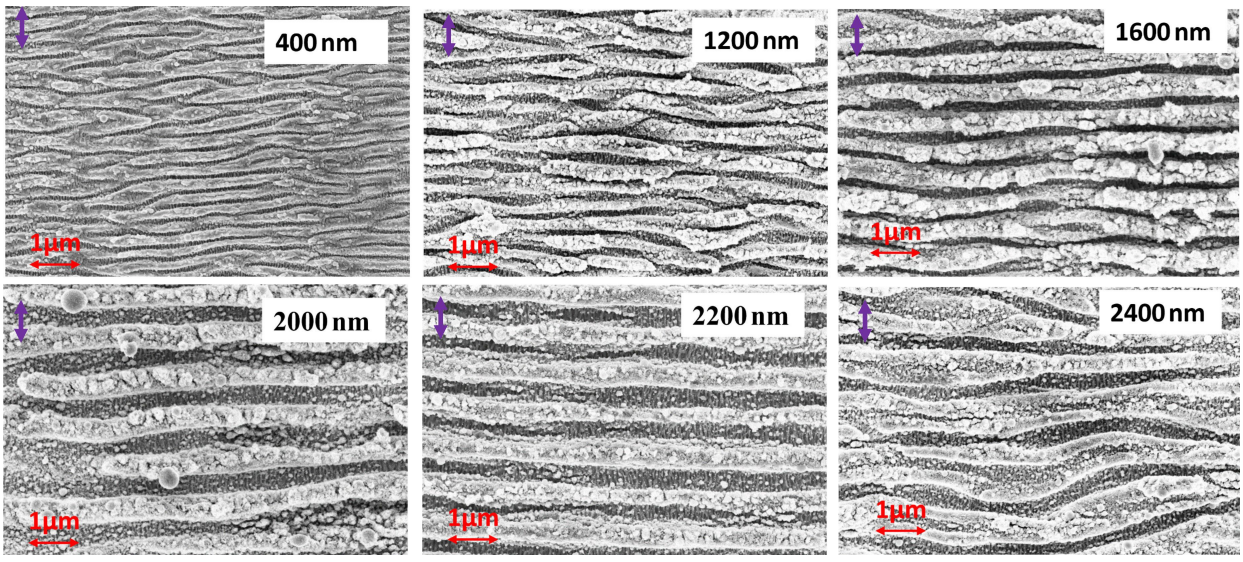

Figure 4: Surface patterns of the optimized ladder structures on a stainless steel surface at various incidence wavelengths.

spot diameter increases with the laser wavelength; hence, achieving the best ladder-like structure requires adjusting the scanning speed and step size between successive scans.

Figure 4 shows the LSFL perpendicular to the incident beam polarization, with the HSFL forming deep inside the grooves of the LSFL. The orientation of these embedded HSFL is perpendicular to the LSFL and parallel to the incident beam polarization. In all FESEM images, the incident polarization direction is represented by a violet arrow at the top left corner. High-resolution images of the embedded HSFL ladder-like structure is shown in Figure 5 for two wavelengths for better understanding. The aspect ratio of these HSFL is smaller compared to the LSFL grooves and cannot be quantified accurately due to instrumental limitations. Many theories suggest that the formation of HSFL structures is due to the metal surface's self-organization after laser irradiation [62], and some theories suggest the formation is due to the second harmonic generation at the surface [32].

Table 1 presents the obtained LSFL and HSFL periodicities for each wavelength along with the laser irradiation parameters. The spatial periodicity of both LSFL and HSFL exhibits an upward trend as the wavelength reaches 2000 nm, but subsequently displays a decline with further increases in wavelength. This decline is less pronounced compared to our previous report, as we maintained a constant incident power. The HSFL variation trend is very similar to the LSFL trend, as evident from Figure 6, but their orientation is perpendicular to the LSFL and embedded inside the grooves.

Cross-sectional depth measurements

In the previous section, we examined how LIPSS vary with the wavelength of the laser and how they behave under different laser scanning speeds, and scanning intervals. In this section, to investigate the reason behind the variation in the periodicity of LIPSS, we probe the laser penetration depth of the LIPSS structure at different wavelengths. Penetration depth could be a key parameter determining the efficiency and quality of material

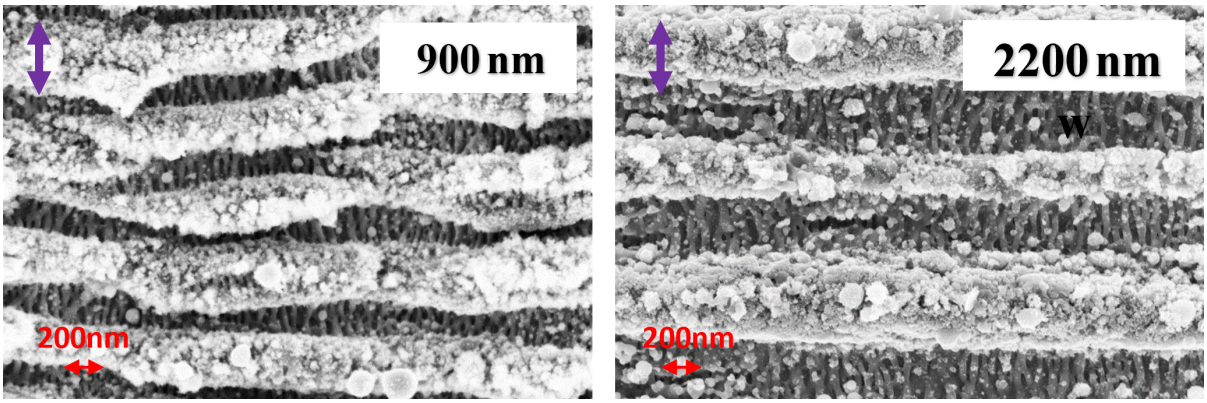

Figure 5: High-resolution images of ladder-like LIPSS formed at two incident wavelengths: 900 and 2200 nm. The violet arrows show the polarization direction.

Table 1: LSFL and HSFL spatial periodicities for each wavelength and corresponding parameters.

Incident wavelength (λ) nm	Spot diameter (μm)	Optimal fluence (J/cm^2)	Effective number of pulses per spot	Λ_{LSFL} (nm)	Λ_{HSFL} (nm)
400	38	49.1	17	298 ± 26	56 ± 7
600	35.7	26.2	16	431 ± 23	58 ± 7
800	17	9.8	24	337 ± 44	63 ± 12
900	52.1	4.9	49	601 ± 65	73 ± 18
1200	50.9	2.7	51	649 ± 50	85.0 ± 15
1600	59.9	5.4	66	697 ± 40	91 ± 16
2000	84.9	2.0	212	1093 ± 126	115 ± 16
2200	93.4	0.8	93	949 ± 28	98 ± 15
2400	95.5	0.6	119	1003 ± 37	103 ± 13

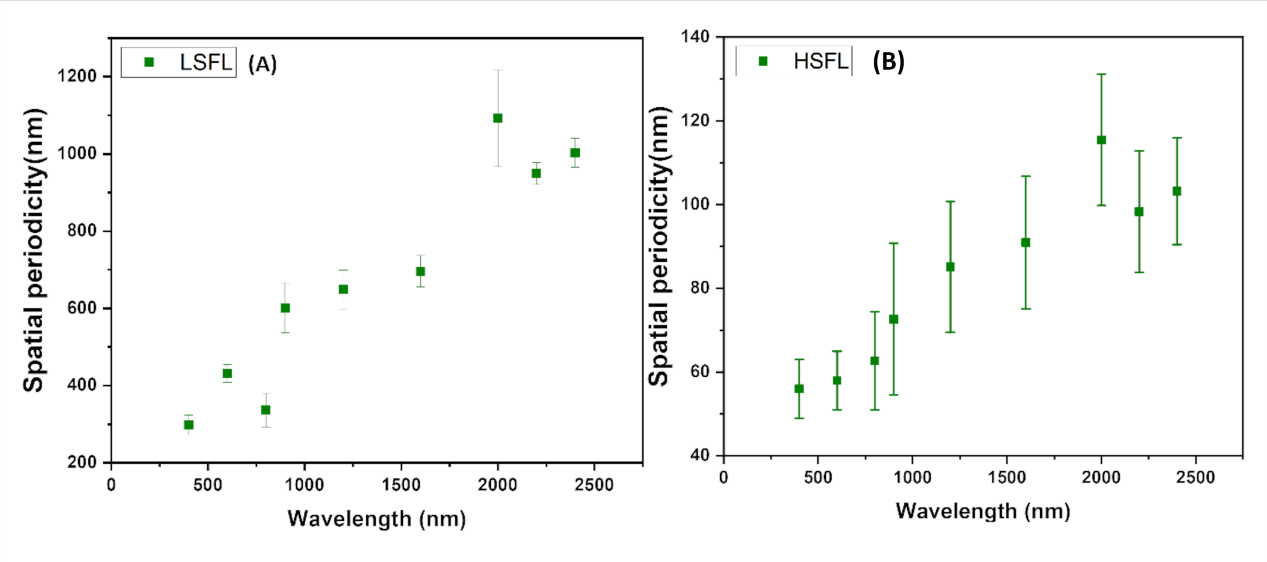

Figure 6: Variations of spatial periodicity of (A) LSFL and (B) HSFL with the incident laser wavelengths.

processing by femtosecond laser pulses. SPPs also experience energy loss due to absorption in the metal and scattering in other directions, which depend on the properties of the metal [43]. The penetration depth of SPPs into the metal measures how far the electric field of the SPP decays exponentially inside the metal.

Ash and colleagues reported the impact of wavelength and beam width on tissue penetration during light–tissue interaction. They found that higher wavelengths result in greater penetration depth, while larger spot sizes do not significantly increase penetration depth [63]. The penetration depth depends on the material's dielectric properties and the interface's geometry. It can also depend on the optical properties of the material, such as the refractive index, absorption coefficient, reflectivity, and laser parameters, such as the wavelength, pulse duration, fluence, incidence angle, and polarization [64]. Generally, penetration depth increases with increasing wavelength and decreases with increasing metal conductivity [53]. In the literature, most researchers used high-intensity pulse lasers for works on laser welding and substrate melting [57,58,61,63-67]. However, we could not find any experimental works dedicated to unraveling the penetration depth of LIPSS for the broadband in the existing literature.

As we know, energy penetration depth under intense femtosecond laser irradiation can be described by the following equation:

$$d = \frac{\lambda}{4\pi \mathrm{Im}\left[\tilde{n}(I)\right]},$$

where d is the skin depth of the material, $\tilde{n}(I)$ is the intensity-dependent complex refractive index, and $\mathrm{Im}\left[\tilde{n}(I)\right]$ is the imaginary part of the refractive index, responsible for absorption at the given intensity [68,69]. If the incident light wavelength increases, the skin depth of the material also increases. This means that longer wavelengths can penetrate deeper into the metal than shorter wavelengths, creating a larger plasma volume. However, under femtosecond laser processing, the material response depends on specific properties of the material, such as plasma formation, nonlinear absorption, and multiphoton ionization. In such a high-intensity regime, the optical constant of the material becomes dynamically dependent on the laser intensity. In the linear regime, pure metals such as copper, aluminum, and silver, which have low electrical resistivity, exhibit a low penetration depth for EM waves. In contrast, composite alloys such as stainless steel have higher resistivity and show a higher penetration depth than pure metals [70-72].

Figure 7 displays cross-sectional surface morphology images for samples irradiated with 600, 1200, 2000, 2200, and 2400 nm laser wavelength. As depicted in Figure 8 and Table 2, the diagram reveals a contradiction to the established principle of skin depth, as the depth of penetration increases with increasing wavelengths up to 2000 nm. However, beyond 2000 nm, the penetration depth in stainless steel diminishes. The trend of penetration depth variation is almost similar to the LSFL periodicity variation with wavelength, as shown in Figure 6A. This indicates that the amount of plasma created by the femtosecond laser on the surface plays a role in determining the periodicity of the LIPSS. In general, the plasma properties depend on the material, including the number of electrons present per unit

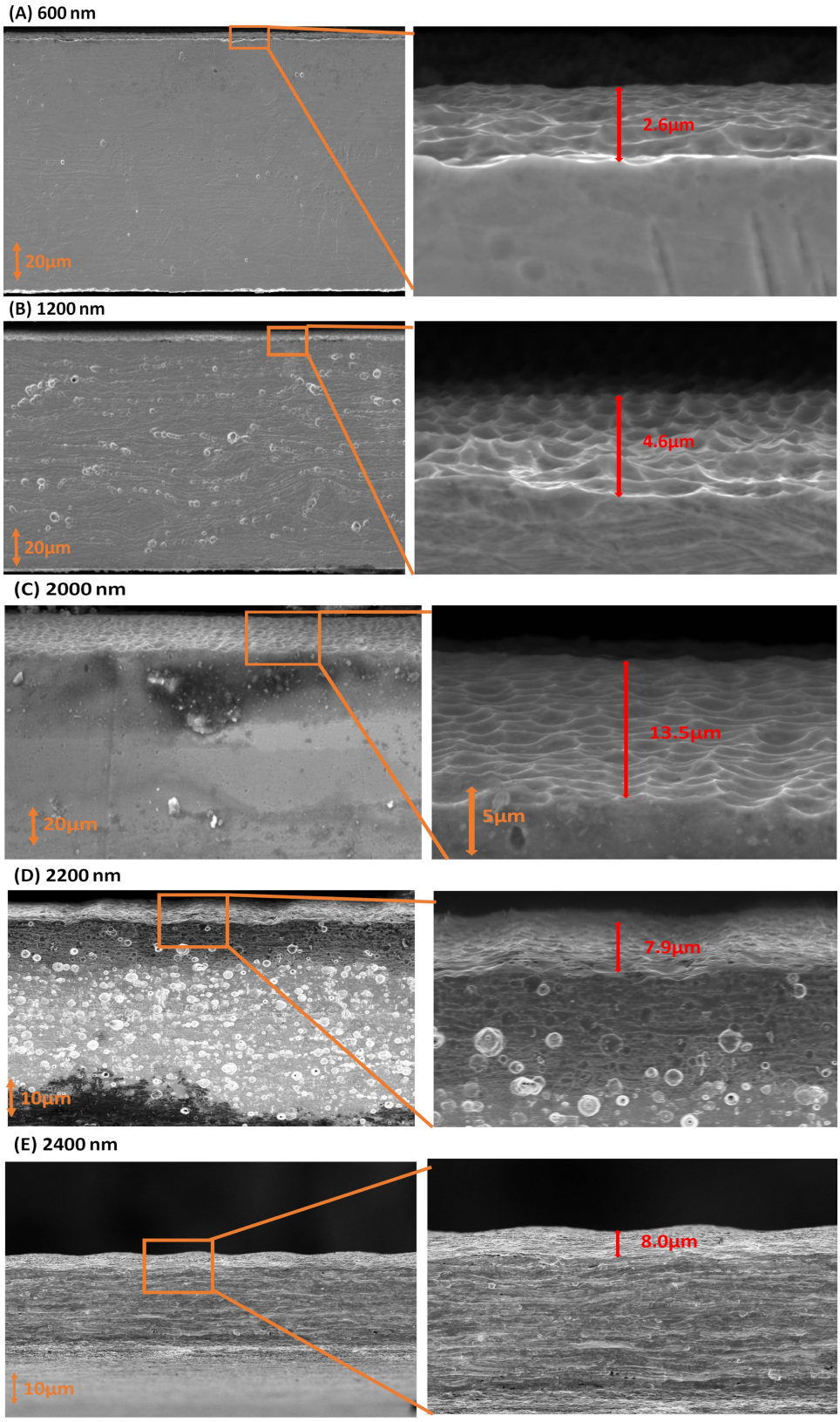

Figure 7: FESEM cross-sectional images of samples irridiated with wavelegths of (A) 600 nm, (B) 1200 nm, (C) 2000 nm, (D) 2200 nm, and (E) 2400 nm.

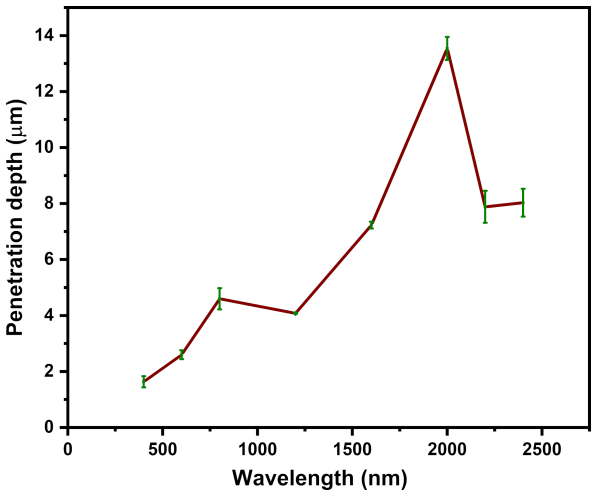

Figure 8: Penetration depth as function of the incident wavelength (400–2200 nm).

Table 2: Shows the penetration depth and aspect ratio corresponding to the different incident laser wavelengths.

Wavelength (nm)	Penetration depth *d* (μm)
400	1.7 ± 0.1
600	2.6 ± 0.2
800	4.5 ± 0.3
1200	4.1 ± 0.0
1600	7.2 ± 0.1
2000	13.5 ± 0.4
2200	7.9 ± 0.6
2400	8.0 ± 0.5

volume in the plasma and their characteristic frequency. The frequency at which unbound electrons within stainless steel oscillate in the presence of an electromagnetic field is known as the plasma frequency. The metallic substance's electron density and effective electron mass also affect the plasma frequency.

$$\omega_p = \sqrt{\frac{n_e e^2}{m_e \varepsilon_0}},$$

where ω_p is the plasmonic frequency, n_e is the electron density, and m_e is the effective mass of the electron.

Stainless steel has a more complex electron density than pure metals because it is composed of a mix of iron, chromium, nickel, and other elements. Stainless steel's electron density varies depending on the composition and microstructure of the alloy, typically falling around 10^{22} to 10^{23} cm^{-3} [73,74]. It is conceivable that the plasma frequency can have an effect at wavelengths exceeding 2000 nm, leading to a reduction in penetration depth for larger wavelengths (2200 and 2400 nm); detailed theory and experimental work are needed with pure metals to confirm this.

Depth of the patterned substrate at different powers

In this section, we investigated the penetration depth of irradiated stainless steel samples across different laser power values, employing a single wavelength of 800 nm. As the power is increased, it is well known that more material from the surface can be removed. However, the point of investigation is how the laser-affected zone or penetration depth varies with power in the remaining part of the material. To explore this, we irradiated large areas of stainless steel surfaces using laser powers of 20, 150, and 300 mW at a constant scanning speed of 0.8 mm/s. LIPSS are observed up to 150 mW. At higher powers, these structures are destroyed. As highlighted in our previous discussions, the integrity of the LSFL and HSFL began to deteriorate at significantly high fluence values (Figure 2). Regardless of the HSFL quality of formation, we investigated the penetration depth of the laser with increasing incident power. At higher powers, the depth of laser ablation into the material increases.

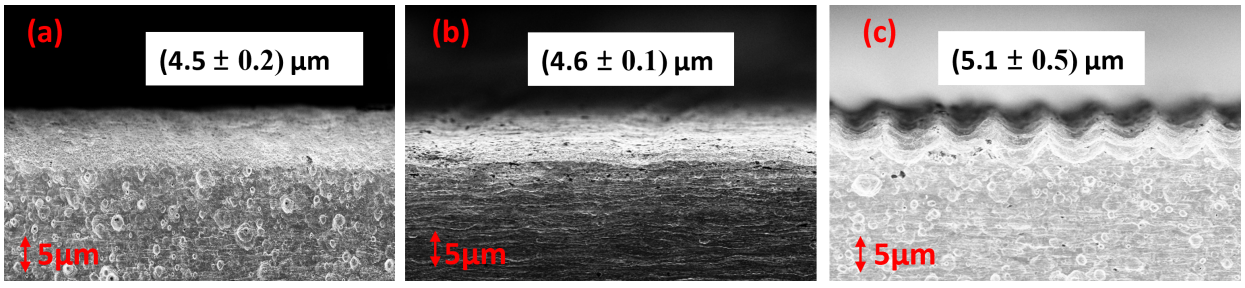

Figure 9: Penetration depth as function of the incident power at a wavelength of 800 nm. (a) 20 mW, (b) 150 mW, and (c) 300 mW.

Delving deeper, Figure 9 offers a cross-sectional view of the large-area patterned surface, providing crucial insights into the observed phenomena.

Our analysis revealed that the average penetration depth varied marginally across different fluence levels, that is 4.5 µm for 20 mW, 4.6 µm for 150 mW, and 5.1 µm for 300 mW (Figure 9). This observation leads us to conclude that under fluences of optimal LIPSS conditions, the penetration depth exhibits minimal variance in response to fluctuations in fluence levels.

Elemental distribution on the surface of LIPSS at different wavelengths

When subjecting a material's surface to pulsed laser irradiation, a fascinating phenomenon occurs, namely, the ablation of material along the laser path, accompanied by redistribution of metallic particles in the surrounding areas. This rapid process leads to the formation of intricate surface nanostructures, as elucidated in the previous sections. Here, we examine whether the fundamental composition of SS undergoes any alterations with varying incident wavelengths.

To investigate this, we conducted energy-dispersive X-ray spectroscopy (EDS) analysis on laser-treated stainless steel samples across different wavelengths alongside untreated stainless steel for comparison, as outlined in Table 3. Specifically, we examined the weight percentage of Cr, Fe, and Ni in three distinct areas of the laser-treated surface exhibiting ladder-like LIPSS.

Figure 10b–d present spectra corresponding to the three regions, that is, deep inside the grooves, at the upper side of the grooves, and at a large area (as depicted in Figure 10a). Remarkably, the EDS analysis revealed consistent weight percentages of Cr, Fe, and Ni across all three areas. This uniformity suggests that the elemental composition remains unchanged throughout the whole laser-treated surface.

For a comparative study, we also measured the elements on a polished stainless steel surface, depicted in Figure 10e. Figure 10f–h exhibits the EDS spectra of three different regions of the untreated surface, highlighting the presence of Cr, Fe, Ni, Mg, and C. However, magnesium and carbon are comparatively lower in abundance and not uniformly distributed in the unablated sample, and these peaks do not appear after the ablation at all wavelengths. This slight variation in elements between the laser-treated and untreated samples can be attributed to the highly intense femtosecond laser and its interaction with matter and the fact that these low-atomic-weight species could have escaped from the system.

Conclusion

For the first time, we demonstrated the fabrication of ladder-like LIPSS over a large area, with controllable periodicities ranging from 250 to 1200 nm by selecting the appropriate femtosecond laser irradiation wavelength. These controlled nanoscale LIPSS can be created over a large surface area, limited only by the scanning range of the instruments, offering a facile method for industrial applications. Our findings revealed that the periodicity of LIPSS increased with the laser wavelength up to 2000 nm, followed by a decrease at 2200 and 2400 nm. Current theories and mechanisms could not explain this anomalous trend, indicating a complex interplay of factors influencing material processing by femtosecond laser pulses. We investigated cross-sectional depth measurements on fabricated sheets to unravel this puzzle. Our studies demonstrated a perfect correlation between the penetration depth of the laser at each wavelength and the periodicity achieved at that wavelength. These results reveal that the reorganization of the material or the plasma created by the femtosecond lasers play an important role in forming LIPSS, along with the electromagnetic interactions of the surface plasmon modes. Furthermore, our EDS analysis showed that the material distribution is homogeneous, regardless of the irradiation wavelength. Overall, our study provides valuable insights into the mechanisms and optimization of

Table 3: Weight percentages of ablated stainless steel surface on different incident wavelength.

Elemental analysis by EDS			
Wavelength (nm)	Cr (wt %)	Fe (wt %)	Ni (wt %)
400	20.73	73.46	8.69
600	20.66	73.48	8.88
800	20.54	72.85	8.56
1200	20.33	72.06	8.74
1600	20.52	73.48	8.37
2000	20.56	73.48	8.37
2200	20.41	70.96	8.64

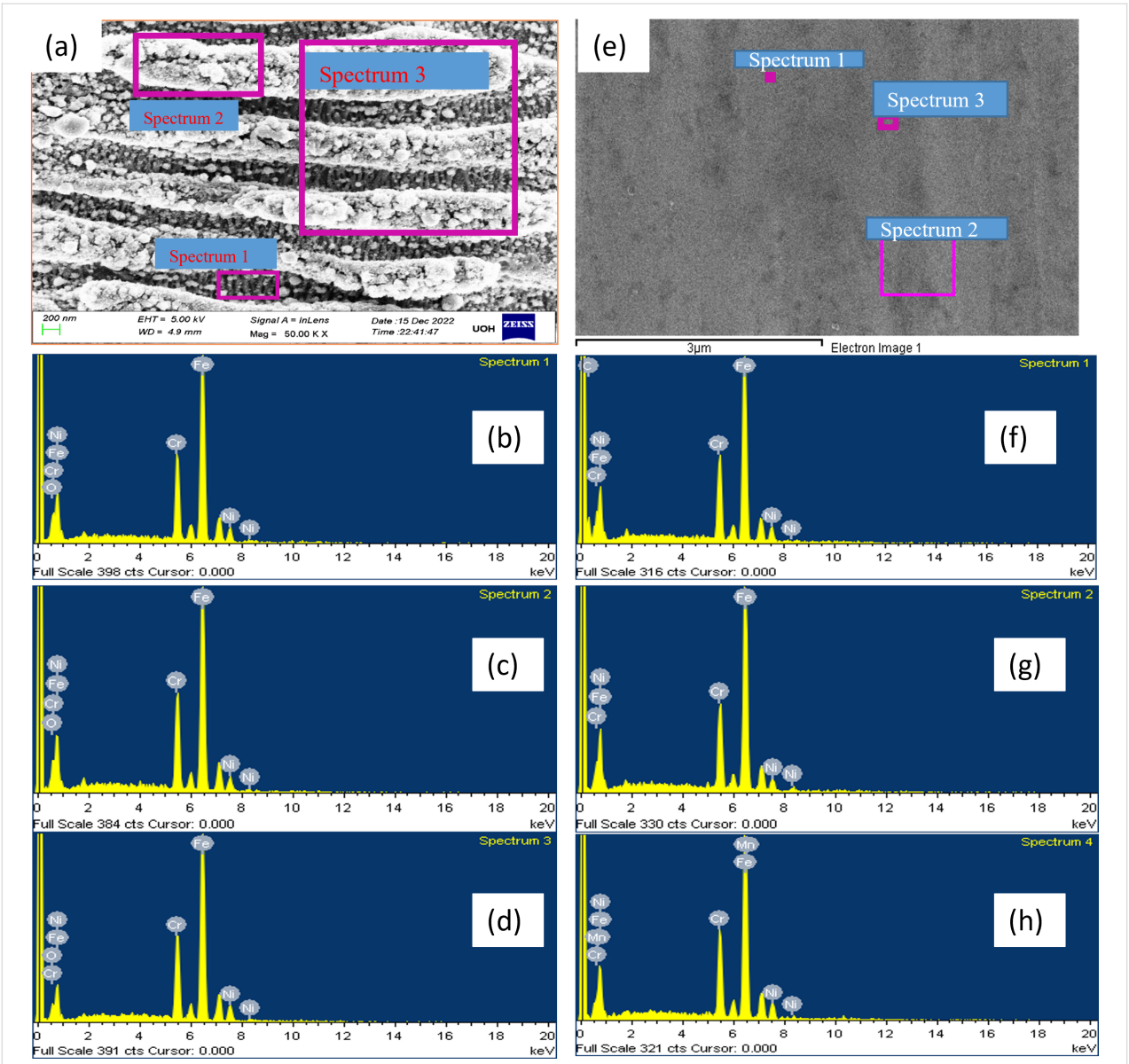

Figure 10: Showing the EDS elemental analysis for laser-treated and untreated stainless steel surface. (a) SEM image of laser-treated SS substrate, we picked three areas whose EDS spectra are shown in b, c, and d. (e) SEM image of bare SS surface, (f–h) elemental distribution corresponding to the different untreated polished stainless steel substrate areas.

LIPSS formation on stainless steel surfaces using femtosecond laser pulses. The findings have significant implications for developing new theories of light–matter interaction and various applications such as surface functionalization, microfabrication, and developing advanced materials with tailored surface properties.

Funding

The authors acknowledge financial support from the Respond Project (ISRO/RES/3/799/17-18), Indian Space Research Organization (ISRO), UoH Institute of Eminence (IoE) grant RC1-20-011, DST-SERB (EMR/000516), and DST-Purse. Nitin Chaudhary acknowledges the PMRF (Prime Minister Research Fellowship) fellowship funding.

Author Contributions

Nitin Chaudhary: data curation; formal analysis; investigation; methodology; validation; visualization; writing – original draft; writing – review & editing. Chavan Akash Naik: investigation. Shilpa Mangalassery: investigation. Jai Prakash Gautam: investigation. Sri Ram Gopal Naraharisetty: conceptualization; formal analysis; funding acquisition; investigation; methodology; project administration; supervision; validation; visualization; writing – original draft; writing – review & editing.

ORCID® iDs

Nitin Chaudhary - https://orcid.org/0000-0003-1900-9980
Chavan Akash Naik - https://orcid.org/0000-0001-6867-1351
Shilpa Mangalassery - https://orcid.org/0000-0002-4566-7592
Jai Prakash Gautam - https://orcid.org/0000-0001-6275-413X
Sri Ram Gopal Naraharisetty - https://orcid.org/0000-0002-6407-2017

Data Availability Statement

All data that supports the findings of this study is available in the published article and/or the supporting information of this article.

References

1. Kim, J.; Na, S. *Opt. Laser Technol.* **2007,** *39,* 1443–1448. doi:10.1016/j.optlastec.2006.10.001
2. Hu, M.; JJ Nivas, J.; Salvatore, M.; Oscurato, S. L.; Guarino, A.; Fittipaldi, R.; Amoruso, S.; Vecchione, A. *Adv. Phys. Res.* **2023,** *2,* 2300049. doi:10.1002/apxr.202300049
3. Yu, Y.; Deng, Y.; Al Hasan, M. A.; Bai, Y.; Li, R.-Z.; Deng, S.; Joshi, P.; Shin, S.; Hu, A. *Nanoscale Adv.* **2020,** *2,* 1195–1205. doi:10.1039/c9na00740g
4. Chen, T.; Wang, W.; Tao, T.; Pan, A.; Mei, X. *ACS Appl. Mater. Interfaces* **2020,** *12,* 49265–49274. doi:10.1021/acsami.0c16894
5. Liu, H.; Peng, J.; Liu, W.; Wang, Y.; Wu, J.; Zhang, G.; Wang, X.; Yan, Y. *NPG Asia Mater.* **2018,** *10,* 309–317. doi:10.1038/s41427-018-0011-z
6. Liu, S.; Tso, C. Y.; Lee, H. H.; Zhang, Y.; Yu, K. M.; Chao, C. Y. H. *Sci. Rep.* **2020,** *10,* 11376. doi:10.1038/s41598-020-68411-6
7. Taher, M. A.; Ponnan, S.; Prasad, H.; Rao, D. N.; Naraharisetty, S. R. G. *Nanotechnology* **2020,** *31,* 175301. doi:10.1088/1361-6528/ab674e
8. Taher, M. A.; Rao, D. N.; Naraharisetty, S. R. G. *Asian J. Phys.* **2021,** *30,* 1637–1646.
9. Su, Q.; Bai, S.; Han, J.; Ma, Y.; Yu, Y.; Deng, Y.; Wu, M.; Zheng, C.; Hu, A. *J. Laser Appl.* **2020,** *32,* 022013. doi:10.2351/1.5131528
10. Thirunaukkarasu, K.; Abu Taher, M.; Chaudhary, N.; Rajput, V. K.; Akash Naik, C.; Prakash Gautam, J.; Naraharisetty, S. R. G. *Opt. Laser Technol.* **2022,** *150,* 107935. doi:10.1016/j.optlastec.2022.107935
11. Florian, C.; Kirner, S. V.; Krüger, J.; Bonse, J. *J. Laser Appl.* **2020,** *32,* 022063. doi:10.2351/7.0000103
12. K, T.; Chaudhary, N.; Ponnan, S.; Taher, M. A.; Rajput, V. K.; Sharma, A. K.; K. V, S. R.; Naraharisetty, S. R. G. *ACS Appl. Eng. Mater.* **2023,** *1,* 1255–1262. doi:10.1021/acsaenm.3c00059
13. Tabares, I.; Soldera, M.; Voisiat, B.; Lasagni, A. F. *Sci. Rep.* **2024,** *14,* 9599. doi:10.1038/s41598-024-60420-z
14. Li, G.; Li, J.; Hu, Y.; Zhang, C.; Li, X.; Chu, J.; Huang, W. *Appl. Phys. A: Mater. Sci. Process.* **2015,** *118,* 1189–1196. doi:10.1007/s00339-014-8868-3
15. Liu, H.; Lin, W.; Hong, M. *APL Photonics* **2019,** *4,* 051101. doi:10.1063/1.5089778
16. Rajendran, R.; Krishnadev, E. R.; Anoop, K. K. *Photonics* **2023,** *10,* 793. doi:10.3390/photonics10070793
17. Banerjee, D.; Akkanaboina, M.; Kumar Kanaka, R.; Rao Soma, V. *Appl. Surf. Sci.* **2023,** *616,* 156561. doi:10.1016/j.apsusc.2023.156561
18. Bharathi, M. S. S.; Banerjee, D.; Soma, V. R. Femtosecond Laser Ablation Assisted Single-Step Fabrication of Metal-Semiconductor Interfaced SERS-Active Substrate. *Laser Congress 2023 (ASSL, LAC);* Technical Digest Series; Optica Publishing Group: Tacoma, WA, USA, 2023; JW2A.7. doi:10.1364/assl.2023.jw2a.7
19. Gaddam, A.; Sharma, H.; Dimov, S. *Proc. SPIE* **2024,** *13005,* 130050G. doi:10.1117/12.3017465
20. Höhm, S.; Rosenfeld, A.; Krüger, J.; Bonse, J. *Phys. Scr.* **2017,** *92,* 034003. doi:10.1088/1402-4896/aa5578
21. Stoian, R.; Colombier, J.-P. *Nanophotonics* **2020,** *9,* 4665–4688. doi:10.1515/nanoph-2020-0310
22. Fieser, D.; Lan, Y.; Gulino, A.; Compagnini, G.; Aaron, D.; Mench, M.; Bridges, D.; Shortt, H.; Liaw, P.; Hu, A. *Nanomaterials* **2024,** *14,* 554. doi:10.3390/nano14060554
23. Taher, M. A.; Prasad, H.; Navanith Krishnan, P. K.; Desai, N. R.; Naraharisetty, S. R. G. *Surf. Topogr.: Metrol. Prop.* **2019,** *7,* 035001. doi:10.1088/2051-672x/ab2d80
24. Bonse, J.; Kirner, S. V.; Höhm, S.; Epperlein, N.; Spaltmann, D.; Rosenfeld, A.; Krüger, J. *Proc. SPIE* **2017,** *10092,* 100920N. doi:10.1117/12.2250919
25. Müller, F. A.; Kunz, C.; Gräf, S. *Materials* **2016,** *9,* 476. doi:10.3390/ma9060476
26. Feng, Y.; Liang, M.; You, R.; Li, T.; Zhu, L. *Front. Phys.* **2022,** *10,* 918372. doi:10.3389/fphy.2022.918372
27. Maurya, R. S.; Chaudhary, N.; Srujana, P.; Rajput, V. K.; Naraharisetty, S. R. G.; Radhakrishnan, T. P. *Adv. Opt. Mater.* **2024,** *12,* 2302279. doi:10.1002/adom.202302279
28. Mangalassery, S.; Chaudhary, N.; Naraharisetty, S. R. G. *Surf. Interfaces* **2023,** *42,* 103454. doi:10.1016/j.surfin.2023.103454
29. Wang, X.; Du, W.; JJ Nivas, J.; Zhao, B.; Zhao, X.; Amoruso, S. *ACS Appl. Mater. Interfaces* **2024,** *16,* 2921–2931. doi:10.1021/acsami.3c15234
30. Rivera-Sahún, J.; Porta-Velilla, L.; de la Fuente, G. F.; Angurel, L. A. *Polymers (Basel, Switz.)* **2022,** *14,* 5554. doi:10.3390/polym14245554
31. Yulianto, N.; Titok Sugiarto, I.; Panji Tresna, W.; Suwardy, J.; Majid, N.; Herbani, Y.; Isnaeni; Anggoro Ardy Nugroho, F. *J. Phys.: Conf. Ser.* **2024,** *2696,* 012002. doi:10.1088/1742-6596/2696/1/012002
32. Dar, M. H.; Kuladeep, R.; Saikiran, V.; D., N. R. *Appl. Surf. Sci.* **2016,** *371,* 479–487. doi:10.1016/j.apsusc.2016.03.008
33. Kobayashi, T.; Wakabayashi, T.; Takushima, Y.; Yan, J. *Precis. Eng.* **2019,** *57,* 244–252. doi:10.1016/j.precisioneng.2019.04.012
34. Reif, J.; Costache, F.; Henyk, M.; Pandelov, S. V. *Appl. Surf. Sci.* **2002,** *197–198,* 891–895. doi:10.1016/s0169-4332(02)00450-6
35. Zhang, D.; Ranjan, B.; Tanaka, T.; Sugioka, K. *Nanomaterials* **2020,** *10,* 1573. doi:10.3390/nano10081573
36. Rivera, L. P.; Munoz-Martin, D.; Chávez-Chávez, A.; Morales, M.; Gómez-Rosas, G.; Molpeceres, C. *Mater. Sci. Eng., B* **2021,** *273,* 115393. doi:10.1016/j.mseb.2021.115393
37. Zhang, H.; Colombier, J.-P.; Li, C.; Faure, N.; Cheng, G.; Stoian, R. *Phys. Rev. B: Condens. Matter Mater. Phys.* **2015,** *92,* 174109. doi:10.1103/physrevb.92.174109
38. Garcia-Lechuga, M.; Puerto, D.; Fuentes-Edfuf, Y.; Solis, J.; Siegel, J. *ACS Photonics* **2016,** *3,* 1961–1967. doi:10.1021/acsphotonics.6b00514
39. JJ Nivas, J.; Anoop, K. K.; Bruzzese, R.; Philip, R.; Amoruso, S. *Appl. Phys. Lett.* **2018,** *112,* 121601. doi:10.1063/1.5011134
40. Bonse, J.; Munz, M.; Sturm, H. *J. Appl. Phys.* **2005,** *97,* 013538. doi:10.1063/1.1827919
41. Borowiec, A.; Haugen, H. K. *Appl. Phys. Lett.* **2003,** *82,* 4462–4464. doi:10.1063/1.1586457

42. Hwang, J. S.; Park, J.-E.; Kim, G. W.; Lee, H.; Yang, M. *Appl. Surf. Sci.* **2021,** *547,* 149178. doi:10.1016/j.apsusc.2021.149178
43. Wang, X.; Li, C.; Ma, C.; Feng, J.; Hong, W.; Zhang, Z. *Opt. Express* **2018,** *26,* 6325. doi:10.1364/oe.26.006325
44. Le Harzic, R.; Dörr, D.; Sauer, D.; Stracke, F.; Zimmermann, H. *Appl. Phys. Lett.* **2011,** *98,* 211905. doi:10.1063/1.3593493
45. Pan, A.; Dias, A.; Gomez-Aranzadi, M.; Olaizola, S. M.; Rodriguez, A. *J. Appl. Phys.* **2014,** *115,* 173101. doi:10.1063/1.4873459
46. Bonse, J.; Gräf, S. *Laser Photonics Rev.* **2020,** *14,* 2000215. doi:10.1002/lpor.202000215
47. Le Harzic, R.; Dörr, D.; Sauer, D.; Neumeier, M.; Epple, M.; Zimmermann, H.; Stracke, F. *Opt. Lett.* **2011,** *36,* 229–231. doi:10.1364/ol.36.000229
48. Fedorov, V. Yu.; Colombier, J.-P. *arXiv* **2024,** 2405.10873. doi:10.48550/arxiv.2405.10873
49. Vorobyev, A. Y.; Guo, C. *J. Appl. Phys.* **2008,** *103,* 043513. doi:10.1063/1.2842403
50. Kunz, C.; Engel, S.; Müller, F. A.; Gräf, S. *Nanomaterials* **2020,** *10,* 1187. doi:10.3390/nano10061187
51. Taher, M. A.; Rajput, V. K.; Krishnan P K, N.; Naraharisetty, S. R. G. *J. Phys. D: Appl. Phys.* **2022,** *55,* 055305. doi:10.1088/1361-6463/ac30b8
52. Taher, M. A.; Chaudhary, N.; Thirunaukkarasu, K.; Rajput, V. K.; Naraharisetty, S. R. G. *Surf. Interfaces* **2022,** *28,* 101622. doi:10.1016/j.surfin.2021.101622
53. Shi, Y.; Kim, H. K. *Nano Convergence* **2018,** *5,* 16. doi:10.1186/s40580-018-0148-z
54. Hu, A.; Rybachuk, M.; Lu, Q.-B.; Duley, W. W. *Appl. Phys. Lett.* **2007,** *91,* 131906. doi:10.1063/1.2793628
55. Florian, C.; Fuentes-Edfuf, Y.; Skoulas, E.; Stratakis, E.; Sanchez-Cortes, S.; Solis, J.; Siegel, J. *Materials* **2022,** *15,* 7468. doi:10.3390/ma15217468
56. Wang, S. Y.; Ren, Y.; Cheng, C. W.; Chen, J. K.; Tzou, D. Y. *Appl. Surf. Sci.* **2013,** *265,* 302–308. doi:10.1016/j.apsusc.2012.10.200
57. Dauscher, A.; Feregotto, V.; Cordier, P.; Thomy, A. *Appl. Surf. Sci.* **1996,** *96–98,* 410–414. doi:10.1016/0169-4332(95)00495-5
58. Pastras, G.; Fysikopoulos, A.; Giannoulis, C.; Chryssolouris, G. *Int. J. Adv. Manuf. Technol.* **2015,** *78,* 723–736. doi:10.1007/s00170-014-6674-x
59. Barnes, W. L.; Dereux, A.; Ebbesen, T. W. *Nature* **2003,** *424,* 824–830. doi:10.1038/nature01937
60. Jyothi, J.; Biswas, A.; Sarkar, P.; Soum-Glaude, A.; Nagaraja, H. S.; Barshilia, H. C. *Appl. Phys. A: Mater. Sci. Process.* **2017,** *123,* 496. doi:10.1007/s00339-017-1103-2
61. Baccarelli, P.; Frezza, F.; Simeoni, P.; Tedeschi, N. *Materials* **2018,** *11,* 1595. doi:10.3390/ma11091595
62. Nakhoul, A.; Maurice, C.; Agoyan, M.; Rudenko, A.; Garrelie, F.; Pigeon, F.; Colombier, J.-P. *Nanomaterials* **2021,** *11,* 1020. doi:10.3390/nano11041020
63. Ash, C.; Dubec, M.; Donne, K.; Bashford, T. *Lasers Med. Sci.* **2017,** *32,* 1909–1918. doi:10.1007/s10103-017-2317-4
64. Miyasaka, Y.; Hashida, M.; Nishii, T.; Inoue, S.; Sakabe, S. *Appl. Phys. Lett.* **2015,** *106,* 013101. doi:10.1063/1.4905353
65. Faucon, M.; Mincuzzi, G.; Morin, F.; Hönninger, C.; Mottay, E.; Kling, R. *Proc. SPIE* **2015,** *9351,* 93510Q. doi:10.1117/12.2078915
66. Ho, C. Y.; Ma, C.; Tsai, Y. H. *Appl. Mech. Mater.* **2015,** *764-765,* 102–106. doi:10.4028/www.scientific.net/amm.764-765.102
67. Zavalov, Y. N.; Dubrov, A. V.; Makarova, E. S.; Dubrov, V. D. *J. Phys.: Conf. Ser.* **2019,** *1396,* 012045. doi:10.1088/1742-6596/1396/1/012045
68. Boyd, R. W. The Intensity-Dependent Refractive Index. *Nonlinear Optics,* 3rd ed.; Academic Press: Burlington, MA, USA, 2008; pp 207–252. doi:10.1016/b978-0-12-369470-6.00004-6
69. Boyd, R. W. Quantum-Mechanical Theory of the Nonlinear Optical Susceptibility. *Nonlinear Optics,* 3rd ed.; Academic Press: Burlington, MA, USA, 2008; pp 135–206. doi:10.1016/b978-0-12-369470-6.00003-4
70. Leng, Y.; Yang, D.; Ming, P.; Li, B.; Zhang, C. *World Electr. Veh. J.* **2021,** *12,* 101. doi:10.3390/wevj12030101
71. Chu, T. K.; Ho, C. Y. Thermal Conductivity and Electrical Resistivity of Eight Selected AISI Stainless Steels. In *Thermal Conductivity 15;* Mirkovich, V. V., Ed.; Springer: Boston, MA, USA, 1978; pp 79–104. doi:10.1007/978-1-4615-9083-5_12
72. Griffiths, D. J. *Introduction to Electrodynamics,* 4th ed.; Pearson: Boston, MA, USA, 2013.
73. Halid, N. S. T.; Zainal, R.; Daud, Y. M. *J. Teknol.* **2016,** *78,* 99–103. doi:10.11113/jt.v78.7472
74. Johnson, O. *J. Phys. Chem. Solids* **1984,** *45,* 811–819. doi:10.1016/0022-3697(84)90079-9

License and Terms

BEILSTEIN JOURNAL OF NANOTECHNOLOGY

Evaluating metal-organic precursors for focused ion beam-induced deposition through solid-layer decomposition analysis

Benedykt R. Jany*[1], Katarzyna Madajska[2], Aleksandra Butrymowicz-Kubiak[2], Franciszek Krok[1] and Iwona B. Szymańska[2]

Full Research Paper

Open Access

Address:
[1]Marian Smoluchowski Institute of Physics, Faculty of Physics, Astronomy and Applied Computer Science, Jagiellonian University, Lojasiewicza 11, 30348 Krakow, Poland and [2]Faculty of Chemistry, Nicolaus Copernicus University in Toruń, Gagarina 7, 87-100 Toruń, Poland

Email:
Benedykt R. Jany* - benedykt.jany@uj.edu.pl

* Corresponding author

Keywords:
backscattered electrons (BSE); carboxylates; energy-dispersive X-ray spectroscopy (EDX); focused ion beam (FIB); focused ion beam-induced deposition (FIBID); machine learning; scanning electron microscopy (SEM)

Beilstein J. Nanotechnol. **2025,** *16,* 1942–1951.
https://doi.org/10.3762/bjnano.16.135

Received: 17 July 2025
Accepted: 06 October 2025
Published: 04 November 2025

This article is part of the thematic issue "Energetic ions and photons for engineering nanomaterials".

Guest Editor: V. R. Soma

Abstract

The development of modern metal deposition techniques like focused ion/electron beam-induced deposition (FIBID/FEBID) relies heavily on the availability of metal-organic precursors of particular properties. To create a new precursor, extensive testing using specialized gas injection systems is required along with time-consuming and costly chemical analysis typically conducted using scanning electron microscopy (SEM). This process can be quite challenging due to its complexity and expense. Here, the response of new metal-organic precursors, in the form of supported thick layers, to the ion beam irradiation is studied through analysis of the chemical composition and morphology of the resulting structures. This is done using SEM backscattered electron/energy-dispersive X-ray spectroscopy along with machine learning data processing techniques. This approach enables a comprehensive fast examination of precursor decomposition processes during FIB irradiation and provides valuable insights into how the precursor's composition influences the final properties of the metal-rich deposits. Although solid-layer irradiation differs from gas-phase deposition, we think that our method can be employed to optimize pre-screen and score new potential precursors for FIB applications by significantly reducing the time required and conserving valuable resources.

Introduction

A variety of nanomanufacturing techniques, such as optical and electron-beam lithography, nanoimprint lithography, atomic layer deposition, chemical mechanical polishing, and laser nanopatterning, enable the creation of nanostructures and nanoscale devices. However, a major limitation of these methods is their inability to effectively produce high-resolution three-

dimensional nanostructures [1-4]. In contrast, focused electron or ion beam-induced deposition (FEBID/FIBID) allows for the precise fabrication of two- and three-dimensional nanostructures with well-defined shapes and dimensions ranging from 5 to 10 nm [1,5-10]. This high spatial resolution is achieved by precisely controlling the position and duration of the electron or ion beam pulses. In FEBID and FIBID, volatile precursor molecules are delivered to the substrate surface via a gas injection system (GIS), where they adsorb and are subsequently decomposed by a focused electron or ion beam with energies in the kiloelectronvolt range. While commercial FIBID systems commonly employ Ga^+ ions, alternative ion species such as He^+, Ne^+, Ar^+, or Xe^+ can also be used [11-14]. The resulting FEBID/FIBID deposits are widely used for repairing photolithographic masks and printing or modifying integrated circuits. In addition, they are applied for the fabrication or modification of cantilevers in AFM and scanning optical near-field microscopy, and as plasmonic materials [15-19]. FEBID/FIBID techniques combine the advantages of direct-write lithographic processes, for example, high spatial resolution, site-specificity, no need for masks, and resistance, with the flexibility of depositing materials on non-planar surfaces [4,5,14].

The FIBID method has several advantages compared to the FEBID technique in depositing thin films on substrates. First, ions generate more secondary electrons on the substrate surface than electrons, leading to faster deposition growth (around 100 times). Second, FIBID deposits have higher metal content and lower resistivity compared to FEBID. However, there are some disadvantages to FIBID, such as the larger size of noble gas and metal ions that penetrate to smaller depths in solids and result in significant beam-induced substrate defects (e.g., Ga atom implantation). Additionally, material growth is required to compete with the FIB milling process [4,9]. The use of ions instead of electrons, like in FEBID, offers several benefits, including enhanced film quality and adhesion, better control over the growth process, and greater flexibility in material selection (the ability to deposit a variety of different materials). The usage of ions opens new possibilities for materials development and applications [20,21].

Until now, the development of FEBID has relied on precursors used for chemical vapor deposition (CVD), a thermally driven process. However, these kinds of precursors were not optimized for the electron- and ion-driven FEBID and FIBID processes [4,5,14]. Important classes of FEBID-tested compounds for group-11 elements have been β-diketonates and carboxylates. These compounds were used previously in CVD, and β-diketonates are the most common CVD precursors, yielding films of high purity up to 99 atom % [5,15,22-26]. In FEBID, silver(I) carboxylates, in contrast to β-diketonates, result in high metal content in the deposits. Recent research [5] using $[Ag_2(\mu\text{-}O_2CR)_2]$, where R = CF_3, C_2F_5, C_3F_7, *t*-Bu, or $C(Me)_2Et$, showed that these carboxylates can be dissociated via focused electron beams, yielding deposits with satisfying metal content (purity up to 76 atom % Ag). However, for the copper(II) carboxylate $[Cu_2(\mu\text{-}O_2CC_2F_5)_4]$, the fabricated materials have only up to 23 Cu atom % [5,15,22-26]. This shows that the electron beam-induced decomposition is influenced by the ligand and also by the coordination center.

Due to the key role played by secondary electrons in the decomposition of FIBID precursors, FIBID precursor compounds are limited to those used and tested in FEBID processes. Preliminary studies of new or potential FEBID precursors employ electron ionization mass spectrometry and gas-phase cross-beam experiments (dissociative ionization and dissociative electron attachment), but more informative are investigations into the interactions of molecules adsorbed on the surface, such as electron-stimulated desorption, high-resolution electron energy loss spectroscopy, and focused electron beam secondary ion mass spectrometry [5].

To characterize compounds in terms of their applicability in the FIBID process, comparisons are made with the FEBID process, and decomposition mechanisms are proposed. Studies have been conducted on ion–molecule interactions in both solid and gas phases. Ultrahigh vacuum experiments on a few monolayers of FIBID precursors, such as $[Ru(CO)_4I_2]$, $[(\eta^5\text{-}C_5H_5)Fe(CO)_2Re(CO)_5]$, and $[Fe(CO)_5]$, have been used to elucidate decomposition pathways. These studies also enabled a clear distinction between the processes occurring under ion irradiation and under electron irradiation. Furthermore, investigations on the gold complex $[AuMe_2(hfac)]$ have allowed for the assessment of the influence of ion type (mass) and ion energy on molecular decomposition. Gas-phase interactions between $[Fe(CO)_5]$ molecules and ions of helium, neon, argon, and krypton were carried out. However, the authors noted that these results may not accurately reflect the behavior of the precursor on the surface during actual FIBID processing since the conditions under which the study was conducted (pressure and cleanliness) differ significantly from those of a typical FIBID process [14].

To guide the development of more effective precursors for FEBID, a pre-screening strategy combining electron ionization mass spectrometry (EIMS) and volatility testing is typically applied. EIMS reveals how ligands respond to electron irradiation; simple molecules such as CO and CO_2 detach cleanly, making them “favorable” in FEBID. In contrast, anionic or polyhapto ligands, such as cyclopentadienyl (Cp) or allyl fragments, readily fragment form C_xH_y matrices, leading to film

contamination and degradation of structural quality. Halogen atoms (e.g., Cl and Br) remain bound during initial irradiation and are typically released only at high electron doses, posing risks of side reactions or inhomogeneous film formation. Volatility is assessed via the sublimation temperature; precursors with an onset below 100 °C are considered suitable for efficient transport through a GIS. Those with higher sublimation points are unlikely to reach the deposition zone and are thus disqualified early. Despite its advantages, EIMS pre-screening has significant limitations; it cannot determine the final film composition, metal oxidation states, or actual deposition efficiency. Results are also sensitive to sample purity and ionization conditions, and the method does not replicate the real gas-phase or ion-beam environments encountered in FIBID [27].

One has to mention that testing new metal-organic precursors for the use in FEBID/FIBID is a tedious time-consuming task, which requires costly experimental (non-commercial) GIS systems. The primary objective of this precursor testing is to optimize deposition parameters, specifically targeting high metal content (favoring minimal impurities of gallium from the FIB source) and reduced ion currents. It is also important to optimize beam energy for the deposition. Tripathi et al. [27] correlated ion beam parameters to the deposition characteristics using Ga FIB and various available precursors. Several tests of many different new precursors have to be done before deciding which compound is the most promising one. Therefore, we used in our studies copper(II) and silver(I) carboxylate complexes such as non-fluorinated pivalate $[Cu_2(\mu\text{-}O_2C\textit{t}\text{-}Bu)_4]_n$ [28,29], perfluorinated pentafluoropropionates $[Cu_2(\mu\text{-}O_2CC_2F_5)_4]$ [30], $[Ag_2(\mu\text{-}O_2C_2F_5)_2]$ [31] and the heteroligand complex with the same carboxylate and pentafluoropropamidine $[Cu_2(NH_2(NH{=})CC_2F_5)_2(\mu\text{-}O_2CC_2F_5)_4]$ [32], as new potential precursors for the applications in focus ion beam induced deposition (FIBID) using gallium ions. We focused on a commonly used 30 keV FIB ion beam energy in our systematic decomposition studies.

Here, we present a pathway for unraveling how the chemical composition of metal-organic precursors affects their decomposition when irradiated with FIB in the form of supported layers. A decomposition process of the studied layer was quantitatively monitored by scanning electron microscopy backscattered electron (SEM BSE) analysis. For each studied precursor, an optimal ion fluence was determined, defined as the ion fluence at which the sputtering of the formed metal-rich structures becomes the dominant process, exceeding the rate of precursor decomposition and material buildup. While sputtering occurs throughout ion irradiation, this point marks the transition beyond which further irradiation leads primarily to material removal rather than the structure growth. The structures formed at “the optimal” ion fluence were examined by scanning electron microscopy energy-dispersive X-ray spectroscopy (SEM EDX) together with machine learning-based hyperspectral data processing, which uses non-negative matrix factorization (NMF) to separate the EDX signals of structures from the ones of the substrate. As already shown, this type of analysis greatly enhances the applicability of SEM EDX for the analysis of nanostructures [33]. Finally, we determined the quantitative chemical composition of the formed metal-rich deposits (structures). While the decomposition of precursor layers presents a significant challenge compared to gas-phase deposition driven by differing mechanisms, our approach of layer analysis offers crucial insights into the fundamental physics of metal deposition from metal-organic precursors. Furthermore, we believe that our methodology could be effectively utilized as a valuable tool for precursor screening. The use of a new compound as a FIBID/FEBID precursor necessitates a series of preliminary tests to confirm volatility and sensitivity to secondary electrons. Refining the conditions for efficient precursor delivery via the GIS system and its subsequent decomposition under ion beam influence requires testing in a difficult-to-access experimental reactor. Given the time- and cost-intensive nature of analyzing the morphology and composition of the deposits, we propose a method/approach to minimize studies within the experimental reactor and identify promising potential precursors.

Testing Pathway and Methods Used

The proposed approach for effectively testing new metal-organic precursors involves a series of steps that are crucial to ensure accurate and comprehensive results. These stages include: (1) Deposition of the precursor onto a Si(111) substrate through sublimation using previously established parameters [22,29,32,34]. This step allows for precise control of the thickness of the precursor layer on the substrate. (2) Performing SEM imaging of the growth layers, which provide detailed information about the surface structure and composition of the precursor layer. They are essential for understanding how the precursors are decomposed under the following FIB irradiation and what kind of morphology is developed for the finally formed metal-rich structures. (3) Analyzing BSE images of the evolving surface morphology at successive stages of FIB irradiation in order to determine “the sputtering point”, that is, the threshold ion fluence at which the sputtering becomes the dominant process over structure growth, leading to the erosion of the formed metal-rich deposits. This threshold provides insight into the precursor’s resistance to ion bombardment and is crucial for assessing its stability and reactivity under processing conditions. (4) Collecting SEM EDX hyperspectral data, which involves acquiring multiple X-ray spectra from different points of the final sample morphology. This step allows for a

more detailed analysis of the chemical composition and distribution of elements within the irradiated sample. (5) Decomposing SEM EDX hyperspectral data using advanced algorithms to separate and identify individual components within the irradiated sample. This process is essential for obtaining accurate and reliable information about the chemical composition of developed deposits. (6) Determining the chemical composition of the developed structures using the EDX ZAF technique, which is a high-resolution analytical method that can provide elemental information at the nanoscale. This step ensures precise identification and quantification of all elements present in the grown structures. (7) The final step involves examining the chemical composition of the resulted precursor layers and coupling it with ion beam parameters to score the precursor usability. This stage is crucial for determining the potential applications and limitations of new metal-organic precursors in various fields.

In the following, each of these steps will be explored in greater detail, providing a more in-depth understanding of the proposed pathway for successful testing of the new potential FIBID precursors.

The Fabrication of the Precursor Thin Layer

The metal-organic precursors films for the FIB/SEM experiments were deposited by sublimation using a glassware sublimation apparatus. The Si(111) wafer was placed in the special holder on the cold finger of the apparatus. The process was performed under a pressure of 10^{-2} mbar and at the following temperatures: 418 K – $[Cu_2(\mu\text{-}O_2Ct\text{-}Bu)_4]$ [29] (**1**), 393 K – $[Cu_2(NH_2(NH{=})CC_2F_5)_2(\mu\text{-}O_2CC_2F_5)_4]$ [32] (**2**), 413 K – $[Cu_2(\mu\text{-}O_2CC_2F_5)_4]$ (**3**), and 413 K $[Ag_2(\mu\text{–}O_2CC_2F_5)_2]$ (**4**) (Figure 1). The conditions for depositing layers of compounds **1** and **2** were previously determined [29,32]. In a similar way, the layers of the complexes **3** and **4** were prepared. The grown layer compositions were checked by IR spectroscopy before electron beam irradiation. IR spectra were registered with a Vertex 70V spectrometer (Bruker Optik, Leipzig, Germany) using a single reflection diamond ATR unit (400–4000 cm^{-1}). IR spectra of the obtained layers and the initial compounds **1**–**4** are presented in Figure 1b. The spectra showed characteristic $\nu_{as}(COO)$ and $\nu_s(COO)$ bands of bonded carboxylate ligands (compounds **1**–**4**), as well as $\nu_{as}(NH_2)$, $\nu(=NH)$, $\delta(NH_2)$, and $\nu(N{=}C{-}N)$ bands of coordinated amidine ligands for complex **2** (Figure 1b and Supporting Information File 1, Table S1) confirming the formation of suitable layers of the studied complexes.

SEM operating in secondary electron mode provided clear and precise images of the deposited layers (Figure 1a). The thickness of the grown layers was determined, yielding 8.14 µm for **1**, 6.03 µm for **2**, 1.41 µm **3**, and 1.07 µm for **4**. The experiments were conducted using a dual-beam SEM/FIB microscope "Quanta 3D FEG" manufactured by FEI. The microscope is equipped with a gallium FIB and an EDAX Ametek SDD EDX detector setup.

FIB/SEM Irradiation Experiments and EDX Chemical Composition Quantification

In these experiments, a 30 keV energy beam was employed for raster scanning over a 50 µm × 50 µm square area with a dwell time of 200 ns. Ion beam current and duration of the experi-

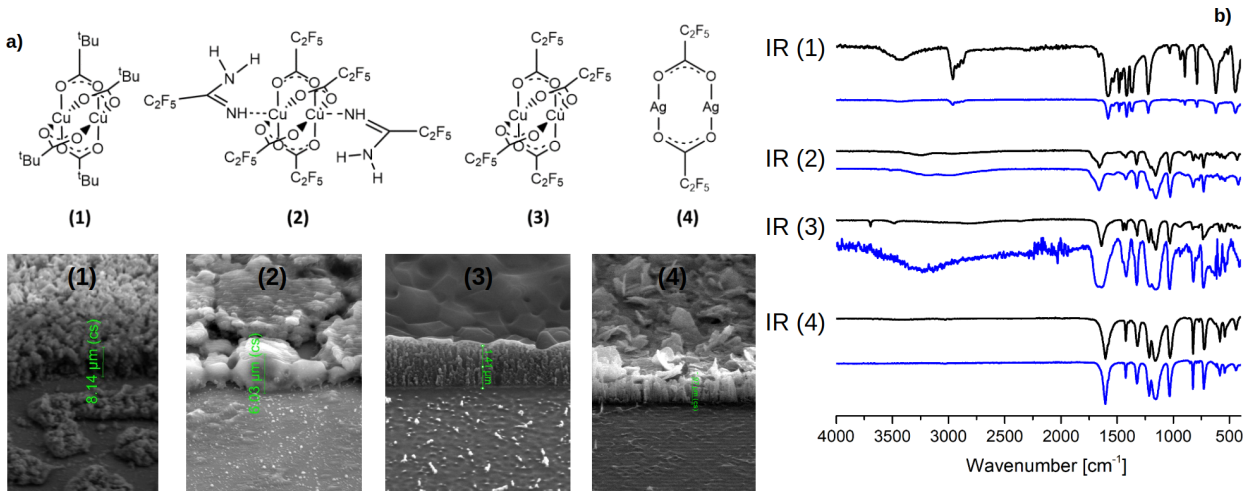

Figure 1: (a) SEM secondary electron images showing thickness and morphology of the precursor layers of **1**–**4**. (b) Infrared spectra before (black) and after sublimation on a silicon wafer (blue) for the compounds **1**–**4** ($p = 10^{-2}$ mbar).

ments were adjusted (within a range of 1 to 10 nA for the ion current, and 10 s to 10 min the irradiation) in order to achieve the optimal ion fluence necessary for the decomposition of the entire precursor layer. Time-dependent changes in the morphology of the irradiated films were tracked using the SEM BSE signal, which is directly proportional to the average atomic number *Z*. BSE morphology changes during Ga FIB experiments for the precursor **4** are presented in Figure 2a. The initial layer consists of grain-like structures, the blurred BSE contrast indicates that the layer has a rather homogeneously distributed chemical composition, and only a few low-contrast grooves are visible. During ion irradiation, the BSE contrast increases strongly already in the very early stages of bombardment. An increasing number of ("grid") dark contrast grooves separating elongated island-like features become more apparent. The precursor layer underwent decomposition leading to the development of surface features enriched with metallic element of the primary film.

The quantitative changes are presented in Figure 2b, which shows the mean BSE signal intensity, acquired while imaging the surface structures formed, as a function of the ion beam irradiation time. It is seen that, at the initial stages of irradiation, the BSE signal rapidly rises (in comparison to the not irradiated reference sample). Next one sees increase of the metal content, and the precursor decomposes. Finally, the BSE signal rapidly drops; all precursor material already decomposed into the metal-rich phase, the sputtering of the metal phase has begun to dominate, and the layer is getting thinner and thinner and finally is sputtered off (as in Figure 1b–e). From this dependence, one can determine the optimal sputtering point, that is, the maximal ion dose to decompose the given precursor layer without dominant sputtering, after which we stop the experiments. In Figure 2c, BSE morphologies of the four studied precursors **1**–**4** are shown. The BSE morphology of the initial (reference) material is presented together with the BSE morphology of the precursors after Ga FIB experiments regarding the optimal sputtering point.

It is seen that, for all precursors the morphology changed significantly; all precursors decomposed into a metal-rich phase. The initially compact films change to a network of interconnected and elongated island-like structures. In order to determine the chemical composition of the resulting structures, EDX data were collected in the hyperspectral mode, that is, for each *x*, *y*-position a full EDX spectrum was collected. The EDX measurements were performed at 20 keV electron beam energy. The EDX data were analyzed first by generating net count (background subtracted) maps of the elements. Figure 3a shows the SEM EDX hyperspectral mapping analysis results for precursor

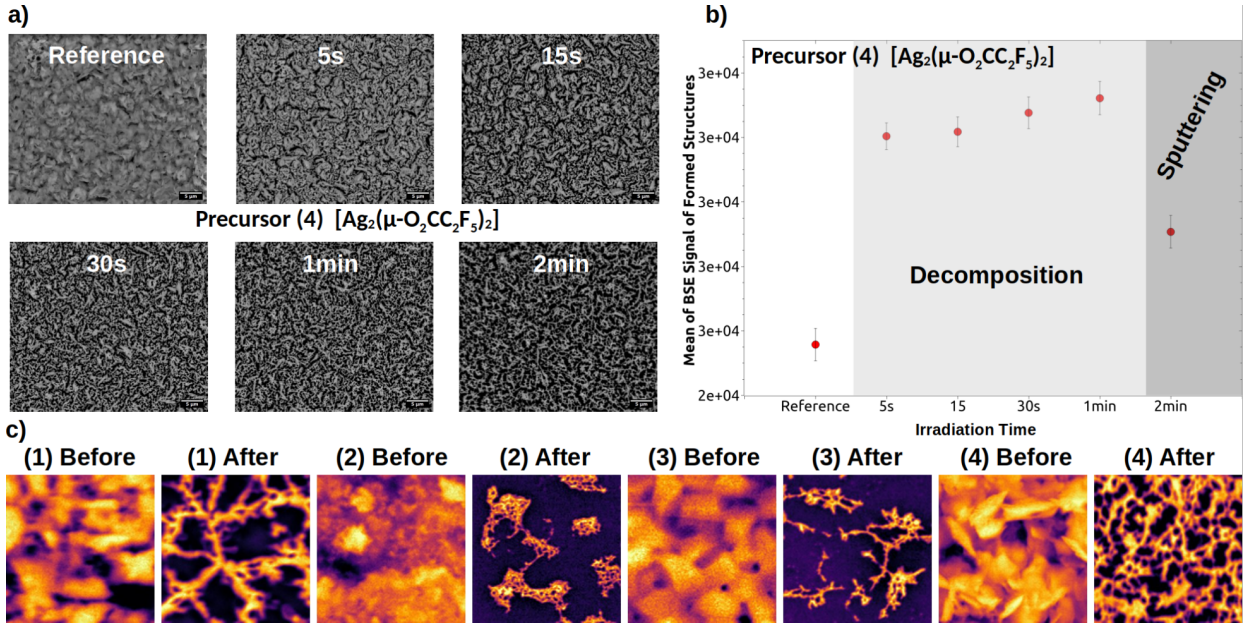

Figure 2: (a) SEM BSE morphology evolution studies of precursor **4** layer decomposition during gallium FIB irradiation experiments. (b) SEM BSE intensity (proportional to the atomic number *Z*) changes of the formed structures, as in (a), during gallium FIB irradiation experiments for precursor **4**. The BSE intensity increases during FIB irradiation (metal content increases), the precursor decomposes up to sputtering point at which the formed metal-rich structures do not further develop and sputtering of the structures by FIB gallium ions dominates. (c) SEM BSE morphology before (initial surface) and after gallium FIB decomposition experiments of the layers of precursors **1**–**4**.

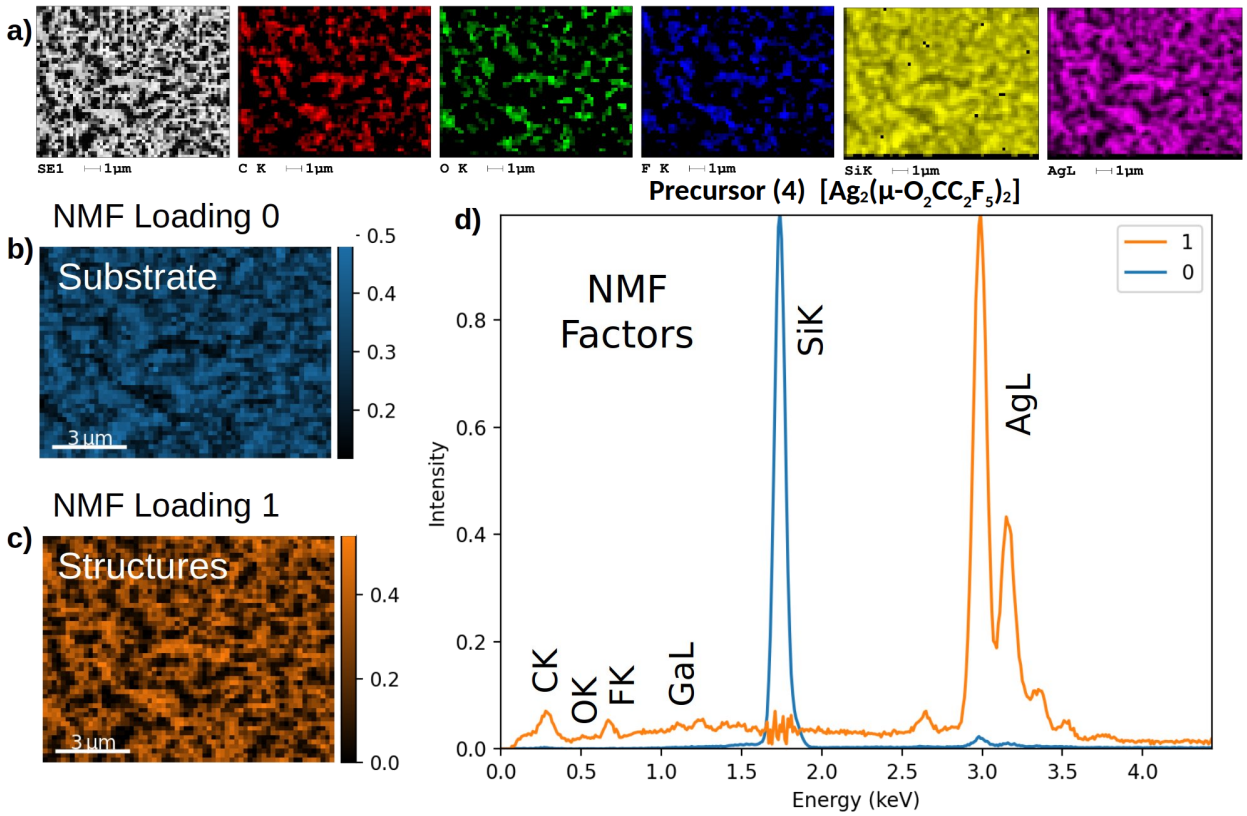

Figure 3: (a) Results of the SEM EDX hyperspectral mapping analysis of the precursor **4** layer after gallium FIB decomposition experiments; from left: BSE image and corresponding elemental net count maps of C K, O K, F K, Si K, and Ag L lines. Results of machine learning NMF decomposition of the collected SEM EDX hyperspectral data b)–d). NMF loadings showing spatial distribution of the NMF decomposition components b) substrate, c) structures together with NMF factors corresponding to the decomposed EDX signal d). It is seen that the EDX silicon substrate signal is succesfully separated from the signal of the metal-rich structures (Si K peak). This allows for the chemical composition quantification via EDX ZAF method.

4 after Ga FIB decomposition experiments, including the BSE image and the corresponding elemental net count Kα maps for the elements C, O, F, and Si, as well as the Ag Lα map (see Supporting Information File 1, Figure S2–S4 for other precursors). In all cases, the maps show that the formed structures are enriched in metal. In the next step, the EDX data were processed by machine learning NMF as described in details in Jany and colleagues [33]. In Figure 3b,c, the spatial distribution of the individual elements derived from NMF is depicted in the form of loading plots for the substrate and the structures. These plots are shown in color to visually distinguish between the different elements. The substrate layer is shown in blue, while the structure features are displayed in orange. Additionally, the NMF factors that correspond to the decomposed energy-dispersive X-ray spectra are shown in Figure 3d. It is evident that the performed NMF has successfully separated the EDX signal originating from the grown structures from the EDX signal coming from the silicon substrate. Subsequently, these distinct EDX signals were employed to quantify the chemical composition of the structures using an energy-dispersive X-ray EDX ZAF method in a standardless approach.

Results and Discussion

The chemical compositions of the formed structures are presented in Table 1. The table shows the parameters of gallium ion FIB experiments carried out on deposited layers of **1**–**4** at their optimal sputtering point, along with SEM EDX chemical composition analysis of the formed structures on the sample surface. For the initial precursor composition please see Table S2 in Supporting Information File 1. To ensure a fair and accurate comparison between different precursor parameters, it was necessary to take into account the different thicknesses of the precursor layers. In order to achieve this, we decided to utilize an ion fluence that had been normalized to the specific height of the individual precursor layer, *Fh* = fluence/(layer height). The fluence [ions·cm^{-2}] and fluence per height [ions·cm^{-2}·µm^{-1}] values are also presented in Table 1 as well as the results from previous FEBID experiments for the complexes **3** and **4** [5,15,23]. In the absence of FIBID data for the precursors, the FEBID experiments provide a valuable means of comparison to the gas-phase studies. The results allow us to evaluate the performance of the new precursors by correlating ion beam parameters with the chemical composition of the forming structures.

Table 1: Fluence and *Fh* = Fluence/(layer height) of the final Ga FIB experiments performed (at optimal sputtering point) on layers of precursors **1**–**4**, together with SEM EDX chemical composition of the formed structures after precursor decomposition. The volume/dose is also estimated for each precursor. Results of previously performed FEBID experiments are given for comparison. In the final column, a metric called precursor score (*Sp*) is included, which is calculated as metal content divided by [gallium content × log(*Fh*)].

Precursor	Parameters of Ga FIB experiments			SEM EDX content of the formed metal-rich structures on the sample surface [atom %]						*Sp*
	fluence [ions/cm^2]	*Fh* [ions·cm^{-2}· µm^{-1}]	volume/dose [µm^3·nC^{-1}]	C	N	O	F	Ga	metal	
1	1.2 × 10^{18}	1.47 × 10^{17}	0.0090 (0.0054)	62.57 (0.13)	–	7.73 (1.5)	–	22.22 (0.44)	Cu: 15.39 (0.31)	0.040
2	4.49 × 10^{16}	7.45 × 10^{15}	0.023 (0.014)	24.5 (4.9)	11.6 (2.3)	6.65 (1.3)	24.2 (4.8)	<0.3	Cu: 33.1 (0.66)	6.951
3	1.5 × 10^{17}	1.06 × 10^{17}	0.0030 (0.0018)	22.21 (0.89)	–	10.98 (2.2)	15.18 (0.61)	8.69 (0.35)	Cu: 42.93 (0.86)	0.290
3 FEBID [15]	–	–	–	51–5	–	2–44	44–8	–	Cu: 19–23	–
4	1.5 × 10^{16}	1.40 × 10^{16}	0.21 (0.13)	17.27 (1.7)	–	2.99 (1.5)	15.74 (1.6)	1.44(0.72)	Ag: 64.0 (1.3)	2.753
4 FEBID [23]	–	–	–	20–47	–	1–34	3–5	–	Ag: 33–76	–
Pt FIBID [35,36]	–	–	0.5	24–58	–	2–4	–	20-28	Pt: 24–46	–

Analysis of the data in Table 1 enables us to determine how the potential new precursor is modified under the Ga FIB ion beam exposure. It is seen that for the precursor **3** and **4**, the final metal content obtained under Ga^+ FIB irradiation is comparable to that obtained in FEBID experiments.

It can be seen that the gallium content increases with *Fh*. It is also worth to notice that the 30 keV gallium ion range in copper and silver is almost the same (the longitudinal ranges of gallium ions as calculated by SRIM are 11.6 nm for copper, 11.0 nm for silver, and 28.6 nm for silicon). Additionally, we calculated the volume-to-dose rate for each studied complex based on the dimensions of the final structures and the applied ion dose. This enables us to compare the ability of studied precursors to form metal-rich structures under gallium ion FIB irradiation with that of the commonly used Pt precursor trimethyl(methylcyclopentadienyl)platinum(IV) [Pt(η^5-CpMe)Me$_3$] [35,36]. The results indicate that precursors **2** and **4** exhibit a performance comparable to that of the Pt precursor, with precursor **4** being the most comparable. Our ultimate goal was to identify the promising precursor that would exhibit a high metal content while minimizing gallium accumulation and decomposing efficiently at low ion fluence *Fh*. Detailed analyses of the chemical composition of the formed structures are presented in Figure 4. It is evident that the precursor **4** gave the highest metal content among the tested compounds, as observed in the atomic percentage values in Figure 4a. Figure 4b presents a visual representation of the ratio of gallium to the total metal content in the final structures. This allows for a comparison of gallium content to other metals within these structures, highlighting variations or trends among the different precursors. The data shows that, in the final metallic structures, precursor **1** yields a significantly higher gallium-to-other-metals ratio compared the other precursors. We also examined the relationship between ion fluence *Fh* and both the total metal content and the gallium content in the resulting structures. This analysis is illustrated in Figure 4c and Figure 4d, which show the metal and gallium atomic percentages normalized to *Fh*. The analysis revealed that precursors **2** and **4** yielded the highest metal content per unit of *Fh*, indicating that they decomposed most efficiently under Ga ion irradiation. In contrast, precursor **1** exhibited a higher propensity for gallium absorption during irradiation. By analyzing the ion beam-induced decomposition of the precursors, which resulted in the formation of structures with varying chemical composition, we were able to assign performance scores to each precursor. To visualize the relationship between the three key parameters, that is, gallium content, metal content, and *Fh*, we presented them in a three-dimensional scatter plot (Figure 4e). To support the selection of the most suitable precursor, we developed a precursor score *Sp* = (metal content)/(galium content × log(*Fh*)), as summarized in Table 1. This scoring system prioritizes precursors that, upon decomposition, yield structures with high metal content and low gallium content at the minimal ion fluence *Fh* and accurately reflects each precursor's overall performance. This parameter allowed for a quick numerical assessment of precursor performance, helping to identify the

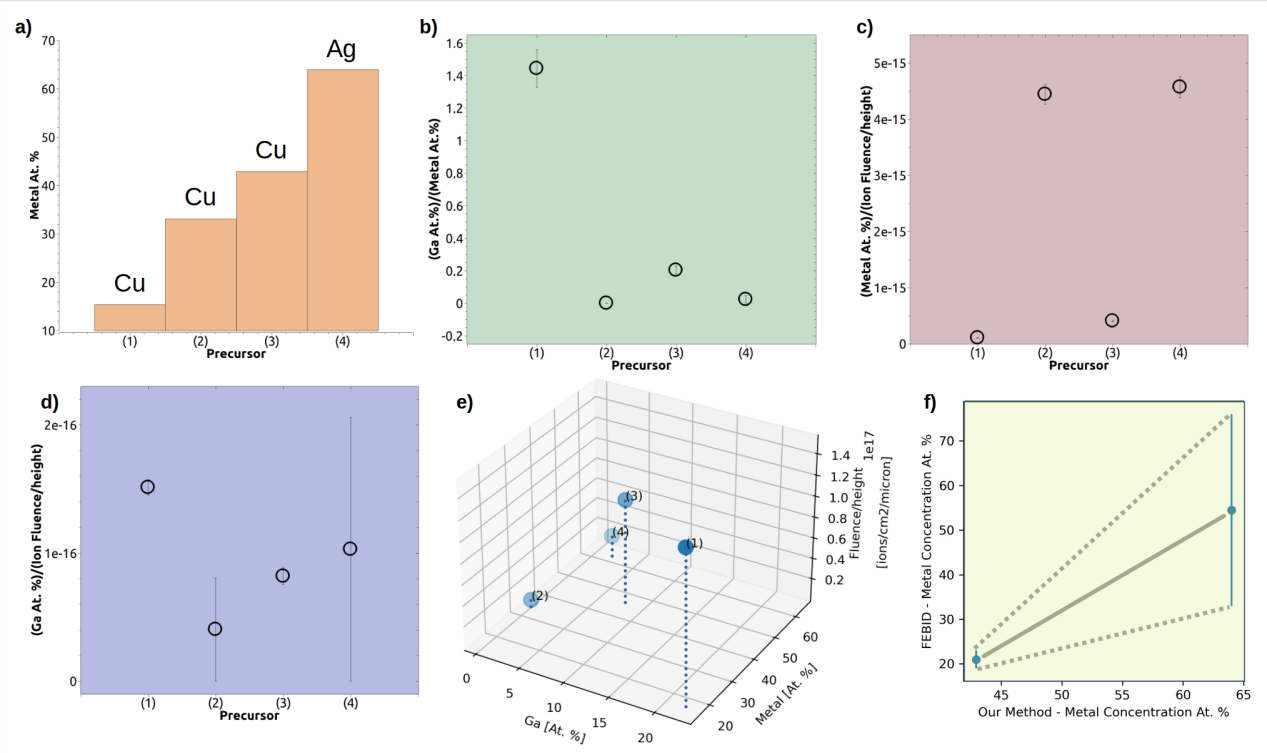

Figure 4: Investigation of chemical composition (precursor performance) for the studied precursors **1**–**4** after gallium FIB experiments. (a) Metal content in atom % in the final structures. It is seen that precursor **4** yields the highest metal content. (b) Ratio of gallium to metal in the final structures. Precursor **1** accumulates the highest amount of gallium in comparison to metal. Ratio of (c) metal and (d) gallium atom % to ion fluence *Fh*. Precursors **2** and **4** decompose most easily during FIB experiments producing the highest amount of metal per ion fluence *Fh*. Precursor **1** absorbs the most gallium in terms of amount of gallium per fluence during irradiation. (e) Three-dimensional representation showing the relationship between gallium content, metal content, and ion fluence *Fh*. (f) Average metal content in atomic percent obtained for precursors **3** and **4** using FEBID versus the metal content of the precursors as determined by our layer decomposition method.

most suitable candidates for further investigation or use in FIBID. In this context, the results indicate that precursors **2** and **4** appeared to yield the best balance among all three optimized parameters and among the four studied compounds. Finally, to validate our approach, we compared the FEBID metal content data available in the literature (Table 1) with the values obtained using the present layer decomposition methodology (Figure 4f). The figure shows the average atomic metal content for precursors **3** and **4** measured in FEBID experiments versus the metal content determined using our ion-beam-based decomposition method. It is seen that, on average, there is a relation between these two values of the metal content. Independently of the different mechanisms governing layer decomposition under ion beam irradiation and gas-phase deposition in FEBID, our results demonstrate that the proposed method provides valuable insight into the behavior of metal deposition from metal-organic precursors. We also believe that our methodology could be used as a valuable tool for rapid precursor screening and evaluation.

All of our precursor tests, as well as the final precursor scoring process, were carried out using a straightforward and widely accessible testing method. This approach involved conducting precursor layer tests on SEM and utilizing both BSE and EDX analyses. By employing this commonly available methodology, we aimed to ensure that our results would be replicable and relevant to a wide range of potential precursors. The collected SEM BSE and EDX data together with an exemplary Python Jupyter notebook to analyze EDX hyperspectral data are freely available from Zenodo [37].

Conclusion

In this research, we studied the ion-beam-induced decomposition of four Cu or Ag metal-organic precursors (i.e., ($[Cu_2(\mu\text{-}O_2Ct\text{-}Bu)_4]$ (**1**), $[Cu_2(NH_2(NH{=})CC_2F_5)_2(\mu\text{-}O_2CC_2F_5)_4]$ (**2**), $[Cu_2(\mu\text{-}O_2CC_2F_5)_4]$ (**3**), and $[Ag_2(\mu\text{-}O_2CC_2F_5)_2]$ (**4**)) exposed to 30 keV gallium FIB irradiation. Individual precursor layers were deposited onto silicon substrates via sublimation and subsequently exposed to gallium FIB irradiation. The optimal ion fluence for each precursor was determined by monitoring changes in the BSE signal intensity associated with the evolving surface morphology. The resulting metal-rich surface structures were analyzed using SEM EDX processed by machine learning techniques to extract the chemical composition. The study revealed that the silver precursor **4** produced the highest overall

metal content in the final structures, while the copper precursor **1** resulted in the highest level of gallium incorporation. The copper precursors **2** and **4** demonstrated superior performance in terms of metal yield per unit of ion fluence per height, *Fh*, indicating that they decomposed more readily compared to the other tested precursors. To evaluate the overall effectiveness of each precursor, a scoring system called precursor score, *Sp*, was introduced, which incorporates metal content, gallium content, and ion fluence per height required for decomposition. The results showed that precursors **2** and **4** achieved the highest precursor scores, indicating their superior ability to balance all three parameters. It is worth to notice that precursor **4**, which is Ag-based, was also tested in FEBID and gave very good results. To validate our approach, we compared our results with FEBID data, revealing a consistent relationship between the two methods regarding the final metal content. The study highlights the importance of understanding the chemical composition of various potential precursors for producing metal-rich structures using Ga FIB techniques. By employing a straightforward testing methodology, we identified promising carboxylate complexes that could potentially be applied across various fields and applications. Analyzing precursor layer decomposition presents unique challenges compared to gas-phase metal deposition due to differing underlying processes. However, our method consistently provides valuable insights into the physics governing metal deposition from metal-organic precursors. This approach shows significant potential as a tool for evaluating and selecting promising precursor materials and could accelerate the development of metal-organic precursors specifically tailored for FIB, offering a cost-effective route to novel nanofabrication applications.

Supporting Information

Supporting Information File 1

Additional data.
[https://www.beilstein-journals.org/bjnano/content/supplementary/2190-4286-16-135-S1.pdf]

Acknowledgements

We would like to acknowledge members of the FIT4NANO Action (COST: CA19140 - Focused Ion Technology for Nanomaterials) for sharing their knowledge. The flask icon in the graphical abstract is from https://openclipart.org/detail/16987/erlenmeyr under the CC0 License, by jean_victor_balin.

Funding

We would like to acknowledge the support of the FIT4NANO Action (COST: CA19140 - Focused Ion Technology for Nanomaterials) for funding the scientific activities. This research was supported in part by the Excellence Initiative - Research University Program at the Jagiellonian University in Krakow and by Nicolaus Copernicus University in Torun Grants4NCUStudents 90-SIDUB.6102.66.2022.G4NCUS5.

Conflict of Interest

There are no conflicts of interest to declare.

Author Contributions

Benedykt R. Jany: conceptualization; formal analysis; investigation; methodology; visualization; writing – original draft. Katarzyna Madajska: investigation. Aleksandra Butrymowicz-Kubiak: investigation. Franciszek Krok: supervision; writing – review & editing. Iwona B. Szymańska: supervision; writing – original draft; writing – review & editing.

ORCID® iDs

Benedykt R. Jany - https://orcid.org/0000-0002-3196-7244
Aleksandra Butrymowicz-Kubiak - https://orcid.org/0000-0002-3885-1623
Franciszek Krok - https://orcid.org/0000-0002-6931-3545
Iwona B. Szymańska - https://orcid.org/0000-0002-1951-3733

Data Availability Statement

The collected experimental data are available from Zenodo https://doi.org/10.5281/zenodo.11354527

Preprint

A non-peer-reviewed version of this article has been previously published as a preprint: https://arxiv.org/abs/2406.10022

References

1. Li, P.; Chen, S.; Dai, H.; Yang, Z.; Chen, Z.; Wang, Y.; Chen, Y.; Peng, W.; Shan, W.; Duan, H. *Nanoscale* **2021,** *13,* 1529–1565. doi:10.1039/d0nr07539f
2. Barth, S.; Huth, M.; Jungwirth, F. *J. Mater. Chem. C* **2020,** *8,* 15884–15919. doi:10.1039/d0tc03689g
3. Bruchhaus, L.; Mazarov, P.; Bischoff, L.; Gierak, J.; Wieck, A. D.; Hövel, H. *Appl. Phys. Rev.* **2017,** *4,* 011302. doi:10.1063/1.4972262
4. De Teresa, J. M.; Orús, P.; Córdoba, R.; Philipp, P. *Micromachines* **2019,** *10,* 799. doi:10.3390/mi10120799
5. Utke, I.; Swiderek, P.; Höflich, K.; Madajska, K.; Jurczyk, J.; Martinović, P.; Szymańska, I. B. *Coord. Chem. Rev.* **2022,** *458,* 213851. doi:10.1016/j.ccr.2021.213851
6. Fang, C.; Chai, Q.; Lin, X.; Xing, Y.; Zhou, Z. *Mater. Des.* **2021,** *209,* 109993. doi:10.1016/j.matdes.2021.109993
7. Córdoba Castillo, R. Ferromagnetic Iron Nanostructures Grown by Focused Electron Beam Induced Deposition. *Functional Nanostructures Fabricated by Focused Electron/Ion Beam Induced Deposition;* Springer: Cham, Switzerland, 2014; pp 71–93. doi:10.1007/978-3-319-02081-5_4
8. Matsui, S.; Kaito, T.; Fujita, J.; Komuro, M.; Kanda, K.; Haruyama, Y. *J. Vac. Sci. Technol., B: Microelectron. Nanometer Struct.–Process., Meas., Phenom.* **2000,** *18,* 3181–3184. doi:10.1116/1.1319689

9. Huang, Y.; Yin, K.; Li, B.; Zheng, A.; Wu, B.; Sun, L.; Nie, M. *Nanoscale Horiz.* **2024,** *9,* 254–263. doi:10.1039/d3nh00407d
10. Sychugov, I.; Nakayama, Y.; Mitsuishi, K. *J. Phys. Chem. C* **2009,** *113,* 21516–21519. doi:10.1021/jp9079684
11. Allen, F. I. *Beilstein J. Nanotechnol.* **2021,** *12,* 633–664. doi:10.3762/bjnano.12.52
12. Utke, I.; Michler, J.; Winkler, R.; Plank, H. *Micromachines* **2020,** *11,* 397. doi:10.3390/mi11040397
13. Indrajith, S.; Rousseau, P.; Huber, B. A.; Nicolafrancesco, C.; Domaracka, A.; Grygoryeva, K.; Nag, P.; Sedmidubská, B.; Fedor, J.; Kočišek, J. *J. Phys. Chem. C* **2019,** *123,* 10639–10645. doi:10.1021/acs.jpcc.9b00289
14. Höflich, K.; Hobler, G.; Allen, F. I.; Wirtz, T.; Rius, G.; McElwee-White, L.; Krasheninnikov, A. V.; Schmidt, M.; Utke, I.; Klingner, N.; Osenberg, M.; Córdoba, R.; Djurabekova, F.; Manke, I.; Moll, P.; Manoccio, M.; De Teresa, J. M.; Bischoff, L.; Michler, J.; De Castro, O.; Delobbe, A.; Dunne, P.; Dobrovolskiy, O. V.; Frese, N.; Gölzhäuser, A.; Mazarov, P.; Koelle, D.; Möller, W.; Pérez-Murano, F.; Philipp, P.; Vollnhals, F.; Hlawacek, G. *Appl. Phys. Rev.* **2023,** *10,* 041311. doi:10.1063/5.0162597
15. Berger, L.; Jurczyk, J.; Madajska, K.; Edwards, T. E. J.; Szymańska, I.; Hoffmann, P.; Utke, I. *ACS Appl. Electron. Mater.* **2020,** *2,* 1989–1996. doi:10.1021/acsaelm.0c00282
16. Córdoba, R.; Ibarra, A.; Mailly, D.; Guillamón, I.; Suderow, H.; De Teresa, J. M. *Beilstein J. Nanotechnol.* **2020,** *11,* 1198–1206. doi:10.3762/bjnano.11.104
17. Manoccio, M.; Esposito, M.; Passaseo, A.; Cuscunà, M.; Tasco, V. *Micromachines* **2021,** *12,* 6. doi:10.3390/mi12010006
18. Lee, J. S.; Hill, R. T.; Chilkoti, A.; Murphy, W. L. *Biomater. Sci.* **2020,** 553–573. doi:10.1016/b978-0-12-816137-1.00037-4
19. Nakagawa, Y.; Yamaoka, T.; Sato, M.; Yamamoto, M.; Glanville, J. *Proc. SPIE* **1988,** *0923,* 114–120. doi:10.1117/12.945640
20. Utke, I.; Hoffmann, P.; Melngailis, J. *J. Vac. Sci. Technol., B: Microelectron. Nanometer Struct.–Process., Meas., Phenom.* **2008,** *26,* 1197–1276. doi:10.1116/1.2955728
21. Jungwirth, F.; Porrati, F.; Knez, D.; Sistani, M.; Plank, H.; Huth, M.; Barth, S. *ACS Appl. Nano Mater.* **2022,** *5,* 14759–14770. doi:10.1021/acsanm.2c03074
22. Martinović, P.; Rohdenburg, M.; Butrymowicz, A.; Sarigül, S.; Huth, P.; Denecke, R.; Szymańska, I. B.; Swiderek, P. *Nanomaterials* **2022,** *12,* 1687. doi:10.3390/nano12101687
23. Berger, L.; Madajska, K.; Szymanska, I. B.; Höflich, K.; Polyakov, M. N.; Jurczyk, J.; Guerra-Nuñez, C.; Utke, I. *Beilstein J. Nanotechnol.* **2018,** *9,* 224–232. doi:10.3762/bjnano.9.24
24. Höflich, K.; Jurczyk, J.; Zhang, Y.; Puydinger dos Santos, M. V.; Götz, M.; Guerra-Nuñez, C.; Best, J. P.; Kapusta, C.; Utke, I. *ACS Appl. Mater. Interfaces* **2017,** *9,* 24071–24077. doi:10.1021/acsami.7b04353
25. Jurczyk, J.; Höflich, K.; Madajska, K.; Berger, L.; Brockhuis, L.; Edwards, T. E. J.; Kapusta, C.; Szymańska, I. B.; Utke, I. *Nanomaterials* **2023,** *13,* 1516. doi:10.3390/nano13091516
26. Höflich, K.; Jurczyk, J. M.; Madajska, K.; Götz, M.; Berger, L.; Guerra-Nuñez, C.; Haverkamp, C.; Szymanska, I.; Utke, I. *Beilstein J. Nanotechnol.* **2018,** *9,* 842–849. doi:10.3762/bjnano.9.78
27. Tripathi, S. K.; Shukla, N.; Kulkarni, V. N. *Nucl. Instrum. Methods Phys. Res., Sect. B* **2008,** *266,* 1468–1474. doi:10.1016/j.nimb.2007.12.071
28. Guan, X.; Yan, R. *Synlett* **2020,** *31,* 359–362. doi:10.1055/s-0037-1610743
29. Butrymowicz-Kubiak, A.; Luba, W.; Madajska, K.; Muzioł, T.; Szymańska, I. B. *New J. Chem.* **2024,** *48,* 6232–6245. doi:10.1039/d3nj04959k
30. Szłyk, E.; Szymańska, I. *Polyhedron* **1999,** *18,* 2941–2948. doi:10.1016/s0277-5387(99)00199-0
31. Szłyk, E.; Łakomska, I.; Grodzicki, A. *Thermochim. Acta* **1993,** *223,* 207–212. doi:10.1016/0040-6031(93)80136-x
32. Madajska, K.; Szymańska, I. B. *Materials* **2021,** *14,* 3145. doi:10.3390/ma14123145
33. Jany, B. R.; Janas, A.; Krok, F. *Nano Lett.* **2017,** *17,* 6520–6525. doi:10.1021/acs.nanolett.7b01789
34. Madajska, K. Ph.D. Thesis, Nicolaus Copernicus University, Torun, Poland, 2022.
35. Tao, T.; Ro, J.; Melngailis, J.; Xue, Z.; Kaesz, H. *J. Vac. Sci. Technol., B: Microelectron. Process. Phenom.* **1990,** *8,* 1826–1829. doi:10.1116/1.585167
36. Puretz, J.; Swanson, L. W. *J. Vac. Sci. Technol., B: Microelectron. Nanometer Struct.–Process., Meas., Phenom.* **1992,** *10,* 2695–2698. doi:10.1116/1.586028
37. Jany, B. R. Data for "Evaluating Metal-Organic Precursors for Focused Ion Beam Induced Deposition through Solid-Layer Decomposition Analysis", Zenodo 2024. doi:10.5281/zenodo.11354527.

License and Terms